

**OUTER SPACE AND FOURIER SPACE:  
UNDERSTANDING FOREGROUNDS FOR NEUTRAL HYDROGEN  
EPOCH OF REIONIZATION MEASUREMENTS**

Saul Aryeh Kohn

A DISSERTATION

in

Physics and Astronomy

Presented to the Faculties of the University of Pennsylvania

in Partial Fulfillment of the Requirements for the Degree of Doctor of Philosophy

2018

Supervisor of Dissertation

Graduate Group Chairperson

---

James E. Aguirre  
Associate Professor of Physics and Astronomy

---

Joshua Klein  
Professor of Physics and Astronomy

Dissertation Committee:

Cullen Blake, Assistant Professor of Physics and Astronomy

Adam Lidz, Associate Professor of Physics and Astronomy

Elliot Lipeles, Associate Professor of Physics and Astronomy

Masao Sako, Associate Professor of Physics and Astronomy

*to my grandparents*

**OUTER SPACE AND FOURIER SPACE:**  
UNDERSTANDING FOREGROUNDS FOR NEUTRAL HYDROGEN  
EPOCH OF REIONIZATION MEASUREMENTS  
© COPYRIGHT  
2018  
Saul Aryeh Kohn

This work is licensed under the  
Creative Commons Attribution  
NonCommercial-ShareAlike 3.0  
License  
To view a copy of this license, visit  
<http://creativecommons.org/licenses/by-nc-sa/3.0/>

# Acknowledgments

While I am the one to have performed the research and compiled it, this thesis is the product of many, of which I must thank a specific few.

It has been a privilege to work alongside the talented and passionate individuals that comprise the PAPER and HERA teams. To my co-conspirators of PAPER analysis: Danny Jacobs, Carina Cheng, Matt Kolopanis and Josh Kerrigan, it has been a struggle and a pleasure, and I will sorely miss working with you. A special thanks to the Penn portion to the effort: David Moore, Paul La Plante, Zac Martinot, Immanuel Washington and Tashalee Billings. I look forward to continued conversations and updates.

The Department of Physics & Astronomy of the University of Pennsylvania is a fantastic place to work. The cohorts of graduate students it brings together are consistently awesome, engaging and friendly. I have made some of my best friends here, including Ashley Baker, Christian Herwig, Elodie Resseguie, Christina Krawiec, Rachel Wolf and Alyssa Barlis. Outside of Physics & Astronomy, but within the Penn umbrella, I must thank my dear friends Julie Westover, Irteza Binte-Farid and Steve Kocher for their loving support. Thank you as well to the School of Arts and Sciences for supporting my final year at Penn with a Dissertation Completion Fellowship.

James, you are an incredible supervisor. I have learned so much from you, and treasure the opportunities you have given me to grow and become the scientist that I am. I know how rare it is to be able to call a PhD supervisor a friend, and I count my luck there daily.

Matt, Debby and Naomi, thank you for your great conversations, encouraging words and hospitality. I can't want to be part of the family.

To my siblings, Hannah, Yosef and Ezra: you are always full of loving support and cutting sarcasm, neither of which I ever want to be without.

Mom and Dad, this thesis belongs to you as much as it does me. Your hard work, encouragement and love made me who I am. Thank you.

Gabby – words here simply won't do justice to how grateful I am for you. You're the best, and I love you.

**ABSTRACT**

**OUTER SPACE AND FOURIER SPACE:**

**UNDERSTANDING FOREGROUNDS FOR NEUTRAL HYDROGEN**

**EPOCH OF REIONIZATION MEASUREMENTS**

Saul A. Kohn

James E. Aguirre

The Epoch of Reionization (EoR) was a cosmic phase transition from a neutral to an ionized state. The first generation of luminous objects were able to heat and ionize their surrounding media, predominantly clouds of neutral hydrogen. Detection of brightness temperature fluctuations from the redshifted hyperfine 21 cm line of neutral hydrogen would provide a direct, inherently three-dimensional probe of astrophysics and cosmology during this transformational stage of cosmic history.

Foreground power dominates the measurements of interferometers that seek a statistical detection of the EoR. The inherent spectral smoothness of synchrotron radiation – the dominant foreground emission mechanism – the chromaticity of the instrument, and the spectral structure of the target signal allows these experiments to delineate a boundary between spectrally smooth and structured emission in Fourier space. These separate components are referred to as the ‘foreground wedge’ and the ‘EoR window’. However, Faraday rotation of polarized synchrotron radiation induces frequency-dependent structure in its spectrum, which will leak power from the foreground wedge into the EoR window. This makes polarization a potential contaminant for EoR measurements.

This work presents investigations into the impact of polarization on EoR measurements, in the Fourier space relevant to current EoR experiments. We show, separately, both the widest and the deepest integrations on polarized power in the EoR window to date. All results are consistent with negligible leakage, to the noise levels attained. Our deep integration also represents the best limits to date on both polarized and unpolarized

power in the EoR window. Polarized redundant calibration is also described and implemented on observations for the first time in this work.

We also present new methods to expand the potential of EoR measurements, while remaining within the EoR window paradigm. Interferometric sensitivity to a monopole signal is explored, with the first ever implementations on observational data. We construct higher-order correlation functions to investigate the connection between the kinetic Sunyaev-Zeldovich effect, mapped into Fourier space, and the 21 cm power spectrum. Finally, we examine the role deep learning could play in the analysis of more futuristic 21 cm image cubes.

# Contents

<b>Title</b>	<b>i</b>
<b>Dedication</b>	<b>ii</b>
<b>Acknowledgments</b>	<b>iv</b>
<b>Abstract</b>	<b>vi</b>
<b>List of Tables</b>	<b>xiii</b>
<b>List of Figures</b>	<b>xiv</b>
<b>I Radiation, Interferometry &amp; Polarimetry</b>	<b>1</b>
<b>1 The Epoch of Reionization</b>	<b>3</b>
1.1 Current Measurements . . . . .	5
1.1.1 High-redshift galaxies . . . . .	5
1.1.2 Observations of the CMB . . . . .	8
1.2 Direct measurements of HI . . . . .	12
1.2.1 The 21cm transition . . . . .	12
1.2.2 Global signal . . . . .	14
1.2.3 Anisotropic signal . . . . .	17
1.3 Current Limits and Future probes . . . . .	22
1.4 This thesis . . . . .	24
<b>2 Astrophysical Radiation</b>	<b>26</b>
2.1 Synchrotron Radiation . . . . .	26
2.2 Stokes parameters . . . . .	29
2.3 Total intensity foregrounds . . . . .	32
2.4 Linearly Polarized Foregrounds . . . . .	34
2.4.1 Faraday Rotation . . . . .	36
2.4.2 Depolarization . . . . .	38

<b>3 Interferometry, Calibration &amp; Polarimetry</b>	<b>41</b>
3.1 The Visibility Equation . . . . .	41
3.1.1 The Classical Visibility Equation . . . . .	42
3.1.2 The Measurement Equation . . . . .	45
3.2 Calibration Techniques . . . . .	48
3.2.1 Diagonal and off-diagonal calibration . . . . .	49
3.2.1.1 Ionospheric effects . . . . .	50
3.2.2 Image-based calibration . . . . .	51
3.2.3 CLEAN . . . . .	52
3.2.3.1 Högbom’s algorithm . . . . .	52
3.2.3.2 Delay Transforms and the 1D-CLEAN . . . . .	55
3.2.4 Redundant calibration . . . . .	57
3.3 Instrumental Polarization . . . . .	59
3.3.1 Direction-Dependent Leakage . . . . .	59
3.3.2 Direction-Independent Leakage . . . . .	63
<b>4 Instruments</b>	<b>65</b>
4.1 Instruments used in this work . . . . .	65
4.1.1 The Donald C. Backer Precision Array for Probing the Epoch of Reionization (PAPER) . . . . .	66
4.1.1.1 The PAPER signal chain . . . . .	67
4.1.1.2 PAPER-32 . . . . .	69
4.1.1.3 PAPER-64 . . . . .	70
4.1.1.4 PAPER-128 . . . . .	71
4.1.2 The Hydrogen Epoch of Reionization Array (HERA) . . . . .	72
4.1.2.1 HERA-19 Commissioning Array . . . . .	73
4.1.2.2 Future HERA Build-Outs . . . . .	75
4.2 Other current and future interferometers . . . . .	76
4.2.1 The Low Frequency Array (LOFAR) . . . . .	76
4.2.2 The Murchison Widefield Array (MWA) . . . . .	76
4.2.3 Square Kilometer Array – Low band (SKA-Low) . . . . .	77
<b>II Structure in Fourier space</b>	<b>78</b>
<b>5 Peering through the EoR Window</b>	<b>80</b>
5.1 Foreground isolation . . . . .	80
5.1.1 Foreground avoidance . . . . .	84
5.1.1.1 Power spectra . . . . .	85
5.1.1.2 Noise spectra . . . . .	86
5.1.2 Foreground subtraction . . . . .	88
5.2 The Problem of Polarization . . . . .	89

<b>6 Data Preparation and Processing</b>	<b>92</b>
6.1 Data Compression . . . . .	92
6.1.1 Delay–Delay-Rate Filtering . . . . .	93
6.1.2 Software Implementation . . . . .	95
6.2 Radio Frequency Interference . . . . .	97
6.2.1 PAPER-128 . . . . .	97
6.2.1.1 Average Properties . . . . .	98
6.2.1.2 Individual Properties . . . . .	105
6.2.1.3 Discussion . . . . .	108
6.2.2 HERA-19 and PAPER-19 . . . . .	108
6.2.2.1 HERA Hex RFI . . . . .	109
6.2.2.2 PAPER Hex RFI . . . . .	112
6.2.2.3 Hex-to-Hex Comparisons . . . . .	112
6.2.2.4 Comparison PAPER-128 stacked flags . . . . .	114
6.2.2.5 Discussion . . . . .	115
6.3 Quality Assurance Metrics . . . . .	116
6.3.1 Mean Amplitude Flagging . . . . .	117
6.3.2 Flagging on omnical $\chi^2$ . . . . .	119
<b>7 Polarimetric Calibration</b>	<b>121</b>
7.1 Redundant Calibration . . . . .	122
7.1.1 Mathematical Overview . . . . .	124
7.1.1.1 Redundant calibration with OMNICAL . . . . .	124
7.1.1.2 Including polarization in redundant calibration . . . . .	125
7.1.1.3 Degeneracies . . . . .	126
7.1.1.4 Expectations from simulation . . . . .	127
7.1.2 Data Processing . . . . .	128
7.1.3 Results . . . . .	132
7.1.3.1 Calibration . . . . .	132
7.1.3.2 Pseudo-Stokes Visibilities . . . . .	133
7.1.4 Discussion & Conclusions . . . . .	138
7.2 Imaging Calibration . . . . .	139
7.2.1 Converting historical PAPER data into Measurement Sets . . . . .	139
7.2.2 Imaging PAPER-32 data with CASA . . . . .	140
7.2.3 D-term calibration . . . . .	147
<b>8 The Ionosphere</b>	<b>149</b>
8.1 Historical measurements of TEC and RMs . . . . .	151
8.2 Low frequency observations: discoveries and challenges . . . . .	153
8.3 Relevance for PAPER and HERA EoR measurements . . . . .	154
<b>9 A view of the EoR window from the PAPER-32 imaging array</b>	<b>159</b>
9.1 Observations & Reduction . . . . .	160

9.1.1	Calibration . . . . .	162
9.1.1.1	Initial calibration . . . . .	162
9.1.1.2	Absolute Calibration . . . . .	162
9.1.1.3	Polarimetric factors . . . . .	166
9.1.2	Creating power spectra . . . . .	168
9.2	Results . . . . .	169
9.3	Discussion and Conclusions . . . . .	177
<b>10</b>	<b>A view of the EoR window from the HERA-19 commissioning array</b>	<b>179</b>
10.1	Polarization Leakage Simulations . . . . .	180
10.2	Observations & Reduction . . . . .	181
10.2.1	Calibration . . . . .	182
10.2.2	Forming power spectra . . . . .	188
10.3	Results & Discussion . . . . .	189
10.3.1	General features of the power spectra . . . . .	190
10.3.2	Day-to-day variability . . . . .	194
10.3.3	Polarimetric results . . . . .	195
10.4	Conclusions . . . . .	198
<b>11</b>	<b>Deep integrations on polarization with PAPER-128</b>	<b>199</b>
11.1	Observations & Reduction . . . . .	199
11.1.1	Overview of PAPER-128 observations . . . . .	200
11.1.2	Reduction of Season 1 Epoch 2 data . . . . .	204
11.1.2.1	Redundant calibration . . . . .	204
11.1.2.2	Foreground removal . . . . .	205
11.1.2.3	Binning in LST . . . . .	209
11.1.2.4	Absolute calibration & fringe-rate filtering . . . . .	209
11.1.3	Forming power spectra . . . . .	212
11.2	Results . . . . .	216
11.3	Discussion & Conclusions . . . . .	218
<b>III</b>	<b>Expanding the potential of EoR measurements</b>	<b>222</b>
<b>12</b>	<b>Interferometric sensitivity to the global signal</b>	<b>224</b>
12.1	Mathematical Formalism . . . . .	225
12.1.1	Spherical Harmonic Transform of the Visibility Equation . . . . .	226
12.1.2	Coupling to the Sky Monopole . . . . .	227
12.2	Analytic and Numeric Calculations . . . . .	228
12.2.1	Toy Model . . . . .	228
12.2.2	Instrument Simulation . . . . .	231
12.2.3	Attenuating other harmonics . . . . .	233
12.3	Time-averages from PAPER . . . . .	234

12.4	Discussion . . . . .	237
<b>13</b>	<b>Higher-order correlation functions between kSZ and 21cm observations</b>	<b>241</b>
13.1	The kSZ-21cm connection . . . . .	242
13.1.1	Simulations . . . . .	243
13.2	kSZ <sup>2</sup> -21cm squeezed-triangle bispectra . . . . .	245
13.2.1	Semi-analytic approximation . . . . .	245
13.2.1.1	$B_{x,x,21\text{cm}}$ . . . . .	247
13.2.1.2	$B_{x,\rho,21\text{cm}}$ and $B_{\rho,\rho,21\text{cm}}$ . . . . .	250
13.2.1.3	$B_{\rho,\rho,21\text{cm}}$ . . . . .	251
13.2.1.4	Full estimator . . . . .	252
13.2.2	Counting triangles . . . . .	252
13.2.3	Results . . . . .	253
13.3	kSZ <sup>2</sup> -21cm <sup>2</sup> squeezed-rectangle trispectra . . . . .	258
13.3.1	Mathematical formulation . . . . .	258
13.3.2	Effects of filtering . . . . .	261
13.3.3	kSZ <sup>2</sup> -21cm <sup>2</sup> cross-power spectrum . . . . .	261
13.4	Foregrounds and Noise . . . . .	264
13.5	Discussion . . . . .	266
<b>14</b>	<b>Deep Learning for 21cm Observations</b>	<b>268</b>
14.1	Neural Networks . . . . .	269
14.2	Classifying reionization models . . . . .	271
14.3	Regressing upon reionization parameters . . . . .	273
14.4	Future directions . . . . .	278
<b>15</b>	<b>Conclusions</b>	<b>280</b>
<b>Appendices</b>		<b>284</b>
<b>A</b>	<b>Software</b>	<b>285</b>
A.1	Astronomical Interferometry in Python (aipy) . . . . .	285
A.2	Astronomy in Python (astropy) . . . . .	286
A.3	Common Astronomy Software Applications (CASA) . . . . .	286
A.4	Deep Learning packages . . . . .	286
A.5	Hierarchical Equal Area isoLatitude Pixelization of the sphere (HEALPix)	286
A.6	pyuvdata . . . . .	287
A.7	The Scientific Python Ecosystem (scipy) . . . . .	287
<b>Bibliography</b>		<b>288</b>

# List of Tables

6.1	PAPER-128 RFI frequencies and brief characterization for the averaged flags.	100
6.2	RFI as flagged by HERA	111
6.2	RFI as flagged by HERA	112
6.3	RFI as flagged by the PAPER Hex	113
8.1	Ionospheric Layers	150
11.1	PAPER-128 Observing Seasons & Epochs	200

# List of Figures

1.1	The Ly $\alpha$ spectra of 19 high-redshift quasars. . . . .	7
1.2	The $TE$ cross-power spectrum from WMAP. . . . .	9
1.3	The history of the EoR global signal. . . . .	16
1.4	Forecasts for constraints on the ionization history, given high signal-to-noise measurements of the HI power spectrum at each redshift from HERA. .	19
1.5	An example cosmological simulation of the EoR and the corresponding density field. . . . .	21
1.6	Current limits on the EoR power spectrum, as a function of redshift. . . .	23
2.1	The low-frequency synchrotron spectrum of the sky, as measured by Rogers & Bowman (2008). . . . .	29
2.2	A representation an elliptically polarized monochromatic wave with respect to the Cartesian grid. . . . .	31
2.3	The Southern Galactic Plane as observed by PAPER-64 at 145 MHz. . . .	33
2.4	The GSM at 150 MHz: a relatively accurate model of diffuse synchrotron across the entire sky. . . . .	34
2.5	The polarized intensity of the sky as viewed by the DRAO 26 m telescope at 1.4 GHz. Figure taken from Wolleben et al. (2006). . . . .	35
2.6	An all-sky map of RMs. . . . .	38
3.1	The geometry of a two-element interferometer, with a plane wave incident from direction $\hat{s}$ . . . . .	42
3.2	Four stages of the Högbom CLEAN. . . . .	54
3.3	A graphical representation of the delay transform. . . . .	57
3.4	Simulations of the instrumental direction-dependent Mueller matrix at 120 MHz and 160 MHz. . . . .	62
4.1	An image of a PAPER dipole element with its groundscreen. . . . .	68
4.2	A diagram of the PAPER-128 signal chain. Square-dotted lines indicate RFI-shielding. . . . .	69
4.3	The array layouts of the PAPER-32 element deployment in South Africa. .	70
4.4	The array layouts of the PAPER-64 deployment. . . . .	71
4.5	The PAPER-128 array layout. . . . .	72
4.6	Future vision and physical commissioning HERA layout. . . . .	73

4.7	Positions of antennae in the HERA-19 Commissioning Array (including the experimental “subarrays”). . . . .	74
4.8	Array sensitivity as a function of $k$ -mode relative to HERA-19 . . . . .	75
5.1	An illustration of the foreground wedge and the EoR window. . . . .	82
5.2	Different instrument receptivity patterns – dipoles, phased arrays and dishes – have different 2D power spectrum morphologies. . . . .	83
5.3	Delay vs. time for a simple sky model of four foreground-like, smooth-spectrum sources and an EoR-like (but greatly amplified), spectrally structured signal. . . . .	85
5.4	A summary of the problem posed by polarization for EoR experiments. .	90
6.1	The schema of the database used to organize and implement PAPER data compression. . . . .	96
6.2	A waterfall plot of RFI flags averaged over 150 days of PAPER-128 data.	101
6.3	The percentage of time that each frequency was flagged over the season. .	102
6.4	Possible FM radio contamination. . . . .	103
6.5	Flights from Cape Town to Johannesburg correspond to RFI. . . . .	104
6.6	The temporal profile of the 5 RFI frequencies with unidentified causes. .	106
6.7	Waterfalls of RFI flags for nights 2456732, 2456958 and 2457038. . . . .	107
6.8	Waterfalls of RFI flags for nights 2456898, 2456924 and 2456965 . . . . .	107
6.9	Frequency vs. percentage flagging for the HERA Hex and PAPER Hex. .	114
6.10	RFI flag waterfalls of frequency vs. South Africa Standard Time for the HERA Hex and PAPER Hex. . . . .	115
6.11	An example of the mean amplitude flagging metrics on exercised on HERA-47 data. . . . .	118
6.12	Flagging Julian Dates based on the median omnical $\chi^2$ values in the 150–180 MHz band. . . . .	120
7.1	Simulations of pseudo-Stokes visibilities, . . . . .	129
7.2	Arrangement of the PAPER-128 array. . . . .	130
7.3	The phase of the complex gain value for the <i>4pol</i> calibration scheme. . . .	133
7.4	Histograms of differences in the ‘x’ gain calibrations per antenna between calibration schemes. . . . .	134
7.5	$w^2$ values, summed across the array. . . . .	135
7.6	Pseudo-Stokes visibility amplitudes and phases. . . . .	136
7.7	Delay-transformed pseudo-Stokes visibilities. . . . .	137
7.8	The beam model and point spread function of the PAPER-32 array, calculated by CASA. . . . .	141
7.9	Full-polarization imaging results from a four-component, Stokes I-only sky model. . . . .	144
7.10	The same field as shown in Figure 7.9, but with the removal of malfunctioning antennas identified by Kohn et al. (2016). . . . .	145

7.11	Imaging results from a file calibrated with gain values derived from the Pictor A transit, which occurred $\sim$ 6 hours after these data were acquired.	146
7.12	The same field as shown in Figure 7.10, but for pseudo Stokes U and V only, with $D$ -terms partially calibrated. . . . .	148
8.1	Distribution of zenithal ionospheric RMs for 3 LSTs in the PAPER-32 observing season . . . . .	155
8.2	An example of widefield ionospheric RMs calculated by radionopy. . . . .	157
8.3	The RM of Cas A as viewed from the LOFAR Core site in the Netherlands on April 11th, 2011, according to ionFR and radionopy. . . . .	158
9.1	The PAPER-32, dual-pol antenna imaging configuration and $uv$ distribution.	161
9.2	Snapshot images of Stokes parameters before and absolute calibration. . . . .	165
9.3	The values of ionospheric RM for different lines of sight a range of LSTs.	167
9.4	The absolute value of delay-transformed visibilities over the bandwidth (146–166 MHz) used to create the power spectra shown in this Chapter. . . . .	173
9.5	Log-scaled 2D power spectra from PAPER-32. . . . .	174
9.6	Wedge power spectra from PAPER-32. . . . .	175
9.7	Average power in $0.093 < k_{\perp} < 0.098 \text{ hMpc}^{-1}$ as a function of $k_{\parallel}$ for each polarization of PAPER-32 data. . . . .	176
10.1	The perimeter of each dish in the HERA-19 array. . . . .	182
10.2	Fractional RFI flag occupancy per time and frequency over the eight days of observations. . . . .	183
10.3	Multi-frequency synthesis pseudo-Stokes images formed from simulation and data. . . . .	185
10.4	Bandpass solutions for the North-South dipole orientation obtained for the functioning antennae in the array on JD 2457548. . . . .	186
10.5	The effect of calibration on the phases of visibilities from three redundantly-spaced 14.7 m baselines. . . . .	187
10.6	Power spectrum results from the high-band (157–167 MHz). . . . .	192
10.7	Power spectrum results from the low-band (120–130 MHz). . . . .	193
10.8	High band power as a function of baseline length for the center of the pitchfork ( $k_{\parallel} = 0 \text{ h/Mpc}$ ) and in the EoR window ( $k_{\parallel} = 0.2 \text{ h/Mpc}$ ) for each JD of observation. . . . .	194
10.9	Simulated and observed power as a function of $k_{\parallel}$ for the shortest baseline (14.7 m). . . . .	197
11.1	An annotated photograph of the PAPER-128 array. . . . .	201
11.2	The challenge of Epoch changes. . . . .	203
11.3	Good, bad and rotated antennas in Season 1 Epoch 2. . . . .	204
11.4	Amplitudes of three redundant visibilities before and after OMNICALibration using the 4pol+minV scheme. . . . .	206

11.5	The same visibilities as shown in Figure 11.4, but showing their phases instead of their amplitudes. . . . .	207
11.6	Images of Pictor A, used to calibrate the absolute scaling to physical units. . . . .	211
11.7	The point-spread function of an array consisting only of the $\sim 30$ m power spectrum baselines. . . . .	212
11.8	The average bandpass scaling used for absolute calibration. . . . .	213
11.9	Delay-rate vs. frequency for a 30 m baseline in the ‘xx’ (East-East) polarization. . . . .	214
11.10	Spherically-averaged PAPER-128 power spectra. . . . .	217
11.11	Spherically-averaged noise power spectra. . . . .	219
12.1	The transfer function for a simple beam and sky model. . . . .	229
12.2	The delay transform of the interferometer response to the monopole moment of the global signal, including only the zeroth-order response of the instrument. . . . .	230
12.3	The delay transform for different values of $\tau_h$ . . . . .	231
12.4	The direction-dependent Mueller matrix for a model PAPER beam at 150 MHz. . . . .	232
12.5	The global signal transfer function as a function of frequency for PAPER. . . . .	233
12.6	Comparison of time-averaged PAPER-128 visibilities to the simulated transfer function. . . . .	236
13.1	The average ionized fraction as a function of redshift in our cosmological simulation. . . . .	244
13.2	An example 21 cm brightness temperature field and integrated kSZ map from our cosmological simulation. . . . .	245
13.3	The $P_{\delta_p, \delta_p}(k)$ , $P_{\delta_x, \delta_x}(k)$ and $P_{\delta_x, \delta_p}(k)$ power spectra relevant to our semi-analytic estimate of the bispectrum. . . . .	255
13.4	The semianalytic expression of the bispectrum, calculated as a function of redshift from our simulation. . . . .	256
13.5	Bispectrum values, binned as a function of angle between the 21 cm and CMB $\vec{k}$ vectors, measured directly from the simulation. . . . .	257
13.6	The geometry of the correlation statistics considered in this Chapter. . . . .	259
13.7	The effect of filtering kSZ and 21cm maps to avoid foreground contamination. . . . .	262
13.8	21 cm <sup>2</sup> power spectra before and after filtering the wedge for several redshifts. . . . .	263
13.9	The cross-power spectrum of the squared 21 cm and kSZ fields, as a function of redshift of the 21 cm contribution. . . . .	264
14.1	21 cm brightness temperature fields for Galaxy-Only and AGN-only models. . . . .	272
14.2	The classification CNN used in this study. . . . .	273
14.3	Training data and results of the classifier. . . . .	274

14.4 An input image propagated through the trained kernels of the first layer of the classifier. . . . .	274
14.5 The effect of changing $\zeta$ on the 21 cm brightness temperature field. . . . .	276
14.6 The CNN used for regression. . . . .	277
14.7 The results of training the CNN regressor. . . . .	277
14.8 True vs. predicted values of $\zeta$ from the test set. . . . .	278

# **Part I**

## **Radiation, Interferometry &**

## **Polarimetry**

... His light is like a niche, within which is a lamp, the lamp within glass, the  
glass as if it were a white star... Light upon light.

*Al Quran, Surah An Nur (24:35)*

# Chapter 1

## The Epoch of Reionization

Shortly after the Big Bang, the Universe existed as an opaque, primordial soup of quarks, leptons, gluons and extremely energetic photons. With density anisotropies formed by hugely inflated quantum fluctuations, ionized hydrogen, deuterium, helium, lithium and beryllium (but mostly hydrogen and helium) filled the Universe as a hot plasma. Black-body photons were continuously scattered throughout this plasma. All the while, the Universe adiabatically expanded, and the plasma cooled.

About 380,000 years after the Big Bang, the number of photons with energies above the 13.6 eV threshold required to ionize neutral hydrogen (astronomers refer to neutral hydrogen as HI, and ionized hydrogen [i.e. protons] as HII) became outnumbered by the number of baryons, and HII was able to recapture electrons without immediately being ionized. During this critical period, known as recombination, the plasma was able to neutralize. The Universe underwent a cosmic transition from optically thick to optically thin as free electrons were captured, allowing light to travel unimpeded, in straight lines for the first time. Fast-forwarding about 14 billion years (bear with me), some of these photons that existed at the time of ‘last scattering’, redshifted by the expansion of the Universe, are observed today as the Cosmic Microwave Background (CMB).

We exist today in a structured, complicated and diverse Universe of stars and galaxies, dark matter and dark energy, but very little neutral gas. At the same time, observations

of the CMB (e.g. Planck Collaboration et al., 2016a,c) and standard cosmological models (referred to under the umbrella term of  $\Lambda$ CDM, standing for Dark Energy & Cold Dark Matter; e.g. Komatsu et al. (2009)) find extraordinary agreement with the story told above. However, there also exists a large observational gap: how did the Universe transition from its neutral state at recombination, to its ionized and structured state today? How, and when, did the Universe *reionize*?

The prevailing theory of the formation of cosmological structure begins with the primordial density anisotropies of the hot plasma. The dark matter that pervaded the Universe should have traced those perturbations, and gravitationally accreted into those regions, increasing the overdensities. Eventually, overdensities above some threshold density<sup>1</sup> collapsed into halos; structures supported by their own gravitational potential. The similarly pervasive HI field should have traced the dark matter overdensities. This gravity-dominated period represents an epoch of relatively simple physics directly driven by  $\Lambda$ CDM. It is known colloquially as the “Dark Ages”, as at that time no luminous structures existed, and the only photons that existed were from the slowly fading CMB<sup>2</sup>.

Within the early dark matter halos, enough HI accreted to a great enough density to fuse, igniting the first stellar cores. These first stars (referred to by astronomers as Population-3 or “PopIII” stars) were the first source of ultraviolet (UV) and X-ray photons capable of ionizing HI since recombination. They were also extremely massive and short-lived, and their supernovae likely provided the seeds for the first galaxies (composed of PopII stars; e.g. Ricotti (2016)). The PopIII era is sometimes referred to as “Cosmic Dawn”, and represents the birth of astrophysics in our Universe. With the origin of galaxies, HI surrounding haloes (the intergalactic medium; IGM) began to be reionized, forming “bubbles” of HII. As more luminous structures formed, UV photon production increased, and the reionization rate overcame recombination.

---

<sup>1</sup>For simple collapse models, this threshold is  $18\pi^2$  above the average density of the Universe; e.g. Press & Schechter (1974).

<sup>2</sup>For most purposes in this thesis, we neglect exotic physics such as Dark Matter annihilations that could in principle be an additional source of radiation at early times.

In our local Universe, the IGM is highly ionized. But without recombination, and therefore a neutral IGM, the CMB could not have arisen. The cosmic phase transition from neutral to ionized: a competition between cosmological physics and astrophysics; the formation of large-scale luminous structure; is known as the Epoch of Reionization (EoR). The myriad contemporary challenges associated with its detection are the subject of this thesis.

This Chapter is structured as follows. In Section 1.1 I will review current evidence for the nature and timing of the EoR. In Section 1.2, I introduce the motivation for my thesis work – directly measuring high-redshift HI via radio emission from the 21 cm hyperfine transition. In Section 1.3, I point to future prospects of observational cosmology at EoR redshifts. Finally, in Section 1.4, I provide some context for the contents of the rest of the thesis.

## 1.1 Current Measurements

The existence of Cosmic Dawn and the Dark Ages, at least as described above, have not yet been observationally confirmed. We do however have tantalizing clues of it's nature, and evidence when it ended. So far, these clues have largely come from high redshift galaxies and the CMB.

### 1.1.1 High-redshift galaxies

Quasars<sup>3</sup> are among the most luminous objects in Universe (e.g. Manti et al., 2017). Powered by accretion of gas onto a supermassive black hole, quasars emit an abundance of UV and X-ray photons. Most notably, they are bright sources of Lyman- $\alpha$  photons ( $\text{Ly}\alpha$ ; rest-wavelength of 121.567 nm).  $\text{Ly}\alpha$  is a spectral line from the  $2p \rightarrow 1s$  transition

---

<sup>3</sup>“Quasar” is a contraction of “quasi-stellar radio source”. They were first identified in radio surveys as extremely bright point-like sources, which might have been characterized as stars when compared to optical images – except that stars do not shine brightly at radio wavelengths.

of HI with a high cross-section, so it will become absorbed if propagating through a neutral region of the IGM.

Gunn & Peterson (1965) exploited this effect, predicting that quasars embedded in a highly neutral IGM would have all emission at wavelengths smaller than Ly $\alpha$  obscured. This was because all spectral emission at bluer wavelengths would redshift into the Ly $\alpha$  wavelength and be absorbed by the IGM. This effect, known as the Gunn-Peterson Trough, was finally detected by Becker et al. (2001). Their investigation of the spectra of four quasars with  $5.80 < z < 6.28$  found the optical depth towards the quasars increasing with redshift, indicating an increasing neutral fraction with redshift. Gunn & Peterson (1965) showed that the optical depth of Ly $\alpha$  through HI is  $\tau_{\text{GP}} \sim 10^4 x_H$ , where  $x_H$  is the fraction of HI out of HI and HII towards the quasar. This meant that Becker et al. (2001) could claim evidence of the IGM having  $x_H \gtrsim 10^{-4}$  in the direction of the quasar at  $z \sim 6$  – and that the EoR did not end before that redshift. Fan et al. (2006b) presented spectra of 19  $z \sim 6$  quasars, finding a sharp increase in  $\tau_{\text{GP}}$  with increasing redshift, suggesting evolution of  $x_H$  at  $z > 5.7$ . Figure 1.1 shows the spectra from their study, featuring Gunn-Peterson troughs. The sharpness of the cut-off – related to the effective optical depth – increases with redshift.

Spectroscopic observations of high-redshift sources are relatively difficult to perform, and require large amounts of integration time. However, the distinctive Ly $\alpha$  limit in the spectra shown in Figure 1.1 is a distinctive property of high-redshift quasars. As an alternative, astronomers have developed a photometric method that is cheaper and easier to perform, called the “Ly $\alpha$  dropout” technique. In this scheme, a survey will use an appropriate set of filters to probe a given redshift (imagine rectangles overlaid on the spectra in Figure 1.1). If an excess is seen towards one galaxy in one filter, and very little signal is seen in the next-bluest filter, that galaxy may be considered a candidate high- $z$  quasar. With some modelling, the luminosity function of Ly $\alpha$  dropout galaxies can be used to measure the mass distribution of galaxies as a function of redshift (e.g. Bouwens et al., 2015, 2016). Using these luminosity functions and comparing to star formation rate

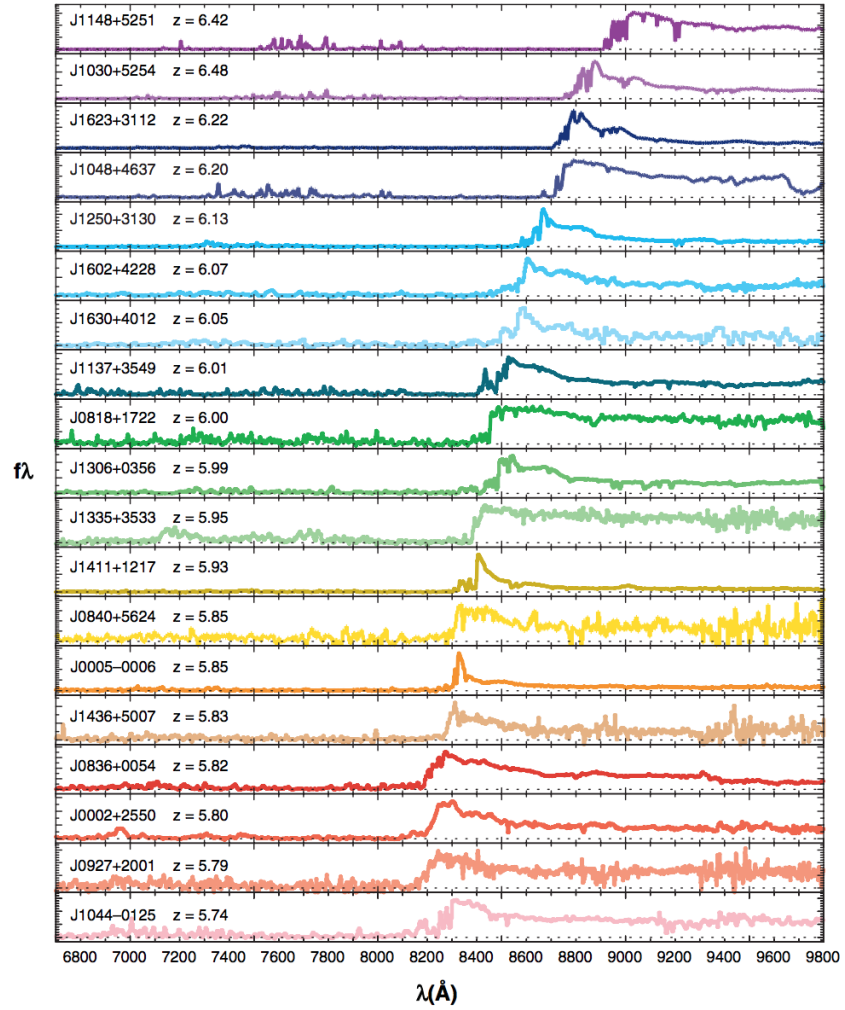


Figure 1.1: The Ly $\alpha$  spectra of 19 high-redshift quasars, as reported by Fan et al. (2006b). The effective optical depth towards each quasar increases with redshift, suggesting an evolution in the neutral fraction of the IGM. This figure was taken from Fan et al. (2006a).

models and measurements, Robertson et al. (2015) argue that current measurements are consistent with quasars playing a relatively minor role in reionization, with the bulk of ionizing photons arising from “normal” galaxies rather than black hole accretion discs. However, this claim is moderately dependent upon uncertain model parameters, such as the escape fraction of ionizing photons from their local halo (Robertson et al., 2013) and the star formation history at high redshifts. The latter is beginning to be answered as more high-redshift gamma-ray bursts are detected and characterized (Wang & Dai, 2009; Robertson & Ellis, 2012; Wang et al., 2015).

At the time of writing, photometric and spectroscopic observations of high- $z$  quasars suggest that the IGM had a neutral fraction  $> 10^{-4}$  at  $z \sim 6$ , indicating that the EoR ended around 1 Gyr after the Big Bang (Barnett et al., 2017). Fan et al. (2006b) reported a direction dependence on their measurements, suggesting that reionization was patchy, rather than homogeneous.

### 1.1.2 Observations of the CMB

CMB photons will Thomson-scatter off-of free electrons in their path, suppressing the observed signal in a given direction. This suppression is described by an optical depth,

$$\tau_{\text{cmb}} \propto \int_0^{z_{\text{recomb}}} x_i(z) a(z) \frac{dl}{dz} dz, \quad (1.1)$$

where  $x_i(z)$  is the average ionized fraction at redshift  $z$ ,  $z_{\text{recomb}} \approx 1100$  is the redshift of recombination (and last scattering),  $a(z) = (1+z)^{-1}$  and  $dl/dz$  is the cosmological line-element to redshift  $z$ . The optical depth to the CMB will suppress the observed primary anisotropies<sup>4</sup> by a factor of  $e^{-\tau_{\text{cmb}}}$ .

The dependence on  $x_i(z)$  is crucial to our current understanding of the EoR; the largest contribution to the value of  $\tau_{\text{cmb}}$  will come from the large injection of electrons into the

---

<sup>4</sup>The CMB is most-usefully described in harmonic  $C_\ell$ -space. Primary anisotropies, due to damped acoustic oscillations in the early hot plasma (Silk, 1968), are strongest at multipoles  $\ell \lesssim 3000$  – equivalent to spatial scales  $\theta \gtrsim 0.1^\circ$ .

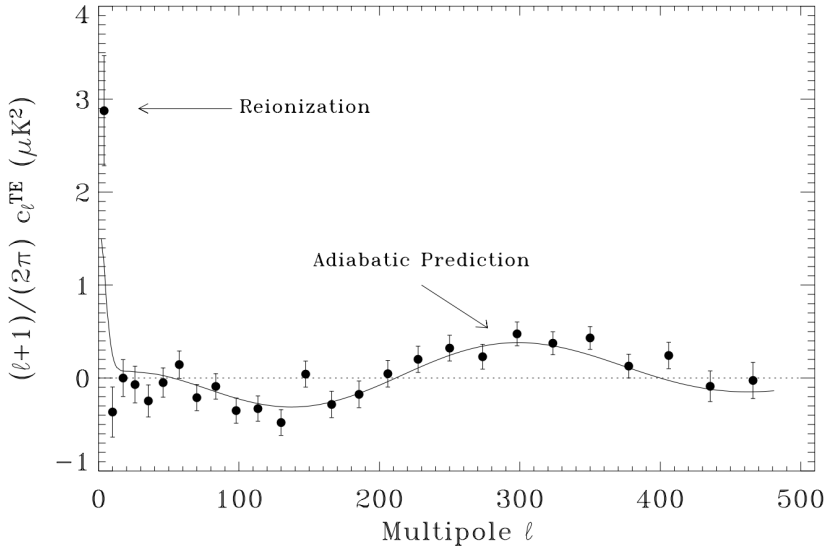


Figure 1.2: The Temperature-Linear Polarization (*TE*) cross-power spectrum from WMAP. The power was consistent with collisionless models save for an excess at large scales, consistent with large amounts of Thomson scattering of CMB photons during the EoR. Figure taken from Spergel et al. (2003).

IGM during the EoR. Its measurement is not without complications: the suppression effect is degenerate with the overall amplitude of the CMB power spectrum, and it is an integrated quantity.

The first complication can be addressed by performing polarized observations of the CMB, which breaks the degeneracy. A CMB photon that scatters off of an electron within a quadrupolar anisotropy will become linearly polarized, boosting polarized power at  $\ell \sim 2\sqrt{\tau_{\text{cmb}}}$  (Zaldarriaga, 1997). The WMAP satellite was the first telescope capable of making all-sky measurements of the CMB polarization, and detected such an excess in polarized power, as shown in Figure 1.2 (Kogut et al., 2003; Spergel et al., 2003).

Such a measurement is able to recover a value of  $\tau_{\text{cmb}}$ , but due to its integral nature does not provide an ionization history. Values of  $x_i(z)$  are therefore extremely model-dependent; typically extracted by assuming “instantaneous reionization” in which  $x_i(z)$

transitions from 0 to 1 quickly and smoothly. These models are often described using the tanh form:

$$x_i(z) \propto 1 + \tanh\left(\frac{z - z_{\text{re}}}{\Delta z}\right), \quad (1.2)$$

where  $z_{\text{re}}$  is the redshift of instantaneous reionization, but is more usefully thought of as the redshift at which  $x_i \approx x_{HI} \approx 0.5$ .  $\Delta z$  is the duration of reionization. Using such models, Planck Collaboration et al. (2016b) reported limits of  $7.8 < z_{\text{re}} < 8.8$  and  $\Delta z < 2.8$ . They also reported that all of their modelling suggested that  $x_i(z \gtrsim 10) < 0.1$ .

The CMB provides us with more than one probe of reionization. Zeldovich & Sunyaev (1969) and Sunyaev & Zeldovich (1970) showed that CMB photons that scattered off of free electrons would introduce secondary anisotropies to the CMB (i.e. additional features in the  $C_\ell$  spectrum). The Sunyaev-Zeldovich (SZ) effect is divided in to two categories: the thermal effect (tSZ) and the kinetic effect (kSZ). The tSZ occurs when CMB photons scatter off of electrons with high energies ( $\sim 10$  keV) due to their temperature; such high temperatures can only occur in high-mass galaxy clusters, and hence at redshifts lower than the EoR.

The kSZ is of relevance to EoR studies. CMB photons scattering off of clouds of electrons in coherent velocity flows can be Doppler-shifted, which will redshift or blueshift (depending on the sign of the line-of-sight velocity) spectral observations of the CMB. Of course, clouds of electrons exist in relatively low-redshift galaxy clusters, and it was their contribution to the kSZ that was first detected (Hand et al., 2012). However, detection of the EoR contribution to the signal would be a powerful probe of dynamics on cosmological scales in the early Universe. The distortion induced by the kSZ on the CMB is given by

$$\frac{\delta T}{T_{\text{CMB}}}(\hat{s}) = \frac{\sigma_T}{c} \int_0^{z_{\text{recomb}}} n_e(z) e^{-\tau(z)} \hat{s} \cdot \vec{q} \frac{ds}{dz} dz, \quad (1.3)$$

where  $\sigma_T$  is the Thomson Cross Section,  $n_e(z)$  is the average number density of electrons at redshift  $z$ ,  $\tau(z)$  is the optical depth to redshift  $z$ , and  $ds/dz$  is the cosmological line

element to redshift  $z$  along direction  $\hat{s}$ . We can model inhomogeneities in the ionization and baryon fraction as vector field

$$\vec{q}(\hat{s}) = (1 + \delta_x)(1 + \delta_b)\vec{v}(\hat{s}), \quad (1.4)$$

where  $1 + \delta_x = x_i / \langle x_i \rangle$ ,  $1 + \delta_b = \rho_b / \langle \rho_b \rangle$  and  $\vec{v}$  is the free electron bulk flow.

This is an optical depth effect much like the optical depth of the CMB in Equation 1.1. However, it has important distinctive features: it is a direction dependent, probing the velocity of electron bulk flows along the line of sight, rather than the average ionization history, and it can create excesses and decrements in power, depending on the sign of the velocity component.

Detection of the kSZ is difficult, as the secondary anisotropies it causes in brightness temperature are a few percent of tSZ. Compared to the primary anisotropies, the tSZ is roughly 10 times weaker in  $\mathcal{D}_\ell = (\ell + 1)\ell C_\ell / 2\pi^2$ , and the kSZ is roughly 100 times weaker. George et al. (2015) reported a detection of the kSZ at  $\ell \approx 3000$  (where the primary anisotropies and the Cosmic Infrared Background, a CMB contaminant at small scales, are both close to their minimum values), using a suite of cosmological and spectral models to remove CMB foregrounds, the primary anisotropies and the tSZ (e.g. Shaw et al., 2010). Again, measurements from the CMB are integrated quantities, so their constraints on reionization are model dependent. Using a symmetric model of reionization history (Zahn et al., 2012), they set the constraint that  $\Delta z < 5.4$ , with their likelihood peaking around  $\Delta z = 1.3$ . Using similar techniques with shallower data from the same telescope, Zahn et al. (2012) set consistent limits that  $\Delta z \geq 2$ , and also that reionization ended at  $z > 5.8$ .

Wide-field measurements of the kSZ would be rewarding, but the foregrounds of the Galaxy, CIB, CMB and tSZ represent contemporary challenges for direct-imaging experiments. However, one could hope to use correlations of the velocity field the kSZ sources, and the density field associated with it, to decorrelate the foregrounds and estimate the underlying fields (e.g. Cooray et al., 2004; Alvarez, 2016). The mathematical formalism for such a technique is laid-out in Chapter 13.

## 1.2 Direct measurements of HI

To borrow a line from Jacobs (2011), the Dark Ages were not dark. Our Universe is dynamic and energetic, and particles constantly seek a lower energy state.

Throughout the Dark Ages and the EoR, HI was shining, weakly, at radio wavelengths. The HI atom is capable of a hyperfine transition between its  $1s_1$  and  $0s_1$  energy levels. The electron spin can spontaneously change from parallel to the proton spin to antiparallel, emitting a photon of frequency  $\nu_{21\text{cm}} \approx 1420.4$  MHz; a rest-wavelength of roughly 21 cm. The emission coefficient of this transition is  $\sim 2.9 \times 10^{-15} \text{ s}^{-1}$ , corresponding to a half-life of approximately 11 million years per atom. This is both the strength and the weakness of observing HI. According to Fermi’s Golden Rule, the probability of emission is equal to that of absorption; a small transition rate leads to a relatively dim signal, but 21 cm photons are extremely unlikely to be observed between their emission and observation. This allows the 21 cm signal to be tomographically mapped – a sharp excess at the relevant frequency indicates a redshift – and constructed into a 3D cube in space and time.

Observations of HI during the Dark Ages and the EoR would directly constrain the ionization history of the Universe, allowing us to probe the evolution of the density field at high redshifts, the properties of the first stars, galaxies and black holes, and map the structure of the IGM as it evolves as a function of redshift. It would also represent the furthest baryons ever detected, and the largest volume of the Universe ever surveyed. This Section reviews the nature of the 21 cm line during the EoR, and two parallel endeavours to detect it, using the monopolar signal (i.e. power averaged over the sky), and the anisotropic signal (power as a function of spatial scale).

### 1.2.1 The 21cm transition

As noted above, the probability of a single HI atom undergoing the 21 cm transition is exceedingly small. However, during the Dark Ages and the EoR, HI was ubiquitous, and

such transitions would be occurring constantly. The relative occupancy of the hyperfine state in HI is given by

$$\frac{N_1}{N_0} = \frac{g_1}{g_0} e^{-h\nu_{21\text{cm}}/k_B T_S}, \quad (1.5)$$

where  $g_1$  and  $g_0$  refer to the triplet and singlet states of the atom and are equal to 3 and 1, respectively. This Equation defines the spin temperature  $T_S$ , an analog of molecular excitation temperature for HI. By solving the radiative transfer equation for this system in the Rayleigh-Jeans limit (e.g. Moore, 2014), we can write the brightness temperature of the emission as:

$$T(z) = T_S \tau_v(z) + T_{\text{bg}}(1 - \tau_v(z)), \quad (1.6)$$

where the optical depth of HI,  $\tau_v$ , is assumed to be small, and the temperature of the background radiation  $T_{\text{bg}}$  is, for EoR observations, the temperature of the CMB at redshift  $z$ . Furlanetto et al. (2006) showed that the optical depth can be expressed in terms of cosmologically-interesting quantities, assuming the IGM is diffuse:

$$\tau_v \approx 9.2 \times 10^{-3} (1 + \delta_b) (1 + z)^{3/2} \frac{x_{HI}}{T_S} \left( \frac{H(z)/(1+z)}{dv_{\parallel}/dr_{\parallel}} \right), \quad (1.7)$$

where  $dv_{\parallel}/dr_{\parallel}$  is the component of the peculiar velocity of the HI cloud per unit depth along the line-of-sight, with respect to the Hubble expansion given by  $H(z)/(1+z)$ . The prefactor of  $9.2 \times 10^{-3}$  justifies the assumption of small  $\tau_v$  made above. Comparison to the optical depth for the Ly $\alpha$  line in Section 1.1 emphasizes that HI observations refer an opposite regime of EoR probes.

Combining the above equations, we can define the brightness contrast between redshifted HI emission and the CMB,

$$\delta T \approx 9\text{mK} \times x_{HI} (1 + \delta_b) (1 + z)^{1/2} \left( 1 - \frac{T_{\text{CMB}}(z)}{T_S} \right) \left( \frac{H(z)/(1+z)}{dv_{\parallel}/dr_{\parallel}} \right). \quad (1.8)$$

Note that  $\delta T$  can saturate if  $T_S \gg T_{\text{CMB}}$ , and can become arbitrarily negative if  $T_S \ll T_{\text{CMB}}$ . The observed emission is ‘backlit’ by the CMB – it’s observability hinges on its relationship to  $T_{\text{CMB}}$ . Also note that the characteristic brightness temperature in Equation 1.8 is of order mK. By the time it is observed, the 21 cm emission from the EoR has redshifted into meter wavelengths. At these wavelengths, Galactic synchrotron dominates the sky with brightness temperatures  $\sim 10^3$  K (see Chapter 2; McQuinn et al. 2007). Foreground removal or avoidance remains the primary challenge for all EoR experiments, and will be discussed extensively throughout this thesis. I believe that the promises of 21 cm tomography, outlined below, make the challenge worth pursuing. For a comprehensive reviews of the theory behind high-redshift 21 cm tomography, see Madau et al. (1997), Furlanetto et al. (2006) and Pritchard & Loeb (2010).

It is important to mention here, and will be re-iterated, that the 21 cm photons generated through the hyperfine transition are highly unpolarized. Primordial magnetic fields could induce circular polarization via Zeeman splitting, but such an effect would be 3 to 4 orders of magnitude smaller than the already faint total intensity signal itself (e.g. Babich & Loeb, 2005, also see Chapter 2).

### 1.2.2 Global signal

The sky-averaged 21 cm signal, sometimes called “global signal”, is a direct measurement of the spin temperature as a function of redshift. Equation 1.6 can be approximated as (Field, 1956):

$$T_S^{-1} = \frac{T_{\text{CMB}}^{-1} + x_c T_K^{-1} + x_\alpha T_c^{-1}}{1 + x_c + x_\alpha} \quad (1.9)$$

where  $x_c$  and  $x_\alpha$  are coupling coefficients for collisions and UV scattering, respectively,  $T_K$  is the kinetic temperature of the gas, and  $T_c$  is the effective temperature of the UV radiation field. The magnitude and sign of  $T_S$  with respect to  $T_{\text{CMB}}$  is therefore proportional to each coupling constant.

At high redshifts, Wouthuysen (1952) and Field (1959) showed that there was good

reason to expect that  $T_c \rightarrow T_K$ , such that  $T_S$  decouples from  $T_{\text{CMB}}$ . The effect – now known as the Wouthuysen-Field Effect – relies on Ly $\alpha$  radiation from early luminous sources exciting HI in the  $1s$  states into the  $2p$  states. The atoms can then decay to the  $1s_1$  state via allowed transitions, overpopulating that hyperfine energy level. This couples the HI to the UV radiation field; the strength of the coupling depends on the spectral shape of the Ly $\alpha$  line. Increasing the coupling to UV scattering would make  $T_S$  large and negative.

A fiducial reionization history is shown in Figure 1.3 (Mirocha et al., 2012), with important turning points and zero-crossings highlighted. Working forwards through history, collisional coupling is relatively large in the Dark Ages, and couples  $T_S$  to a low  $T_K$ , creating an absorption trough. The Universe continues to expand, baryon density drops, and  $T_S$  and  $T_K$  decouple;  $T_S$  tends towards zero as it grows closer to  $T_{\text{CMB}}$ . As the first stars ignite, marking the end of the Dark Ages, their UV emission couples to the spin temperature via the Wouthuysen-Field Effect, creating a sharp absorption feature. As more massive structures form, X-rays begin to dominate the ionizing radiation field, increasing  $T_K > T_{\text{CMB}}$  such that the 21 cm signal is seen in emission for the rest of the EoR. The 21 cm spin temperature goes to zero, as it must, at the end of the EoR (e.g. Pritchard & Loeb, 2010; Sathyana Rayana Rao et al., 2017).

Given the history described above, detection of the global signal would provide key information about the thermal history of the IGM as a function of redshift, and about the high-energy emission spectra of early stars and galaxies. Historically, observational efforts to detect the global signal have been “single dish” experiments, where a single receiving element is characterized to high precision, and then operated in an effort to detect the EoR signal as a function of frequency (and thus redshift). Such experiments typically seek to characterize the location and depth of the turning points, with the advent of X-ray sources giving the highest potential signal-to-noise. Experiments such as the Experiment to Detect the Global EoR Step (EDGES, Bowman & Rogers 2010), Sonda Cosmológica de las Islas para la Detección de Hidrógeno Neutro (SCI-HI, Voytek et al. 2014), and the Cosmic Twilight Polarimeter (CPT, Nhan et al. 2016), have been proposed

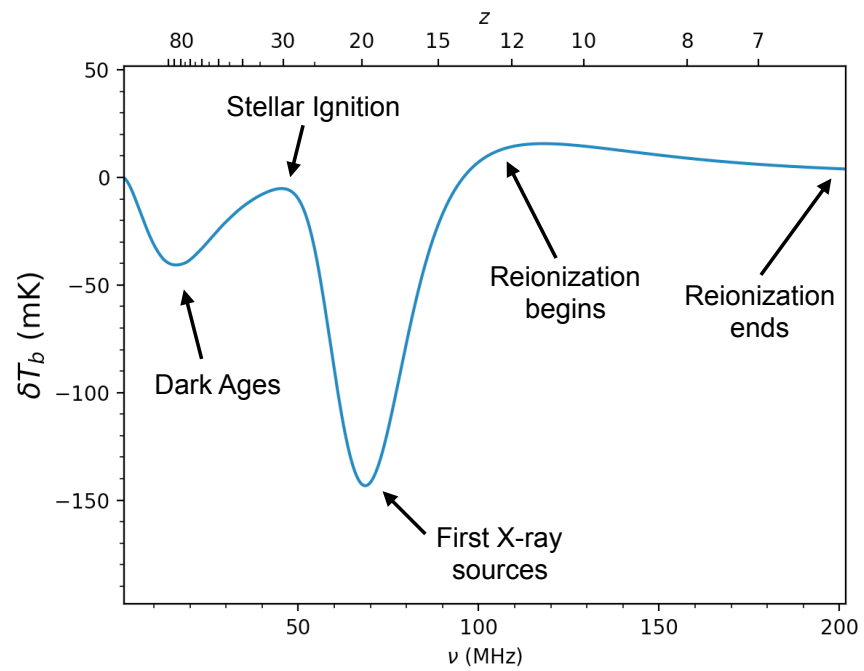


Figure 1.3: The history of the EoR global signal, with important turning-points indicated.  
This figure was produced using the fiducial model of Mirocha et al. (2012).

or constructed seeking to measure the global signal from the Dark Ages or the EoR, through a deep understanding of the properties of the instruments.

In all cases, the instruments consist of a single element, and much of the observational effort contributes toward a thorough understanding of systematic uncertainties of the instrument. Given that the signal is thought to be 4–5 orders of magnitude fainter than the foregrounds, an exquisite understanding of the correlated noise in these instruments is of the utmost importance. At the time of writing, the most mature global experiment is EDGES, an extremely well-characterized radio spectrometer. By subtracting a precise model of the foreground spectrum (Rogers & Bowman 2008, improved upon by Mozdzen et al. 2017), Bowman & Rogers (2010) were able to set a lower limit on the length of the reionization tail (and hence of the EoR itself) of  $\Delta z \geq 0.06$ , ruling-out instantaneous reionization.

Excitingly, as this Chapter was being written, the EDGES team announced a detection of the X-ray heating turning point at 78 MHz (Bowman et al., 2018). Their detected absorption trough was so deep, however, that it exceeds physical models for the (negative) magnitude of  $T_S$ . Bowman et al. (2018) and Barkana (2018) suggested that the excess depth could be accounted for by additional collisions with dark matter. Ewall-Wice et al. (2018) have shown that the excess could also be accounted for by an additional radio background from early black holes formed from PopIII stars. Confirmation from other global signal experiments will be required before the Bowman et al. (2018) result can be fully trusted, but it leaves open the possibility of HI global signal experiments probing exotic particle physics, as well as astrophysics and cosmology.

### 1.2.3 Anisotropic signal

While the global signal may be computed by measuring the average brightness temperature at a given frequency, a richer astrophysical story can be told by measuring the anisotropies in the spin temperature at each redshift. Similarly to the CMB, these anisotropies can be represented through a 2-point correlation function; a power spectrum

in Fourier space. Unlike the CMB, of course, this power spectrum can be measured at each frequency observed, allowing us to construct a history of HI emission on different spatial scales.

Inspection of Equation 1.8 shows that the fluctuations will trace the underlying baryonic density field, but with a complicated bias depending upon the ionization fraction, peculiar velocities and importantly the nature of the ionizing sources, their clustering and their UV and X-ray spectra. This convolution of astrophysical and cosmological dependencies means that the redshift dependence of a given Fourier mode will give clues about the ionization history. Maxima represent high contrasts in the brightness temperature field, suggesting middle stages of the EoR. However, the bulk of information contained in power spectra will require models to extract. This requirement is not as onerous as it might sound, thanks to decades of theoretical work (an exhaustive list is impossible, but the literature reviews of Greig & Mesinger 2017 and Kern et al. 2017 provide useful starting points).

For example, Figure 1.4 shows the enormous improvement in modelling the ionization history, given high signal-to-noise measurements of the 21 cm power spectrum. Including HI data leads to precise constraints on  $x_{HI}(z)$  – but the constraints may be inaccurate in their timing of the EoR without including CMB polarization measurements.

As discussed in Section 1.1, parametrizing the optical depth to the CMB can grant a model-dependent measurement of the ionization history, but one must rely on models in which reionization occurs very quickly. Curves such as those shown in Figure 1.4 would eliminate the need for such models by providing a measurement of the ionization history. This in turn can break degeneracies in other measurements from the CMB. For example, Liu et al. (2016) showed that estimates of the sum of neutrino masses<sup>5</sup> can be improved by  $\sim 10\%$  – importantly, with likelihood contours perpendicular to other probes.

---

<sup>5</sup>Understanding the sum of the masses of the three flavors of neutrinos is a critical measurement in the realm of quantum chromodynamics. It is informed by the CMB, as neutrinos can suppress the formation small-scale anisotropies.

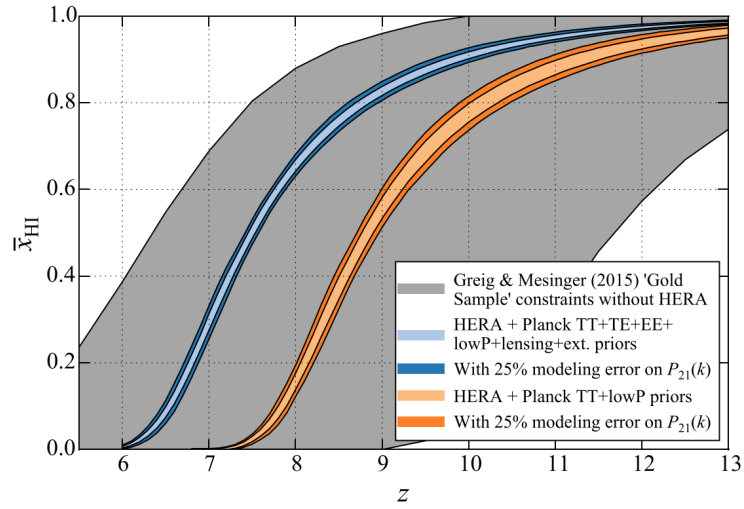


Figure 1.4: Forecasts for constraints on the ionization history, given high signal-to-noise measurements of the HI power spectrum at each redshift from HERA. The grey band shows constraints on the ionization history without measurements of HI, while the blue and orange curves include power spectrum measurements in their modelling. Without CMB polarization measurements, a shift in the timing of reionization can occur. Figure taken from Liu & Parsons (2016).

Kern et al. (2017) used machine-learning techniques to generate a suite of emulators for the HI power spectrum. Given measurements of the power spectrum as a function of redshift, with realistic errors and foreground mitigation, their emulators would be able to constrain cosmological and astrophysical parameters for the EoR and the Dark Ages to relatively high precision. Their constraints on astrophysical parameters were tighter than cosmological ones due to the fact that the brightness contrast is a complicated proxy for the cosmic density field. To illustrate this complication, we show slices of simulation cubes in Figure 1.5, showing the baryon density field and the corresponding 21 cm brightness temperature close the middle of the EoR. In the bottom panel, we show the evolution of the 21 cm field along the line of sight, emphasizing that EoR measurements can provide a rich history of the IGM.

Moving beyond statistical measurements to maps of the EoR<sup>6</sup> opens a rich window for observational cosmology. Performing real-space tomography would allow us to construct cubes of the HI field at different redshifts. Studying the shape and size of bubbles would provide us with a way to identify individual ionizing sources and interpret them. Robertson et al. (2015) showed that there are barely enough galaxies to account for the ionization of the Universe, suggesting that other sources such as quasars must play a role – the signature of which would be detectable in tomographic cubes (Chapter 14, shows an initial machine learning framework to perform this characterization).

Radio interferometers (see Chapter 3), are excellent instruments for probing temperature anisotropies, and their measurements naturally translate into the Fourier space native to power spectrum measurements (see Chapters 4 and 5). Interferometers currently pursuing detection of the EoR power spectrum include the Giant Meterwave Radio Telescope (GMRT; Paciga et al., 2013), the Low Frequency Array (LOFAR; van Haarlem et al., 2013), the Murchinson Widefield Array (MWA; Tingay et al., 2013), the Donald C. Backer Precision Array for Probing the Epoch of Reionization (PAPER; Parsons et al.,

---

<sup>6</sup>The reason for this order is due to the strength of the foregrounds, and strategies employed mitigate them. These will be explored at length in Chapter 5.

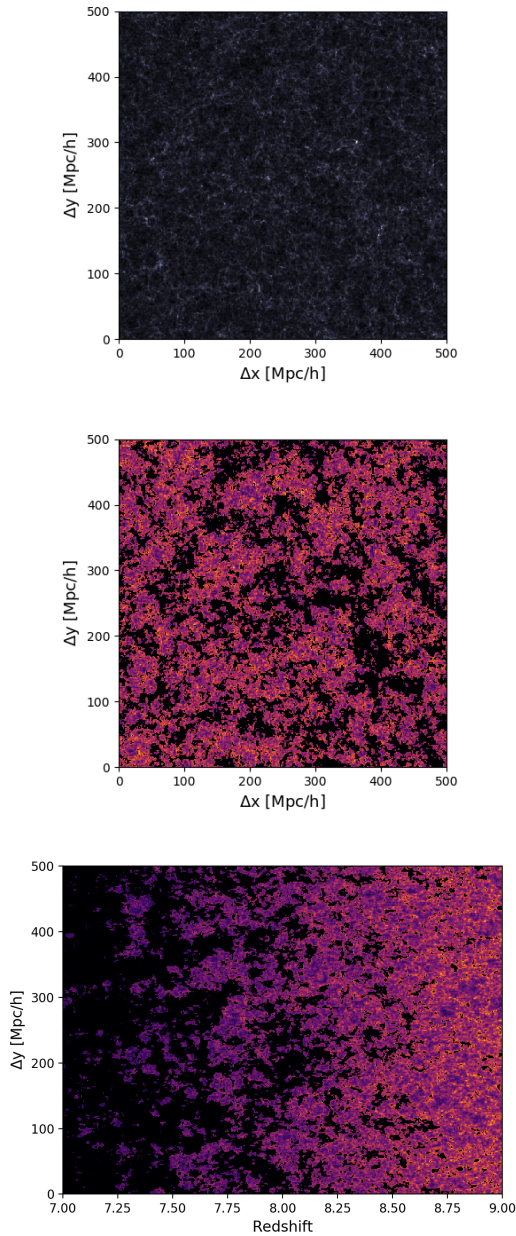


Figure 1.5: An example cosmological simulation of the EoR. The upper panel is the baryon density field, and middle one is the corresponding 21 cm brightness contrast, both at redshift  $z \sim 8$ . Both fields have been normalized for this illustration, the purpose of which is to show that there is not a simple mapping between the cosmological density field and the HI observable. The bottom panel shows the 21 cm brightness contrast as a function of redshift.

2010) and the Hydrogen Epoch of Reionization Array (DeBoer et al., 2017).

Low-frequency radio interferometers such as those listed above have not yet reported results of sufficient depth to claim a detection of the EoR power spectrum. This is largely due to the major challenge faced by all EoR experiments – extremely bright foregrounds. The intensity of the synchrotron radiation that dominates the low-frequency sky scales as a power law in frequency, so probing higher and higher redshifts becomes more and more difficult (see Chapter 2). As we discuss in Chapter 5, the chromatic response of an interferometer may provide a crucial lever arm for disentangling foreground and background radiation. The instrument itself also behaves as a foreground, as at such low frequencies, thermal noise in the electronics is a much larger fraction of the ‘observed’ signal than redshifted 21 cm emission.

### 1.3 Current Limits and Future probes

Over the past decade, immense progress has been made to constrain the global history of the EoR. To review a few limits that have been discussed in this Chapter, limits from quasars and the kSZ have set the end of reionization  $5.8 < z_{\text{end}} < 6.0$ . Measurements of the optical depth to the CMB have set model-dependent limits that put the middle of reionization at  $7.8 < z_{\text{mid}} < 8.8$ . Combining kSZ measurements with the optical depth of the CMB has set an upper limit on the duration of the EoR, and measurements from EDGES have set a lower limit, such that  $0.06 < \Delta z < 2.8$ .

Current kSZ limits and low-significance detections, and measurements from quasars, are consistent with a patchy EoR – bubbles opening to create an inhomogeneous spin temperature field. Figure 1.6 shows current limits on the EoR power spectrum from radio interferometers, as a function of redshift (Kolopanis et al., *submitted*). The limits correspond to different spatial scales, but until some scale-dependence of the EoR power spectrum is detected, plotting them along side one another is valid. Integrations are becoming successively deeper, but there is a ways to go, as shown by a fiducial reionization

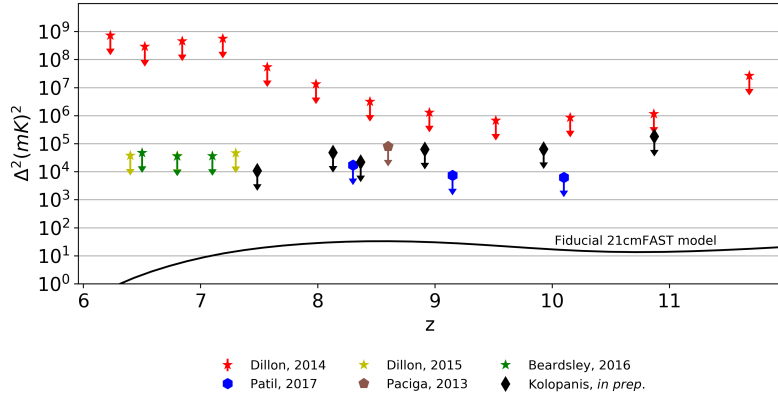


Figure 1.6: Current limits on the EoR power spectrum, as a function of redshift. Different symbol shapes correspond to different instruments, with stars (Dillon et al., 2014, 2015; Beardsley et al., 2016) indicating measurements from the MWA, blue hexagons (Patil et al., 2017) from LOFAR, the brown pentagon from the GMRT (Paciga et al., 2013) and the black diamonds from PAPER-64 (Cheng et al., *submitted*; Kolopanis et al., *submitted*). Figure taken from Kolopanis et al. (*submitted*). Plotted beneath all of the limits is a fiducial 21 cm power spectrum (Mesinger et al., 2011) – there is still a factor of  $\sim 10^3$  to integrate-down upon.

power spectrum curve (Mesinger et al., 2011). Deeper integrations require more interferometric baselines and longer observing seasons, both of which require precision calibration and control of instrument systematics. New techniques for some of these challenges are presented in Part II.

This Chapter has reviewed our current understanding of the EoR, and why it's observation would represent an enormous advancement for modern cosmology. The pursuit of realizing 21 cm tomography is relatively mature, but other atomic transitions could contain similar promise. Silva et al. (2013) suggested that one could perform an intensity-mapping survey of Ly $\alpha$  emission. Such an experiment would involve several narrow-band filters to extract the high-redshift Ly $\alpha$  power spectrum at  $z \sim 7$ , statistically probing the population of ionizing sources towards the end of the EoR, when Ly $\alpha$  is detectable.

Narrow-band surveys for Ly $\alpha$  emission yielded a possible detection of PopIII-like stars at  $z \sim 6.6$  (Sobral et al., 2015).

Carbon is easily ionized by diffuse starlight. The forbidden [CII] transition in ionized carbon could be used to perform tomography with advantages similar to HI, as a probe of star formation history. At EoR redshifts, the emission line would redshift into an atmospheric window detectable in the Far Infra-red from Earth (e.g. Gong et al., 2012; Hunacek et al., 2016; Pentericci et al., 2016). The polar nature of the CO molecule leads to a quantization of its energy states in integer multiples if its angular momentum, appearing as a ‘ladder’ of emission lines that can be used for extremely precise redshift determination, and the relative intensity of which are determined by the temperature of the molecular cloud. Intensity mapping CO emission could provide a cosmic history of star forming giant molecular clouds (e.g. Righi et al., 2008; Lidz et al., 2011). It is worth mentioning that all of these intensity mapping proposals suggest cross-correlation with 21 cm tomographic measurements as a central science objective.

The James Webb Space Telescope is scheduled to launch between October 2018 and June 2019, and will be the most sensitive infra-red telescope ever constructed (Gardner et al., 2009). It is predicted to be able to detect small mass halos ( $\sim 10^5 M_\odot$ ) at  $z \sim 10$  in its planned ultra-deep integrations (Salvaterra et al., 2011; Zackrisson et al., 2011). Its relatively small field of view will not allow for comprehensive surveys of the high-redshift Universe or the EoR, but correlating its measurements with 21 cm maps would provide a probe of the dependence of high-redshift galaxies on their ionization environment (e.g. Beardsley et al., 2015).

## 1.4 This thesis

Everything in this work – algorithmic development, mathematical theory, observations – was carried-out in order to facilitate the detection of the EoR. While these efforts took many forms, they shared that singular motivation of moving the field forward, towards a

detection of HI anisotropies at cosmological distances.

This thesis is divided into three parts. Part I is devoted to introducing concepts used throughout this work and building a mathematical formalism around those concepts. Chapter 2 reviews astrophysical mechanisms for producing polarized and unpolarized radiation at low radio frequencies. Chapter 3 builds a formalism around measuring low frequency radio waves with interferometers (and the challenges associated with accurately measuring polarized radiation), and Chapter 4 introduces the instruments used throughout this work.

In Part II I present the bulk of my efforts: building an understanding of the imprint of the polarized sky, and the instrument itself, in the Fourier space used to set limits on the EoR power spectrum. Chapter 5 reviews the current theory and major results of mapping low frequency interferometric measurements into Fourier space. Chapter 6 details several required quality assurance and compression steps that must be taken to clean and interact with the data. Building from clean data, Chapter 7 presents new algorithms developed to calibrate the measurements. Chapter 8 discusses the impact of Earth's ionosphere on our measurements. In Chapters 9, 10 and 11 I present successively-deeper integrations on polarized foregrounds in successively-narrower regions of Fourier space.

Part III explores other uses of EoR measurements, beyond detection of the power spectrum. In Chapter 12, I discuss the potential of using long time-averages of interferometric measurements to measure some component of the monopole moment of the sky. In Chapter 13, I present a new formalism for cross-correlating 21 cm emission and CMB anisotropies in Fourier space. Chapter 14 describes my initial investigations into utilizing deep learning techniques for recovering cosmological parameters from simulated EoR measurements. I conclude in Chapter 15.

# Chapter 2

## Astrophysical Radiation

As discussed in Chapter 1, the target signal of EoR experiments has a brightness temperature of order  $\sim 10$  mK. At the 50 – 200 MHz frequencies for these experiments, however, foreground radiation from the Milky Way (referred to as “the Galaxy”, with a capital “G” for much of this thesis), extragalactic sources and manmade interference, with total brightness temperature  $\sim 10^4$  times greater than the target signal, is the principle challenge to overcome (e.g. Santos et al., 2005; de Oliveira-Costa et al., 2008; Bernardi et al., 2009, 2010; Pober et al., 2013; Dillon et al., 2014; Kohn et al., 2016, 2018). In this Chapter, I outline our current understanding of polarized and unpolarized foregrounds, and the implications for the dynamic range required for an EoR detection. The Southern Hemisphere is the focus of the chapter, as this is where the instruments used in this work are based (see Chapter 4). For a comprehensive review of radiative processes in astrophysics, see Rybicki & Lightman (1979).

### 2.1 Synchrotron Radiation

Any accelerating charged particle will radiate. For low-frequency radio foregrounds, the radiation we are most interested in is emitted by electrons accelerated by Galactic magnetic fields. At non-relativistic velocities, the radiation of a charged particle accelerated

by magnetic field  $\vec{B}$  is well-described by relatively simple formulae, and is referred to as “cyclotron radiation”. In this case, the emission spectrum is simply determined by gyration frequency about the magnetic field lines. At relativistic velocities, the spectrum becomes more complicated, and is referred to as “synchrotron radiation”.

The equation of motion of a relativistic charged particle of mass  $m$ , charge  $q$  and velocity  $\vec{v}$  can be written as

$$\frac{d}{dt}(\gamma m \vec{v}) = \frac{q}{c} \vec{v} \times \vec{B}, \quad (2.1)$$

where  $\gamma$  is the Lorentz factor, and

$$\frac{d}{dt}(\gamma mc^2) = q \vec{v} \cdot \vec{E} = 0, \quad (2.2)$$

where  $\vec{E}$  is the electric field. Equation 2.2 implies that either  $\gamma$  or  $|\vec{v}| = v$  are constant. Therefore, we may write

$$\gamma m \frac{d\vec{v}}{dt} = \frac{q}{c} \vec{v} \times \vec{B}. \quad (2.3)$$

Decomposing the velocity into components perpendicular and parallel to  $\vec{B}$ ,

$$\frac{d\vec{v}_\parallel}{dt} = 0; \quad \frac{d\vec{v}_\perp}{dt} = \frac{q}{\gamma mc} \vec{v}_\perp \times \vec{B}, \quad (2.4)$$

we find that  $\vec{v}_\parallel$  is constant, and as  $v$  is constant, so  $\vec{v}_\perp$  must be also. This proves that motion along the magnetic field lines is helical, with gyration frequency

$$\omega_B = \frac{qB}{\gamma mc}. \quad (2.5)$$

Using the covariant form of the Larmor Formula with the magnitude of acceleration perpendicular to the magnetic field  $a_\perp = \omega_B v_\perp$ , the total emitted radiation has power

$$P = \frac{2q^2}{3c^3} \gamma^4 a_\perp^2, \quad (2.6)$$

which when accounting for an isotropic velocity distribution, reduces to

$$P = \frac{4}{24\pi} \sigma_T c \beta^2 \gamma^2 B^2 \quad (2.7)$$

Since the electrons follow a helical path, an observer will only see components of the emission when the motion is parallel to the line-of-sight. The observed radiation will be

emitted along path  $\delta s$  with radius of curvature  $r$  and angle  $\delta\theta$ , such that  $\delta\theta = 2/\gamma$  and  $\delta s = 2r/\gamma$ . Equations 2.1 and 2.2 grant

$$r = \frac{v}{\gamma\omega_B \sin \alpha}, \quad (2.8)$$

where  $\alpha$  is the angle between  $\vec{v}$  and  $\vec{B}$ . The time taken for the electron to travel  $\delta s$ , and therefore emit the observed radiation, may be characterized by a critical frequency

$$\omega_c = \frac{3}{2}\gamma^3\omega_B \sin \alpha. \quad (2.9)$$

Deferring to Rybicki & Lightman (1979) for a full discussion, the frequency spectrum of synchrotron radiation is intimately tied to the helical geometry of the problem and  $\omega_c$ , with power per unit frequency proportional to some function  $F(\omega/\omega_c)$ :

$$P(v) = \frac{\sqrt{3}q^3B \sin \alpha}{m_e c^2} F\left(\frac{\omega}{\omega_c}\right) \quad (2.10)$$

where the form of  $F$  depends on the energy distribution of the electrons. For black-body radiators in the Rayleigh-Jeans limit, appropriate for low-frequency radio observations, the number density of particles with energy  $E$  can be described with a power law:

$$N(E)dE = AE^{-p}d\gamma, \quad (2.11)$$

where  $A$  is a constant of proportionality that can vary with angle of observation. In this case, it can be shown that the total energy density per unit frequency is

$$P(v) = \frac{A\sqrt{3}q^3B \sin \alpha}{m_e c^2(p+1)} \left( \frac{2\pi mc}{3qB \sin \alpha} v \right)^{-\frac{p-1}{2}} \Gamma\left(\frac{p}{4} + \frac{19}{12}\right) \Gamma\left(\frac{p}{4} - \frac{1}{12}\right). \quad (2.12)$$

The objective of this exercise was to show that the total power of synchrotron radiation is innately smooth as a function of frequency; it can be described as a power law. An example observation of low-frequency Galactic synchrotron is shown in Figure 2.1. The observed sky spectrum has a spectral index  $\beta_* = 2.52 \pm 0.04$  for brightness temperature  $T(v) \propto v^{-\beta_*}$ . Recall that the HI EoR field has a complex structure in both the image plane and along the line-of-sight (c.f. Figure 1.5). The superposition of emission lines

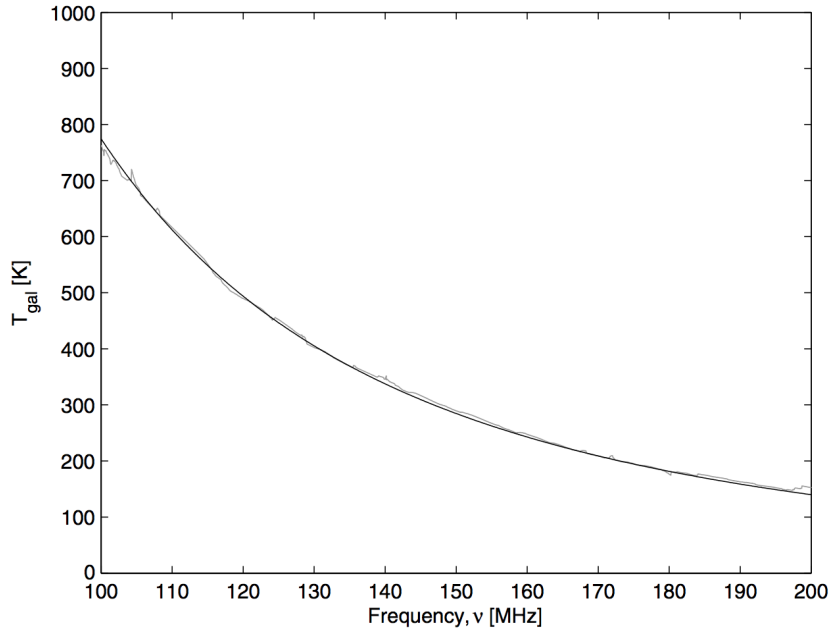


Figure 2.1: The low-frequency synchrotron spectrum of sky, measured by Rogers & Bowman (2008). Their measurement is shown in light grey, overlaid with a well-fit power law of spectral index  $2.52 \pm 0.04$ .

from this field will lead to unsmooth, structured emission per unit frequency. In the face of synchrotron foregrounds being many orders of magnitude brighter than the 21 cm emission, *this difference in spectral behavior is the single most important distinguishing feature between foregrounds and the EoR.*

## 2.2 Stokes parameters

It is extremely unlikely that we will observe radiation from electrons spiralling along magnetic field lines that are exactly parallel or perpendicular to our line-of-sight. Instead, some elliptically polarized component of the radiation is observed. The Stokes parameters are quantities used to describe the polarization state of electromagnetic waves.

We can describe a monochromatic electromagnetic wave propagating towards the ob-

server as the real part of

$$\vec{E} = \vec{E}_0 e^{-i\omega t} = \begin{pmatrix} E_1 e^{i\phi_1} \\ E_2 e^{i\phi_2} \end{pmatrix} e^{-i\omega t} \quad (2.13)$$

It can be shown (e.g. Rybicki & Lightman, 1979) that the real part of the vector above can be mapped, in general, to the principle axes of an ellipse at position angles  $\psi$  and  $\chi$  to the Cartesian plane, as shown in Figure 2.2. These two angles,  $E_1$ , and  $E_2$ , can be used to define the Stokes parameters for monochromatic waves:

$$I \equiv E_1^2 + E_2^2 = E_0^2, \quad (2.14)$$

$$Q \equiv E_1^2 - E_2^2 = E_0^2 \cos 2\psi \cos 2\chi, \quad (2.15)$$

$$U \equiv 2E_1 E_2 \cos(\phi_1 - \phi_2) = E_0^2 \cos 2\chi \sin 2\psi, \quad (2.16)$$

$$V \equiv 2E_1 E_2 \sin(\phi_1 - \phi_2) = E_0^2 \sin 2\chi. \quad (2.17)$$

The interpretation of these parameters is as follows: Stokes I measures the total intensity of the electric field. Stokes Q and U measure the orientation of the electric field relative to, in this case, the  $x$ -axis of the Cartesian plane, where Q measures the projection parallel to the  $x$ -axis and U measures the projection at  $45^\circ$  to the  $x$ -axis. They are clearly linked, as  $\tan \psi = U/Q$ . Stokes V is the circularity parameter, measuring the ratio of the principle axes of the ellipse. For monochromatic waves,  $I^2 = Q^2 + U^2 + V^2$ .

In practice, observed radiation fields are rarely monochromatic (purely elliptically polarized). Instead, we observe a superposition of electric fields, each with its own polarization state. If we assume that the amplitude and phase of the observed radiation change relatively slowly over time, we can express

$$\vec{E}(t) = \vec{E}_0(t) e^{-i\Phi(t)} = \begin{pmatrix} E_1(t) e^{i\phi_1(t)} \\ E_2(t) e^{i\phi_2(t)} \end{pmatrix} \quad (2.18)$$

such that over short times  $\Delta t \sim 1/\omega$  the wave is of a definite elliptical polarization state, but for  $\Delta t \gg 1/\omega$  the polarization state can change by a large amount. Such waves are referred to as ‘quasi-monochromatic’, with coherence time  $\Delta t$  and its conjugate, bandwidth  $\Delta\omega$ . Due to the time-dependent nature of quasi-monochromatic waves, the exact

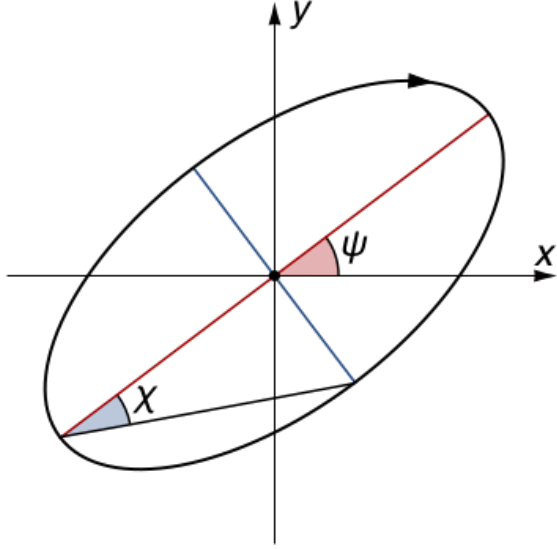


Figure 2.2: A representation an elliptically polarized monochromatic wave with respect to the Cartesian grid.

values of  $E_1$ ,  $E_2$ ,  $\phi_1$  and  $\phi_2$  cannot be precisely measured. Instead, radiometers measure the average sum of squares of the components of  $\vec{E}(t)$ . These can be used to define the Stokes parameters for quasi-monochromatic waves:

$$I \equiv \langle E_1 E_1^* \rangle + \langle E_2 E_2^* \rangle = \langle E_1^2 + E_2^2 \rangle, \quad (2.19)$$

$$Q \equiv \langle E_1 E_1^* \rangle - \langle E_2 E_2^* \rangle = \langle E_1^2 - E_2^2 \rangle, \quad (2.20)$$

$$U \equiv \langle E_1 E_2^* \rangle + \langle E_2 E_1^* \rangle = \langle 2E_1 E_2 \cos(\phi_1 - \phi_2) \rangle, \quad (2.21)$$

$$V \equiv -i(\langle E_1 E_2^* \rangle - \langle E_2 E_1^* \rangle) = \langle 2E_1 E_2 \sin(\phi_1 - \phi_2) \rangle, \quad (2.22)$$

where  $E_i^*$  indicates the complex conjugate of  $E_i$ , and  $\langle \dots \rangle$  indicates an average over some integration time over which the measurement is made. It is easy to see from the Cauchy-Schwarz inequality that for quasi-monochromatic waves,  $I^2 \geq Q^2 + U^2 + V^2$ . Radiation is completely unpolarized if  $Q = U = V = 0$ . It is common to refer to the “polarization fraction” or “degree of polarization” of observed radiation,  $p$ :

$$p \equiv \frac{\sqrt{Q^2 + U^2 + V^2}}{I} \quad (2.23)$$

and ‘‘linear polarized intensity’’,  $P$ :

$$P = \frac{1}{2} \sqrt{Q^2 + U^2} \quad (2.24)$$

The Institute of Electrical and Electronics Engineers (IEEE) defines the standard reference frame for the polarization axes to be the lines of constant Right Ascension ( $\alpha$ ) and Declination ( $\delta$ ) on the sky. Substitution of  $1 \rightarrow \alpha$  and  $2 \rightarrow \delta$  in the definitions above brings those definitions to standard (Cohen, 1958; Ludwig, 1973; van Straten et al., 2010).

## 2.3 Total intensity foregrounds

At EoR frequencies, 50 – 250 MHz, the brightest source of total intensity is the Galactic Plane. While the configuration of the Galactic magnetic field is still a matter of debate (e.g. Haverkorn, 2015), but observations of synchrotron emission suggest it has an average power of  $\sim 6\mu\text{G}$  (e.g. Beck, 2003). Multiple, dynamic sources of HII such as supernova remnants (SNRs) and other contributors to the interstellar medium provide charged particles to radiate synchrotron. This has a brightness temperature of  $\sim 5$  K. Beyond our Galaxy, synchrotron from extragalactic sources (galaxies and galaxy clusters) have brightness temperatures  $\sim 0.5$  K (e.g. Jelić et al., 2010).

With the advent of newly operational low-frequency interferometers (see Chapter 4), detailed maps of low-frequency synchrotron emission in the Southern Hemisphere have only very recently become accessible. The PAPER-64 imaging array (Jacobs et al., 2011, 2013; Stefan et al., 2013, and Chapter 4) was used to make a map of the Southern Galactic Plane at 145 MHz. This array was able to resolve some diffuse components, but mainly focused on relatively small-scale structures such as SNRs and HII regions (i.e. tens of parsecs; Asvarov 2014). That map is shown in Figure 2.3, projected into Galactic coordinates. Synchrotron sources in the plane of the Galaxy include SNRs (most prominently

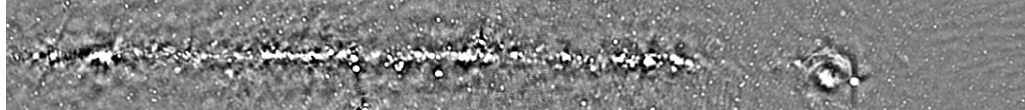


Figure 2.3: The Galactic plane as observed by PAPER-64. Synchrotron sources include supernova remnants (e.g. the Vela and Puppis complexes to the East), HII regions and ionized gas in the plane of the Galaxy. Extragalactic sources are visible above and below the Galactic plane.

the Vela and Puppis complexes to the East), HII regions (almost indistinguishable from SNRs in the plane) and ionized gas. Above and below the Galactic plane, extragalactic point sources are visible (and match the Jacobs et al. (2011) 145 MHz point-source catalog of the region).

Motivated by the sparsity of wide-field, diffuse radio surveys, de Oliveira-Costa et al. (2008) presented the ‘Global Sky Model’ (GSM), in which they amalgamated as many high-fidelity wide-field radio surveys as possible, from 10 MHz to 100 GHz. Zheng et al. (2017) extended the upper limit of this range to 10 THz. Using principal component analysis and an expectation for smooth frequency structure, they were able to build a model that could be interpolated to any requested frequency within their spectral range. An example at 150 MHz is shown in Figure 2.4. It is important to note that the GSM is uncertain at the  $\sim 5\%$  level, and in the southern hemisphere this uncertainty is greater due to fewer well-characterized surveys of diffuse emission. Aside from diffuse Galactic emission, the GSM also includes the ‘A Team’ of bright radio sources, such as Pictor A, Fornax A and Centaurus A. Pictor A is particularly useful as a calibration source: it is relatively unpolarized, unresolved as a point source, and the one of the brightest extragalactic sources of synchrotron emission (Jacobs et al., 2013).

With the advent of the 128-tile Murchison Widefield Array (MWA), the GaLactic and Extragalactic All-sky Murchison Widefield Array (GLEAM) survey took place over two years, imaging most of the sky south of Declination  $+25^\circ$  in Stokes I, Q, U & V with myriad science goals (Bowman et al., 2013; Wayth et al., 2015; Hurley-Walker et al.,

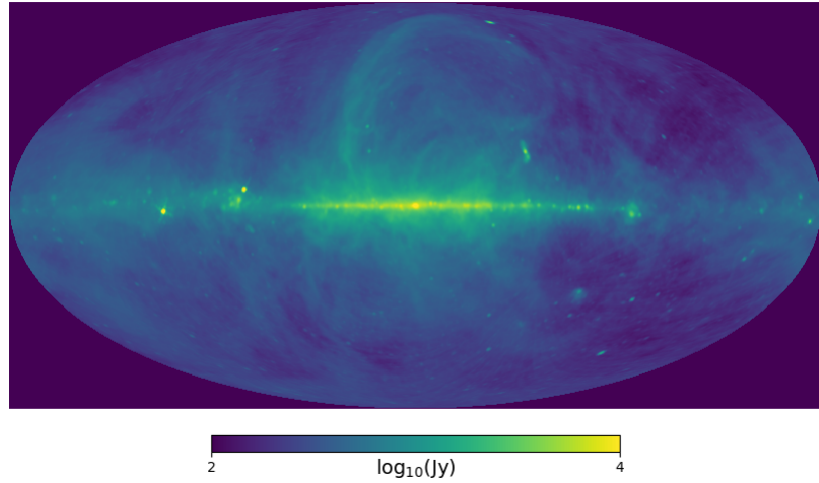


Figure 2.4: The GSM at 150 MHz: a relatively accurate model of diffuse synchrotron across the entire sky.

2017). Covering 70–230 MHz with 10 kHz frequency resolution, sensitivity to a wide range of spatial scales, and reaching theoretical noise levels in Stokes I, GLEAM (the maps of which are not yet public) will have a significant legacy for our understanding of the low-frequency sky.

## 2.4 Linearly Polarized Foregrounds

Polarized foregrounds are less well characterized than total intensity ones, especially in the southern hemisphere, and even then, the measurements were typically at GHz frequencies and must be extrapolated for relevance to EoR studies. The DRAO 26 m (Wolleben et al., 2006) telescope and the VLA (Condon et al., 1998) mapped the entire sky, in Stokes I, Q, U & V, visible from their respective positions in the northern hemisphere. This meant that much of the southern hemisphere was blocked by the Earth. Both of these surveys were performed at 1.4 GHz. The polarized intensity map produced by Wolleben et al. (2006) is shown in Figure 2.5 in Galactic coordinates.

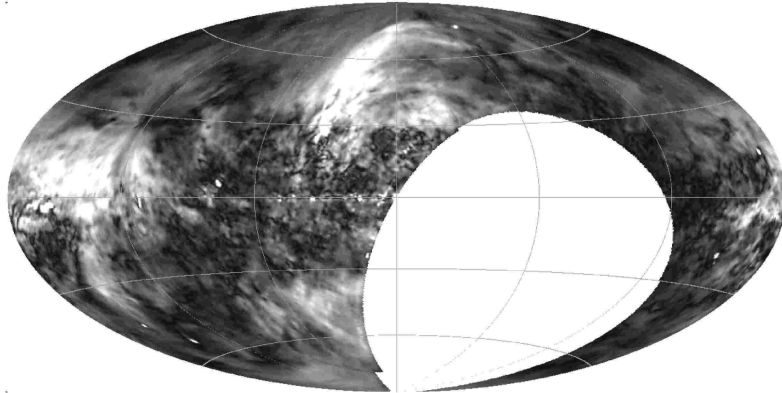


Figure 2.5: The polarized intensity of the sky as viewed by the DRAO 26 m telescope at 1.4 GHz. Figure taken from Wolleben et al. (2006).

Bernardi et al. (2013) surveyed  $2400 \text{ deg}^2$  of the southern hemisphere with the 32-element MWA at 189 MHz in Stokes I, Q and U. They detected large amounts of bright ( $\sim 10 \text{ K}$ ), diffuse polarized emission at hour angles close to the transit of the Galaxy (most likely the contribution of diffuse emission south of the Galactic Plane, as visible in Figure 2.5), but just one polarized extragalactic source with flux density  $> 4 \text{ Jy}$ .

Indeed, most recent observations in the 100–200 MHz band, covering selected sky areas, have revealed that bright Galactic diffuse polarized synchrotron radiation seems to be ubiquitous (Bernardi et al., 2009, 2010; Jelić et al., 2014; Lenc et al., 2016) with peak emission up to 15 K (Jelić et al., 2015), but find a dearth of bright polarized (extragalactic) point sources. The point sources cataloged by Bernardi et al. (2013) showed significant depolarization compared to their polarized flux density at higher frequencies (see Section 2.4.2).

As calibration schemes are refined and modern interferometers grow, a small population of weakly polarized point sources has recently been revealed. Observing  $\sim 625 \text{ deg}^2$  with the 128-element MWA, at 154 MHz, Lenc et al. (2016) found five polarized point sources of polarized intensity order  $10 - 100 \text{ mJy beam}^{-1}$ . Much deeper integrations with the Low Frequency Array (LOFAR) presented by Van Eck et al. (2018) found 92 polarized point sources within  $570 \text{ deg}^2$ , observed at 150 MHz, with polarized intensities of the

order  $1 - 10 \text{ mJy beam}^{-1}$ . In all of these observations, polarized intensity represented a polarized fraction  $p \leq 15\%$ .

Note that we have focused on polarized intensity – Stokes Q and U – for this discussion. At low frequencies, Stokes V is expected to be almost intrinsically zero (e.g. Sokolowski et al., 2017). While at higher frequencies circularly polarized synchrotron has been observed from sources such as relativistic jets (e.g. Macquart & Fender, 2004), very few natural sources of Stokes V are present in the low frequency sky, with the exception of transients such as extrasolar flares (Spreeuw et al., 2010) and aurorae of giant planets (e.g. Zarka & Kurth, 2005; Badman et al., 2015). This makes measurements of Stokes V useful for null tests (e.g. Patil et al., 2017)

### 2.4.1 Faraday Rotation

One of the most important considerations for HI EoR measurements is the Faraday Rotation Measure of polarized foregrounds (the reasons for this are thoroughly enumerated in Chapter 5).

Electromagnetic waves will undergo dispersion and refraction while propagating through and ionized gas or plasma. If an external magnetic field is incident upon the plasma, electrons in the plasma will gyrate about the field with frequency

$$\omega_B = \frac{e}{m_e c} B_0 \approx 1.67 \times 10^7 B_0 \text{ s}^{-1}, \quad (2.25)$$

where  $B_0$  is the magnitude of the magnetic field. This alters the dielectric constant in the plasma. Decomposing linearly polarized radiation in to a circular basis (this basis change is not the equivalent of intrinsically circularly polarized Stokes V radiation) of clockwise ('right-handed'; R) and anti-clockwise ('left-handed'; L) waves, we can express the dielectric constant as

$$\epsilon_{R,L} = 1 - \frac{\omega_p^2}{\omega(\omega \pm \omega_B)}, \quad (2.26)$$

where R and L correspond to + and -, respectively,  $\omega$  is the angular frequency of the

radiation, and  $\omega_P$  is the plasma frequency

$$\omega_P^2 = \frac{4\pi n_e e^2}{m_e}, \quad (2.27)$$

for electron number density  $n_e$ . The index of refraction of a plasma is given by  $\sqrt{\epsilon}$ . Clearly, the handedness of the radiation will experience different angles refraction. The effect of this in the linear basis is to rotate the plane of polarization as the radiation propagates through the magnetized plasma. For a screen of width  $L$ , the change in angle is given by (Rybicki & Lightman, 1979; Thompson et al., 2017):

$$\Delta\phi = \frac{1}{2} \int_0^L \frac{\omega_P^2 \omega_B}{c \omega^2} dl. \quad (2.28)$$

Substituting for  $\omega_B$  and  $\omega_P$ , and observing the radiation along the line-of-sight (as we must), gives

$$\Delta\phi = \frac{e^3}{(m_e c^2)^2} \lambda^2 \int_0^L n_e(l) B_{\parallel}(l) dl \equiv \lambda^2 \Phi \quad (2.29)$$

where we have moved from angular frequency to wavelength, and defined the *Faraday Rotation Measure* (RM)  $\Phi$ . This rotation moves power between Stokes Q and U,

$$(Q + iU)_{\text{observed}} = e^{-2i\Phi\lambda^2} (Q + iU)_{\text{intrinsic}}, \quad (2.30)$$

where  $\Phi$  has units of rad m<sup>-2</sup>.

At GHz radio frequencies, measurements of polarization angle with respect to wavelength can be used to chart the magnetic field of galaxies, given some independent measure of the electron number density. Equation 2.30 also defines a Fourier relationship between  $\Phi$  and  $\lambda^2$ , which can be exploited to obtain a similar measurement, and is referred to as ‘RM synthesis’ (Brentjens & de Bruyn, 2005). Importantly, at low frequencies the large values of  $\lambda$  will cause rapid phase wraps for RMs  $\geq \sim 10$ , inducing spectral structure in what would otherwise be smooth synchrotron spectra (Moore et al., 2013).

Figure 2.6 shows the all-sky RM measurements of Oppermann et al. (2012), obtained by using both of the above methods (fitting in  $\lambda^2$  and RM synthesis) on a number of radio surveys ranging from 1.1 to 11 GHz. Uncertainties in the values reported are typically at the level of  $\sim 10\%$ , with larger uncertainties in the southern hemisphere due to fewer polarization surveys existing in that region, and along the Galactic plane.

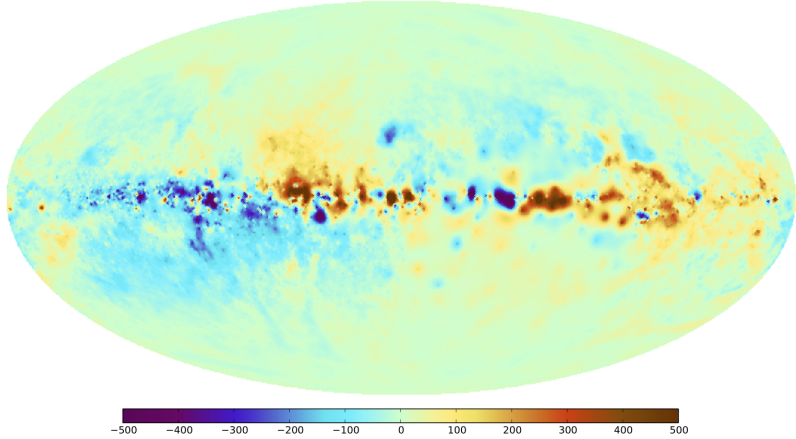


Figure 2.6: An all-sky map of RMs. The colorbar has units of  $\text{rad m}^{-2}$ . Figure taken from Oppermann et al. (2012).

### 2.4.2 Depolarization

Frequently the intrinsic polarization fraction of a radiating source much greater than the observed value; the observed radiation is ‘depolarized’. Modes of depolarization can generally be categorized in to two groups: natural and instrumental.

Instrumental polarization can occur via the beam – the receptivity pattern, or point spread function (PSF) – of the instrument (see Chapter 3). If the polarization angle changes significantly within the area of the beam, which is the case for turbulent Galactic magnetic fields and the very large beam areas of modern instruments (e.g. Chapter 4), the observed polarization fraction can be attenuated during integration over the beam area. When probing RM distributions via RM synthesis, the channel width over which the data are averaged sets the sensitivity to the maximum RM by definition. Sources with higher RMs will suffer from ‘bandwidth depolarization’, and this effect will strengthen at lower frequencies according to the phase-wrapping factor  $2\Phi\lambda^2$ . As we explore in the next Chapter, interferometric polarization measurements are obtained by measuring the projection of the electric vector field on to orthogonal dipole arms. An electrical phase offset between the two arms will almost certainly exist in any instrument. If left uncalibrated,

Stokes U will leak in to Stokes V, consequently depolarizing linear polarized intensity. Likewise, relatively faint polarized emission can be “washed-out” of measurements if Stokes I is able to leak in to Stokes Q and U measurements.

Natural depolarization can arise at the source of the radiation, due to turbulent magnetic fields. Different magnetic field projections along the line-of-sight can produce different angles of polarization, that can on average attenuate the observed polarized intensity. Similarly, radiation emitted from different depths of the source can undergo different amounts of Faraday rotation along the line-of-sight as they pass through regions of different electron densities. This effect is apparent in Figure 2.5: in the plane of the Galaxy, which has a large column depth, the observed polarized intensity is low compared to, for example, the Northern Galactic Spur, which is physically closer to the Earth.

Finally, the ionosphere of the Earth is a turbulent plasma, which when coupled with the Earth’s magnetic field can act as a Faraday screen. If left uncorrected, averaging observations of the same patch of sky observed at different times can lead to a depolarization effect – we explore this further in Chapter 8.

As mentioned in Section 2.4, Bernardi et al. (2013) reported polarization fractions of extragalactic compact sources at 189 MHz significantly lower than reported at higher frequencies. This was corroborated by some of the measurements by Lenc et al. (2016), although not all of the polarized point sources found in their survey showed significant evidence of depolarization. The least depolarized sources in that survey corresponded to hot-spots of large radio galaxies, which perhaps are not as deeply embedded in galactic plasma as the other sources observed, and therefore suffered less natural depolarization. Farnes et al. (2014) showed a systematic trend for depolarization of steep-spectrum point sources as frequency decreased, resulting in very low polarization fractions ( $\ll 1\%$ ) below 300 MHz. They also suggested that natural polarization was the cause, due to turbulent magnetic fields at the source of the radiation.

Recall that in Chapter 1, we stated that 21 cm emission was effectively unpolarized. Why have we gone in to so much detail about polarized radiation? As we will see in subsequent Chapters, polarized power is capable of ‘leaking’ in to Stokes I measurements through effects intrinsic to radiometric instruments, and calibration errors. Recall also that Faraday Rotation can induce spectral structure in otherwise smooth spectrum, polarized synchrotron emission. Coupled with leakage, this additional spectral structure risks contaminating the one lever-arm we have against the bright foregrounds! This effect lead to much of the research presented in this work.

# **Chapter 3**

## **Interferometry, Calibration & Polarimetry**

In this Chapter I wished to build a formalism around wide-field, polarized interferometric measurements that could be used throughout this work. Many traditional assumptions used in radio interferometry are broken in the case of the wide-field, fully-polarized, drift-scanning measurements native to interferometric EoR observations. In Section 3.1, I derive the equation describing the fundamental observable for an interferometer, called a “visibility”. Section 3.2, I describe calibration techniques relevant to this work and in Section 3.3 I review some of the implications of the previous two sections for polarized measurements.

For a comprehensive review of interferometry from a traditional perspective, see Thompson et al. (2017).

### **3.1 The Visibility Equation**

A radio interferometer (a term used interchangeably with “interferometric array” for radio observations) is an ensemble of receiving elements, where each element’s measurement is correlated with every other element’s. The simplest case is a two-element interferometer,

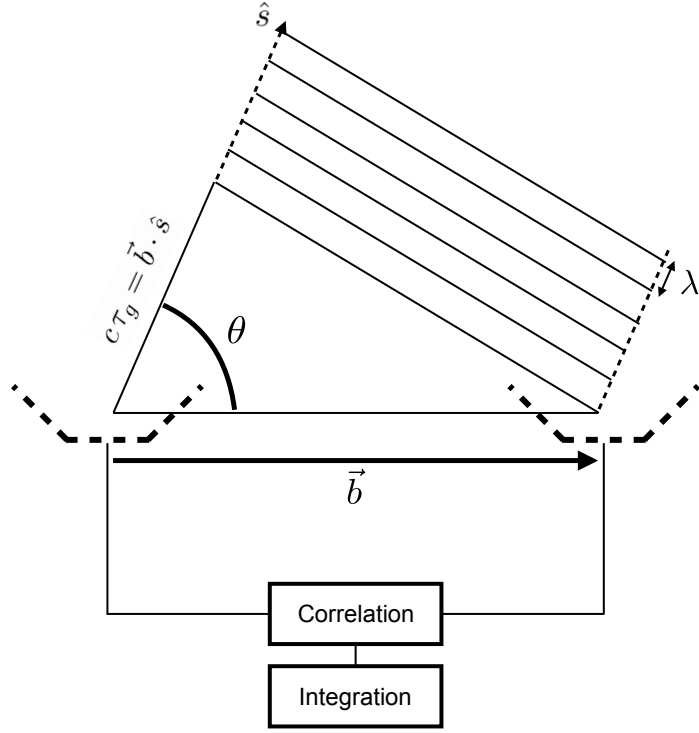


Figure 3.1: The geometry of a two-element interferometer, with a plane wave incident from direction  $\hat{s}$ .

which we will focus on below. We assume that the elements are coplanar and identical.

### 3.1.1 The Classical Visibility Equation

Consider two receiving elements  $i$  and  $j$ , separated by baseline vector  $\vec{b}$ . Suppose a plane wave of wavelength  $\lambda$  is incident upon these elements, with direction of propagation  $-\hat{s}$ . The geometry of this interferometer is illustrated in Figure 3.1.

We can define the electromagnetic wave to have a frequency dependent phase, such that the electric field measured by element  $i$  at time  $t$  is

$$E_i = E_0 e^{-2\pi i v t}. \quad (3.1)$$

The time difference between the arrival at  $i$  and  $j$  is called the “geometrical delay”,

$\tau_g$ :

$$\tau_g = \frac{\vec{b} \cdot \hat{s}}{c}, \quad (3.2)$$

and the electric field measured by element  $j$  is

$$E_j = E_0 e^{-2\pi i v(t+\tau_g)}. \quad (3.3)$$

An interferometer is an instrument which measured voltages induced by these electric fields, and correlates them together, integrating their product over some coherent time-scale. This correlation grants:

$$\langle E_i E_j^* \rangle = \lim_{T \rightarrow \infty} \frac{1}{2T} \int_{-T}^T E_i(t) E_j(t) dt = |E_0|^2 e^{-2\pi i v \tau_g} \quad (3.4)$$

where  $e^{-2\pi i v \tau_g} = e^{-2\pi i v \vec{b}_{ij} \cdot \hat{s}/c}$  is known as the “fringe” term, due to its sinusoidal nature. We can generalize this relationship to include more than a single plane wave from direction  $\hat{s}$ . Many plane waves, from all directions, can be incident upon the interferometer at a given time and frequency. We can represent the power distribution on the sky as  $S(\Omega)$ , where  $S(\Omega)$ . However, no instrument is equally sensitive to radiation from every direction  $\hat{s} \in \Omega$ . Instead, an instrument has some sensitivity pattern – a *beam pattern* – that tapers the power distribution on the sky into an “observed sky”,  $S'(\Omega) = A(\Omega)S(\Omega)$ .

These generalizations lead to the classical visibility equation:

$$V_{ij}(v) = \int A(\Omega, v) S(\Omega, v) e^{-2\pi i v \vec{b}_{ij} \cdot \hat{s}/c} d\Omega \quad (3.5)$$

for a “visibility” – the fundamental interferometric observable –  $V_{ij}$  as a function of frequency.

If we choose to represent the source direction in terms of directional cosines  $\ell$  and  $m$ , and represent the baseline vector in units of wavelengths,  $\vec{b}_{ij}/\lambda = (u, v, w)$ , we can perform a change of variables in Equation 3.5 to give

$$V_{ij}(u, v) = \int \int A(\ell, m) S(\ell, m) e^{-2\pi i(u\ell + vm + w\sqrt{1-\ell^2-m^2})} \frac{d\ell dm}{\sqrt{1-\ell^2-m^2}}. \quad (3.6)$$

This relationship is often simplified by assuming only a small area of the sky is under observation – that is, that  $A(\ell, m)$  falls-off steeply from zenith – and therefore  $\ell^2$  and  $m^2$  are small. This grants

$$V_{ij}(u, v) \approx e^{-2\pi i w} \int \int A(\ell, m) S(\ell, m) e^{-2\pi i(u\ell + vm)} d\ell dm, \quad (3.7)$$

which plainly casts  $V(u, v)$  as the Fourier transform of the observed sky if  $w$  is small: that is, the array is co-planar and no appreciable curvature of the sky is probed. Modern low frequency interferometers used in this work greatly violate this approximation, the consequences of which I will discuss in the proceeding sections.

Even though it is often violated, the Fourier relationship shown in Equation 3.7 is an extremely useful one to work with when translating between visibilities and images. Images can be created by inverse Fourier transforming all of the visibilities measured by an array. Following Equation 3.6, a reconstructed image  $\tilde{S}(\ell, m)$  is given by

$$\frac{A(\ell, m)\tilde{S}(\ell, m)}{\sqrt{1-\ell^2-m^2}} = \int \int \Xi(u, v)V(u, v)e^{2\pi i v(u\ell + vm)} du dv. \quad (3.8)$$

In Equation 3.8, we see that the reconstructed image  $\tilde{S}(\ell, m)$  is attenuated by the beam response  $A(\ell, m)/\sqrt{1-\ell^2-m^2}$ . The function  $\Xi(u, v)$  defines the sampling of the  $u, v$  - plane. It is equal to 1 at the points sampled by the interferometer (baselines of length and direction defined by the vector  $\vec{b} = (u, v)$  exist in the array) and 0 elsewhere. As an example, the array shown in Figure 3.1 would be described by a  $\Xi(u, v)$  function that was zero at all points except for a single  $(u, v)$  coordinate described by baseline vector  $\vec{b}$ .

The effect of the sampling function  $\Xi(u, v)$  is that the true sky  $S(\ell, m)$  can never be completely reconstructed, since it is impossible to build an interferometer that samples every  $u, v$  mode. The true sky is convolved with the Fourier transform of  $\Xi(u, v)$ , which astronomers refer to as the “dirty beam”.  $\Xi(u, v)$  contains zeros, so a complete deconvolution of  $\tilde{S}(\ell, m)$  is impossible.

We now note that an important aspect of light has been absent throughout the derivations above: the polarization state of the radio wave that induces the electric field in Equation 3.1. Interferometers are typically constructed with two feeds, sensitive to polarization states of an incident radio wave along two separate axes. In the case of all of the instruments used in this work (see Chapter 4), an antenna  $i$  had two dipole feeds perpendicular to one another. These were along the North-South direction ('n') and the East-West direction ('e'). We can attempt to generalize Equation 3.5 to include polarization, setting antenna  $i$  to have orientation  $p$  and antenna  $j$  to have orientation  $q$ ,  $p, q \in (e, n)$ :

$$V_{ij}^{pq} = \int A_{pq}(\Omega, v) S_{pq}(\Omega, v) e^{-2\pi i v \vec{b}_{ij} \cdot \hat{s}/c} d\Omega. \quad (3.9)$$

However, two aspects of this equation are unsatisfactory. As explored in Chapter 2, the polarized sky is defined with the four Stokes parameters; an ' $S_{pq}$ ' polarized sky does not exist. Likewise, a dipole is not purely sensitive to a single vector orientation from the sky, but probes a wide range of angles<sup>1</sup>. Therefore a  $A_{pq}$  polarized beam is ill-defined. These shortcomings lead us to rewrite the visibility equation, cohesively including polarization from the outset.

### 3.1.2 The Measurement Equation

The Radio Interferometric Measurement Equation (RIME) provides an extremely useful framework for describing wide-field polarized observations. Formulated by Hamaker et al. (1996), it was re-introduced to the radio astronomy community through a series of papers by O. M. Smirnov (Smirnov, 2011a,b,c,d). In this section I review the portions of his work most relevant to this thesis, and defer the reader to the series for a useful and thorough walk-through of wide-field radio interferometry and high dynamic-range calibration.

---

<sup>1</sup>In the case of the PAPER instrument, described in the next Chapter, the dipole feeds probed the entire hemisphere of the sky.

Returning to Equation 3.1, a radio wave incident on an antenna induces a voltage in along feed arm

$$\vec{E} = (e_p, e_q); \vec{v} = (v_p, v_q) = \mathbf{J}\vec{E} \quad (3.10)$$

where  $\mathbf{J}$  is a  $2 \times 2$  complex matrix termed the “Jones matrix” (Jones, 1941). Jones matrices represent linear transformations along the signal path, from the emission of the radio wave onwards. Multiple stages along the signal propagation can be represented by multiplying different Jones matrices together as a “Jones chain”, which may be expanded or collapsed as convenient.

Interferometric visibilities are pairwise correlations of the components of  $\vec{v}$  between antennas  $i$  and  $j$ , integrated over some small time span (Equation 3.4), which we can represent hold in matrix form (the layout of which will become clear in a moment):

$$\mathbf{V}_{ij} = \begin{pmatrix} \langle v_i^p v_j^{p*} \rangle & \langle v_i^p v_j^{q*} \rangle \\ \langle v_i^q v_j^{p*} \rangle & \langle v_i^q v_j^{q*} \rangle \end{pmatrix} = \langle \vec{v}_i \vec{v}_j^H \rangle. \quad (3.11)$$

Above,  $H$  represents the Hermitian transpose operation.

Using this formalism allows us to map the emitted electric field to the observed visibilities,

$$\mathbf{V}_{ij} = \mathbf{J}_i \begin{pmatrix} \langle e_i^p e_j^{p*} \rangle & \langle e_i^p e_j^{q*} \rangle \\ \langle e_i^q e_j^{p*} \rangle & \langle e_i^q e_j^{q*} \rangle \end{pmatrix} \mathbf{J}_j^H = \mathbf{J}_i \mathbf{C}_{ij} \mathbf{J}_j^H \quad (3.12)$$

where  $\mathbf{J}_{i,j}$  may be Jones chains of arbitrary length. We have assumed instrument stability to move them out of the time averages in the central matrix. We refer to  $\mathbf{C}_{ij}$  as the “coherency matrix”.

In Chapter 2 the Stokes parameters we introduced. Hamaker & Bregman (1996) showed that the components of the coherency matrix are closely related to the Stokes parameters:

$$\begin{pmatrix} \langle e_i^p e_j^{p*} \rangle & \langle e_i^p e_j^{q*} \rangle \\ \langle e_i^q e_j^{p*} \rangle & \langle e_i^q e_j^{q*} \rangle \end{pmatrix} = \begin{pmatrix} I+Q & U+iV \\ U-iV & I-Q \end{pmatrix}. \quad (3.13)$$

The Jones formalism allows for a construction of the visibility equation that does not make explicit assumptions regarding polarization or field-of-view, in which we can map the Stokes parameters into the instrumental basis that visibilities are computed in:

$$\mathbf{V}_{ij} = \int \mathbf{J}_i(\hat{s}) \mathbf{C}_{ij}(\hat{s}) \mathbf{J}_j^H(\hat{s}) e^{-2\pi i v \vec{b}_{ij} \cdot \hat{s}/c} d\Omega, \quad (3.14)$$

which Smirnov (2011a) refers to as the “Full Sky Radio Interferometric Measurement Equation”<sup>2</sup>. Note that all of these quantities are functions of frequency as well, in general.

So far, the formalism shown has used the  $2 \times 2$  “Jones basis”. It is sometimes more useful to work in the  $4 \times 4$  “Mueller basis” (Mueller, 1948), which acts on visibilities in  $4 \times 1$  vector form:

$$\begin{pmatrix} V^I \\ V^Q \\ V^U \\ V^V \end{pmatrix} = \mathbf{S} \vec{V}_{ij} = \begin{pmatrix} 1 & 0 & 0 & 1 \\ -1 & 0 & 0 & 1 \\ 0 & 1 & 1 & 0 \\ 0 & -i & i & 0 \end{pmatrix} \begin{pmatrix} V^{PP} \\ V^{PQ} \\ V^{QP} \\ V^{QQ} \end{pmatrix}. \quad (3.15)$$

It is important to note that Equation 3.15 lists a vector of “Stokes-polarized visibilities” on the left-hand side, whereas Equation 3.13 shows that the coherency matrix contains linear combinations the Stokes parameters. This is not an inconsistency. While visibilities are quantities that are integrated over the sky, the Stokes parameters are only defined *on* the sky. One must transform the visibilities from the *uv*-plane onto the image-plane and deconvolve the beam in order to measure the Stokes parameters. Instead, linear combinations of visibilities measure a proxy for each the Stokes parameters. To make the inequality between visibilities and Stokes parameters explicit, I will refer to the “Stokes-polarized visibilities” as “pseudo-Stokes visibilities” from now on.

One can translate between these two formalisms using the definition of  $\vec{V}_{ij}$  (c.f. Equation 3.10),

$$\vec{V}_{ij} = (\mathbf{J}_i \otimes \mathbf{J}_j^H)(\vec{E} \otimes \vec{E}^H). \quad (3.16)$$

---

<sup>2</sup>We choose to explicitly show the exponent in this formulation for ease of comparison with Equation 3.5. This term can written as a “phase delay Jones matrix” and absorbed into the Jones chain.

Comparison of Equation 3.5 and 3.14 shows that the Jones chain must, at the very least, encapsulate the beam pattern of the instrument. We can build such a Jones matrix by considering the response of feed  $p$  on antenna  $i$  to an electric field from infinity in the direction  $(\theta, \phi)$ :

$$\vec{A}_i^p(\hat{s}) = A_{i,\theta}^p(\hat{s})\hat{\theta} + A_{i,\phi}^p(\hat{s})\hat{\phi}, \quad (3.17)$$

where we have suppressed the frequency dependence. The antenna patterns may be written as components of a “Beam Jones matrix” for an antenna,

$$\mathbf{J}_i^B(\hat{s}) = \begin{pmatrix} A_{i,\theta}^p(\hat{s}) & A_{i,\phi}^p(\hat{s}) \\ A_{i,\theta}^q(\hat{s}) & A_{i,\phi}^q(\hat{s}) \end{pmatrix}. \quad (3.18)$$

These are the essential components for understanding the fundamental measurement performed by an interferometer. However, there are several effects one must take into account for the equations to truly reflect an interferometric measurement; effects such as instrumental gains, reflections between antennas, Faraday rotation in the ionosphere, etc. Most importantly, we must consider how these factors affect the measurement of polarization.

## 3.2 Calibration Techniques

The purpose of calibration is to remove effects of the instrument and the atmosphere from the data. Visibilities are measured in “data units”. That is, a given feed on an antenna will record some measurement of power, but some scalar conversion factor is required to calibrate that power to units of flux density. As visibilities measure the pairwise correlations of antenna powers, the estimation of the calibration factors can quickly become difficult as the number of antennas increases. In this Section we explain different approaches to such a challenge.

### 3.2.1 Diagonal and off-diagonal calibration

The calibration term that converts the power measured by an antenna to physical units is referred to as the “antenna gain”. This may be summarized per feed as a direction-independent “Gain Jones matrix”,

$$\mathbf{J}_i^G = \begin{pmatrix} g_i^p & 0 \\ 0 & g_i^q \end{pmatrix}, \quad (3.19)$$

where we have suppressed the frequency dependence. The components of  $\mathbf{J}_i^G$  are complex numbers, the argument of which represents instrumental phase, and the modulus represents instrumental amplitude. Note that this formulation of  $\mathbf{J}_i^G$  is only appropriate for linear antenna feeds. Circular feeds, which we will not comment on for the rest of this work, require an additional rotation matrix applied to move from a linear to a circular polarization frame.

Unfortunately, a direction-independent scaling is not the only term that requires estimation. As Equation 3.18 makes clear, a given feed is not receptive to a single plane of polarization. In general, we expect some fraction of power measured by feed  $p$  to be transferred into feed  $q$  via imperfect electronics (clever feed designs can attempt to minimize this effect, e.g. Parashare & Bradley, 2006; Parsons et al., 2010). This kind of power leakage is described by an off-diagonal matrix, and the components are known as “ $D$ -terms”,

$$\mathbf{J}_i^D = \begin{pmatrix} 1 & D_i^p \\ D_i^q & 1 \end{pmatrix}. \quad (3.20)$$

$D$ -terms are often left un-calibrated, as they are generally a few percent of the gain term for a given feed. However, a  $\sim 5\%$  error in calibration could represent an error large enough to inhibit an EoR detection. Unless an EoR instrument is shown to have very low  $D$ -terms, they must be taken in to account.

### 3.2.1.1 Ionospheric effects

Chapter 8 details the importance of the ionosphere for EoR measurements. Briefly put, the ionosphere is an upper layer of the Earth's atmosphere; an ionized plasma formed from solar radiation. Coupled with the Earth's magnetic field, it becomes a time- and position-variable Faraday screen (see Chapter 2) capable of rotating the polarization axis of an incident electromagnetic wave. This adds an additional term to the Jones chain in Equation 3.14. Representing the ionospheric Faraday screen as  $\Phi(\hat{s}, t)$ , this term is

$$\mathbf{J}_i^I = \begin{pmatrix} \cos(2\Phi(\hat{s}, t)c^2/v^2) & \sin(2\Phi(\hat{s}, t)c^2/v^2) \\ -\sin(2\Phi(\hat{s}, t)c^2/v^2) & \cos(2\Phi(\hat{s}, t)c^2/v^2) \end{pmatrix}. \quad (3.21)$$

The ionosphere's effect on polarized radiation is the most important one to consider for this work. However, the more commonly worried-about effect of the ionosphere (among radio astronomers) is its diffractive property. Neglecting the Earth's magnetic field, the refractive index  $\eta$  of a cold, collisionless plasma is (Thompson et al., 2017)

$$\eta = \sqrt{1 - \frac{v^2}{v_P^2}}, \quad (3.22)$$

for an electromagnetic wave of frequency  $v$  and plasma frequency  $v_P$ , given by

$$v_P = \frac{1}{2\pi} \sqrt{\frac{n_e e^2}{m_e \epsilon_0}} \quad (3.23)$$

where  $n_e$  is the number density of electrons,  $e$  and  $m_e$  are the electron charge and mass and  $\epsilon_0$  is the permittivity of free space. This term is typically of the order of a few MHz (Vedantham & Koopmans, 2015). This causes a direction- and time-dependent phase shift in the propagating wave. This shift is

$$\gamma(\hat{s}, v) = \int dl \frac{2\pi v}{c} \eta(\hat{s}) \approx \int dl \frac{2\pi v}{c} - \frac{1}{2} \int dl \frac{2\pi v_P^2}{cv} \quad (3.24)$$

where  $l$  is the distance through the ionosphere, and we have Taylor-expanded Equation 3.22 for the approximation. This effect can be represented as a diagonal, direction-dependent Jones matrix,

$$\mathbf{J}_i^{\Gamma}(\hat{s}, v) = \begin{pmatrix} \exp(i\gamma(\hat{s}, v)) & 0 \\ 0 & \exp(i\gamma(\hat{s}, v)) \end{pmatrix}, \quad (3.25)$$

where we have made the frequency dependence explicit.

Due to the turbulent nature of the ionosphere, both of these terms are extremely difficult to calibrate (Intema et al., 2009; Vedantham & Koopmans, 2015). In Chapter 8, we present the effects *not* calibrating the polarized component when averaging together large numbers of polarized visibilities.

### 3.2.2 Image-based calibration

Traditionally, the approach taken for estimating the components of all of the above was to observe a calibration source. A calibrator source would be unresolved, such that its position and phase is a direct measure of ionospheric diffraction and instrumental phase. Deviation from its catalogued position can be subtracted off, calibrating the phase (the argument of the components of  $\mathbf{J}_i^G$ ; Equation 3.19). For an interferometer that cannot point in a given direction, but instead “drift-scans”, observing the sky as the Earth rotates, calibration takes place when the calibrator source is at zenith (for a telescope that can point, the calibrator source would be observed in the center of the field-of-view). With a well-catalogued flux density and minimal beam attenuation, the amplitude of the visibility can be scaled appropriately to estimate the moduli of instrumental gains.

If the polarization state of the calibration source was known (and non-zero), forming Stokes parameters in the image plane can provide a measure of instrumental polarization, as gain errors and  $D$ -terms move power between the Stokes parameters (see Section 3.3 and Chapter 7). If the calibration source is known to be unpolarized, then the same method can be used to place a limit on the  $D$ -term magnitudes by maximizing Stokes I while minimizing Stokes Q, U and V.

The approach described above is only as good as the sky and instrument models used, as one must “simulate” the expected visibilities for a given sky model passing over a simulated instrument. For the wide field-of-view observations that are native to low-

frequency instruments, obtaining a sky model that accurately describes the point sources and diffuse structure on the sky is a daunting task. Barry et al. (2016) included the 4,000 brightest catalog sources in their sky (unpolarized) model of the one of the Murchinson Widefield Array’s (MWA; see Chapter 4) EoR observation fields, but this granted insufficient dynamic range to allow for an EoR measurement. They found too much contamination from a large population of faint, unmodelled point sources.

### 3.2.3 CLEAN

An uncalibrated array is one where the power in the  $uv$ -plane is incorrectly distributed. Transforming an uncalibrated  $uv$  distribution to the image plane will result in power scattered throughout the image plane; this is referred to as a “dirty image”. By precisely calibrating visibility complex gains (etc.), one is in effect rearranging the power distribution on the sky into the distribution astrophysical sources. An accurate calibration is one that does so and reproduces the flux density measured by other studies.

To perform an image-based calibration, one must be able to move easily between the  $uv$  and image planes. There are two major challenges in doing so: the limited distribution of spatial scales probed by an interferometer, as encapsulated by the  $\Xi(u,v)$  sampling function, and errors in instrumental calibration. The former challenge can be faced by using deconvolution techniques that estimate the missing information, known under the umbrella term of “CLEANing algorithms”. The latter can be faced by precise calibration – in which an image can be of great utility to iterate upon.

#### 3.2.3.1 Högbom’s algorithm

Högbom (1974) devised the first deconvolution algorithms to become widely used by the radio astronomy community, known as CLEAN. It is an iterative numerical deconvolution process applied in the image plane, based on the assumption that the sky is composed of a distribution of point sources<sup>3</sup>.

---

<sup>3</sup>In the era of wide field-of-view instruments, many more accurate and precise deconvolution algorithms

The Högbom algorithm proceeds as follows:

1. Compute the amplitude and position of the point of greatest intensity (the ‘peak’) in the dirty image.
2. Subtract from the dirty image, at the position of the peak, the peak strength multiplied by the dirty beam pattern (recall that the dirty beam is the Fourier transform of  $\Xi(u, v)$ ) and a factor  $\gamma \leq 1$  (the ‘loop gain’). Record the position and amplitude of the subtracted component, as this will form the model that will become the CLEANed image.
3. Repeat Steps 1 & 2 iteratively until all significant structure has been removed from the image (where the value of ‘significance’ is set by the astronomer). This may be constrained to ‘CLEAN-windows’ within a larger image.
4. Convolve the accumulated point model with a ‘CLEAN beam’, usually a Gaussian with Full-Width Half-Max equal to the central lobe of the dirty beam. This is the ‘CLEAN image’
5. Add the residuals of the dirty image to the CLEAN image.

An example of different CLEANing stages is shown in Figure 3.2.

A major shortcoming of the Högbom algorithm is its proliferation of small-scale structures around the locations of point sources. This is because the subtraction in Step 2, above, leaves new, local maxima around the perimeter of subtracted region. Later deconvolution algorithms, such as the one devised by Cornwell (1983), avoid this by padding the surrounding region according to an additional smoothness parameter.

Imaging with extremely wide field-of-view instruments is explored in Chapter 7.

---

have been developed that are able to calibrate images of diffuse structures, rather than point sources. There are also many other algorithms besides Högbom’s that focus on point sources, such as Clark or Cotton-Schwab. However, for the purposes of this descriptive chapter, we focus on the Högbom CLEAN.

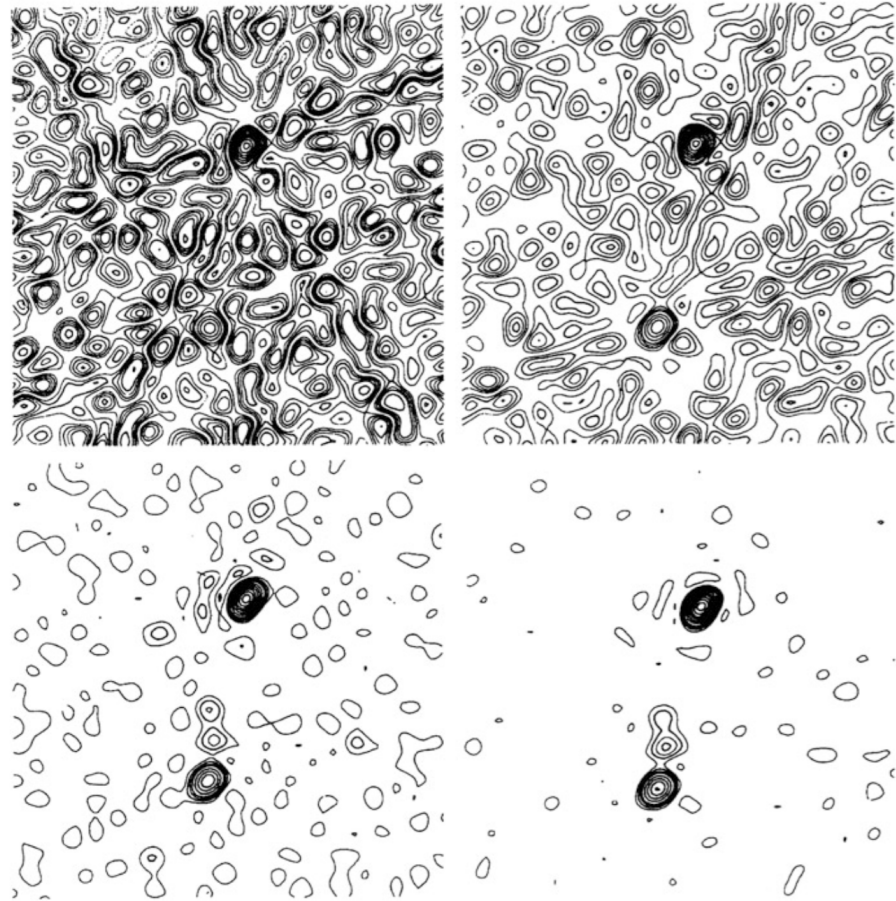


Figure 3.2: Four stages of the Högbom CLEAN, as implemented on data from the Green Bank Interferometer. The top left panel shows the dirty image, with power scattered throughout the image plane. The top right panel shows the image after a single iteration with  $\gamma = 1$ . The bottom left and bottom right panels show the image after two and six iterations, respectively. Contours are steps of 5% from the maximum in each image. Figure taken from Högbom (1974); Thompson et al. (2017).

### 3.2.3.2 Delay Transforms and the 1D-CLEAN

There are a variety of CLEANing techniques that are central to this thesis, but do not operate on images at all. Parsons & Backer (2009) and Parsons et al. (2012b) introduced the 1D-CLEAN, a deconvolution algorithm that operates on visibilities Fourier-transformed along the frequency axis, never gridding them on the  $uv$ -plane. Much more about Fourier-transformed visibilities will be spoken of throughout this work, and we discuss the basic points here.

A Fourier transform along the frequency axis of a visibility is called a ‘delay transform’. This nomenclature comes from the fact that Fourier conjugate of frequency is a quantity in units of time – and the correct interpretation of this value is the time delay between a wavefront incident upon antenna  $i$  and  $j$ . The delay  $\tau_g$  of a source at (R.A.,Dec.)=( $\alpha, \delta$ ) is

$$\tau_g = \frac{\vec{b}}{c} \cdot \begin{pmatrix} \cos \delta \cos(h - \alpha) \\ -\cos \delta \sin(h - \alpha) \\ \sin \delta \end{pmatrix}, \quad (3.26)$$

for local sidereal time  $h$ . This value can be isolated in “delay space” via a delay transform (where it is convenient to use the classical visibility equation for clarity, but all steps can be folded into the Jones formalism),

$$\begin{aligned} \tilde{V}_{ij}(\tau, t) &= \int d\nu g_i^*(\nu, t) g_j(\nu, t) V_{ij}(\nu, t) e^{2\pi i \nu \tau} \\ &= \tilde{g}_i(\tau, t)^* \tilde{g}_j(\tau, t) * \sum_n^N [\tilde{A}(\tau, \hat{s}_n(t)) * \tilde{S}_n(\tau) * \delta_D(\tau_g + \tau_{e,i,j} - \tau)] \end{aligned} \quad (3.27)$$

which is true for any polarization, so we have dropped our polarization indexing. Like the Högbom algorithm, this explicitly assumes the sky can be expressed by  $N$  point sources at positions  $\hat{s}_n$ . Instrumental absolute gains and phases are expressed as  $g_i$ ,  $g_j$  and  $\tau_{e,i,j} = \tau_j - \tau_i$ . Clearly, this procedure isolates a source  $n$  as a delta function with amplitude  $\tilde{S}_n$  at a given delay (assuming a smooth spectrum; see below), convolved by a kernel that describes the chromaticity of the instrument. If the instrument is designed to have a

smooth frequency response, the  $\tilde{g}_{i,j}(\tau)$  and  $\tilde{A}(\tau)$  terms will be narrow functions in delay space and the value of  $\tau_g + \tau_{e,i,j}$  will be well-constrained. If the instrument has an unsmooth spectral response, many more  $\tau$ -modes will be required to describe it, resulting in a spread of power in delay space.

Figure 3.3 shows a graphical representation of a two-source sky model mapping from celestial coordinates to delay space. Note that the delay transform is not a one-to-one mapping – sources in a plane perpendicular to the baseline vector share the same  $\tau_g$ . Dotted lines in the delay-space plot demarcate an extremely important value of  $\tau$ . A given baseline will have a *maximum delay value*,  $\tau_{\max} = |b|/c$ , the light travel time between the antennas. With sufficient bandwidth and frequency resolution, this boundary can be clearly resolved, and all sources with smooth spectra (as is the case for unpolarized synchrotron radiation, but not for Faraday rotated polarized radiation or HI; see Chapter 2 and almost all of Part II) will have their maximum power values within the  $-\tau_{\max} \leq \tau \leq \tau_{\max}$  region.

By delay-transforming simulated visibilities with a simple sky model of the brightest sources and comparing to an observed sky with those sources close to zenith, one can estimate the instrumental delays and gains and obtain a delay-based calibration for  $\mathbf{J}_i^G$ . However, Fourier-transforming along an axis with discontinuities – such as spikes or divets caused by Radio Frequency Interference (RFI) and its subsequent flagging – will result in sinc-like side lobes throughout delay space. Some interpolation is required to bridge these gaps, presented in Parsons & Backer (2009) as the complex 1D-CLEAN. The algorithm proceeds as follows:

1. Delay-transform the visibility containing nulled frequency channels – this is the “dirty image”.
2. As in the Högbom algorithm, iteratively propagate the largest magnitude feature, by  $\tau$  bin, to a model after convolving it with the Fourier transform of the flags themselves – this is the “dirty beam”.

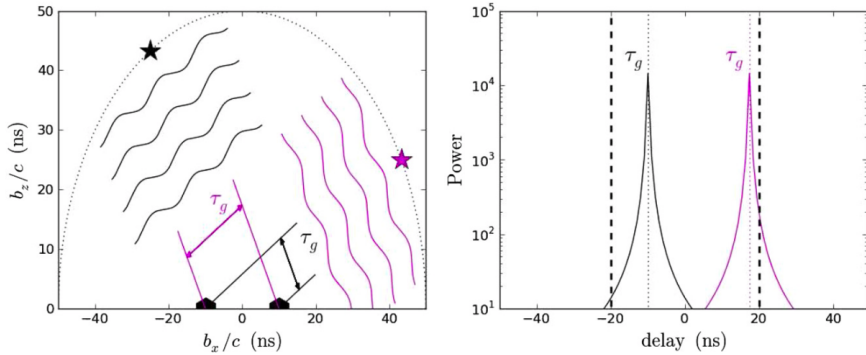


Figure 3.3: A graphical representation of the delay transform. The left panel shows the relationship between celestial position and geometrical delay relative to a 60 m baseline (which has a  $\sim 20$  ns light-travel-time between antennas). The right panel shows an example delay transform of the visibilities recorded by this model interferometer. With perfect phase calibration, power from the sources is isolated to their geometrical delay, with some spread in delay space due to the chromaticity of the instrument. Figure taken from Parsons et al. (2012b).

3. Stop when the residual power in delay space is beneath some defined threshold.  
Add this residual power to the model.

The importance of the delay transform for EoR studies is discussed in Chapter 5, and a variant of it is presented in Chapter 11.

### 3.2.4 Redundant calibration

Thus far we have discussed calibration techniques that require some model of the sky to begin with. For an interferometer without any repeated baseline vectors, these methods are sufficient. However, some EoR studies, such as those discussed in this thesis, have opted to construct highly redundant arrays, with many repeated baselines. Such interferometers sample comparatively few modes of the  $uv$ -plane, leading to poor images – but their visibilities can be averaged together in order to reduce noise for EoR measurements on specific spatial scales.

We defer detailed discussion of redundant calibration to Chapter 7, but provide a brief overview here (studies that explore this technique in depth include Wieringa (1992); Liu et al. (2010); Zheng et al. (2014) and Dillon et al. (2017)). In a redundant array, there are several examples of a given “visibility type”. Assuming the antennas have identical beams (understanding non-redundant beams is a contemporary effort), the only difference between the visibilities should be due to their complex gains. For a visibility type  $V_{|i-j|}^{pq}(\nu, t)$ , all baselines with baseline vector  $\vec{b}_{|i-j|}$  may be described as

$$V_{ij}(\nu, t) = g_i^p(\nu, t)g_j^q(\nu, t)V_{|i-j|}^{pq}(\nu, t) + n_{ij}(\nu, t), \quad (3.28)$$

where the  $n_{ij}$  term represents noise on that visibility. For a redundant array, this system of equations is highly overdetermined to solve for  $g_i^p$  and  $g_j^q$ , as long as  $V_{|i-j|}^{pq}$  can be formed (this can simply be the median of all of the visibilities of that type in the data). Again, for a fuller mathematical overview we defer to Chapter 7.

We have made the frequency and time dependence explicit in order to emphasize that the complex gains can be solved-for each every frequency, time sample. This is unlike the delay transform (which requires a frequency bandwidth to transform over) or imaging calibration (which can in principle be implemented per-time and frequency, but is difficult due to the resultant very noisy dirty images).

Using redundant calibration, when available, can reduce the number of diagonal gains to solve for from  $\frac{1}{2}N_{\text{ants}}(N_{\text{ants}} - 1)$  to just a few unknowns. These unknowns are degeneracies of the system of equations defined in Equation 3.28, and arise from the fact that no information from the sky is required to obtain diagonal gains that are self-consistent between antennas. For the simplest implementation of such a system, as presented in Zheng et al. (2014), there are four degeneracies per feed arm (so eight overall). These are:

- Overall amplitude scaling (to obtain the correct flux density of the sky),
- Overall phasing (an arbitrary additional phase ramp),

- Phasing along the  $\hat{\theta}$  direction (correct positions on the sky),
- Phasing along the  $\hat{\phi}$  direction (correct positions on the sky).

These additional parameters can be obtained by making an image of a calibration field – no CLEANing should be required, since power should be self-consistently distributed in the  $uv$ -plane – where the sky will likely be incorrectly centered and of incorrect amplitude.

### 3.3 Instrumental Polarization

An interferometer is capable of measuring pseudo-Stokes visibilities, which contain components of Stokes power, somehow convolved by the instrumental response. Understanding this instrumental response is crucial for performing polarimetry at low frequencies. As we will see, the instrument will inherently ‘leak’ power between polarizations in direction dependent (effects that occur inside the visibility integral) and independent (outside of the visibility integral) ways. These leakage modes must be well-understood in order to make any statements about the nature of the polarized sky.

Synthesizing the Jones formalism introduced in Section 3.1 and the calibration terms in Section 3.2, we seek to understand how the Jones chain,

$$\mathbf{J}_i = \mathbf{J}_i^D(v) \mathbf{J}_i^G(v) \mathbf{J}_i^I(\hat{s}, v) \mathbf{J}_i^\Gamma(\hat{s}, v) \mathbf{J}_i^B(\hat{s}, v), \quad (3.29)$$

influences the power in pseudo-Stokes visibilities.

#### 3.3.1 Direction-Dependent Leakage

The direction-dependent terms in the Jones chain concern the beam, and ionospheric effects. In this section, we will concentrate on the beam Jones matrix – the ionospheric effects are discussed in detail elsewhere (e.g. Intema et al., 2009; Vedantham & Koopmans, 2015, 2016, Martinot et al. (*in prep.*)).

Unless  $\mathbf{J}_i^B(\hat{s}, v)$  is both diagonal and, at any given point on the sphere, the diagonal elements are equal, there will be mixing or “leaking” of different Stokes parameters together into each element of  $\mathbf{V}_{ij}$  in a direction dependent way (e.g. Geil et al., 2011; Smirnov, 2011a,b; Nunhokee et al., 2017). Focusing on pseudo-Stokes I and neglecting other Jones terms for a moment,

$$\begin{aligned} V_{ij}^I(v) &= \text{Tr}(\mathbf{V}_{ij}) = \int \text{Tr}(\mathbf{J}_i^B \mathbf{C}_{ij} \mathbf{J}_j^{BH}) \exp(-2\pi i v \vec{b} \cdot \hat{s}/c) d\Omega \\ &= \int \mathbf{M}_{00} I + \mathbf{M}_{01} Q + \mathbf{M}_{02} U + \mathbf{M}_{03} V \exp(-2\pi i v \vec{b} \cdot \hat{s}/c) d\Omega \end{aligned} \quad (3.30)$$

where I, Q, U and V are the true Stokes sky and are functions of direction and frequency, and the  $\mathbf{M}_{ab}$  terms are components of the direction dependent instrumental Mueller matrix, also functions of direction and frequency:

$$\mathbf{M}_{ab}(\hat{s}, v) = \text{Tr}(\sigma_a \mathbf{J}_i^B \sigma_b \mathbf{J}_j^{BH}) \quad (3.31)$$

and  $\sigma_k$  are the Pauli matrices, where the indices are reordered from the quantum mechanical convention such that

$$\sigma_0 = \begin{pmatrix} 1 & 0 \\ 0 & 1 \end{pmatrix}, \sigma_1 = \begin{pmatrix} 1 & 0 \\ 0 & -1 \end{pmatrix}, \sigma_2 = \begin{pmatrix} 0 & 1 \\ 1 & 0 \end{pmatrix}, \sigma_3 = \begin{pmatrix} 0 & -i \\ i & 0 \end{pmatrix} \quad (3.32)$$

$$V^I = \text{Tr}(\sigma_0 \mathbf{V}), V^Q = \text{Tr}(\sigma_1 \mathbf{V}), V^U = \text{Tr}(\sigma_2 \mathbf{V}), V^V = \text{Tr}(\sigma_3 \mathbf{V}).$$

Equation 3.30 explicitly shows that the pseudo-Stokes I visibility is inherently composed of the weighted sum of all of the Stokes parameters, where the weighting is direction- and frequency-dependent, given by the Mueller terms  $\mathbf{M}_{ab}(\hat{s}, v)$  in Equation 3.31. In turn, the  $\mathbf{M}_{ab}(\hat{s}, v)$  terms are completely determined by the beam Jones matrix; a collection of complex voltage beam patterns. With a simulated instrument, one can obtain the  $4 \times 4$   $\mathbf{M}(\hat{s}, v)$  matrix and model the contribution of each Stokes parameter to each pseudo-Stokes visibility. The key to such a Mueller matrix is

$$\mathcal{M}_{ab}(\hat{s}, v) = \begin{pmatrix} I \rightarrow V^I & I \rightarrow V^Q & I \rightarrow V^U & I \rightarrow V^V \\ Q \rightarrow V^I & Q \rightarrow V^Q & Q \rightarrow V^U & Q \rightarrow V^V \\ U \rightarrow V^I & U \rightarrow V^Q & U \rightarrow V^U & U \rightarrow V^V \\ V \rightarrow V^I & V \rightarrow V^Q & V \rightarrow V^U & V \rightarrow V^V \end{pmatrix} \quad (3.33)$$

Fagnoni & de Lera Acedo (2016) simulated the feed, faceted parabolic dish and analog signal chain for the Hydrogen Epoch of Reionization Array (HERA) instrument using the CST<sup>4</sup> package. They generated the  $\vec{E}$ -field receptivity patterns that could be used to form  $\mathbf{J}_i^B$  and  $\mathbf{M}(\hat{s}, v)$ . Examples of  $\mathbf{M}(\hat{s}, v)$  at 120 MHz and 160 MHz are shown in Figure 3.4, projected in the R.A., Dec. basis. Note that this basis has a singularity at the South Pole, leading to wide-field asymmetries in components to do with Stokes Q and U. Due to the large spread in dynamic ranges between  $\mathbf{M}_{00}$ , other diagonal terms, and off-diagonal terms, we use separate color maps for each. All of the dynamic ranges are normalized to the peak of  $\mathbf{M}_{00}$ , which is 1 at zenith. The off-diagonal terms are 2- to 8-orders of magnitude less than the diagonal terms.

As discussed in Chapter 2, at the low frequencies and large scales relevant to EoR experiments, the Stokes I sky is extremely bright compared to the other Stokes parameters, and few polarized point sources have been found. This makes the first column of  $\mathbf{M}(\hat{s}, v)$ , representing  $I \rightarrow V^I V^Q V^U V^V$  the most interesting for characterizing the polarized response of an instrument observationally. It can be reasonably expected that even a small amount of leakage from Stokes I into the other Stokes parameters will dominate over Stokes Q, U and V power alone.

Deconvolution of  $\mathbf{M}(\hat{s}, v)$  for wide field-of-view instruments is not at all a solved problem, with contemporary studies “learning to live with it”. Hypothetically, with accurate polarized sky and instrument models, one could use the linear nature of the Jones formalism to compute each “visibility component”,

$$\hat{V}_{ij}^{ab} = \int \mathbf{M}_{ab}(\hat{s}, v) S_P(\hat{s}, v) \exp(-2\pi i \vec{v} \cdot \hat{s}/c) d\Omega, \quad (3.34)$$

---

<sup>4</sup>[www.cst.com](http://www.cst.com)

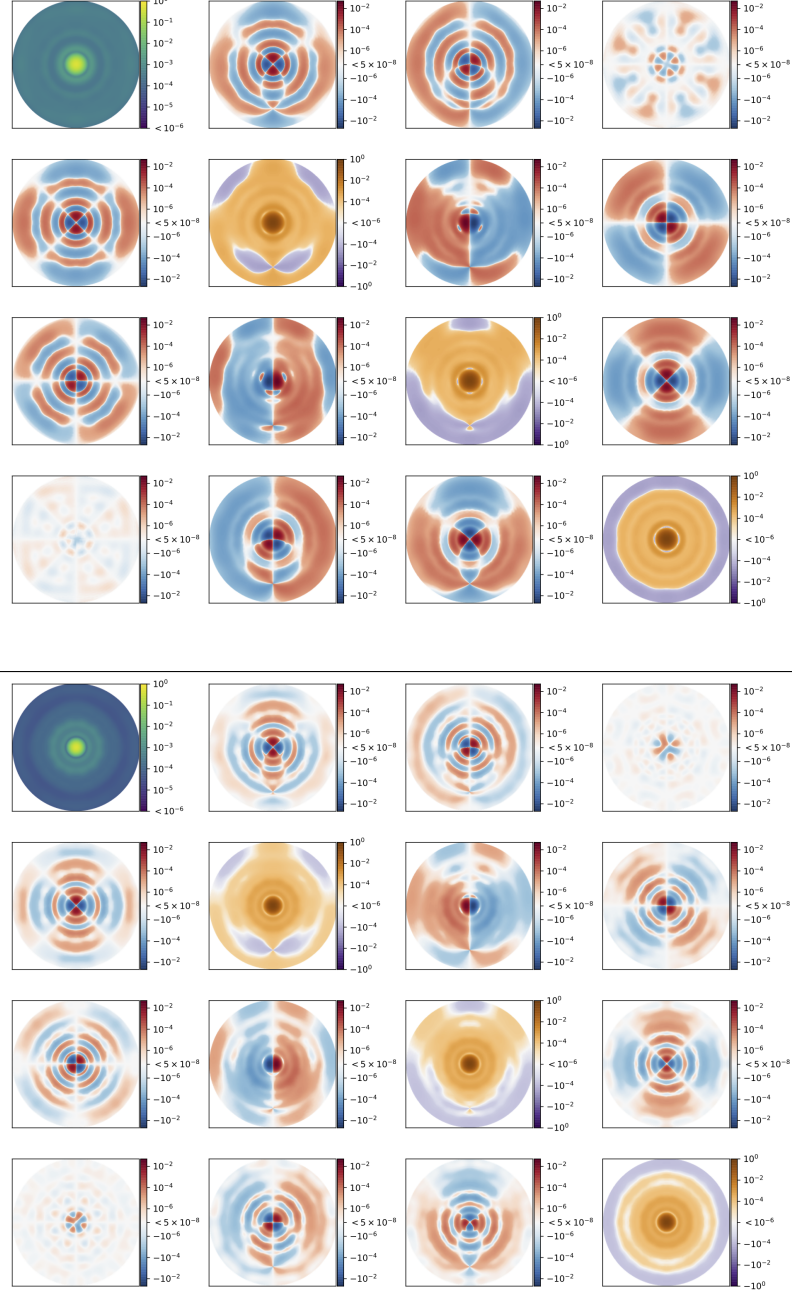


Figure 3.4: Simulations of the instrumental direction dependent Mueller matrix at 120 MHz and 160 MHz (*above* and *below*, respectively) projected into the RA, Dec basis. Color scales for frequencies are relative to the peak of  $\mathbf{M}_{00}$  (which itself is normalized to 1 at zenith). To account for the wide variety of dynamic ranges required to show detail, we use separate color maps for  $\mathbf{M}_{00}$ , diagonal, and off-diagonal terms. The off-diagonal terms are 2- to 8-orders of magnitude less than the diagonal terms. For a key to these matrices, see Equation 3.33.

where  $S_P \in (I, Q, U, V)$ . Subtracting the additional components from a given pseudo-Stokes visibility could isolate that Stokes parameter. While accurate instrument models are presently becoming available (see Chapter 10 for verification of the simulations shown in Figure 3.4, at least for pseudo-Stokes I), verifying the accuracy of such a method would require precise expectations of the nature of the low frequency polarized sky. At the time of writing, this is only beginning to become clear through polarized sky surveys from the Low Frequency Array (LOFAR; e.g. Van Eck et al. (2018)) and the MWA (e.g. Lenc et al., 2016, 2017).

### 3.3.2 Direction-Independent Leakage

In addition to the mixing of Stokes parameters due to the primary beam, it is possible to mix them in a direction independent way. Calibration errors – errors in the estimation of the components of  $\mathbf{J}_i^D(v)$  and  $\mathbf{J}_i^G(v)$  – are capable of leaking signal between pseudo-Stokes visibilities independent of the sky. Writing the gains as  $g_i^p(v) + \delta g_i^p(v)$ , and  $\mathbf{J}_i(v) = \mathbf{J}_i^D(v)\mathbf{J}_i^G(v)$ , a direction-independent Mueller matrix may be composed (Thompson et al., 2017):

$$\mathbf{M}'(v) = \mathbf{J}_i(v) \otimes \mathbf{J}_j^H(v) \quad (3.35)$$

such that

$$\begin{pmatrix} V'_I \\ V'_Q \\ V'_U \\ V'_V \end{pmatrix} = (\mathbf{I} - \frac{1}{2}\delta\mathbf{M}') \begin{pmatrix} V_I \\ V_Q \\ V_U \\ V_V \end{pmatrix} \quad (3.36)$$

where

$$\delta\mathbf{M}' = \begin{pmatrix} \delta g_i^p + \delta g_i^q + \delta g_j^{p*} + \delta g_j^{q*} & \delta g_i^p - \delta g_i^q + \delta g_j^{p*} - \delta g_j^{q*} & D_i^p - D_i^q + D_j^{p*} - D_j^{q*} & -\mathbf{i}(D_i^p + D_i^q - D_j^{p*} - D_j^{q*}) \\ \delta g_i^p - \delta g_i^q + \delta g_j^{p*} - \delta g_j^{q*} & \delta g_i^p + \delta g_i^q + \delta g_j^{p*} + \delta g_j^{q*} & D_i^p + D_i^q + D_j^{p*} + D_j^{q*} & -\mathbf{i}(D_i^p - D_i^q - D_j^{p*} + D_j^{q*}) \\ D_i^p - D_i^q + D_j^{p*} - D_j^{q*} & -(D_i^p + D_i^q + D_j^{p*} + D_j^{q*}) & \delta g_i^p + \delta g_i^q + \delta g_j^{p*} + \delta g_j^{q*} & \mathbf{i}(\delta g_i^p - \delta g_i^q - \delta g_j^{p*} + \delta g_j^{q*}) \\ -\mathbf{i}(D_i^p + D_i^q - D_j^{p*} - D_j^{q*}) & -\mathbf{i}(D_i^p - D_i^q - D_j^{p*} + D_j^{q*}) & \mathbf{i}(\delta g_i^p - \delta g_i^q - \delta g_j^{p*} + \delta g_j^{q*}) & \delta g_i^p + \delta g_i^q + \delta g_j^{p*} + \delta g_j^{q*} \end{pmatrix}$$

where we have approximated the components to first order in  $\delta g$  and  $D$ , dropped the frequency dependence of each term, and  $\mathbf{i}$  indicates the imaginary unit.  $V'_I$  denotes the observed value of the pseudo-Stokes I visibility. In the regime of leaked pseudo-Stokes I power dominating over pseudo-Stokes Q, U and V, this shows that pseudo-Stokes I appears in pseudo-Stokes Q through errors in diagonal gain calibration, and pseudo-Stokes U and V through uncalibrated  $D$ -terms.

A fraction of the  $D$ -term leakage from pseudo-Stokes I into U and V may approximated by a delay between the  $p$  and  $q$  feeds,  $\tau_{pq}$ . This is a valid approximation, as a time delay between a wavefront incident upon two feed arms is exactly what circular polarization is, so signal appearing in Stokes V should be able to be described in this form. In Chapter 9 we present a fit for this parameter across the array, and find that through such a fit pseudo-Stokes V signal can be transferred to pseudo-Stokes U. In Chapter 7, we present a method that combines such a fit with redundant calibration, allowing us to minimize leaked power into pseudo-Stokes V on a per-time and -frequency sample basis.

This Chapter has reviewed the fundamentals of radio interferometry, providing a formalism generalized to wide field-of-view observations, and polarization. The importance of understanding the polarized response of the instrument has been emphasized many times. In the Part II, this emphasis will be justified from several data- and theory-based approaches.

# Chapter 4

## Instruments

In the following chapters I present data and results from a variety of configurations of two massively redundant low frequency interferometers, PAPER and HERA. In this Chapter I describe these instruments (Section 4.1), along with other current and future low frequency interferometers contributing to EoR science (Section 4.2).

### 4.1 Instruments used in this work

The vision of Hydrogen Epoch of Reionization Arrays was first laid out in the Backer et al. (2010) White Paper. That work proposed three consecutive efforts, improving upon their predecessors, to construct low frequency interferometers capable of detecting the EoR. While the physical feeds and elements of low frequency interferometers were relatively simple to construct, signal processing, calibration and imaging required new hardware and software to be invented. A research community of observational cosmologists interested in cosmological HI had to be nurtured.

The first of the three stages of Reionization Arrays was a parallel effort. The Precision Array for Probing the Epoch of Reionization (PAPER; Section 4.1.1) and the Murchinson Widefield Array (MWA; Section 4.2.2) investigated separate approaches to<sup>1</sup> antenna

---

<sup>1</sup>Among other things; see Section III B of Backer et al. (2010) for an enumerated list.

design, array layout and calibration techniques, with the objective of setting upper limits on and perhaps detecting the power spectrum of the EoR.

The second stage of the Reionization Arrays brought together the teams from the first stage to design and construct a new interferometer based on the lessons learned from PAPER and the MWA. This new instrument, named *the* Hydrogen Epoch of Reionization Array (HERA; Section 4.1.2) is currently under construction with a build-out schedule that brings new antennas online as they are commissioned. HERA’s objective is not only the detection of the EoR power spectrum, but its characterization at very high signal-to-noise. Attempts at low-fidelity imaging of ionized bubbles will be made.

The nature of the third stage is, at the time of writing, somewhat undetermined and contingent on the next decade of funding for low frequency radio astronomy. In the vision of Backer et al. (2010), its objective will be to image structure evolution throughout the EoR.

#### **4.1.1 The Donald C. Backer Precision Array for Probing the Epoch of Reionization (PAPER)**

Much of this thesis presents data from PAPER. PAPER was planned, like HERA, as a staged build-out to larger and larger arrays. In each build-out the correlator was replaced, and (nominally) identical antennae and signal chains were added to the existing array. The first iterations of PAPER consisted of 8 dipole antennae in Green Bank, West Virginia and 4 in Western Australia (Parsons et al., 2010). While the Australian site had a far better observing environment in terms of human-generated radio interference, the site in the USA was easier for the team to design and test on. Green Bank was intended as a test site – brighter foregrounds in the Northern Hemisphere and an unprotected low frequency band inhibited the science goals of the experiment. Nonetheless, the array in Green Bank was build-up to 32 antennae and reconfigured from a more traditional imaging configuration to a redundant grid, in order to experiment with redundant calibration and increased sensitivity to discrete Fourier modes (Parsons et al., 2012a; Pober et al., 2012). Simulta-

neously, the PAPER-32 array and correlator were constructed in the Karoo Radio Quiet Zone (KRQZ) in South Africa.

#### 4.1.1.1 The PAPER signal chain

The PAPER signal chain changed little throughout the PAPER build-outs in South Africa, and it remained in operation for the HERA-19 Commissioning Array out to HERA-127. HERA elements are actually PAPER feeds, turned upside-down and suspended over a 14 m dish. This heritage was important to understand when interpreting PAPER or HERA data. We briefly describe the PAPER signal chain below. For a more thorough description, refer to Parsons et al. (2010).

Radio waves were incident upon, and induced a voltage in, a dual-polarization PAPER feed. The feed was a sleeved copper dipole protected by a wire-mesh groundscreen. The sleeve broadened the frequency response of the dipole element, and the groundscreen was used to increase sensitivity to emission from zenith (see Figure 4.1 for a photograph).

Electronics next to the dipole element amplified the voltage by a factor of  $10^6$ , which then propagated down a 150 foot  $75\ \Omega$  coaxial cable. All cables were of the same length to minimize the amount of extra calibration required per feed, and were above-ground. These cables ran to 8 “receiverators”; RFI-shielded mini-fridges which contained amplifiers which re-amplified the voltage signals by a factor of  $10^4$  (to correct for signal loss along the 150 ft coaxial cables) and applied an analog bandpass filter. The filter was designed to have a smooth frequency response which was relatively flat between 120 and 180 MHz (e.g. Moore, 2014).

More 50 foot,  $75\ \Omega$  foot coaxial cables ran from these to an RFI-shielded enclosure for further processing. For PAPER and the HERA-19 commissioning array, this enclosure was a specialized shipping container next to the array. For future HERA build-outs, processing will occur in the Karro Array Processing Building (KAPB) and the receiverator architecture will be replaced with underground “nodes” (see DeBoer et al. (2017) for more detail).



Figure 4.1: An image of a PAPER dipole element with its groundscren.

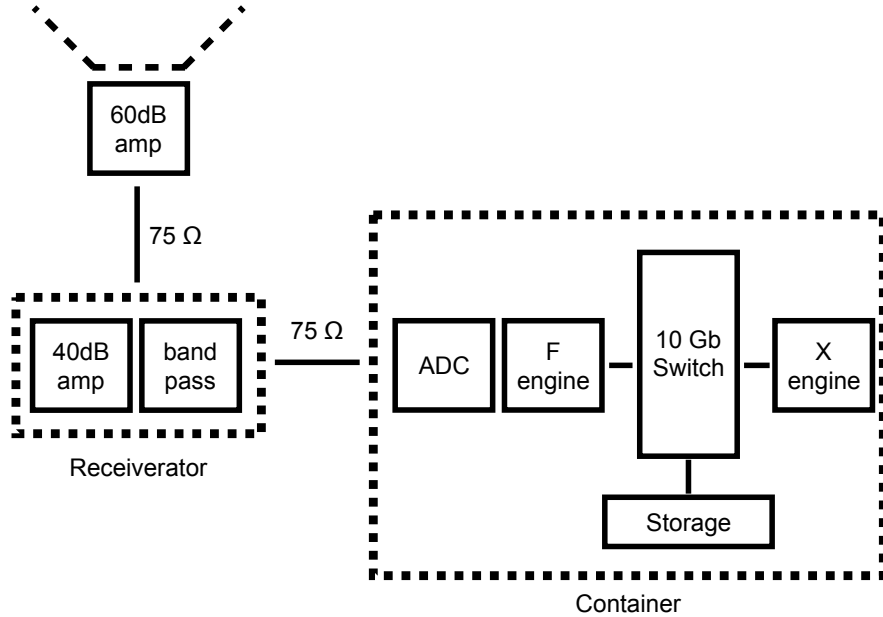


Figure 4.2: A diagram of the PAPER-128 signal chain. Square-dotted lines indicate RFI-shielding.

The filtered analog signal was then digitized with a sampling rate of 100 MHz and passed through an F-engine which Fourier transforms the signal using a 4-tap polyphase filter bank (which allowed for a smooth frequency and Fourier-space response; Price (2016b)). The integration time of each Fourier transform was 10 s. The Fourier transformed signals were distributed over a 10 Gigabit Ethernet switch to the X-engine (Parsons et al., 2008), which cross-multiplied all signals with each other to form visibilities, storing them in MIRIAD files.

A summary of the system described above is shown in Figure 4.2.

#### 4.1.1.2 PAPER-32

The PAPER-32 array in South Africa used a highly redundant configuration in order to take the measurements resulting in, at the time, the strongest upper limits on the EoR

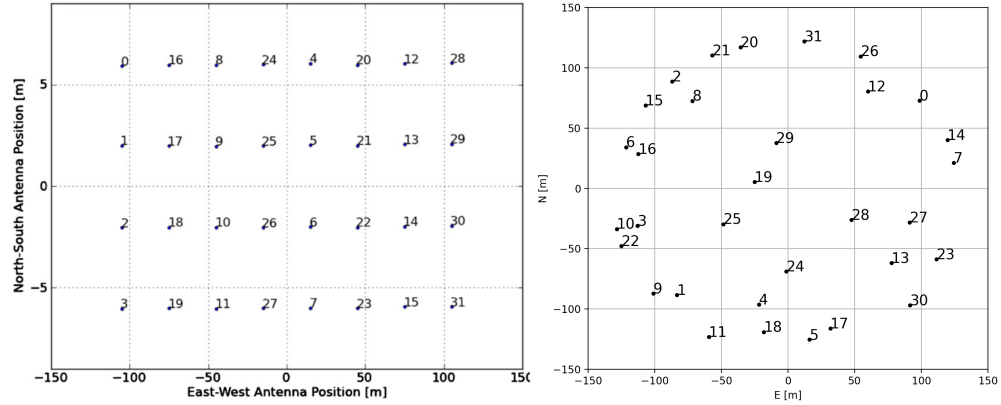


Figure 4.3: The array layouts of the PAPER-32 element deployment in South Africa. *Left:* The redundant grid. Four rows, with each element 30 m from the next in the East-West direction, and closely-packed ( $\sim 4$  m) in the North-South direction. Figure taken from Parsons et al. (2014). *Right:* The polarized imaging array. Elements were arranged in a pseudo-random scatter.

power spectrum (Parsons et al., 2014; Jacobs et al., 2015; Moore et al., 2017, sections of Moore et al. 2017 are presented in Chapter 8). The array was in redundant configuration from December 2011 to February 2012. For three nights in September 2011, the 32 elements were reconfigured into an polarized imaging configuration. The results from this deployment were used to make the first 2D power spectra of polarization, presented in Kohn et al. (2016) and in Chapter 9. For images and a brief description, see Figure 4.3.

#### 4.1.1.3 PAPER-64

During the PAPER-32 EoR integration, there were actually 64 antennas present in the Karoo, South Africa. However, the correlator at that time could only process 64 voltage streams – enough for 32 dual-polarization antennae. This is why 64 element single-instrument-polarization imaging results were published prior to any PAPER-32 studies (Jacobs et al., 2013; Stefan et al., 2013). EoR integrations in the 64 element redundant

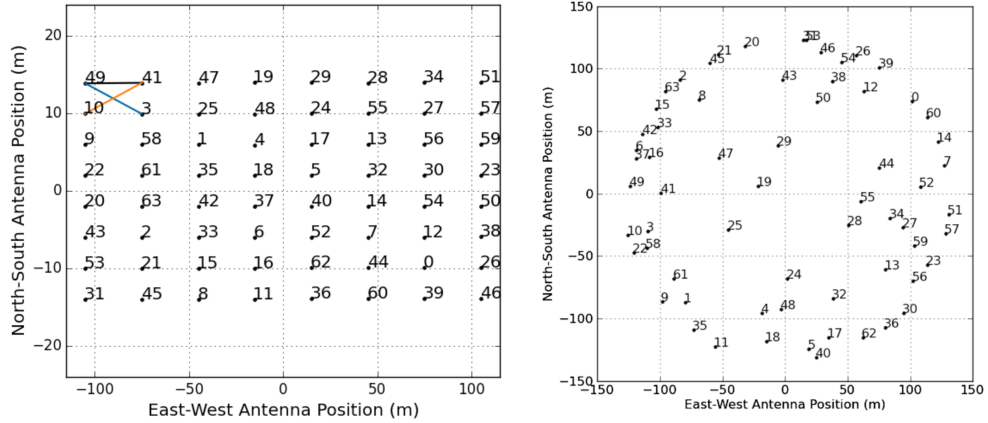


Figure 4.4: The array layouts of the PAPER-64 deployment. *Left:* The redundant grid, built-out from the PAPER-32 grid. Figure taken from Ali et al. (2015), which highlights the baseline-types used for power spectrum measurements. *Right:* the imaging array, used by Jacobs et al. (2013) to set an absolute flux scale for PAPER experiments. Figure taken from Jacobs et al. (2013).

configuration were only possible after a new correlator was produced in 2012. Results from this array were published in (Ali et al., 2015; Pober et al., 2015, Cheng et al. *submitted*; Kolopanis et al. *submitted*). The array layouts are shown in Figure 4.4.

#### 4.1.1.4 PAPER-128

The culmination of the PAPER experiment was the 128 element deployment. There were two observing seasons recorded: November 2013 to March 2014, and July 2014 to January 2015. In this configuration, 112 antennas were laid-out in a redundant grid with 15 m East-West spacings and 4 m North-South spacings. The remaining 16 antennas were arranged in ‘out-rigger’ and ‘in-rigger’ positions to increase *uv*-coverage and enable some level of imaging. Results from the first observing season of this array are presented in Chapters 6, 7 and 11. The array layout is shown in Figure 4.5.

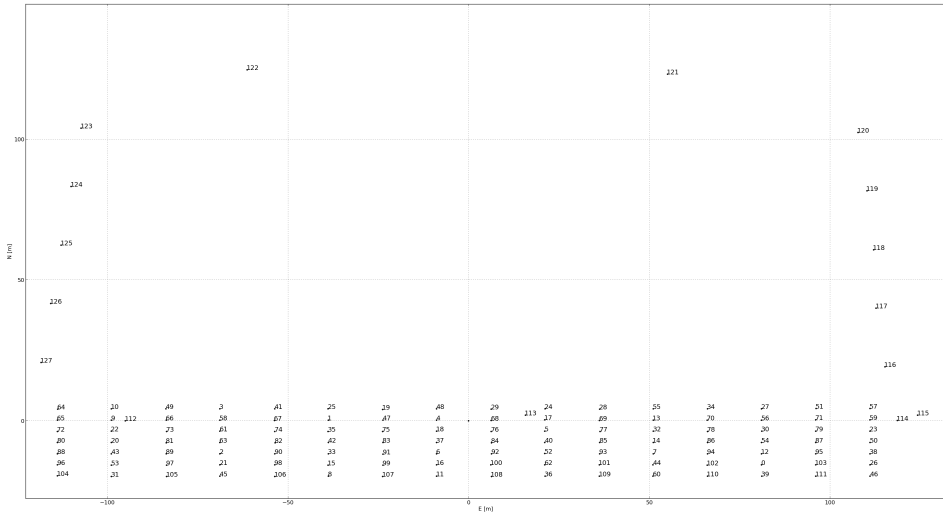


Figure 4.5: The PAPER-128 array layout. 112 antennas were laid-out in a redundant grid with 15 m East-West spacings and 4 m North-South spacings, and the remaining 16 antennas were arranged in ‘out-rigger’ and ‘in-rigger’ positions to increase  $uv$ -coverage.

### 4.1.2 The Hydrogen Epoch of Reionization Array (HERA)

HERA was ranked as the “top priority in the Radio, Millimeter, and Sub-millimeter category of recommended new facilities for mid-scale funding” by the National Research Council Decadal Survey in astronomy and astrophysics (NRC, 2010). It brought together the largely US-based experts working on PAPER and the MWA to construct a new low-frequency array on the PAPER site in South Africa. The array, comprised of 14 m diameter dishes, was designed to be build-out in stages of close-packed hexagons of increasing size. For a full description of the instrument, refer to DeBoer et al. (2017).

The design of the HERA dish, feed, antenna layout and signal chain are intimately related to lessons learned by the PAPER and MWA EoR teams about the nature of EoR measurements (e.g. Thyagarajan et al., 2015b). One of the major considerations was how the instrument couples to the bright foregrounds, and how to control that coupling – the paradigm of the “wedge” and the “EoR Window”, which are discussed in detail in Chapter 5. Measurements based on prototype feeds were presented in (Ewall-Wice et al.,



Figure 4.6: *Left:* a rendering of the 320 element HERA core. *Right:* the 19 element commissioning array (with the construction team). Leftover PAPER dipoles can also be seen in the background, forming three experimental arrays (described in Section 4.1.2.1). Figure taken from DeBoer et al. (2017).

2016a; Neben et al., 2016, Patra et al. *submitted*).

HERA is a staged experiment, building-out in close-packed hexagons from a 19 element commissioning array, to 37, 127, 240 and finally 350 elements (320 in a dense, fractured core and 30 out-ridgers, see Dillon & Parsons 2016 for more detail). Figure 4.6 shows a rendering of the core alongside an image of the HERA-19 commissioning array.

#### 4.1.2.1 HERA-19 Commissioning Array

In October 2015 a HERA commissioning array was completed, connected to the PAPER-128 256-input correlator. This array comprised of four separate components: the first 19 HERA dishes in a close-packed hexagon (HERA-19), 19 PAPER dipoles at the central locations of a hexagon of future HERA dishes (the “PAPER-Hex”), 40 PAPER dipoles in a redundant grid where every-other dipole was rotated  $45^\circ$  (to experiment with different polarization bases; “PAPER Pol”), and the remaining inputs filled with PAPER dipoles arranged in a pseudo-random scatter for imaging (“PAPER-Img”). Studies with this array are presented in Chapter 6 and 10. A diagram of the commissioning setup is shown in Figure 4.7.

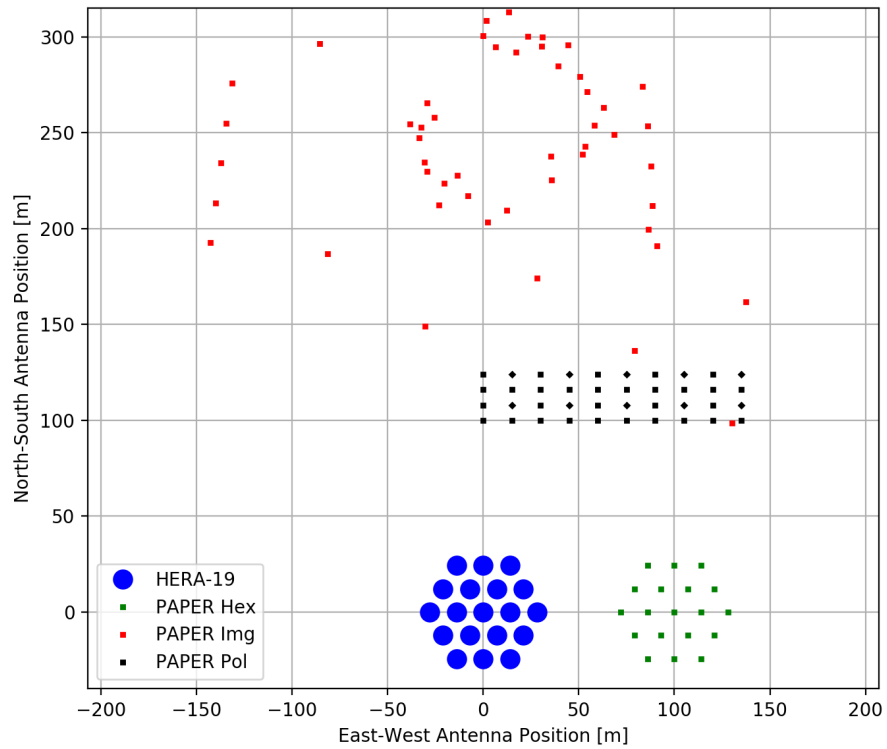


Figure 4.7: Positions of antennae in the HERA-19 Commissioning Array (including the experimental “subarrays”).

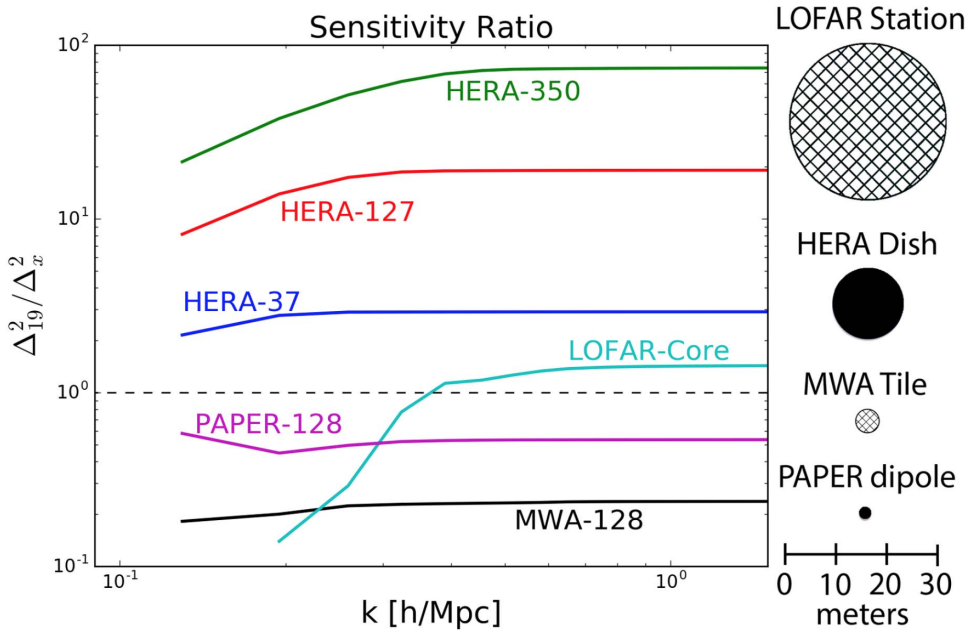


Figure 4.8: Instantaneous array Sensitivities as a function of  $k$ -mode (e.g. Chapter 5) relative to HERA-19. Differing element collecting areas are shown on the right. Taken from DeBoer et al. (2017).

#### 4.1.2.2 Future HERA Build-Outs

Each HERA element is much more sensitive than a PAPER element, based purely on collecting area. Figure 4.8 illustrates the varying sensitivities and collecting areas of different arrays and their elements, respectively. PAPER-128 was forecast to make marginal detections of the EoR power spectrum after  $\sim 1000$  hours of integration – HERA-127 should be capable of characterizing the EoR power spectrum at high significance, and the full HERA-350 array will be an extremely powerful survey instrument (e.g. Pober, 2015). We present forecasts for this future instrument in Chapter 13.

## 4.2 Other current and future interferometers

PAPER and HERA were not the only instruments researching the EoR and how to detect it. Several low-frequency interferometers around the world are contributing to the understanding of the EoR and the difficulties of observing it. Below I briefly describe a few of the leaders of the field – but it is not an exhaustive list.

### 4.2.1 The Low Frequency Array (LOFAR)

The LOw Frequency ARray (LOFAR) is an interferometer made-up of “stations”, the core of which are arranged in a random scatter near Exloo in the Netherlands (van Haarlem et al., 2013). LOFAR baselines extend across Europe with stations in Ireland, Sweden, Germany, Poland and other locations. These extremely long baselines can provide LOFAR with exquisite imaging capabilities.

LOFAR has detected diffuse, linear polarization structures that may be related to the Milky Way’s magnetic field and interstellar medium (Jelić et al., 2015). Patil et al. (2017) presented deep limits on the EoR power spectrum from one night of LOFAR data (also see Yatawatta et al. 2013). A series of publications has investigated polarization in Fourier space (Jelić et al., 2014; Asad et al., 2015, 2016, 2017) – results that we build upon and verify throughout this work.

### 4.2.2 The Murchinson Widefield Array (MWA)

The Murchinson Widefield Array (MWA), based in Murchison Radio-astronomy Observatory in Western Australia, is composed of 256 ‘tiles’ of 16 feeds each. At the time of writing, 72 tiles are arranged in compact hexagonal configurations in an effort to increase EoR sensitivity while retaining imaging capabilities with the rest of the array. The most complete low-frequency catalog of the southern sky, GLEAM, was presented by Hurley-Walker et al. (2017).

The MWA uses separate analysis pipelines for its EoR measurements (Sullivan et al.,

2012a; Jacobs et al., 2016; Trott et al., 2016), an concept that will be implemented on future HERA measurements. The MWA has detected polarized signal from diffuse Galactic emission (Lenc et al., 2016, 2017) and set deep limits on the EoR power spectrum (e.g. Dillon et al., 2014, 2015). Pioneering work on the ionosphere was accomplished using MWA data (e.g. Loi et al., 2015), which we discuss in Chapter 8.

#### **4.2.3 Square Kilometer Array – Low band (SKA-Low)**

The Square Kilometer Array (SKA) will be built on two sites: the Karoo Radio Quiet Zone, currently occupied by HERA, will be the central location of the “high–mid band” (350 MHz – 14 GHz; “SKA-Mid”) observatory and the Murchinson Radio-astronomy Observatory, currently occupied by the MWA, will be the central location of the “low band” observatory (50 – 350 MHz; “SKA-Low”).

SKA-Low will consist of over 100,000 receiving elements in an imaging configuration. It will be the most powerful low-frequency radio telescope ever created, and be used not only for EoR science but a host of low-frequency science objectives (e.g. Carilli & Rawlings, 2004; Schilizzi et al., 2007; Dewdney et al., 2009). Learning from the work of EoR teams working on PAPER, HERA, MWA, LOFAR and other instruments will be crucial to the success of SKA-Low’s EoR science goals.

## **Part II**

### **Structure in Fourier space**

The Gemara asks: Do we not see that comets pass Orion? The Gemara rejects this: The aura of the comet passes Orion and it appears as though the comet itself passes. Rav Huna, son of Rav Yehoshua, said a different answer: It is merely that veil, one of the firmaments, rips and furls and the light of the next firmament is seen, and this appears like a comet. Rav Ashi said another explanation: It is not a comet that passes Orion, but a star that is uprooted from one side of Orion, and another star, from the other side of Orion, sees it and gets startled and shudders, and appears as if it is passing.

*Talmud Berakhot (58b:11)*

# Chapter 5

## Peering through the EoR Window

Chapter 1 argued the promise of direct observations of HI during the EoR. A direct detection has not yet been made, largely due to the overwhelming power of foregrounds compared to the target signal. As shown in Chapter 2, foreground radiation is a factor of roughly  $10^4 - 10^5$  times brighter than predicted 21 cm anisotropies . In the past decade, however, enormous improvements have been made in understanding how to decontaminate interferometric visibilities, and excavate the target signal. The leverage astronomers have to use is the exceptional smoothness of low-frequency synchrotron radiation, the dominant foreground emission mechanism. In this Chapter, I review the ‘Foreground Wedge & EoR Window’ paradigm used to delineate foreground power from noise and HI emission. In Section 5.1 I introduce the concept of the foreground wedge, and methods used by astronomers to take advantage of it: either avoiding it, or subtracting it. In Section 5.2, I make plain how astrophysical and instrumental polarization complicates this picture.

### 5.1 Foreground isolation

Mitigation of foregrounds is essential for accessing the EoR. This fact was recognized by Madau et al. (1997) in one of the first in-depth studies of the promises and challenges

of 21 cm tomography. To overcome foreground radiation, they suggested that fitting the synchrotron spectra, relying on its smoothness, may have been sufficiently accurate to subtract the foregrounds from the total signal. However, for the next two-or-so decades, there were few low-frequency instruments powerful and well-characterized enough to attempt an EoR detection, and precise observations of low-frequency foregrounds did not exist. The first work to concentrate solely on the foreground challenge was Di Matteo et al. (2002). Their outlook was pessimistic, but they suggested the challenge was surmountable with sufficiently accurate and precise multi-frequency fitting. Oh & Mack (2003) were among the first to point out that interferometers are inherently chromatic, and therefore the instrument itself must be taken in to account when considering the frequency dependence of EoR foregrounds.

Wang et al. (2006) were among the first to discover the advantages of describing the foregrounds statistically in Fourier space. Working with numerical simulations, they recognized that forming 1-dimensional power spectra of brightness temperature anisotropies allowed them to isolate the foreground signal to low  $k$  values (inverse spatial scales; units h/Mpc), while the EoR signal and noise dominated at high  $ks$ . With sufficient bandwidth and frequency resolution, one would be able to delineate a boundary between these regions of Fourier space.

Simulating the GSM (de Oliveira-Costa et al., 2008), a point source model, and an EoR model transiting a 512-element MWA, Datta et al. (2010) ‘discovered’ the Wedge. They gridded power observed by a baseline in to  $(k_{\perp}, k_{\parallel})$  space, where  $k_{\perp}$  is proportional to the  $u$  coordinate in the  $uv$ -plane (implying that  $k_{\perp}$  is a measure of transverse scales) and  $k_{\parallel}$  is proportional to the Fourier-conjugate of frequency (for redshifted 21 cm emission, a measure of line-of-sight distance). This two-dimensional power spectrum was a generalization of the findings by Wang et al. (2006), localizing foreground power to low  $k_{\parallel}$  values (the ‘wedge’) while 21 cm power was not as contained, leaving EoR signal and noise at high  $k_{\parallel}$  for any given baseline length, proportional to  $k_{\perp}$  (see Figure 5.1 for an illustration).

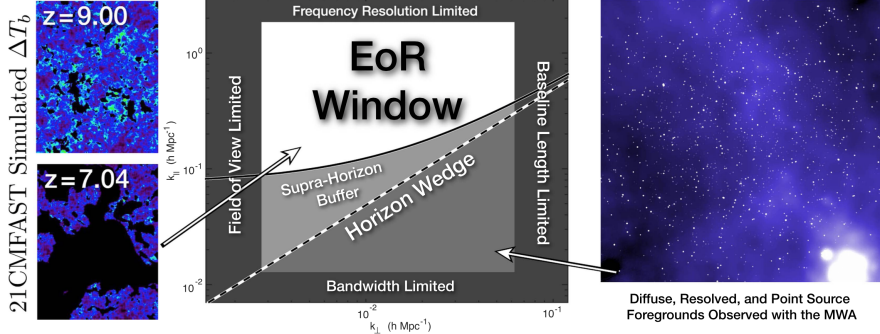


Figure 5.1: An illustration of the foreground wedge and the EoR window. Bright synchrotron foregrounds (such as those imaged by the MWA, on the right) are localized in  $(k_{\perp}, k_{\parallel})$  to a wedge-shaped region, while spectrally-structured 21 cm power (simulations from Mesinger et al. (2011) on the left) exists throughout Fourier space – crucially, outside of the wedge, in an EoR window. Pober et al. (2013) identified the requirement of a buffer region where instrumental effects could spill power just beyond the wedge region. Figure taken from DeBoer et al. (2017).

Parsons et al. (2012b) were the first to provide a quantitative explanation of this structure in Fourier space. In their numerical simulations they recognized that visibilities dominated by smooth synchrotron foregrounds could be Fourier transformed along their frequency axis, and mapped into a narrow region of Fourier space. This is because the sinusoidal structure of the fringe term in the visibility equation, coupled with smooth sky emission and a smooth evolution of the beam term, produced a visibility that could be described with a relatively low number of Fourier modes. However, the inherent spectral structure of 21 cm emission caused its power to scatter to high  $k_{\parallel}$ . Crucially, they realized that this allowed per-baseline access to a statistical power spectrum measurement of the EoR.

The wedge & window paradigm has been continually refined. First-principles derivations from, e.g., Trott et al. 2012, Vedantham et al. 2012, Hazelton et al. 2013 and Liu et al. 2014a,b have provided solid theoretical grounding for observational efforts. Pober et al. (2013) identified the requirement of a ‘supra-horizon buffer’ to account for excess power

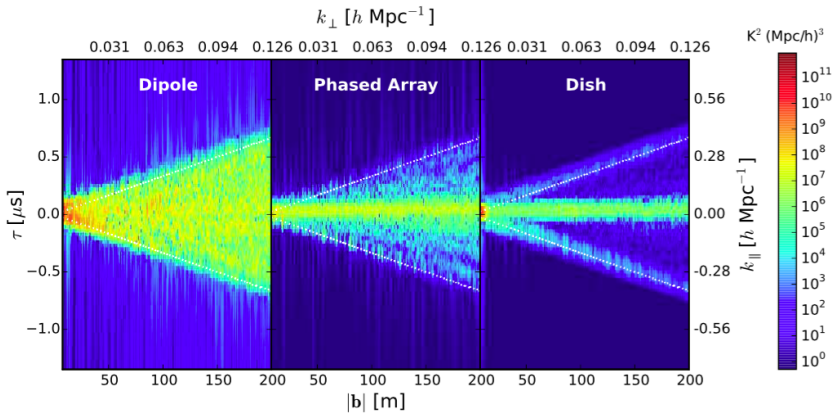


Figure 5.2: Different instrument receptivity patterns – dipoles, phased arrays and dishes – have different 2D power spectrum morphologies. Figure taken from Thyagarajan et al. (2015a).

at the boundaries of the wedge, due to a convolution of instrumental spectral structure and beam side-lobes. The buffer is larger for short baselines, since the diffuse structure they probe is typically brighter, and its leaked can dominate over the noise in the EoR window.

Thyagarajan et al. (2015a) identified the importance of the beam for the structure of the EoR window. Forming ‘pitchfork’ (i.e. accounting for the negative Fourier conjugates of frequency; see Figure 5.2) power spectra simulations of dipole, phased array and dish-type beams they showed that an identical sky model produced radically different morphologies in Fourier space. Dipole feeds which are capable of observing the entire hemisphere of the sky, such as those used for PAPER, created full ‘wedges’ compared to, for example, dish elements, the tapered response of which isolated power to much narrower regions of Fourier space. Phased arrays, such as those used by the MWA, lay in a middle-ground of sorts. Their findings are reproduced in Figure 5.2.

Once the wedge and window have been formed, how does one proceed to extract the 21 cm EoR signature from the noise? As mentioned above, the instrument used to make the measurement will play a key role in this decision, and PAPER, the MWA and LOFAR have approached extraction of the signal from different directions. These can be roughly

placed in to two categories: foreground avoidance and foreground subtraction.

### 5.1.1 Foreground avoidance

The foreground avoidance strategy is roughly synonymous with the ‘delay spectrum’ approach. Parsons & Backer (2009) defined the delay spectrum as the Fourier transform of a visibility with respect to the frequency axis (c.f. Chapter 3; Section 3.2.3.2),

$$\tilde{V}_{ij}(\tau, t) = \int d\nu V_{ij}(\nu, t) e^{2\pi i \nu \tau}, \quad (5.1)$$

for delay  $\tau$ . This transform maps flat-spectrum emitters to Dirac delta functions in delay space, where the delay of the source is the geometrical time delay for their radiation to be received by antenna  $i$  and antenna  $j$  (see Figure 3.3). Note that this implies a maximum possible delay value, given by the light travel-time along the baseline vector. This maximum occurs at the horizon, and is referred to as the ‘horizon delay’ or ‘horizon limit’,  $\tau_h$ . With sufficient bandwidth and frequency resolution, this boundary can be clearly delineated, shown as black dashes lines for baselines of increasing length in Figure 5.3. Synchrotron sources are not typically flat-spectrum, but their spectra are smooth. This creates a broadening kernel that convolves the delta function at a given delay. Emission with more frequency structure will have a broader signature in delay space. This is the primary motivation of the delay spectrum. Fourier-transforming foreground emission will contain it at delay values  $\tau \leq \tau_h$ , whereas spectrally structured EoR and noise power will scatter in to modes  $\tau > \tau_h$ . Figure 5.3, adapted from Parsons et al. (2012b), illustrates this by simulating the delay spectra of visibilities containing four smooth-spectrum sources and a greatly-amplified EoR signature in one portion of the sky. A Blackman-Harris window was used during the delay transform to minimize sidelobes. Time increases up the vertical axis; as time goes by, sources rise and set from horizon to horizon, but the EoR signature exists both inside and outside of horizon delays. The baseline dependence of the maximum delay foregrounds are allowed to occupy is what gives rise to the pitchfork shown in Figure 5.2.

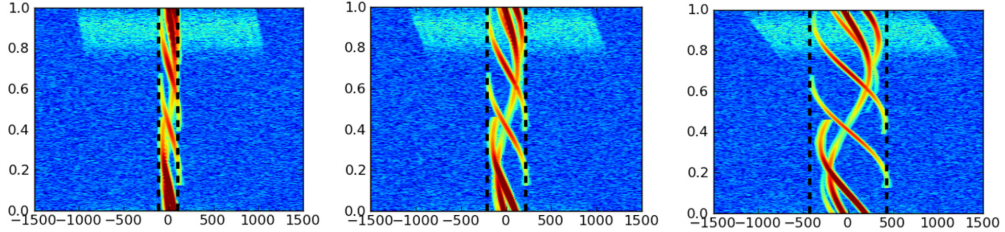


Figure 5.3: Delay vs. time for a simple sky model of four foreground-like, smooth-spectrum sources and an EoR-like (but greatly amplified), spectrally structured signal. The foregrounds are contained within horizon delays (black dashed lines), but the EoR signal scatters outside of the boundaries. The three panels show the same sky observed by progressively longer baselines (left to right: 32, 64, and 128 m). The horizontal is in units of nanoseconds, and the vertical axis is in units of days. A Blackman-Harris window was used during the delay transform to minimize sidelobes. Figure adapted from Parsons et al. (2012b).

### 5.1.1.1 Power spectra

To extract cosmological information from observed intensity in delay space, it is useful to form power spectra, which we define for the delay spectrum paradigm below. To convert  $u$  to  $k_{\perp}$  and  $\tau$  to  $k_{\parallel}$ , Parsons et al. (2012a) defined cosmological scalars:

$$X = 6.5 \times 10^3 \sqrt{\frac{0.27}{\Omega_m}} \left( \frac{1+z}{10} \right)^{0.2} h^{-1} \text{Mpc rad}^{-1}, \quad (5.2)$$

$$Y = 1.7 \times 10^{-2} \sqrt{\frac{0.27}{\Omega_m}} \sqrt{\frac{1+z}{10}} h^{-1} \text{Mpc GHz}^{-1}, \quad (5.3)$$

such that  $X$  describes a comoving transverse scale,  $Y$  describes a comoving line-of-sight distance, and

$$2\pi(u l + v m + \tau v) = k_x x/X + k_y y/X + k_z z/Y, \quad (5.4)$$

where  $l$  and  $m$  are directional cosines,  $k_i$  measure cosmological wavemodes for comoving coordinates  $x, y, z$ .  $k_z$  and  $k_{\parallel}$  are interchangeable in this convention, and  $k_{\perp} = \sqrt{k_x^2 + k_y^2}$ .

The power measured by a delay-transformed visibility is given by a cross-multiplication

of two instances of the visibility. Using the classical visibility equation for simplicity,

$$\tilde{V}^*\tilde{V} \approx \int^{(6)} A(l, m, v)A(l', m', v')S(l, m, v)S(l', m', v') \\ \times e^{-2\pi i(u(l-l')+v(m-m')+\tau(v-v'))} dl dl' dm dm' dv dv'. \quad (5.5)$$

We can convert from intensity to brightness temperature using  $S(l, m, v) = 2k_B T(l, m, v)/\lambda^2$ . This leads to a correlation function  $\xi_T$  within the integral. For a beam that spans area  $\Omega$  and a delay transform over  $\Delta v$ , Parsons et al. (2012b) showed that the power can be expressed as

$$|\tilde{V}(u, v, \tau)|^2 \approx \frac{\Omega \Delta v}{X^2 Y} \left( \frac{2k_B}{\lambda^2} \right)^2 \int_{-X\sqrt{\Omega}}^{X\sqrt{\Omega}} \int_{-X\sqrt{\Omega}}^{X\sqrt{\Omega}} \int_{-Y\Delta v}^{Y\Delta v} \xi_T(\vec{r}) e^{-i\vec{k}\cdot\vec{r}} d^3 r. \quad (5.6)$$

In the limit of the integral spanning many phase-wraps of  $e^{-i\vec{k}\cdot\vec{r}}$ , the integral can be expressed as a power spectrum of  $\vec{k}$ , and the above equation can be rearranged to give

$$P(\vec{k}) = \left( \frac{\lambda^2}{2k_B} \right)^2 \frac{(\Omega \Delta v)^2}{D^2 \Delta D} |\tilde{V}(u, v, \tau)|^2 \quad (5.7)$$

for comoving area  $D^2 = X^2 \Omega$  and comoving distance  $Y \Delta v = \Delta D$ . For 21 cm emission, we can describe the transverse and line-of-sight components of  $\vec{k}$  as

$$k_{\parallel} = \frac{2\pi v_{21\text{cm}} H(z)}{c(1+z)^2} \tau; \quad k_{\perp} = \frac{2\pi}{D\lambda} b \quad (5.8)$$

The definition in Equation 5.7 allows us to describe delay-transformed visibilities in terms of cosmological power, as a function of  $\vec{k}$ . In the foreground avoidance scheme, filters or masks can be implemented to remove or ignore power at values of  $k_{\parallel}$  corresponding to delays  $\tau \leq \tau_h + \tau_{sh}$ , where  $\tau_{sh}$  is the supra-horizon buffer discovered by Pober et al. (2013) and chosen by the observer. This nominally leaves only noise and EoR signals in the power spectra.

### 5.1.1.2 Noise spectra

To estimate the sensitivity of the delay spectrum to 21 cm anisotropies, we must map the thermal noise of the interferometer in to delay space. Noise in visibilities is described by

the *system temperature*, consisting of two components: the receiver temperature ( $T_{\text{rxr}}$ ), representing the noise due to the electronics and outside noise from ground reflections and ohmic loss, and the sky temperature ( $T_{\text{sky}}$ ), representing the variance in power emitted from the field of observation (Thompson et al., 2017).

Concentrating on the  $I \rightarrow I$  component of the direction dependent Mueller matrix (c.f. Chapter 3),

$$T_{\text{sky}}(\nu) = \frac{\int d\hat{s} A(\hat{s}, \nu) S(\hat{s}, \nu)}{\int d\hat{s} A(\hat{s}, \nu)} \quad (5.9)$$

which at low-frequencies and wide fields-of-view is expected to dominate over  $T_{\text{rxr}}$ . Measuring the average root mean square difference between every-other visibility recorded for a given baseline typically gives a good estimate of the system temperature  $T_{\text{sys}} = T_{\text{sky}} + T_{\text{rxr}}$ . Parsons et al. (2012a) (and also see public HERA memo #27) showed that the power spectrum due to system noise is approximately

$$P_N(k) \approx \frac{1}{2\Delta t} X^2 Y \Omega_{\text{eff}} B_{\text{NE}} T_{\text{sys}}^2, \quad (5.10)$$

where  $\Delta t$  is the integration time,  $B_{\text{NE}}$  is the noise-effective bandwidth given by the choice of window used during the delay transform, and  $\Omega_{\text{eff}}$  is the effective beam area, defined in Parsons et al. (2014) as

$$\Omega_{\text{eff}}(\nu) = \frac{|\int d\hat{s} A(\hat{s}, \nu)|^2}{\int d\hat{s} |A(\hat{s}, \nu)|^2}. \quad (5.11)$$

The system temperatures of PAPER and the MWA are between 200 and 300 K (public HERA memo #10). These levels make the instrument itself a substantial noise source to overcome in order to reach EoR power levels. This forces EoR experiments to integrate noise down over long observing seasons – and the data under integration must be noise limited, rather than systematic limited (c.f. Chapter 6) – to obtain limits, and in the future, detections, of the EoR. Cheng et al. (*submitted*) showed in detail that many factors of the observation season contribute to averaging-down the noise. Specifically,

$$P_N(k) \propto \frac{T_{\text{sys}}^2}{\sqrt{N_{\text{LST}} N_{\text{seps}} t_{\text{int}} N_{\text{days}} N_{\text{bl}} N_{\text{pol}}}} \quad (5.12)$$

where  $N_{\text{LST}}$  are the number of LST hours sampled,  $N_{\text{seps}}$  are the number of baseline types averaged incoherently (in Chapter 11, this number is 3),  $t_{\text{int}}$  is the effective integration

time after fringe-rate filtering (see Chapters 6 and 11),  $N_{\text{days}}$  is the effective number of days analyzed, given LST-coverage per day,  $N_{\text{bl}}$  is the total number of baselines used, and  $N_{\text{pol}}$  is the number of instrumental polarizations – which for all power spectra in this thesis is 2.

In Chapter 11 I present the deepest limits achieved by the PAPER experiment using foreground-avoidance techniques. Figure 1.6 showed the current best limits on the EoR power spectrum, most of which were noise-limited. The best limits still require a factor of  $10^3$  more sensitivity before a marginal detection is possible. This in turn requires larger arrays, integrating for longer amounts of time – an effort that the construction of HERA represents progress on.

### 5.1.2 Foreground subtraction

Given a finite bandwidth, increasing the length of baselines shrinks the size of the EoR window for that  $k_{\perp}$  value. It is possible to construct arrays with such long baselines that the EoR window effectively disappears, and the delay spectrum approach becomes inappropriate. Instead, the wedge must be interacted with in some way. Substantial progress has been made by modelling and subtracting point source contributions from visibilities (e.g. Patil et al., 2017). Point sources dominate the wedge at high  $k_{\perp}$  values (e.g. Trott et al., 2012) – subtraction of point source power has the effect of ‘flattening’ the top of the wedge and opening-up some region of it for EoR analysis. However, Barry et al. (2016) showed that an incomplete point source catalog can lead to contamination large enough to prohibit a statistical detection of the EoR. Both Kohn et al. (2016) and Patil et al. (2017) found – for very different regions of  $k$ -space – that improved phase calibration had a similar effect to point source subtraction, lowering the amplitude of the high  $(k_{\perp}, k_{\parallel})$  region of the wedge.

## 5.2 The Problem of Polarization

Polarized, Faraday-rotated radiation represents a challenge for both foreground avoidance and subtraction strategies. This challenge is summarized in Figure 5.4. The top panel shows example spectra for various sources of radiation that we are interested in. The largest contribution to overall power observed by our instruments is from Stokes I, where synchrotron emission dominates and emits smooth-spectrum synchrotron. The spectrum of Stokes Q is represented by a  $p = 1\%$  polarization fraction of Stokes I. The Stokes Q spectrum is also shown Faraday-rotated (see Chapter 2), and subsequently a fraction  $\gamma_{+-} = 1\%$  of that Faraday-rotated spectrum can be direction-independently rotated in to Stokes I (see Chapter 3). We choose not to visualize the direction-dependently leaked component as its overall contribution is similar to the direction-independently leaked one. The lower panel shows the delay transform of each spectrum; black dashed lines indicate the horizon delay for a 30 m baseline.

While Figure 5.4 should be considered an illustration, insofar that the absolute values are physically motivated but not precise, its implication is clear. Faraday rotation of polarized foregrounds will, at low frequencies, induce large amounts of spectral structure in the Stokes Q (and Stokes U) spectra. Interferometers can leak power from the Stokes Q and U sky into pseudo-Stokes I visibilities through direction dependent and independent mechanisms – and this leaked polarized power can represent a foreground with a similar spectral signature to the EoR<sup>1</sup>.

Moore et al. (2013) was the first work to quantify the problem of polarization for the foreground avoidance scheme. Through statistical realizations of the polarized sky, they showed that increasing the average Rotation Measure (RM) contaminated higher  $k$  values of the power spectrum. In essence, RMs alias power in the wedge to higher  $k_{\parallel}$  values (Nunhokee et al., 2017). Recent measurements have shown that on large scales (low  $k_{\perp}$ ),

---

<sup>1</sup>It should also be clear that radio frequency interference from human communications, which manifests as sharp spikes in narrow frequency bands, will have a similar effect to spectrally-structured emission in the delay paradigm.

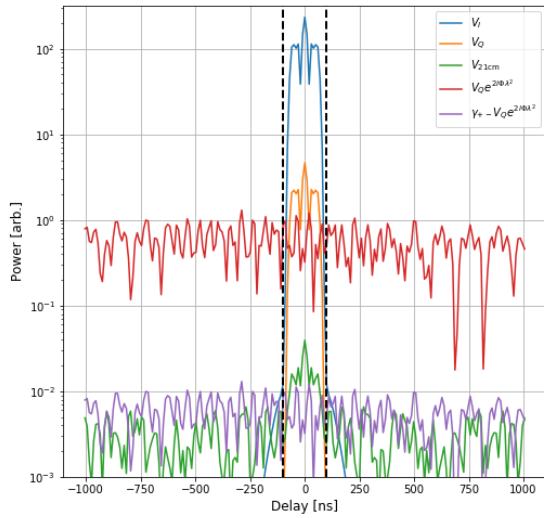
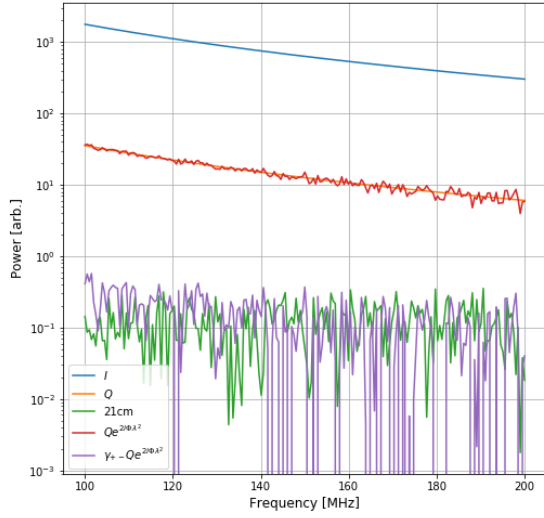


Figure 5.4: A summary of the problem posed by polarization for EoR experiments. This is somewhat of a cartoon representation, so the overall power levels should not be taken as accurate forecasts, but they are physically motivated (see Chapter 2). Above are spectra for unpolarized and polarized synchrotron, the EoR, Faraday-rotated Stokes Q, and a fraction  $\gamma_{+-}$  of Faraday-rotated Stokes Q that can leak in to Stokes I. Below, those spectra multiplied by a model bandpass and delay-transformed; the horizon delay for a 30 m baseline is shown in black. Leaked, Faraday-rotated Stokes Q resembles the EoR.

diffuse emission can be bright, with polarization fractions of 1–4%, but are observed to have very low rotation measures (Bernardi et al., 2013; Lenc et al., 2016). This may mean that polarized power does not represent a large risk to EoR power spectra formed in the foreground avoidance scheme, as leaked power would still remain within the wedge. In the foreground subtraction scheme, one must model each point-source spectrum and subtract it. At the dynamic range required for EoR studies, this necessitates modelling of leaked Faraday-rotated power (e.g. Jelić et al., 2014). Polarized point sources are a greater risk for this approach; Van Eck et al. (2018) observed polarized point sources with both high polarization fractions and high rotation measures.

In this Part, I have recorded my efforts to reduce interferometric observations from PAPER and HERA, taking as much care as possible to avoid introducing spectral structure to the visibilities through calibration, and investigating the impact of polarized emission on our measurements. In the following Chapters, I discuss quality assurance metrics and data compression (Chapter 6), polarized calibration (Chapter 7), the effect of the ionosphere on polarized power spectra (Chapter 8), and three successively deeper integrations on polarized power, concentrating on successively thinner slices of  $k_{\perp}$  (Chapters 9 – 11).

# Chapter 6

## Data Preparation and Processing

The data volume of interferometric measurements inherently scale as the square of the number of antennas in the array ( $N_{\text{ant}}$ ). Not only does the sheer volume of data from large- $N_{\text{ant}}$  arrays pose a problem for data storage, but also it requires precise and efficient efforts to quality assure (QA) the data.

In this chapter, I will outline some of the efforts involved in data preparation, pre-processing and QA that are required for an EoR power spectrum estimate.

### 6.1 Data Compression

The PAPER-128 correlator produced 288 MIRIAD files per night. Each of these contained 8126 baselines, and each baseline contained visibilities over 1024 98 kHz frequency channels and 56 10 s time integrations. The four instrumental polarizations were in separate files. In sum, each file was 4.2 GB which meant that each night 1.2 TB of data were recorded.

In order to efficiently transport the data over Gigabit Ethernet from the Karoo Radio Quiet Zone (KRQZ) to Cape Town, and from Cape Town under transatlantic cables to Philadelphia, some compression was required. It was also required that such a compression, while lossy, did not effect the targeted cosmological signal.

### 6.1.1 Delay–Delay-Rate Filtering

The compression algorithm implemented for PAPER observations, Delay–Delay-Rate (DDR) filtering, was introduced in Parsons & Backer (2009) described in Parsons et al. (2014), and we briefly review it below.

The geometric delay of a celestial signal, originating from direction  $\hat{s}$ , incident on an interferometric baseline described by vector  $\vec{b}$ , is

$$\tau_g = \frac{|\vec{b} \cdot \hat{s}|}{c} \quad (6.1)$$

where  $c$  is the speed of light. This relationship implies that  $\tau_g$  is bounded for a given baseline

$$-|\vec{b}|/c \leq \tau_g \leq |\vec{b}|/c \quad (6.2)$$

Equation 6.2 therefore gives the maximum value of  $|\tau_g|$  physically meaningful for a given array – the maximum baseline length in that array, divided by  $c$ . For PAPER, the maximum baseline length is 300 m, corresponding to  $\max(|\tau_g|) = 1\mu\text{s}$ . As reviewed in Chapter 5, the delay axis may be accessed by Fourier transforming a visibility along the frequency axis. Once in delay space, power at delays larger in magnitude than  $1\mu\text{s}$  could be removed. With a sufficiently large frequency bandwidth, this would not produce aliased signal, according to the critical Nyquist rate. By using the  $1\mu\text{s}$  as a delay bound for all visibilities, the frequency axes of all compressed visibilities remained the same (reduced in number from 1024 to 203), which while sub-optimal from a compression point of view, allowed for ease of programming at later stages.

A similar geometric bound can be obtained by Fourier transforming the time axis of visibilities, provided that they were obtained in drift-scan mode (see Chapter 3). Parsons & Backer (2009) showed that the rate at which the geometric delay on an interferometric baseline changes is governed only by the position of the array on Earth, and the Earth’s rotation:

$$\dot{\tau}_g = -\frac{\omega_{\oplus} \cos \delta}{c} (b_x \sin \alpha + b_y \cos \alpha) \quad (6.3)$$

where  $\omega_{\oplus}$  is the angular frequency of the Earth's rotation,  $\alpha$  and  $\delta$  are the hour-angle and declination of a point on the celestial sphere, respectively, and  $\vec{b} = (b_x, b_y, b_z)$  is the baseline vector expressed in equatorial coordinates.

For arrays not close to the geographic poles,  $|b_y| \gg |b_x|$ , there is a maximum rate of change (corresponding to  $(\alpha, \delta) = (0, 0)$ ), producing a bound on  $\dot{\tau}_g$ :

$$-\omega_{\oplus} |b_y|/c \leq \dot{\tau}_g \leq \omega_{\oplus} |b_y|/c \quad (6.4)$$

for a 300 m East-West baseline, the maximum delay-rate is approximately  $\max(|\dot{\tau}_g|) = 0.07 \text{ ns s}^{-1}$ . This delay-rate was not Nyquist sampled by a single PAPER file: requiring the previous and next files generated for that polarization to be appended on either side of each visibility's time axis to prevent aliasing from the decimation. For the large scale processing of months of data, this required a software pipeline described in Section 6.1.2.

There are also other issues with DDR compression, largely associated with instrument systematics. Delay transforms rely on the fact that the bright foregrounds that dominate the measured signal are spectrally smooth, and that the frequency response of the instrument is also spectrally smooth: this of course is the basis for the EoR window paradigm reviewed in Chapter 5. Likewise, delay-rate filtering assumes temporal smoothness. Radio Frequency Interference (RFI) signals created by human communications violate both models of smoothness, since they are typically confined to narrow bandwidths (creating sharp spikes along the frequency axis) and may be transient (creating sharp spikes along the time axis). This requires steadfast identification and flagging algorithms for RFI (see Section 6.2), and some variety of interpolation, fitting, or CLEANing across the flagged regions prior to compression.

By DDR filtering of PAPER-128 data using a 300 m baseline to set the width of the filters we were able to reduce the volume of the data by an approximate factor of 70.

### 6.1.2 Software Implementation

The first season of PAPER-128 data, due to a variety of circumstances, required compression on the computing cluster at the University of Pennsylvania. The raw data were stored on a high-volume drive that was able to connect with the cluster via a low-speed switch. The hardware capable of performing any sort of high-performance processing (i.e. holding the data in RAM) were ten ‘compute nodes’ connected to the cluster via a high-speed switch, and mounted in an NFS architecture. The compute nodes could only hold  $\sim 10$  PAPER-128 files in storage.

The processing stages for compression of a night of PAPER data, described below, required knowledge of the location and compression state of not only individual files, but also the neighbors-in-time of the file in question, in order to implement the DDR filter described above. To supervise the compression we created a MySQL database, which we interacted with via Shell and Python scripts. The database contained a table for the data files under processing and their compression state, a table of neighbor-relations, a table of file details, and a table of the processing nodes available. The schema of this database is shown in Figure 6.1.

To implement the compression, per file, the following steps were required:

1. Copying the file from the storage volume to the cluster. For a single night of data, this required roughly 8 hours.
2. Copying the file from the cluster to the compute node. This required roughly 5 minutes.
3. Generate copy of the file, with metadata corrections. This required roughly 1 minute.
4. Delete the raw file.
5. RFI-flag the high frequency-resolution data. This required roughly 2 minutes.
6. Delete the metadata-corrected file.

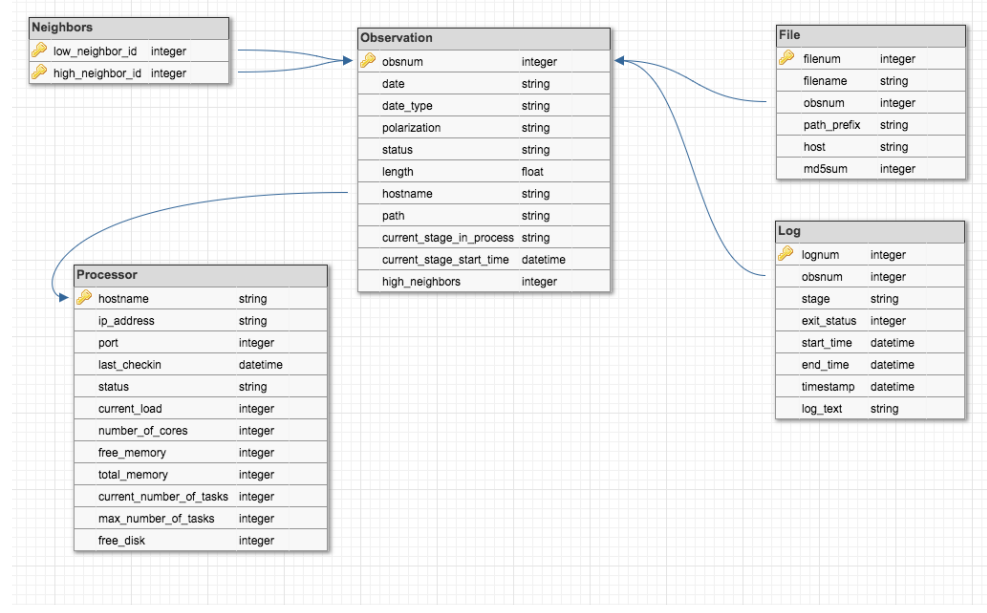


Figure 6.1: The schema of the database used to organize and implement PAPER data compression.

7. Acquire time-neighbors to the file in question, and bring them to the RFI-flagged stage. The time required for this stage varied with cluster activity, but usually required roughly 20 minutes.
8. DDR filter the RFI-flagged data, using an high-tolerance iterative CLEAN. This required roughly 20 minutes.
9. RFI flag the compressed data (coarse flagging), saving the flags to a separate file. This required roughly 1 minute.
10. Apply the coarse RFI flags to the *uncompressed*, RFI-flagged data. This required roughly one minute.
11. DDR filter the now twice-RFI-flagged data, using a low-tolerance iterative CLEAN. This required roughly 120 minutes.
12. Copy compressed data to the cluster.

13. Delete the twice-RFI-flagged data.
14. If the once-RFI-flagged data are not required as neighbors, delete them.
15. Delete the compressed data from the compute node.
16. If neighbors have already been compressed, delete them, otherwise begin their compression.
17. After all files are compressed, delete the uncompressed files from the cluster.

In total, this meant that across ten compute nodes, and efficient use of the fact that the neighbors could progress through the processing stages while the central file was being compressed, meant that it took roughly 20 to 24 hours to compress a night of observations.

## 6.2 Radio Frequency Interference

As noted above, RFI was able to introduce spectral and temporal structure that would cause ringing in the data during compression if it was not flagged. This meant that both identification and characterization of RFI was crucial to the scientific goals of the PAPER and HERA experiments. In Section 6.2.1, I present characterization of RFI in the second season of PAPER-128 data. By averaging flags in local time I was able to investigate “repeat offender” frequency bands and identify outlying “quiet” and “loud” days. In Section 6.2.2 I analyze RFI flags from the first Internal Data Release (IDR1) of HERA commissioning data, which contained 19 HERA feeds suspended above 5 m dishes in a close-packed hexagon, and 19 PAPER feeds in the same positions as the central dishes, allowing us to investigate the difference in flagging between feeds at different altitudes.

### 6.2.1 PAPER-128

The PAPER-128 2014 observation season ran from 18th June 2014 through the 30th April 2015. During this run, some 150 nights of data were recorded. A “night”, which I will

refer to using the JD at the start of observations, consists of twelve hours of observation from 6pm to 6am South African Standard Time (SAST). Observations as processed by the PAPER correlator are recorded in MIRIAD uv files. These files contain visibilities for each antenna pair in the array. Each integration is 20 seconds long over 1024 frequency bins from 100 to 200 MHz. Each uv file contains 56 integrations per antenna pair, and 72 uv files are recorded per linear polarization (xx, xy, yx, yy) per night.

Early in the PAPER data compression process, visibilities are flagged for RFI. This is accomplished by the aipy script *xrfi\_simple.py*, which takes the derivative of the frequency axis of all baselines associated with a single antenna, and flags any frequencies with a derivative  $\geq 6\sigma$  above the mean. We always flag the band-edges ( $\sim 7$  MHz on each side), since these frequencies are not useful to us, and always flag the  $137 \pm 0.6$  MHz band associated with ORBCOMM satellite network transmissions. This process is repeated per integration within each uv file and stored in a Python numpy zip (npz) file. This means that any baseline associated with antenna 1 can contribute a flag to the resultant npz file, which in turn is applied to the data.

The result is 280 files of high-time and -frequency resolution files per night per linear polarization containing information about the RFI environment of the HERA site. I report on the properties of these flags in time- and frequency-space over the 2014 observation season. This section is organized it as follows: in Section 6.2.1.1, I analyse the average properties of RFI over the season by stacking flags in local time and normalizing appropriately. In Section 6.2.1.2 I address nights with particularly strange RFI properties. I discuss the implications of my findings in Section 6.2.1.3.

### 6.2.1.1 Average Properties

In order to assess the average properties of the RFI environment, I calculated a weighted average of flags over the season. Over 150 nights, one-time occurrences are washed-out beneath the 1% level, allowing me to assess persistent issues.

Nominally, each night should grant 3920 integrations-worth of flags over 1024 fre-

quency bins, per linear polarization. In reality, most of the time this holds true, but occasionally not all files are compressible (hence failing to generate flags) or observations fail to start at the correct time (so there are no data to flag). Also, in the event of an X-engine failure within the correlator, contiguous chunks of the band (in eighths, i.e. 25 MHz across) are flagged-out, usually for the rest of the night.

For this reason, I calculated a weighted average of the flags across the season, but neglected nights with correlator failures or late starts. Weights were simply the number of nights that contained that integration-bin in SAST. The resultant “flag density waterfall” is shown in Figure 6.2. The color scale is indicative of flagging frequency across the season, and line plots above and to the right of the the waterfall showing the percentage of times and frequencies that were flagged, respectively.

A summary of the persistent (flagged  $\geq 1\%$  of the time per channel) RFI frequencies can be found in Table 6.2.1.1. I have investigated each frequency and tried to find the most likely source for each. In most cases, this required looking at the properties in time as well as frequency. Others were more obvious from frequency alone, e.g. the 149.8 MHz transmission frequency from the International Space Station (ISS). Still others I could not track down a convincing explanation for, and these are listed with a ‘?’ . A ‘?’ next to a possible cause indicates that the listed cause is the most prevalent at that frequency, but that the temporal properties of that cause do not necessarily make sense. Many of the characterizations arise from the South African Table of Frequency Allocations (SATFA; Staatskoerant (2008)).

Figure 6.3 shows the detail of the top panel of Figure 6.2. This figure highlights the broad swath of the band from roughly 150 to 180 MHz that was, on average, clear of RFI. This roughly corresponds to 21 cm redshifts  $z = 6.9$  to  $8.5$ . This is one of the reasons that the Parsons et al. (2014) and Ali et al. (2015) limits on the 21 cm power spectrum concentrated on this redshift range – there were simply more unflagged data to average-down with. Furlanetto et al. (2006) show that the  $z \sim 8$  universe can be considered roughly coeval over an  $\sim 8$  MHz bandwidth. As such, the 30 MHz chunk could be used to

Table 6.1. PAPER-128 RFI frequencies and brief characterization for the averaged flags.

$\nu$ MHz	Flagged %	Cause (Possible)	Notes or Time (SAST) Characterization
103 ± 3	100	BAND EDGE	Built-in to flagger.
107.25 ± 0.25	2.6	FM radio	Constant background at 2% level
107.55 ± 0.05	1.9	FM radio	Constant background at 2% level
108.1 ± 0.4	9	FM radio?	Rises with time, peaking at midnight and 4am
109 ± 0.4	11.5	FM radio?	Rises with time, peaking around 4am
112.8 ± 0.1	1.4	Aircraft?	Constant background at 1% level
114.05 ± 0.85	3.7	?1	Decreases till midnight; peak at 4am
116.55 ± 0.35	2.2	?2	Peak at midnight
120.15 ± 0.35	3.2	Aircraft	Roughly follows CPT↔JNB flight times
124.95 ± 0.35	5.5	Aircraft	Roughly follows CPT↔JNB flight times
130.25 ± 0.55	4.3	?3	Falls (7pm) and rises (3am) steeply
131.75 ± 0.35	10.3	Aircraft?	Peaks at 6:30, 7:30, 8:30, 9:30, 10 and then a steep falloff
136.05 ± 0.45	33.1	Radar?	Decreases over night
137.35 ± 0.85	100	ORBCOMM	
141.45 ± 0.35	2.1	Mobile phones?	High until 9pm, then at background 1% level
145.85 ± 0.45	10.7	Amateur radio	Strong 9pm-1am – this is the official downlink for ISS-HAM
149.75 ± 0.55	90.7	ISS	“Beeps”, but in stacked data peaks 2am
175.15 ± 0.35	20.5	VHF TV (video)	Channel 4. Peaks at 8:30pm, then falls to background 7%
181.15 ± 0.15	1.6	VHF TV (audio)	Channel 4. 2% level turns-off at 10pm
182.15 ± 0.35	75	?4	Decreases until 10pm (to 15%), when it begins a slow rise again
183.2 ± 0.5	89.7	VHF TV (video)	Channel 5. Rises throughout night.
186.25 ± 0.35	4.6	?5	Extreme turn-off at 9:45
189.15 ± 0.35	41.4	VHF TV (audio)	Channel 5. Rises throughout night.
189.9 ± 0.4	100	VHF TV	Channel 6. Built-in to flagger.
191.1 ± 0.3	100	VHF TV	Channel 7. Built-in to flagger.
196 ± 4	100	BAND EDGE	

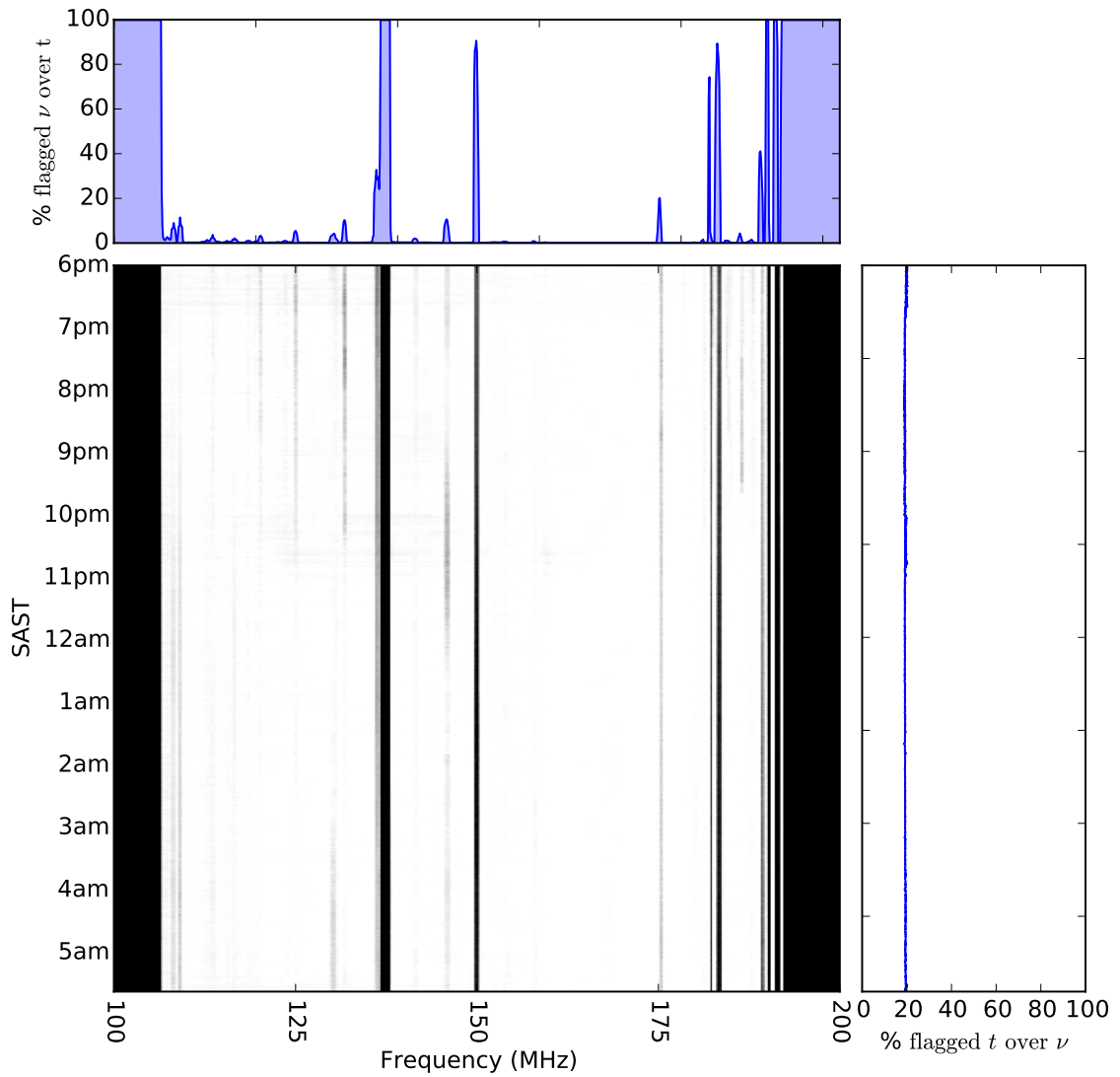


Figure 6.2: A waterfall plot of RFI flags averaged over 150 days of data. The gridding process is described in the text. Above the waterfall I show the percentage of the season each frequency is flagged, and to the right I show the percentage of frequencies that are flagged per integration.

create  $\sim 3$  power spectra, as demonstrated in Jacobs et al. (2015). As we show below, the deactivation of VHF TV broadcasts could enable measurements up to the band edge.

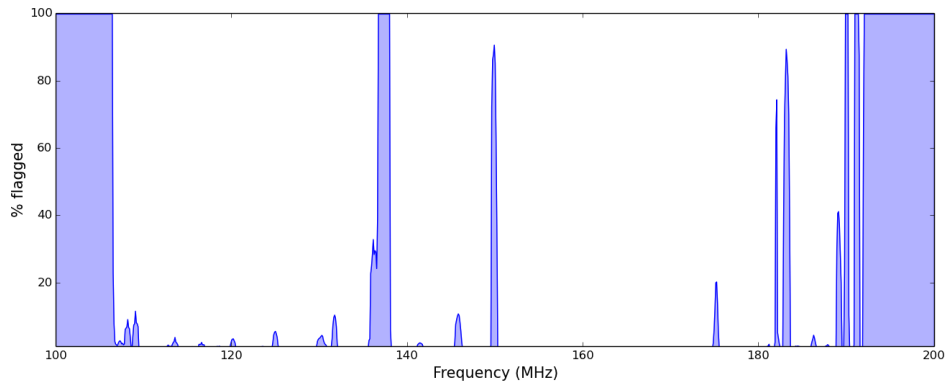


Figure 6.3: The percentage of time that each frequency was flagged over the season.

## FM Radio

SATFA lists the frequency band 87.5–108 MHz as available for FM radio broadcasts, leading me to postulate that the low-level RFI we observed in the  $107.25 \pm 0.25$  and  $107.55 \pm 0.05$  MHz bands had FM radio as the leading cause. The  $108.1 \pm 0.4$  and  $109 \pm 0.4$  MHz bands were outside of the official range, and exhibit odd temporal properties for human activity – two peaks at midnight and 4am – with a increasing number of flags throughout the average night (see Figure 6.4).

## Aircraft communications

It was difficult to argue that the  $112.1 \pm 0.1$  MHz signal is caused by aircraft communications since it maintained a constant background level. However, SATFA listed this frequency as reserved for aircraft communications and it has been used in the past as a calibration frequency for aircraft instruments South African Civil Aviation Authority (2008).

The other aircraft frequencies were obvious, because they closely traced the 2-hour flight from Cape Town to Johannesburg<sup>1</sup>. An example ( $120.15 \pm 0.35$  MHz) is shown in

---

<sup>1</sup>Credit to Danny Jacobs for first spotting this and noting it in an internal PAPER circular in December 2009.

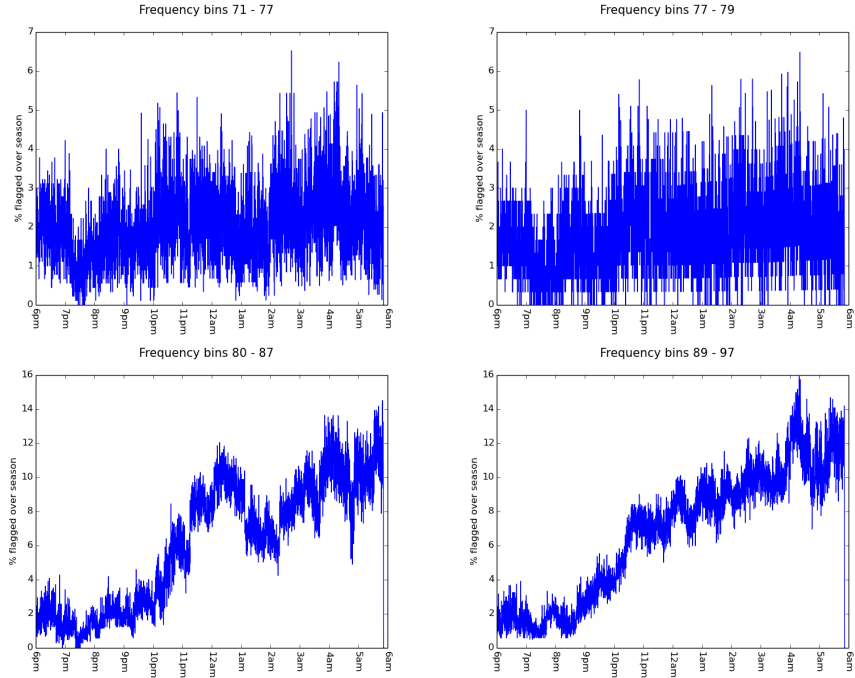


Figure 6.4: Possible FM radio contamination in the *Top, left to right*:  $107.25 \pm 0.25$  and  $107.55 \pm 0.05$  MHz bands, and *Bottom, left to right*:  $108.1 \pm 0.4$  and  $109 \pm 0.4$  MHz bands.

Figure 6.5. SATFA reserved frequencies 108–117.975 MHz for aeronautical radionavigation and 117.975–137 MHz for aeronautical mobile. In Table 6.2.1.1 I listed  $131.75 \pm 0.35$  MHz as caused by aircraft since it falls in the aeronautical mobile band, but it does not follow the flight patterns as closely as the other bands.

## Orbital communications

ORBCOMM Inc.’s constellation of 29 LEO communication satellites is a well-known contaminant of the low-frequency sky, dominating over any astronomical signal at 137–138 MHz (although each satellite emits within a 20 kHz band). For this reason there was built-in flagging at  $137.35 \pm 0.85$  MHz within the compression pipeline.

The largest contaminant without built-in flags in the pipeline were communications from the ISS. The  $149.75 \pm 0.55$  MHz transmissions were semi-regular in time; they ‘beep’.

Onboard the ISS are HAM radio devices. Some countries have also launched satel-

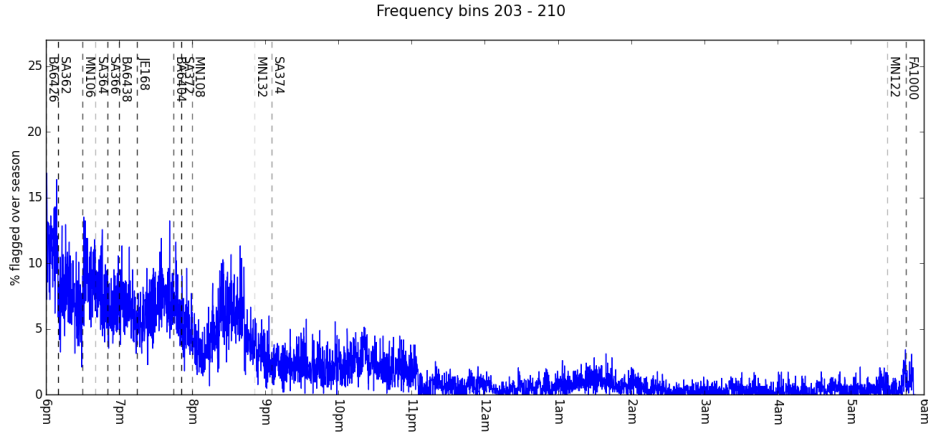


Figure 6.5: Flights from Cape Town to Johannesburg correspond to RFI in the  $120.15 \pm 0.35$  MHz channels. Vertical dashed lines indicate a flight leaving Cape Town (flights from Johannesburg are roughly concurrent) and the flight code is listed. The transparency of a line is inversely proportional to how many days a week that flight is scheduled for. The flight is 2 to 2.5 hours long – and about 2 hours after the last flight of the day, the flags fall to background level (but notably, not always to zero).

lites with these onboard, one of the purposes of which is to provide HAM radio operators something in space to communicate with. These devices are licensed to operate at 145.2 and 145.8 MHz, and SATFA listed the 144-146 MHz band as reserved for ‘Amateur–Satellite’ communications. We detected RFI at  $145.85 \pm 0.45$  MHz, although strong signal across  $\sim 10\%$  of the season that occurs 9pm-1am argues against human operation.

### Mobile phones and VHF TV

A weak RFI signal at  $141.45 \pm 0.35$  MHz was within the ‘mobile 1 BTX’ and aeronautical mobile band in SATFA, but other than this single listing I did not build a strong case for the signal’s cause.

VHF TV is broadcast over specifically-spaced video and audio frequencies. The strong signals at  $183.2 \pm 0.5$  MHz and  $189.15 \pm 0.35$  MHz had almost identical gradients for the percentage of flagging as a function of time of night. These frequencies corre-

sponded exactly to Channel 5 of South African System I 625-line VHF TV signals for video and audio transmission, respectively. Similarly, the weaker signals at  $175.15 \pm 0.35$  and  $181.15 \pm 0.15$  MHz corresponded to Channel 4's video and audio transmission, respectively, but they did not share the same temporal properties.

## Unidentified sources

There were 5 RFI frequencies in the averaged data that I could not identify the sources of: weak emissions (flagged < 5% of the season) at  $114.05 \pm 0.85$ ,  $116.55 \pm 0.35$ ,  $130.25 \pm 0.55$  and  $186.25 \pm 0.35$  MHz, and one strong emission at  $182.15 \pm 0.35$  MHz. The variation of each source with time is shown in Figure 6.6. The  $186.25 \pm 0.35$  MHz had a sharp turn-off around 9:45pm each night, suggesting that it originated from some kind of automated device.

### 6.2.1.2 Individual Properties

Using the flags per night, I was able to assess the total number of flags as a percentage of the waterfall (i.e.  $N_{\text{flags}} / (3920 \times 1024)$ ). The average flagging per night was  $19.2 \pm 0.5\%$ , which was dominated by the permanent flagging of ORBCOMM and band edges. Four nights deviated from the average by a  $\geq 2\sigma$  excess: JDs 2456965, 2456732, 2456958 and 2457038. Their flag waterfalls are shown in Figure 6.7 (2456732, 2456958 and 2457038) and Figure 6.8 (2456965). While the strange nature of night 2456965 is discussed below, the three others followed the pattern of having strong contamination from FM and aircraft communication bands, but also had broadband ‘pulses’ up to about 20 minutes in length. The source of these broadband pulses is not well understood, although it was clear that ORBCOMM tends to spill outside of its allocated band on occasion.

JD 2456965 was easily the worst offender, and it exhibited a strange signal that wanders in frequency and time close to the ISS band. An event of note on this date (23rd November 2014) was a Soyuz FG launch that docked with the ISS – this may have been

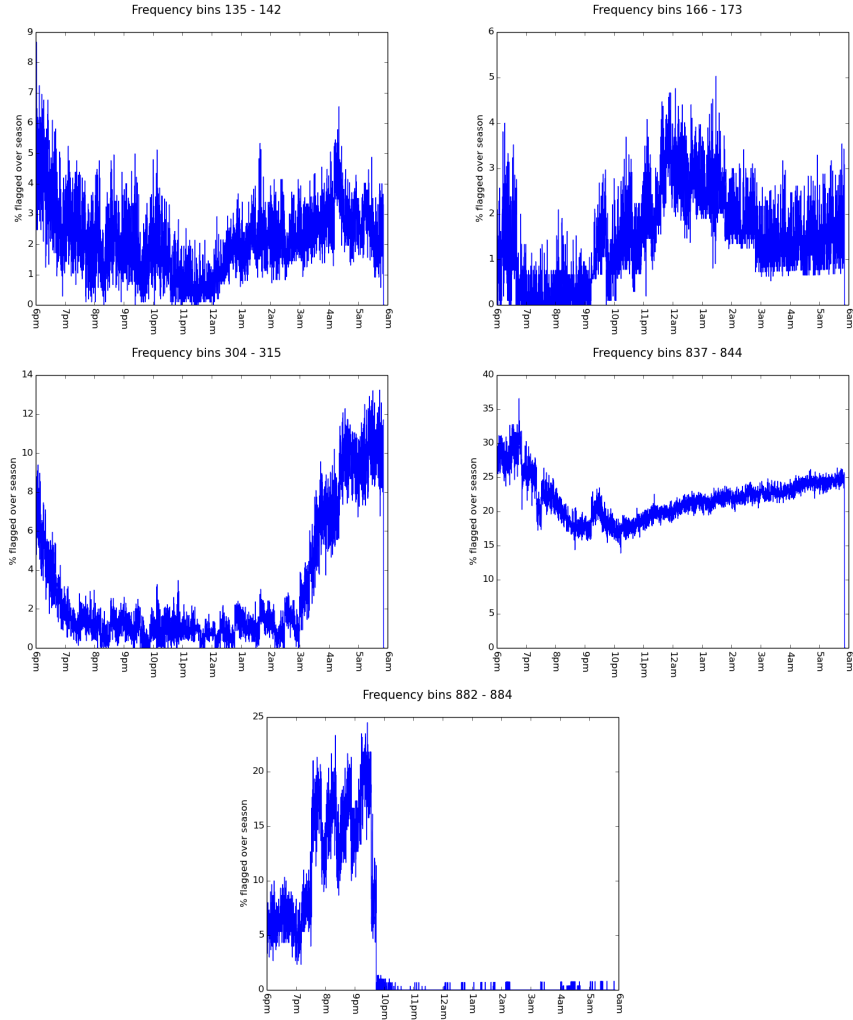


Figure 6.6: The temporal profile of the 5 RFI frequencies with unidentified causes. *Top, left to right:*  $114.05 \pm 0.85$  and  $116.55 \pm 0.35$  MHz. *Middle, left to right:*  $130.25 \pm 0.55$  and  $182.15 \pm 0.35$  MHz. *Bottom:*  $186.25 \pm 0.35$  MHz. The  $182.15 \pm 0.35$  MHz frequency is flagged a large amount of the time, making it our most-offending unidentified source.

a signature of their transmissions<sup>2</sup>. Similar signals were seen on 2456898 (28th August 2014; although only at the beginning of the night) and 2456924 (23rd September 2014). There was no listed orbital or suborbital activity for 2456898. There was an US ICBM

---

<sup>2</sup>The internet also suggests... less plausible explanations: <https://www.youtube.com/watch?t=11&v=VtZx8iP04zs>.

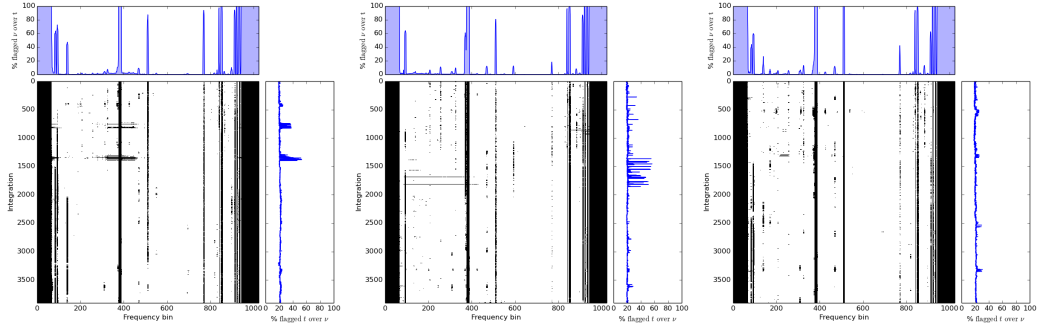


Figure 6.7: *Left to right*: waterfalls of flags for nights 2456732, 2456958 and 2457038. These three nights, along with 2456965, are  $>20.2\%$  flagged;  $>2\sigma$  above the average flagging amount per night.

test off of the coast of Virginia on 2456924, but this was probably not the cause of the RFI. The flag waterfalls for these nights are shown in Figure 6.8.

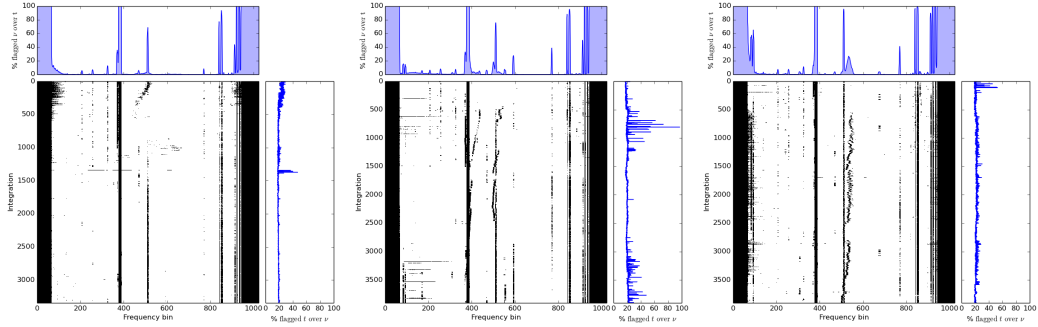


Figure 6.8: *Left to right*: waterfalls of flags for nights 2456898, 2456924 and 2456965. These three nights exhibit a strange behaviour of RFI that changes in frequency and time. JD 2456965 is by far the worst, and during this night as well as 2456898, we see a broadband ‘comb’ of flagged frequencies near the band edges

Another property that the flag waterfalls in Figures 6.7 and 6.8 highlight is the presence of broadband RFI signals, typically present at frequencies lower than the ORB-COMM band. However, while we flagged at the low-end of the band (which had higher noise levels to begin with), it is likely that such broadband pulses dominated the band at those times, and that we failed to flag all of the integrations. Our flagging routine

*xrfi\_simple.py* does contain a thresholding option for flagging the entire integration given some arbitrary number of frequencies flagged during that integration: some experimentation will be required to decide if that threshold should change.

### 6.2.1.3 Discussion

Based on my findings, I was able to recommend some actions that could be taken in the KRQZ to enable better measurements:

- Steps to reduce and ideally eliminate the VHF TV transmissions in the area would be very helpful, since these were clearly interfering with our measurements in the high-end of the band.
- The ISS  $149.75 \pm 0.55$  MHz band should be permanently flagged within the compression pipeline.
- Pursuing re-routing of flight paths will not do much to help: we see aircraft signals for the duration of their flight, not just when they're over the Karoo.
- A lower threshold for identifying broadband RFI should be investigated.

A new, lower-frequency feed is currently under development by the HERA analog group. This would nominally allow measurements to be taken in the range 50–250 MHz, allowing science observations of the Dark Ages and the post-reionization Universe. It should be noted that at the lowest frequencies FM radio will be a constant harassment to these measurements. At the higher frequencies, VHF TV will be the primary contaminant, but should be much easier to remove as it is both narrow-band and within the KRQZ's power to shut off.

## 6.2.2 HERA-19 and PAPER-19

The HERA-19 IDR1 consisted of four subarrays: the HERA-19 hexagon of dishes (the ‘HERA Hex’), a hexagon of 19 PAPER dipoles in the exact positions of not-yet-constructed

HERA dishes (the ‘PAPER Hex’), an imaging array and an experimental array for polarization measurements. I will concentrate on the two Hexes in this Section. I analyzed RFI as flagged in the linear  $xx$ -polarization only. Asymmetric beams can in principle receive different RFI events for different linear polarizations, but analysis of that was outside the scope of this diagnostic study.

IDR1 consisted of one ‘golden day’, JD 2457458. This ran from 6pm on March 10th 2016 to 6am the following day. This gave, per baseline, roughly 4000 integrations of 10 seconds each over 1024, 100 kHz frequency channels from 100 to 200 MHz.

In order to flag RFI I used the aipy script *xrfi\_simple.py*. I took the union of all baseline flags as data to analyze. Unlike in Section 6.2.1, these data did not have a-priori flagging of band edges, which allowed me to make a more complete study of RFI in the HERA band. I did have to implement custom flags in order to get more than a zeroth-order view of the RFI (since these would dominate the flagging routine unless they are flagged already), but my results from Section 6.2.1 gave a better idea of what was flagged to get there.

Below I present measurements of high-power, mostly narrow-band RFI channels as flagged in HERA Hex data and PAPER Hex data separately. In both cases, I was able to list any channels that are flagged for  $\geq 1\%$  of the night. I could then compare the flagging Hex-to-Hex, and to PAPER-128.

### 6.2.2.1 HERA Hex RFI

Table 6.2.2.1 shows all narrowband frequency ranges flagged in HERA-19 visibilities, with columns of the frequency range in MHz, % flagging over time, plausible identification, whether or not it was identified in PAPER-128 data, and other notes (often details of the possible identification). Frequencies with 100% flagging indicate manual flags required for *xrfi\_simple* to work on the rest of the channels.

Clearly, the low-end of the band was swamped by FM radio broadcasts. One notable frequency was the  $109.2 \pm 0.3$  MHz band, which was heavily flagged in HERA visibil-

ities, but was only flagged a few percent in PAPER-128 data. As seen before, ORB-COMM satellite emissions spilled out of their allocated 137-138 MHz band down to 136.3 MHz. There were many narrowband RFI channels, across the band, that PAPER-128 did not pick-up. Most of these were flagged only at low levels, with two exceptions:  $111.3 \pm 0.2$  MHz and  $113.5 \pm 0.1$  MHz. Both of these were in the aircraft navigation band. There is some evidence (Civil Aviation Authority, 2016) that 111.3 MHz band is for air force communications. The 113.5 MHz band is a known band for radionavigation beacons ('VOR navaids' World Aero Data, 2016). A particularly annoying 'new' emitter was in the  $153.8 \pm 0.2$  MHz region, which is close to the center of our nominal EoR band. It could correspond to mobile phones being used close to site.

Table 6.2. RFI as flagged by HERA

$\nu$ MHz	Flagged %	Cause (Possible)	Seen by PAPER-128	Notes
100.7 ± 0.2	50	FM Radio	n/a	RSG “Dis Die Een” Prieska
101.5 ± 0.3	36	FM Radio	n/a	RSG “Dis Die Een” Calvinia
102.4 ± 0.1	100	FM Radio	n/a	RSG “Dis Die Een” Carnarvon
102.8 ± 0.3	57	FM Radio	n/a	RSG “Dis Die Een” Pofadder
104.2 ± 0.1	100	FM Radio	n/a	SAfm Prieska
105.1 ± 0.2	100	FM Radio	n/a	SAfm Calvinia
106.2 ± 0.3	100	FM Radio	n/a	SAfm Carnarvon
106.9 ± 0.1	15	FM Radio	n/a	Sentech
107.2 ± 0.1	18	FM Radio	Yes	
107.8 ± 0.2	15	FM Radio	Yes	
108.3 ± 0.1	31	FM Radio?	Yes	
109.2 ± 0.3	93	FM Radio?	Yes...	...but not to this degree
111.3 ± 0.2	25	Air force?	No	
112.5 ± 0.1	5	Aircraft?	No	
113.5 ± 0.1	21	Aircraft	No	VOR navaids
115.5 ± 0.1	3	Navaids?	No	
115.9 ± 0.1	3	Navaids?	No	
116.6 ± 0.2	9	Aircraft?	Yes	VOR-DME navaids
120.1 ± 0.2	5	Aircraft	Yes	CPT< – >JNB
125.0 ± 0.2	6	Aircraft	Yes	CPT< – >JNB
130.0 ± 0.2	4	Aircraft	No	Communication
131.6 ± 0.2	15	Aircraft	Yes	KLM OPS
136.4 ± 0.1	9	ORBCOMM	Yes	
136.7 ± 0.1	10	ORBCOMM	Yes	
137.4 ± 0.4	100	ORBCOMM	Yes	
145.7 ± 0.4	18	ISS/Amateur Radio band	Yes	
149.9 ± 0.1	100	ISS	Yes	
153.8 ± 0.2	7	Mobile phones?	No	
175.0 ± 0.1	100	VHF TV	Yes	Channel 4 Video
178.3 ± 0.2	8	VHF TV	No	Channel 7?
181.2 ± 0.1	100	VHF TV	Yes	Channel 4 Audio
182.2 ± 0.2	9		Yes	
183.5 ± 0.6	100	VHF TV	Yes	Channel 5 Video
184.1 ± 0.1	2	VHF TV?	Yes	Channel 5?
184.7 ± 0.1	6	Broadcasting	No	
187.8 ± 0.1	4		No	
189.1 ± 0.1	52	VHF TV	Yes	Channel 5 Audio
190.1 ± 0.3	13		n/a	

Table 6.2—Continued

$\nu$ MHz	Flagged %	Cause (Possible)	Seen by PAPER-128	Notes
$191.1 \pm 0.1$	100	VHF TV	n/a	Channel 7
$197.2 \pm 0.2$	18		n/a	
$199.4 \pm 0.5$	100	BAND EDGE	n/a	

### 6.2.2.2 PAPER Hex RFI

Table 6.2.2.2 has the same description as Table 6.2.2.1, but for the PAPER Hex. There were far fewer RFI frequencies flagged in PAPER visibilities, almost all of which were seen by HERA. The only RFI seen by the PAPER Hex and not the HERA Hex was the  $123.5 \pm 0.1$  MHz emission, which I could find a plausible identification for.

### 6.2.2.3 Hex-to-Hex Comparisons

As mentioned above, the PAPER Hex saw far fewer narrowband RFI channels than HERA does. This highlighted an interesting trade-off between dipoles and dishes: at first glance, one might have expected PAPER dipoles to be more susceptible to RFI given their broader effective beams. However, HERA dipoles are lifted several meters above the ground, and this change in height may have been the source of the greater susceptibility to RFI. RFI comes from the horizon, which would be more easily received in the far sidelobes of the beam.

Even for the RFI channels they did share, HERA flagged them more often. Taking the difference in percentage-flagging for the common RFI channels (think of the left panel subtracted from the right panel for common channels in Figure 6.9), those channels had an average of 8% more flagging in HERA visibilities. The difference was particularly high in the aeronautical radionavigation bands, where HERA had on average 38% more flagging than the PAPER Hex.

Figure 6.10 shows the flags on a per-sample basis (these were averaged over time to

Table 6.3. RFI as flagged by the PAPER Hex

$\nu$ MHz	Flagged %	Cause (Possible)	Seen by PAPER-128	Notes
100.0 ± 0.1	100	BAND EDGE	n/a	
100.7 ± 0.1	11	FM Radio	n/a	RSG “Dis Die Een” Calvinia
101.6 ± 0.2	6	FM Radio	n/a	RSG “Dis Die Een” Calvinia
102.4 ± 0.1	100	FM Radio	n/a	RSG “Dis Die Een” Carnarvon
102.7 ± 0.1	100	FM Radio	n/a	RSG “Dis Die Een” Pofadder
104.2 ± 0.2	100	FM Radio	n/a	SAfm Prieska
105.1 ± 0.2	100	FM Radio	n/a	SAfm Calvinia
106.2 ± 0.3	100	FM Radio	n/a	SAfm Carnarvon
108.2 ± 0.1	3	FM Radio?	Yes	
109.1 ± 0.1	26	FM Radio?	Yes	
113.6 ± 0.1	2	Airplane Communications	No	VOR navaid
120.2 ± 0.3	3	Aircraft	Yes	CPT< – >JNB
123.5 ± 0.1	1		No	Not seen by HERA
125.0 ± 0.2	6	Aircraft	Yes	CPT< – >JNB
130.0 ± 0.3	3		No	
131.7 ± 0.2	14	Aircraft	Yes	
136.4 ± 0.2	6	ORBCOMM	Yes	
136.7 ± 0.2	6	ORBCOMM	Yes	
137.4 ± 0.4	100	ORBCOMM	Yes	
145.8 ± 0.3	14	ISS/Amateur Radio band	Yes	
149.9 ± 0.1	100	ISS	Yes	
153.8 ± 0.2	3	Single frequency mobile phones?	No	
175.1 ± 0.2	100	VHF TV	Yes	Channel 4 Video
178.3 ± 0.2	100	VHF TV	No	Channel 7?
181.2 ± 0.1	100	VHF TV	Yes	Channel 4 Audio
183.2 ± 0.2	100	VHF TV	Yes	Channel 5 Video
189.2 ± 0.1	100	VHF TV	Yes	Channel 5 Audio
191.2 ± 0.1	100	VHF TV	n/a	Channel 7
199.8 ± 0.2	100	BAND EDGE	n/a	

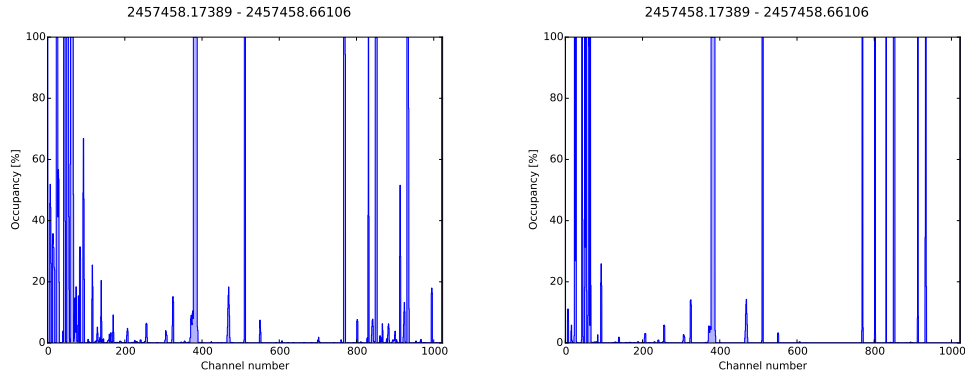


Figure 6.9: Frequency vs. percentage flagging for the HERA Hex (*left*) and PAPER Hex (*right*). Any band with greater than 1% flagging is reported in Tables 6.2.2.1 and 6.2.2.2.

create Figure 6.9). Most apparent was the occupancy of the HERA plot compared to the PAPER Hex one. An important component of this plot is the averages over frequency in the right-hand panels. We saw that the average flagging for a given time sample was about 5% higher for HERA than for the PAPER Hex, mostly due to the higher occupancy of the FM band. But we also saw something new; HERA appeared to be much more sensitive to broadband bursts of RFI. The PAPER Hex caught one of these events (around 1.30am SAST) at high significance, but most of them hardly rose above average flagging. HERA saw five to seven bursts across the night.

#### 6.2.2.4 Comparison PAPER-128 stacked flags

Section 6.2.1 presented RFI flags stacked over 150 days of observations. This method washed-out single events that effect analysis on a single-night basis, but was sensitive to repeatedly offending frequencies. Due to the PAPER-128 analysis pipeline, many channels were automatically flagged (particularly large portions of the band edges), which artificially boosted the average flagging per time and did not allow for closer inspection of the ends of the band. There was some evidence of broadband emission (see Figure 6.2) but the band was largely free of RFI in the middle of the night. Obviously, the data presented in this section shows a less-clean band, but it also only concentrated on a single

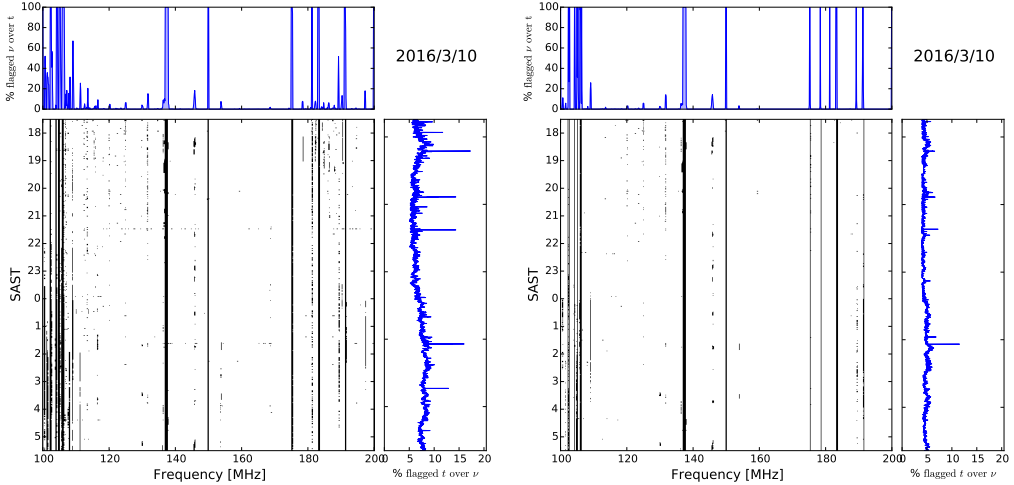


Figure 6.10: RFI flag waterfalls of frequency vs. South Africa Standard Time for the HERA Hex (*left*) and PAPER Hex (*right*). The top panels show the average over time (identical to Figure 6.9), while the right panels show the average over frequency.

night’s data, so it may be that IDR1 was conspicuous compared to an ‘average’ night of observations.

Traits shared between the two analyses were:

- Aircraft communications disrupting data until around local midnight.
- ORBCOMM spilling out of its band.
- VHF TV frequencies emitting throughout the night in the high end of the band.

Table 6.2.2.1 highlighted many frequencies seen by HERA and not by PAPER-128. Again, given the fact that flags were stacked and averaged in Section 6.2.1, these may not have been ‘new’, but they could have been. Particularly conspicuous were the emissions in the aeronautical radionavigation band.

### 6.2.2.5 Discussion

I have presented a first look at RFI in HERA-19 Commissioning data. Probably due to the height of the receiving element on HERA versus PAPER dipoles, much more RFI

was apparent, especially on the low and high ends of the band. Luckily, the EoR band was largely clean of RFI, except for an emitter at about 154 MHz, which could have corresponded to single-frequency mobile phone communications. Such communications are officially banned in the SKA Radio Quiet Zone (SKA Panel, 2012), which HERA is in the center of.

Only looking at a single night of RFI flags limited the predictive power of this study. More data will be required to establish whether or not this level of RFI was ‘normal’. Broadband RFI bursts require closer investigation. Efforts to extend the HERA band to lower and possibly higher frequencies are currently under way. The FM radio band extends to around 65 MHz, while the VHF TV band extends to around 230 MHz, so the RFI environment should be a consideration for these efforts. Meanwhile, I note that the RFI flagging routine used here, `xrfi_simple`, is indeed ‘simple’. More advanced RFI flagging algorithms such as AOFlagger (Offringa et al., 2012) should be tested in later studies.

### 6.3 Quality Assurance Metrics

Throughout reduction of PAPER-128 data, we found a number of ways for data to become corrupted, including failure of analog or digital components, incorrect cable connections, or improper feed installation. Many of these can cause failure of redundant calibration algorithms that are sensitive to non-redundancies within an array. In the case of a real-time calibration pipeline, such as the one implemented for HERA, it is essential to have quickly-generated metrics to assess the overall health of the array. Much of the heritage of PAPER-128 data processing is present in the HERA Real Time Calibration Pipeline (RTC; Ali et al. *in prep.*).

### 6.3.1 Mean Amplitude Flagging

The most critical and likely failure that an antenna could have was malfunctioning electronics losing power and temporarily ‘killing’ it. This failure mode was characterized with unusually low signal coming from the antennas, causing the visibilities associated with that antenna to have much lower than average amplitude. This leads to the definition of the mean visibility metric for antenna  $i$ :

$$M_i = \frac{\sum_{j,v,t} |V_{ij}|}{N - 1} \quad (6.5)$$

where  $V_{ij}$  is the visibility for the baseline involving antennas  $i$  and  $j$ ,  $N$  is the number of antennas in the array, and the sum is taken over all antennas  $j$  ( $i \neq j$ ), times, and frequencies. When  $M_i$  is compared across the array, it can reveal antennas with anomalously low signal to noise.

Erroneously cross-polarized antennas were ones where the feed was rotated 90 degrees, or the cables were swapped for the two polarizations along the signal path (such a failure mode could be expected for a large array under active construction). This caused the linear polarization visibilities ( $EE$  or  $NN$ ) to have a lower amplitude or correlation relative to the cross-polarizations ( $EN$  and  $NE$ ). While these could appear to be dead antennas, the cross-polarization visibilities would show that one of the antennas in a given visibility is cross-polarized.

We defined the mean visibility cross-polarization metric as

$$P_i = \frac{M_i^{NE} + M_i^{EN}}{M_i^{NN} + M_i^{EE}}, \quad (6.6)$$

where  $M_i$  is defined in Equation 6.5 and are calculated for all the polarization pairs. If  $P_i$  is larger than some threshold, then antenna  $i$  may be cross-polarized. This method is effective when applied to long baselines, but for the shortest baselines in HERA, large-scale astrophysical polarization (e.g. Lenc et al., 2016) is observed by in all the instrumental visibilities (since, for example, the  $NN$  visibility is equal to the sum of the Stokes I and Q

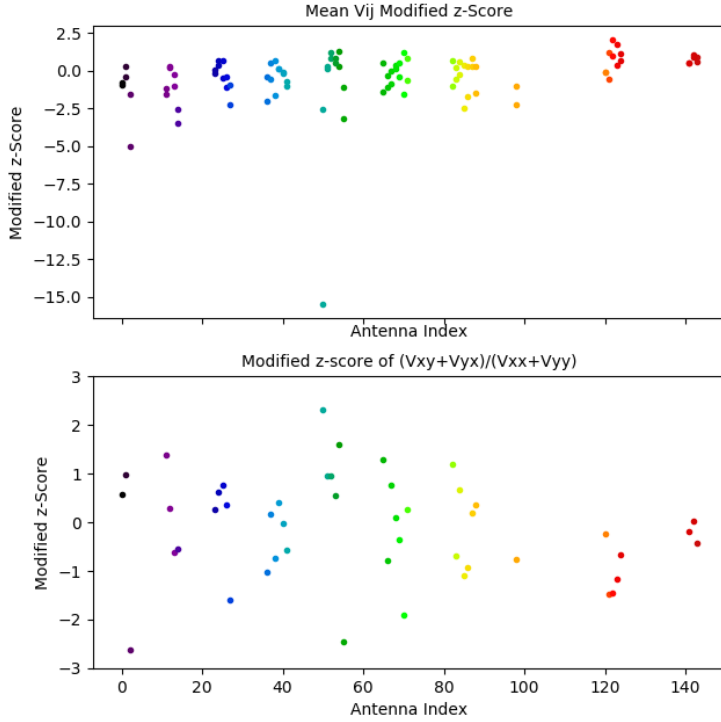


Figure 6.11: An example of the mean amplitude flagging metrics on exercised on HERA-47 data. The top panel shows the mean amplitude flagging metric  $M_i$ , and the lower panel shows the cross-polarization metric  $P_i$ . The  $E$  feed of antenna 50 shows at  $\sim 15\sigma$  deviation, causing it to be flagged from further processing.

visibilities). This brings  $P_i$  closer to unity for any antenna  $i$ .

Figure 6.11 shows the application of the metrics described above to raw HERA-47 data in the RTC system. Note that we plotted the modified  $z$ -score and not the raw metric. Traditionally the  $z$ -score is defined as the deviation from the mean divided by the standard deviation, and is a method to detect outliers. However, since our metrics were not necessarily normally-distributed, we use the modified  $z$ -score defined as

$$MZ_i = 0.6745 \frac{|x_i - \tilde{x}|}{MAD}, \quad (6.7)$$

where  $x_i$  is some data point (in our case this was a metric),  $\tilde{x}$  is the median of  $\{x_i\}$ , and MAD is the median absolute deviation. Iglewicz & Hoaglin (2010) recommend that modified  $z$ -scores with an absolute value greater than 3.5 should be flagged as outliers. In the analyses shown in Figure 6.11, we took the cut-off to be 5, to account for greater acceptable variation in our metrics.

The top panel of figure 6.11 shows the modified  $z$ -score for the mean visibility metric as a function of antenna number. Antenna 50E (East-West polarization) was a  $\sim 15\sigma$  outlier, indicating a problem with amplification along the signal chain. Upon further inspection, antenna 50E was shown to exhibit strange behavior, dropping in and out of the signal chain. Further investigation is needed to know the root cause of this misbehavior.

The bottom row of figure 6.11 shows the modified  $z$ -score for the cross polarization metric as a function of antenna number. There were no modified  $z$ -scores outside of the [-5,5] range, indicating that there were no cross polarized antennas. Further inspection of the raw visibility data validated this finding.

### 6.3.2 Flagging on omnical $\chi^2$

We developed a metric that identified days of PAPER-128 observations with poor overall omnical  $\chi^2$  values. Using the median of the  $\chi^2$  values in the EoR band (channels 100–160; 150–180 MHz), over all days of observation, we flagged days that exceeded the average of the median by one standard deviation from the mean. Figure 6.12 shows an example of this flagging method used on the latter half of the first PAPER-128 observing season. Clearly, there were just a few JDs that had exceptionally high  $\chi^2$  values. Our metric captures almost all of these outliers – the possible exceptions being JDs 2456717 and 2456718.

The omnical software also provides  $\chi_a^2$  values for each antenna  $a$  – that is, how much each antenna contributed to the overall non-redundancy of the array. The above sigma-clipping metric was applied to  $\chi_a^2$ , and was able to identify the same bad antennae using the mean amplitude flagging metric described in Equation 6.5.

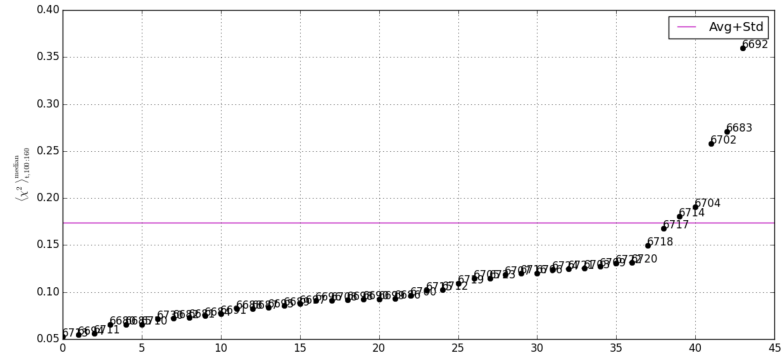


Figure 6.12: Flagging Julian Dates (JDs) based on the median omnical  $\chi^2$  values in the 150–180 MHz band. Shown in pink is the flagging boundary. The JD labels have been abbreviated to drop the ‘245’ prefix that they all share. Clearly, there are just a few JDs that have exceptionally high  $\chi^2$  values.

# Chapter 7

## Polarimetric Calibration

Hypothetically, integrating over long observing seasons should average-down the noise in the EoR window, allowing for the study of the EoR without the risk of foreground contamination. However, the wedge-window paradigm arises due to the chromaticity of the interferometer as well as the signal. Spectral structure can be imparted to interferometric visibilities by the frequency evolution of the antenna beam and by calibration. Spectral structure can also be induced on otherwise-smooth foregrounds via Faraday rotation of polarized foregrounds. In of itself Faraday rotation is not a problem, since HI emission should be largely unpolarized, but errors in calibration and beam deconvolution can leak polarized signal into unpolarized visibilities (e.g. Thompson et al., 2017, ; Chapter 3).

Interferometers with  $N$  antennae that are sensitive to  $N_{\text{pol}}$  polarizations will generate  $N_{\text{pol}}N(N - 1)/2$  visibilities per time-frequency sample, defined as:

$$V_{ij,pq}(\nu, t) = g_{p,i}^*(\nu, t)g_{q,j}(\nu, t)\exp(-2\pi\nu\tau_{pq}) \times \int d\Omega A_{pq}(\nu, \hat{s})S_P(\nu, \hat{s})\exp(i\vec{b}_{ij} \cdot \hat{s}\nu/c) \quad (7.1)$$

where  $p, q \in x, y$  denote instrumental polarizations, i.e. the response to signal projected into the North-South direction or the East-West direction, or whichever direction the dipole arms of the instrument are oriented;  $i, j$  refers to two antennae with baseline

vector  $\vec{b}_{ij}$ ,  $S_P(v, \hat{s})$  is the sky temperature for Stokes parameter  $P$ , and  $A_{pq}(nu, \hat{s})$  is the spatial sensitivity of the instrument to  $S_P$  (projected into the instrumental basis). Outside the integral are three direction-independent variables that must be calibrated: the complex gain of each dipole arm  $g_{p,i}(v, t)$  and the phase between dipole arm  $p$  and  $q$ ,  $\tau_{pq}$ . For  $p = q$ ,  $\tau_{pq} = 0$ .

All the above presents a data processing challenge: these visibilities must be precisely calibrated over long observing seasons to ensure that the cosmological signal is not averaged away by calibration errors and not contaminated by spectral structure. One way of overcoming part of this challenge is to construct large arrays of redundantly-spaced elements. The redundancy of the visibilities of such an interferometer allows the gain terms to be solved-for precisely by least-squares minimization algorithms (Liu et al., 2010). In Section 7.1, I explore the implications of implementing full-polarization redundant calibration on PAPER-128 data. However, redundant calibration is not the only tool radio astronomers posses that can be used to obtain precise calibration solutions. In Section 7.2, I present a basic implementation of full-polarization image-based calibration on data from the PAPER-32 polarized imaging array.

## 7.1 Redundant Calibration

Unpolarized redundant calibration has been pursued by the Donald C. Backer Precision Array for Probing the Epoch of Reionization (PAPER; Parsons et al. (2010)), the Hydrogen Epoch of Reionization Array (HERA; DeBoer et al. (2017)) and part of the Murchison Widefield Array (MWA; Tingay et al. (2013)). For EoR studies this has the advantage of being able to average-down noise in the EoR window once all redundant visibilities are calibrated, for potentially very high signal-to-noise measurements of narrow regions of  $k$ -space. However, it sacrifices  $uv$ -coverage, leading to poor imaging capabilities.

Redundant calibration of low-frequency interferometers has been demonstrated by Zheng et al. (2014) with the MIT EoR experiment, Parsons et al. (2014); Jacobs et al.

(2015); Ali et al. (2015) and Kolopanis et al. (*submitted*) with PAPER and Li et al. (*in review*) with part of the MWA. All of these studies calibrated linearly-polarized instrumental visibilities.

Moore et al. (2017) used the same calibration parameters as Parsons et al. (2014) and Jacobs et al. (2015), but also solved for a single value of  $\tau_{pq}$  for the observing season, since their analysis was for cross-polarized visibilities also. These PAPER studies took linear combinations of instrumental visibilities to form ‘pseudo-Stokes’ visibilities (e.g. Thompson et al. (2017), Moore et al. (2013)). In this Chapter, we use the notation and convention

$$\begin{pmatrix} V_I \\ V_Q \\ V_U \\ V_V \end{pmatrix} = \frac{1}{2} \begin{pmatrix} 1 & 0 & 0 & 1 \\ 1 & 0 & 0 & -1 \\ 0 & 1 & 1 & 0 \\ 0 & -i & i & 0 \end{pmatrix} \begin{pmatrix} V_{xx} \\ V_{xy} \\ V_{yx} \\ V_{yy} \end{pmatrix} \quad (7.2)$$

for these quantities.

As noted above, the spectrally-structured HI emission from the EoR should only be detected in  $V_I$ , but fractions of Faraday-rotated (spectrally structured)  $V_Q$  and  $V_U$  are capable of leaking into  $V_I$  via calibration errors and intrinsic properties of the complex beam. Short of detecting the polarized power spectrum of  $V_Q$  and  $V_U$ , which may be at levels beneath the EoR signal, we require confidence that we are accurately calibrating our data to prevent as much leakage as possible into  $V_I$ .

At these low frequencies and inherently large scales probed by modern instruments, the Stokes V sky appears to be empty. Indeed, Patil et al. (2017) used the spherical power spectra of their Stokes V images as a proxy for the thermal noise power spectrum. In wedge-space, one test of polarimetric calibration is therefore to see how close to thermal noise  $V_V$  is. Kohn et al. (2016) observed a direction-independent bias in  $V_V$ , but that study implemented a Moore et al. (2017)-style polarimetric calibration of  $\tau_{pq}$ , solving for a single value across the array, which could indeed lead to a direction-independent bias (but was more powerful than not calibrating it at all; see their Figure 5).

In Section, we explore different schemes of redundant calibration which include polar-

ization. We present three different calibration schemes, all based around the OMNICAL<sup>1</sup> package (Zheng et al., 2014), and compare their uses and shortcomings. We structure the discussion as follows: in Section 7.1.1 we give a mathematical overview of the least-squares minimization algorithms implemented for the different calibration schemes and show basic simulations of each algorithm in action. We describe the real data used to test the calibration schemes, and the results of those tests, in Sections 7.1.2 and 7.1.3, respectively. We discuss our findings and conclude in Section 7.1.4.

### 7.1.1 Mathematical Overview

In this section we briefly describe the fundamental steps of the redundant calibration scheme implemented in OMNICAL. For a more thorough discussion of the algorithm, see Wieringa (1992), Liu et al. (2010), Zheng et al. (2014) and Dillon et al. (2017).

#### 7.1.1.1 Redundant calibration with OMNICAL

We can express visibilities for baseline separation  $|i - j|$ , polarization  $pq$  as a system of equations, of form

$$V_{ij,pq} = g_{p,i}^* g_{q,j} V_{|i-j|,pq} + n_{ij} \quad (7.3)$$

where we have dropped the frequency and time dependence; this is true for every time-frequency sample. This system is overdetermined for a highly redundant array configuration. We assume that all polarizations have the same noise statistics for noise  $n_{ij}$ . An initial estimate for the least-squares fit can be obtained by solving the linearized equation in logarithmic space (termed *logcal*)

$$\log V_{ij,pq} = \log g_{p,i}^* + \log g_{q,j} + \log V_{|i-j|,pq} \quad (7.4)$$

which can constrain the parameter space, but produces biased results since noise is

---

<sup>1</sup><https://github.com/HERA-Team/omnical>

additive in linear space. Taylor expanding Equation 7.3 around the estimated values (denoted with bars) for each parameter as found by 7.4 grants a system of linearized equations (termed *lncal*)

$$V_{ij,pq} = \bar{g}_{p,i}^* \bar{g}_{q,j} \bar{V}_{|i-j|} + g_{p,i}^* \bar{g}_{q,j} \bar{V}_{|i-j|} + \bar{g}_{p,i}^* g_{q,j} \bar{V}_{|i-j|} + \bar{g} *_{p,i} \bar{g}_{q,j} V_{|i-j|} \quad (7.5)$$

which can be solved iteratively, minimizing the least-squares statistic  $w$

$$w^2 = \sum_{\text{all } i \neq j} \sum_{p,q \in x,y} \frac{|V_{ij,pq} - g_{p,i}^* g_{q,j} V_{|i-j|,pq}|^2}{\sigma_{ij}}. \quad (7.6)$$

### 7.1.1.2 Including polarization in redundant calibration

We test three different calibration schemes for polarization.

- Use OMNICAL separately on the two linearly polarized visibilities  $V_{xx}$  and  $V_{yy}$  to obtain independent estimates for all gain terms, and apply those gains to all four instrumental polarizations of visibilities. We will refer to this scheme as *2pol* calibration.
- Include all four instrumental polarizations in the least-squares statistic. This means that, for example, information on the  $g_{x,i}$  term will come from  $V_{xx}$  and  $V_{xy}$ . This will be referred to as *4pol* calibration.
- Use a scheme in which the cross-polarized visibilities  $V_{xy}$  and  $V_{yx}$  share values of the model visibility  $V_{|i-j|,pq}$ . This means that we are minimizing the value of  $V_{yx} - V_{xy}$  during calibration; effectively minimizing the pseudo-Stokes V visibility. There is validity to assuming the pseudo-Stokes V visibility to be noise-like, as discussed above. We refer to this calibration scheme as *4pol+minV* calibration.

### 7.1.1.3 Degeneracies

One virtue of OMNICAL is that it can calibrate all antennas relative to one another without reference to an explicit sky model. However, this results in known degeneracies in the minimization of  $w^2$  that cannot be resolved with OMNICAL and must be fixed afterwards with absolute calibration of the whole array using external information. The number of degeneracies is equal to the number of zero eigenvalues that arise in the linearized  $w^2$  minimization algorithm. For a single polarization, there are 4 degenerate modes, which can be interpreted physically as overall amplitude, overall phase, phase tilt, and phase tip. Phase tilt and tip can be interpreted as a two-dimensional phase slope across the array. It is clear that these factors do not affect the product  $g_{p,i}^*(\nu, t)g_{q,j}(\nu, t)V_{ij,pq}(\nu, t)$  (and we again refer the reader to Dillon et al. (2017) for a comprehensive description):

- Overall amplitude:  $g_{p,i} \rightarrow Ag_{p,i}$  and  $V_{ij,pq} \rightarrow V_{ij,pq}/A^2$ .
- Overall phase:  $g_{p,i} \rightarrow g_{p,i}e^{i\phi}$
- Two-dimensional phase slope: for a co-planar array, define a phase vector  $\vec{\Upsilon} = (\Upsilon_X, \Upsilon_Y)$  where  $\Upsilon_X, \Upsilon_Y$  refer to Cartesian directions as opposed to polarizations. For an antenna at position  $\vec{v}_i$ , and defining  $\vec{d}_{ij} = \vec{v}_i - \vec{v}_j$ , then  $g_{p,i} \rightarrow g_{p,i}e^{i\vec{\Upsilon} \cdot \vec{v}_i}$  and  $V_{ij,pq} \rightarrow V_{ij,pq}e^{i\vec{\Upsilon} \cdot \vec{d}_{ij}}$ . This is allowed because  $\vec{d}_{ij}$  is the same for all redundant visibilities.

OMNICAL ‘fixes’ the amount that the amplitude degeneracy is able to drift between samples by imposing that the average of the absolute of the gains over the array average to unity. Similar tricks can be played with the other degeneracies to project them into a space that does not adversely effect calibration.

The phenomenon of ‘degeneracy fixing’ in polarized redundant calibration was explored in depth by Dillon et al. (2017). In that work, they showed how the number of degeneracies changes with polarized calibration scheme, focussing on what we refer to as the *2pol* and *4pol* schemes in this work. We briefly review their results here.

In the *2pol* scheme, there are the 8 expected redundancies as expected for two independent calibrations; it is as if there are two co-located arrays for  $xx$  and  $yy$ , each with the four degeneracies listed above. However, in the *4pol* scheme, the number of degeneracies is reduced to 6. Introducing  $V_{xy}$  and  $V_{yx}$  breaks the phase tilt and tip degeneracies per polarization, and leaving a polarization-independent phase tilt and tip. Extending this formalism to the *4pol+minV* scheme<sup>2</sup>, the number of degeneracies is further reduced to 5. By imposing equality between  $V_{xy}$  and  $V_{yx}$ , the ‘overall phase’ degeneracies per polarization are broken and there remains only a single overall phase for the array.

Dillon et al. (2017) emphasized the importance of understanding how fixing degeneracies can effect the amplitude of noise in redundant calibration solutions. They found that although the number of degeneracies decreased in the *4pol* scheme,  $V_{xy}$  and  $V_{yx}$  had low enough signal to noise that their inclusion in calibration greatly increased the noise in the gain solutions. Fixing only the 6 degeneracies of that scheme introduced much greater noise amplitude in the calibration solutions. However, fixing the 8 degeneracies from the *2pol* scheme *while still calibrating* with the *4pol* scheme gave almost identical gain solutions. Learning from this, we fix the 8 degeneracies from the *2pol* scheme throughout the rest of this work, independent of the calibration scheme used.

#### 7.1.1.4 Expectations from simulation

Using the formalism of Nunhokee et al. (2017) and Chapter 3, and the HFSS<sup>3</sup> complex voltage simulations of the PAPER beam described therein, we simulated the polarized response of the instrument to an unpolarized sky. That is, we passed a Stokes I - only sky model (de Oliveira-Costa et al., 2008) over a 30 m East-West baseline – the baseline vector of interest for the PAPER experiment (Parsons et al., 2014; Jacobs et al., 2015; Ali et al., 2015; Moore et al., 2017). This meant that whatever was observed in the pseudo-Stokes Q, U and V visibilities could be interpreted as direction-dependent leakage from

---

<sup>2</sup>As explored in the public HERA Memo #30.

<sup>3</sup><http://www.ansys.com/Products/Electronics/ANSYS-HFSS>

Stokes I (the expected regime for a single night of observations with PAPER; Kohn et al. (2016)). The 2008 Global Sky Model used for the simulation was primarily diffuse in nature, with the ‘A-Team’ of bright low-frequency sources (Fornax A, Pictor A, etc.) also included. The diffuse nature was appropriate for the fringe profile of a 30 m baseline. The output of the simulation is shown in Figure 7.1 with and without the inclusion of an instrumental noise model, with the system noise drawn from Moore et al. (2017).

### 7.1.2 Data Processing

We tested these different calibration schemes on one night (JD 2456680.20 – .65; January 22nd-23rd 2014; 6pm – 6am South African Standard Time; Local Siderial Time 2 – 13.5 hours) of PAPER 128-element observations. The PAPER-128 signal chain and full observation season results will be discussed in forthcoming publications, but we will provide a brief overview here.

PAPER-128 consisted of 128 dual-polarization dipole receivers, 112 of which are arranged in a highly-redundant configuration, and the rest placed as in- and outriggers to the array in order to improve *uv*-coverage; see Figure 7.2. Since all dipole arms were oriented North-South (‘x’) and East-West (‘y’), *xy* and *yx* correlations have very low signal-to-noise compared to *xx* and *yy*.

All visibilities were RFI flagged using PYTHON scripts from the AIPY<sup>4</sup> library. These took the derivative of the frequency axis of all baselines associated with a given antenna and flagged any frequencies with a derivative  $6\sigma$  above the mean, per integration. We took the union of all baseline flags and applied them to the data. The 5 MHz on both band-edges were always flagged. Compression proceeded as described in Appendix A of Parsons et al. (2014), filtering to critical Nyquist sampling rates for the longest (300 m) baseline of 493 kHz along the frequency axis (203 channels) and 42.9 s along the time axis.

After RFI flagging and compression, *xx* and *yy* visibilities were checked for erroneous

---

<sup>4</sup><https://github.com/HERA-Team/aipy>

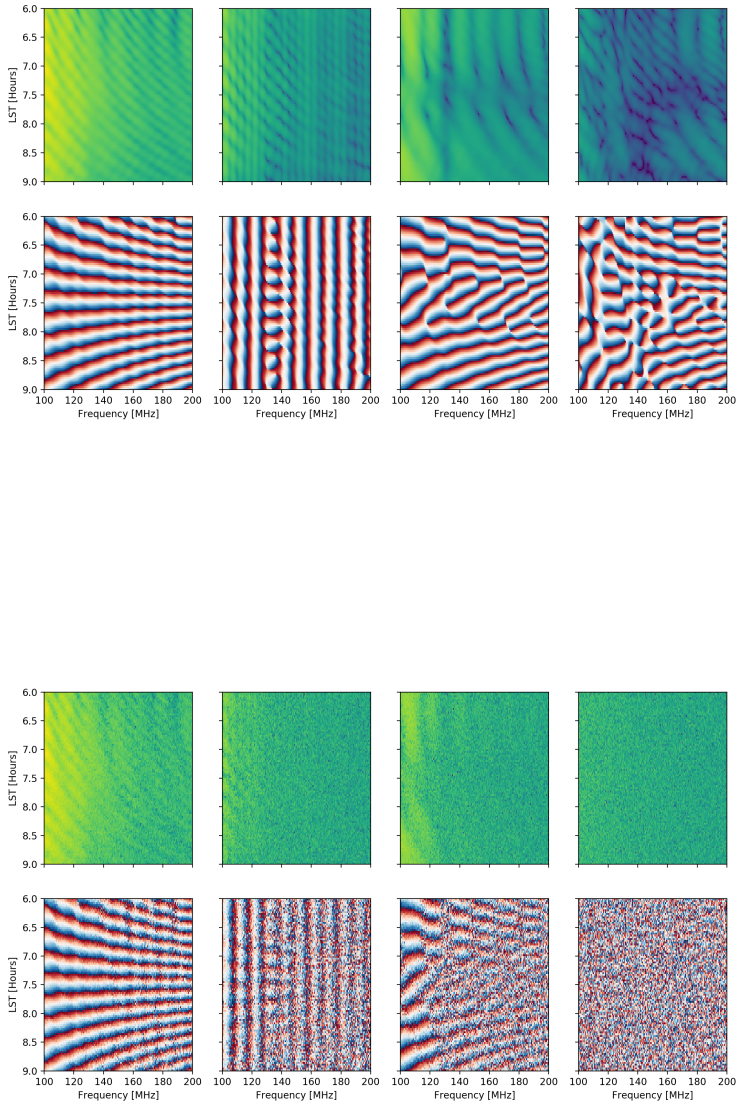


Figure 7.1: Simulations of absolute value (*upper panels*) and phase (*lower panels*) of pseudo-Stokes visibilities (left to right:  $V_I$ ,  $V_Q$ ,  $V_U$  and  $V_V$ ), as measured by a 30m East-West PAPER baseline. The upper group shows a noiseless simulation, and the lower shows the same simulation with the addition of a realistic noise model. Only a Stokes I sky was used – all of the structure seen in  $V_Q$ ,  $V_U$  and  $V_V$  can be attributed to direction-dependent leakage.

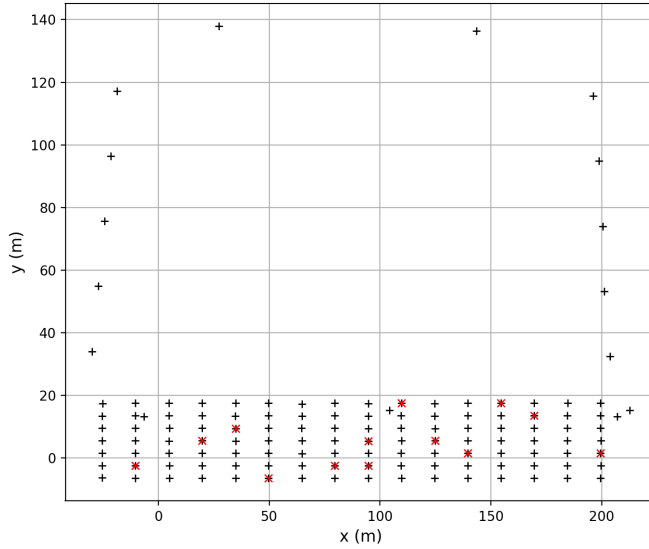


Figure 7.2: Arrangement of the PAPER-128 array. Antennae determined to be malfunctioning are shown with red crosses and were excluded from analysis.

behavior including  $2\sigma$  deviations from the median in number of RFI flags and mean visibility amplitude. Antennae exhibiting these behavior were excluded from further analysis (and are shown with red crosses in Figure 7.2). If an antenna qualified as ‘bad’ in one polarization, it was excluded in all of them. Also note that we could only calibrate the 112 antennae in the redundant grid using OMNICAL.

For the least-squares fit to converge at the *logcal* stage of calibration, visibilities cannot exhibit phase-wraps, since the system of equations solved at this stage are insensitive to additive offsets of  $2\pi$  in their imaginary parts (*lincal* will be able to re-insert these as required; Liu et al. 2010). Therefore we had to flatten the phases on all visibilities prior to any implementation of OMNICAL. We were able to do this redundantly without reference to the sky; taking the ratio of redundant (uncalibrated) visibilities together and averaging over time, defined as:

$$\mathcal{V}(\nu) = \langle V_{ij,pq}(\nu, t) V_{kl,pq}^*(\nu, t) \rangle_t. \quad (7.7)$$

Because this is the ratio of two nominally-redundant visibilities (i.e. baselines  $ij$  and  $kl$  belong to the same redundant group with model visibility  $V_{|i-j|,pq}$ ), and the measurements are not yet calibrated, we can expand Equation 7.7 as

$$\mathcal{V}(\nu) = \langle g_{p,i}^* g_{q,j} g_{p,k} g_{q,l}^* |V_{|i-j|,pq}|^2 \rangle_t. \quad (7.8)$$

Writing the complex gains as  $g_{p,a} = G_{p,a} e^{-i\nu\tau_{p,a}}$  for antenna  $a$ , we can reduce the product of gain-amplitudes and the squared visibility into some frequency-dependent function, and an exponential product of gain phase terms

$$\mathcal{V}(\nu) = K(\nu) \exp(i\nu(\tau_i - \tau_j - \tau_k + \tau_l)). \quad (7.9)$$

A Fourier transform along the frequency axis (which we term a *delay transform*; Parsons et al. 2012b) of  $\mathcal{V}(\nu)$  gave a function that was sharply-peaked at a given delay

$$\tilde{\mathcal{V}}(\tau) = \tilde{K}(\tau) * \delta_D(\nu(\tau_i - \tau_j - \tau_k + \tau_l)). \quad (7.10)$$

We can define a variable as the maximum of the above function:

$$\mathcal{T}_{ijkl}(\tau) = \max |\tilde{\mathcal{V}}(\tau)|, \quad (7.11)$$

which will occur at value

$$\tau = \tau_{\max} = \nu(\tau_i - \tau_j - \tau_k + \tau_l). \quad (7.12)$$

With enough redundant baselines involving antennae  $i, j, k \& l$  this is a linearly-solvable set of equations for each value of  $\tau$ . Multiplying  $V_{ij}$  by  $e^{-2\pi i\nu(\tau_i - \tau_j)}$  by definition flattened the phase across the band. This method was very sensitive to signal-to-noise, so these initial phase estimates were created with  $p = q$ ; that is  $xx$  and  $yy$  visibilities only. The estimates were then applied to all visibilities appropriately. We could then run OMNICAL according to each of the schemes described in Section 7.1.1.2.

### 7.1.3 Results

We ran OMNICAL using the *2pol*, *4pol* and *4pol+minV* schemes, which granted complex gain values for each antenna feed in the redundant grid. In this Section we chose to concentrate our analysis on the 30 m East-West spacings used for PAPER power spectrum studies.

#### 7.1.3.1 Calibration

The complex-gains dataset alone was highly multidimensional. We chose to analyze short time- and frequency- averages for these data. For example, the  $\langle |g_{x,a}^{2\text{pol}}| \rangle_{t,v}$  notation indicates the average of the absolute value of the gain value for antenna  $a$ , polarization ‘x’ in the *2pol* calibration scheme. The average was over 10 minutes (the length of a single MIRIAD file produced by the PAPER correlator) and a 10 MHz band running from 145 to 155 MHz (the center of the PAPER band, generally clear of RFI and used for power spectrum analyses).

Figure 7.3 shows  $\langle \arg(g_a^{2\text{pol}}) \rangle_{t,v}$ , the average phase of the gain calibration for ‘x’ and ‘y’ polarizations. It very clearly shows the phase-slope degeneracy present for both dipole orientations, sloping in opposite directions.

Figure 7.4 shows the differences in ‘x’ gain solutions between calibration schemes. The difference between *4pol* and *4pol+minV* was consistently smaller than the difference of either of these with the *2pol* scheme.

As noted in Section 7.1.1.3, OMNICAL tried to fix the average gain amplitude over the array to unity to avoid drifts in the amplitude degeneracy from sample to sample, so we were able compare amplitude calibrations in terms of percentage deviation. The average difference in gain amplitude per antenna between *2pol* and *4pol* was 3.5%, between *2pol* and *4pol+minV* was 2.9%, and was 0.7% between *4pol* and *4pol+minV*. The  $\sim 30$  degree spread in the differenced phases between the *2pol* scheme and the other two was likely due to different realizations of phase degeneracies between these calibration schemes.

Figure 7.5 shows the sum of  $w^2$  values (see Equation 7.6) over all antennas in the

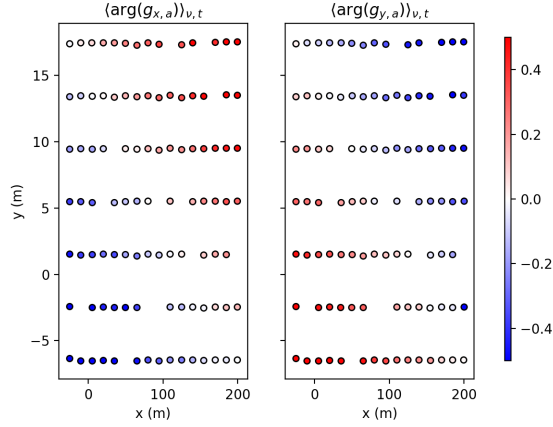


Figure 7.3: The phase of the complex gain value for the *4pol* calibration scheme is shown on the color axis (radians) for the redundant grid. The phase of the ‘x’ gains is shown on the left, and the ‘y’ gains on the right. The phase-slope degeneracy is clear in both panels, as is the fact that the slope is in opposite directions for the two dipole orientations.

array for each feed polarization in each of the three calibration schemes. The color scale is logarithmic. Clearly, the *2pol* scheme achieves a much greater level of redundancy in each feed polarization throughout the band. Towards the end of the night, the Galaxy was in the far side-lobes of the PAPER beam and introduces higher sky temperatures, which accounted for the trend in all calibration schemes performing worse towards the end of the night. However, the reason for rapid transitions in  $w^2$  at Local Sidereal Time  $\sim 10.5$  in the *4pol* and *4pol+minV* schemes is not well understood. In general,  $w^2$  was an order of magnitude higher for the *4pol* and *4pol+minV* schemes.

#### 7.1.3.2 Pseudo-Stokes Visibilities

Applying the complex gains to the visibilities, we constructed pseudo-Stokes visibilities. These data are shown in Figure 7.6. Figure 7.7 shows the delay-transformed pseudo-Stokes visibilities. The stripe of power across the frequency axis within the first 100 integrations was a thermal effect due to the sun not yet being fully below the horizon.

The upper panels in Figure 7.6 – the absolute-valued visibilities – show that Stokes

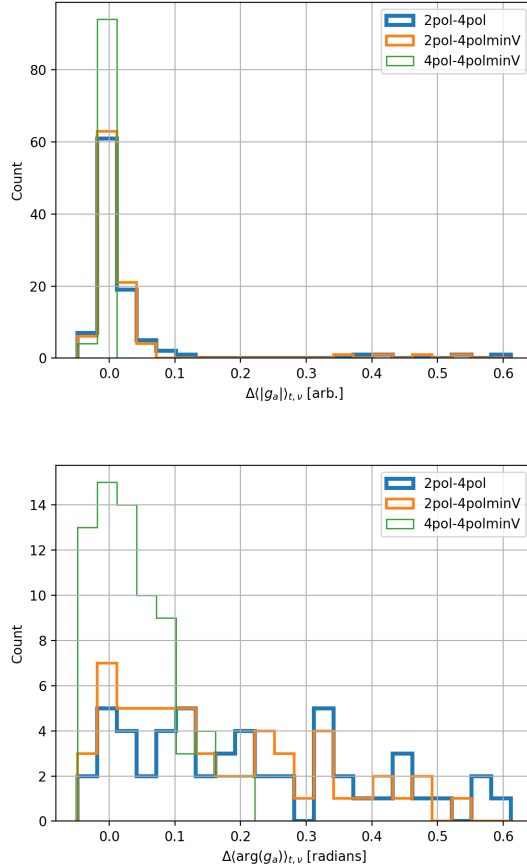


Figure 7.4: Histograms of differences in the ‘x’ gain calibrations per antenna between calibration schemes. Above: difference in absolute value. Below: difference in phase. For most antennae, absolute value of the gain does not change by large amounts between calibration schemes; most of the change takes place in the phase. The difference between *4pol* and *4pol+minV* is consistently smaller than the difference of either of these with the *2pol* scheme. This is likely a sign of different realizations of phase degeneracies between calibration schemes.

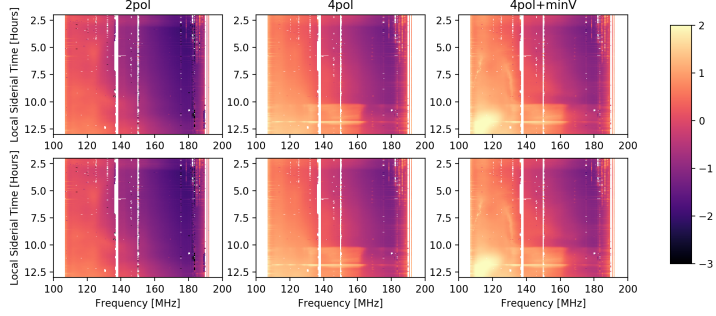


Figure 7.5:  $w^2$  values, summed across the array, for the  $x$  (above) and  $y$  (below) feeds in different calibration schemes. From left to right: *2pol*, *4pol* and *4pol+minV*. The color axis is logarithmic, in arbitrary data units. The white gaps are due to RFI flagging.

I power was dominant given any calibration scheme used. This was expected, since the linear polarizations had much higher signal-to-noise than the cross polarizations that form  $V_U$  and  $V_V$ . We saw that the amplitude of pseudo-Stokes Q was reduced across the band in the *4pol* and *4pol+minV* schemes. This was also expected, given that these calibration schemes allowed information in  $xx$ -polarized visibilities to influence the calibration of  $yy$ -polarized ones, and vice-versa. In the regime of a single night's observation, we did not expect to observe substantial power from the Stokes Q sky (Kohn et al., 2016; Lenc et al., 2016; Moore et al., 2017). Although we set no specification on the Stokes Q sky during calibration, we observe our gain solutions tending towards lower Stokes Q power during polarized redundant calibration.

A similar but less-substantial difference was seen in the pseudo-Stokes U visibility amplitudes, but an interesting interplay between pseudo-Stokes U and V was more clearly seen in the delay-transformed visibilities in Figure 7.7. First, we must observe that the *4pol+minV* calibration scheme worked as expected, reducing the amplitude of pseudo-Stokes V across most of the band. In Figure 7.7, we show that the difference between the foreground signal for pseudo-Stokes U and V in the *4pol* case, compared to the *4pol+minV* case, was the increase in U signal and the decrease of V. This effect was observed in Kohn et al. (2016) when minimizing pseudo-Stokes V using an array-wide

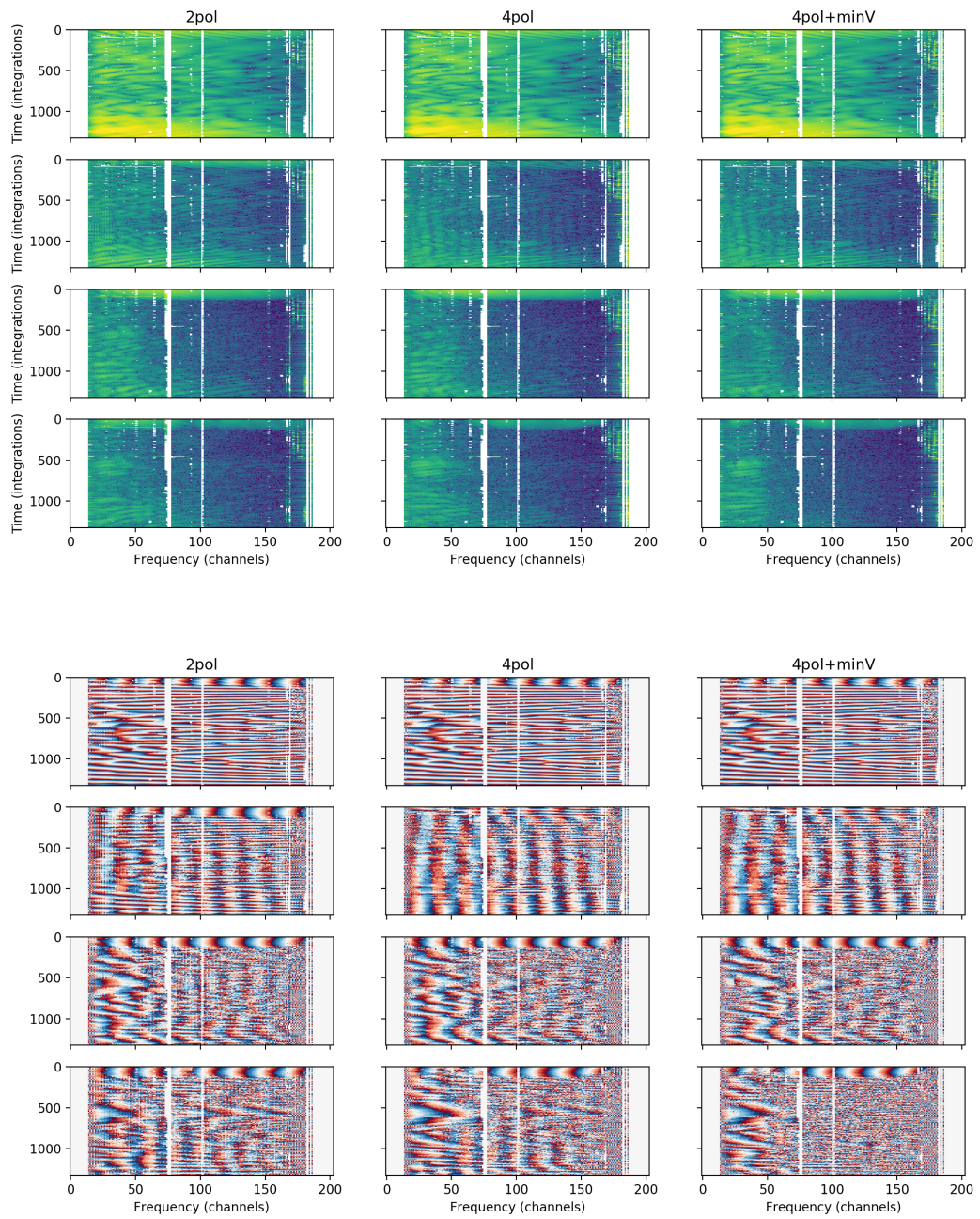


Figure 7.6: Pseudo-Stokes visibility amplitudes (*top*) and phases (*bottom*). Amplitudes are plotted on a logarithmic color scale that spans 3 orders of magnitude (without absolute calibration, this scale is in arbitrary units). Phases are on a linear scale of  $-\pi$  to  $\pi$ . The three columns correspond to the three different calibration schemes. Rows are from top to bottom:  $V_I$ ,  $V_Q$ ,  $V_U$ , and  $V_V$ .

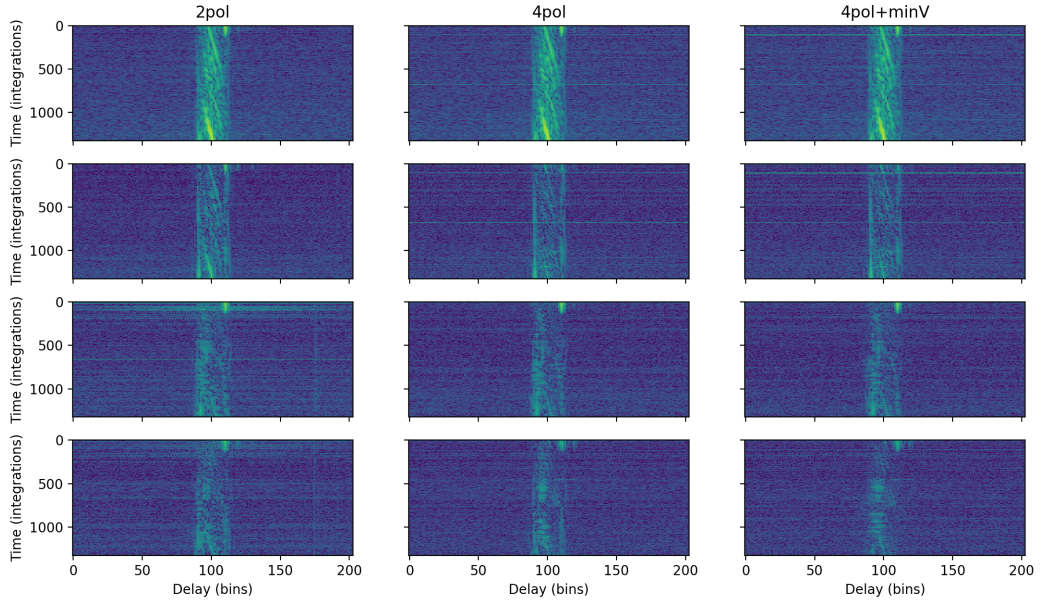


Figure 7.7: Delay-transformed pseudo-Stokes visibilities. Plotted on a logarithmic color scale that spans 4 orders of magnitude (without absolute calibration, this scale is in arbitrary units). The three columns correspond to the three different calibration schemes. Rows are from top to bottom:  $V_I$ ,  $V_Q$ ,  $V_U$ , and  $V_V$ .

constant, as opposed to the per-sample basis implemented in this work. It is mathematically consistent with partially accounting for uncalibrated  $D$ -terms on each feed.

We also note that the lowest frequencies in the band (below channel 70) are consistently poorly behaved. This is a property seen in many PAPER measurements (e.g. Jacobs et al., 2015; Moore et al., 2017) and is due to brighter foregrounds at low-frequencies, a larger solid angle of the beam, and higher receiver temperatures at lower frequencies.

A comparison of the simulations presented in Figure 7.1 is best made using the phase panels of Figure 7.6. Comparison of phase structure in frequency and time showed that the  $4pol+minV$  scheme gave the best match with simulation. The  $2pol$  scheme did not allow pseudo-Stokes Q visibilities to be constructed in a way that replicates the constant-in-time striping seen in the simulations. Instead, we see an imprint of the fringing as seen in

pseudo-Stokes I. This was most likely direction-independent leakage from this parameter. The *4pol* and *4pol+minV* schemes contained most of this fringing to the pseudo-Stokes I visibilities. The *4pol+minV* scheme achieves a noise-like pseudo-Stokes V, whereas the *4pol* scheme shows V at a higher signal-to-noise than expected from PAPER system temperature measurements.

### 7.1.4 Discussion & Conclusions

The OMNICAL software package was optimized to calculate diagonal gains as efficiently as possible (Zheng et al., 2014). Of course, this meant that it is impossible to fully address the *D*-terms in the instrumental Jones matrix (e.g. Thompson et al., 2017) within the OMNICAL framework. This incomplete modelling of the instrument will result in biased gain solutions (e.g. Barry et al., 2016; Dillon et al., 2017).

Dillon et al. (2017) showed that the relative gain error incurred through redundantly calibrating in the presence of 1% *D*-terms was  $\sim 0.3\%$  in the *2pol* scheme, and systematically higher in the *4pol* scheme by an additional  $\sim 0.2\%$ . Additional work is required to understand how the *4pol+minV* calibration scheme interacts with *D*-terms.

In this Section we have demonstrated the capacity for polarized redundant calibration of radio interferometric data from the PAPER-128 array. The three redundant calibration schemes we investigate have different strengths. Neglecting the polarized component of the measurements in the *2pol* scheme grants lower values of  $w^2$  than the other schemes. Imposing that the Stokes V sky be empty in the *4pol+minV* gives the best agreement with simulation. Conservatively, this points to using the *2pol* scheme to give the most precise gain calibrations. However, given that *2pol* matches full-polarization simulations the least well, the calibrations it produces may be inaccurate, even if they are precise.

Unlike PAPER, HERA is designed to be both highly-redundant and a capable imaging array, since outrigger antennae, although physically separated from the redundant core, are arranged on their own redundant sub-grid, and the redundant core itself is fragmented into three redundantly-calibrate-able sub-grids (see Dillon & Parsons 2016 for

full details). The utility of redundant and imaging calibration routines will allow for more thorough tests of the nature of the polarized sky at low frequencies.

## 7.2 Imaging Calibration

The PAPER-32 imaging array sampled a large region of the *uv*-plane at relatively low signal-to-noise (see Chapters 4, 9 and Kohn et al. (2016)). The extreme wide field of view of the PAPER feeds provided an interesting opportunity to test polarized imaging calibration. In this Section we provide an initial exploration of PAPER-32 data using the CASA software package (McMullin et al., 2007).

### 7.2.1 Converting historical PAPER data into Measurement Sets

As described in Chapter 4, PAPER-32 was arranged in an imaging configuration for three nights in September 2011. In order to interact with these data using modern software packages, including the conversion into “Measurement Set” format used by CASA, several changes to the MIRIAD files had to be implemented.

1. After the first night of integration, it was discovered that antenna number 24 was malfunctioning, and it was replaced with antenna number 63. This presents complications for conversion into Measurement Sets, since this format requires a constantly-incremented antenna axis – no numbers may be “skipped”. A simple work-around is to relabel the data from antenna 63 to that of antenna 24.
2. The PAPER-32 imaging configuration was really a subset of the PAPER-64 imaging configuration. The existing correlator had only 64 inputs, so the 64-element imaging configuration could be run in single-polarization mode, or half of it could be used in full-polarization mode. However, within the MIRIAD files, 64 antennas are listed, with only half of them containing data. These must be specifically down-selected upon.

3. PAPER correlators incorrectly labelled the  $uv$  coordinates of all baselines. This was by design, since PAPER build outs were purposefully reconfigurable and therefore the antenna positions were not built-in to hardware. However, correct  $uv$  information is essential for imaging algorithms. These coordinates must be placed inside the MIRIAD file, instead of supplied externally.
4. CASA cannot convert MIRIAD files to Measurement Sets on its own, but it can do so for UVFITS files. Seamless MIRIAD to UVFITS conversions are implemented by the `pyuvdata` Python package (Hazelton et al., 2017). During conversion, antenna diameters and physical antenna positions must be supplied as metadata.
5. CASA’s `importfits` function can then be used for the UVFITS to Measurement Set conversion.

After a successful conversion, an additional step needs to take place within the CASA Measurement Set. The MIRIAD files could have their antenna indices out of order, such that a baseline could be referenced as  $i, j$  where  $i > j$ . This can be easily corrected within the CASA console.

### 7.2.2 Imaging PAPER-32 data with CASA

To calibrate the complex gains, we had to provide CASA with a *model image*, from which it will create model visibilities by convolving with a model beam (assumed to be Gaussian, with Full-Width Half Max based on the antenna diameter) and sampling the  $uv$ -plane according to the antenna positions provided. Images of the primary beam model and point spread function of the PAPER-32 array are shown in Figure 7.8. The model visibilities were compared to the observed ones, and CASA’s internal fitting algorithms determined complex gains to bring the ratio close to unity.

The times observed by the PAPER-32 imaging array contained the transits of Pictor A and Fornax A. Pictor A is one of the brightest sources in the low frequency sky, is an unresolved point source, and has a simple spectrum (Jacobs et al., 2013):

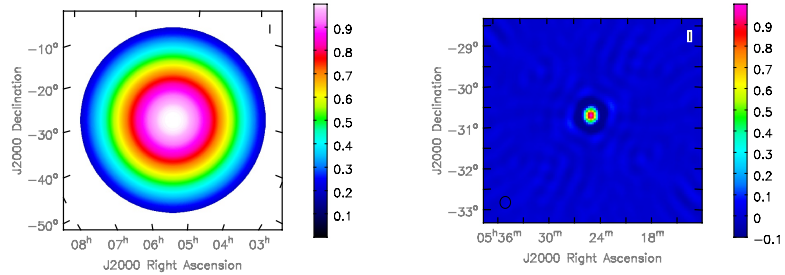


Figure 7.8: The beam model and point spread function of the PAPER-32 array, calculated by CASA. In reality, the beam is far less symmetric (e.g. Parsons et al., 2010). The PSF is likely more accurate. Note the difference in axis scales between the two panels.

$$S_{\text{PicA}}(\nu) = 382 \pm 5.4 \text{Jy} \times (\nu/150\text{MHz})^{-0.76 \pm 0.01}, \quad (7.13)$$

making it an ideal flux-calibrator. While it is highly polarized at optical wavelengths ( $\sim 50\%$  Thomson et al., 1995), it has a low polarization fraction at radio frequencies ( $< 5\%$ ; Perley et al. (1997); Huffenberger et al. (2015)). Little-to-no expected polarization is useful for obtaining diagonal gains, but a polarized point source is more useful for precisely calculating the off-diagonal  $D$ -terms (see, for example, Chapter 3 or Thompson et al. (2017)). There is a dearth of low-frequency polarized point sources in the low frequency sky (Bernardi et al., 2013; Asad et al., 2016; Lenc et al., 2016), and only one that is bright enough to be detected by PAPER-32 – PMN J0351-2744 – and this we were not able to detect.

To increase the precision of our calibration model, we included a model of Fornax A as well as Pictor A. Fornax A is a bright, resolved radio galaxy which we modelled using three spherical components for its East lobe, West lobe and central core according to MWA observations at 154 MHz (McKinley et al., 2015):

$$S_{\text{East}}(\nu) = 260 \text{Jy} \times (\nu/154\text{MHz})^{-0.77}, \quad (7.14)$$

$$S_{\text{West}}(\nu) = 480 \text{Jy} \times (\nu/154\text{MHz})^{-0.77}, \quad (7.15)$$

$$S_{\text{Core}}(\nu) = 12 \text{Jy} \times (\nu/154\text{MHz})^{-1.00}. \quad (7.16)$$

$$(7.17)$$

Fornax A has been found to have a low polarized fraction at higher frequencies (20 GHz López-Caniego et al., 2009), and a  $\sim 20\%$  polarized fraction at 1.51 GHz (Fomalont et al., 1989). Bernardi et al. (2013) found no evidence for polarized emission at 151 MHz using the MWA-32, which may have been partially due to beam depolarization (an effect that would only increase with PAPER-32).

Using this two-source (but with four points) sky model, we used the CASA `gaintab` and `bandpass` routines to calibrate a 10 minute snapshot of the transit of Pictor A. We were able to specify a “Stokes Vector” for each source, and we used  $S = (1, 0, 0, 0)$ : that is, all components were strictly unpolarized. Applying the calibration solutions and gridding to the  $uv$ -plane and CLEANing granted the pseudo-Stokes images shown in Figure 7.9. As expected, Pictor A dominated the sky in pseudo-Stokes I. However, an excess at its position in the pseudo-Stokes Q image suggested a mis-calibration in the diagonal gains at the  $\sim 10\%$  level. No sources are visible above the noise in pseudo-Stokes U and V. However, these parameters (as well as pseudo-Stokes Q) exhibited a high fringe-rate oscillation in the North-West to South-East direction, which suggested that a long baseline of that orientation was poorly calibrated, or the antenna was malfunctioning. A similar effect was seen with a low fringe-rate from North-East to South-West, suggesting a problem on a short baseline with that orientation. Indeed, Kohn et al. (2016) found three

malfunctioning antennas during their study using the PAPER-32 imaging array, which match the orientation and lengths indicated by the fringing (see Chapter 9, Figure 9.1). Removing those antennas resulted in cleaner images with lower noise-floors, as shown in Figure 7.10. New fringing is seen at various angles, the source of which would be more difficult to identify. Excesses at the position of Pictor A in pseudo-Stokes U and V are likely the result of uncalibrated D-terms, which will be addressed in Section 7.2.3. The morphology of point sources in pseudo-Stokes I matched the PSF shown in Figure 7.8, showing that the CLEAN algorithm converged when during imaging.

We were able to test the stability of the instrument by applying the calibration solutions derived from the Pictor A transit to a completely different field. The imaging results of such a test at  $LST \approx 0.5$  hours are shown in Figure 7.11. The pseudo-Stokes I image showed a point-source dominated field, as expected for this LST, and pseudo-Stokes Q, U and V were dominated by noise. These results were proof of instrument stability in time at the  $\sim 6$  hour level.

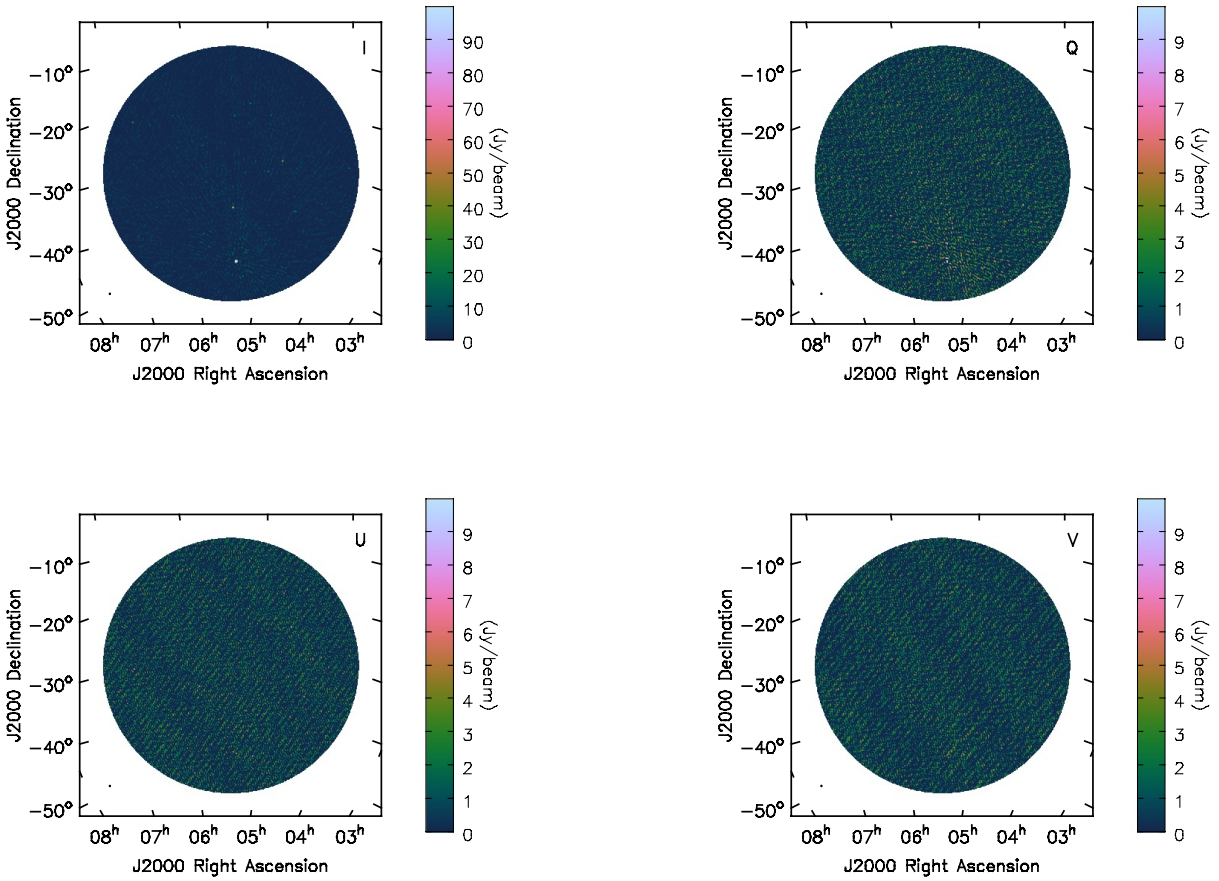


Figure 7.9: Full-polarization imaging results from a four-component, Stokes I-only sky model. Images are multi-frequency syntheses from 110 to 180 MHz. Pictor A, the brightest unresolved source in the Southern Sky at our frequencies, is in transit and dominates the sky in pseudo-Stokes I. An excess in pseudo-Stokes Q at the  $\sim 10\%$  level indicates inaccuracies in the gain calibration. Pseudo-Stokes U and V are noise-like, save for a fringe that rises above the noise – indicating a poor calibration of a single baseline of that orientation.

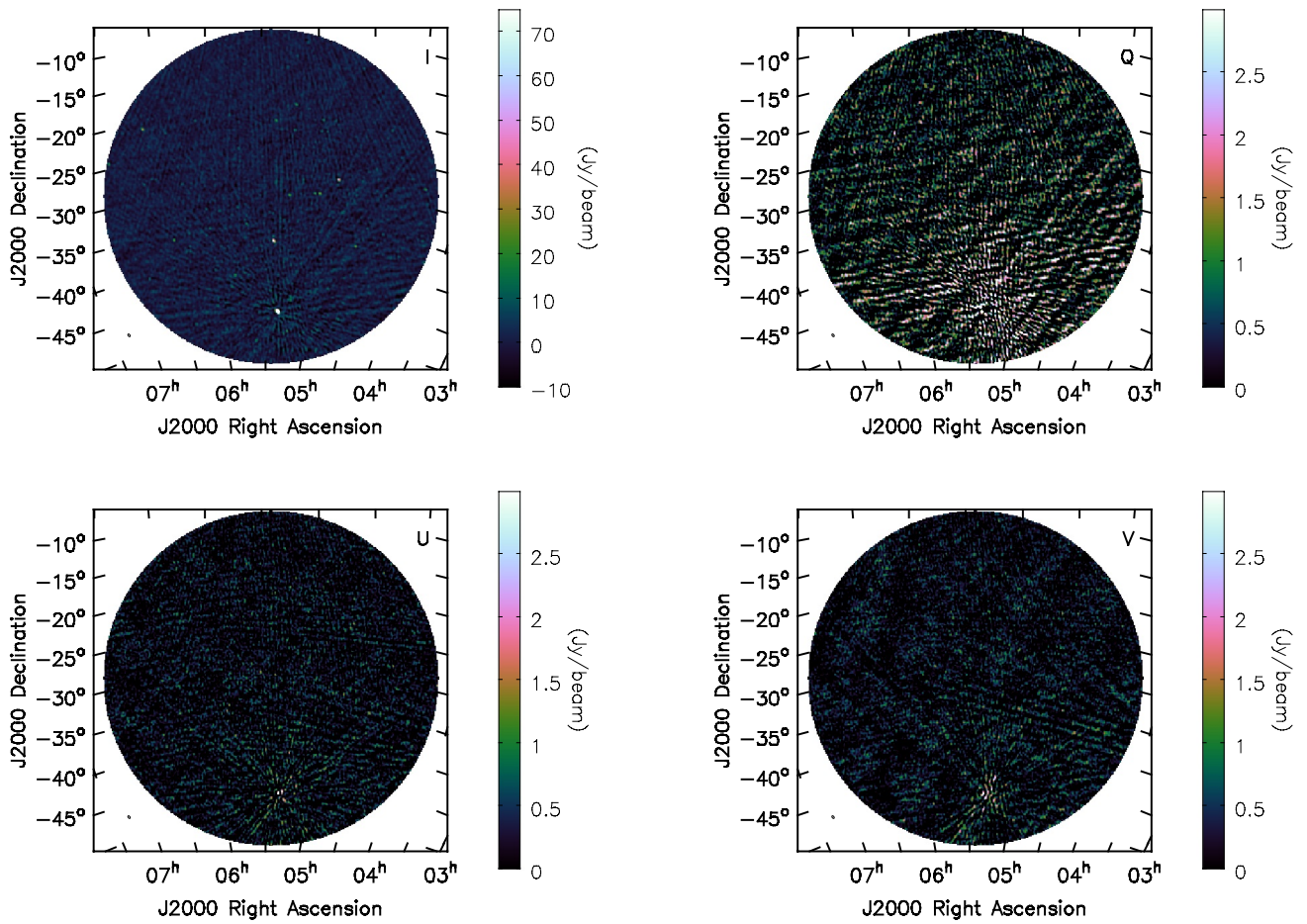


Figure 7.10: The same field as shown in Figure 7.9, but with the removal of malfunctioning antennas identified by Kohn et al. (2016). The noise level drops and much of the fringing in pseudo-Stokes Q, U and V disappears (note the change in color scales and zoom level).

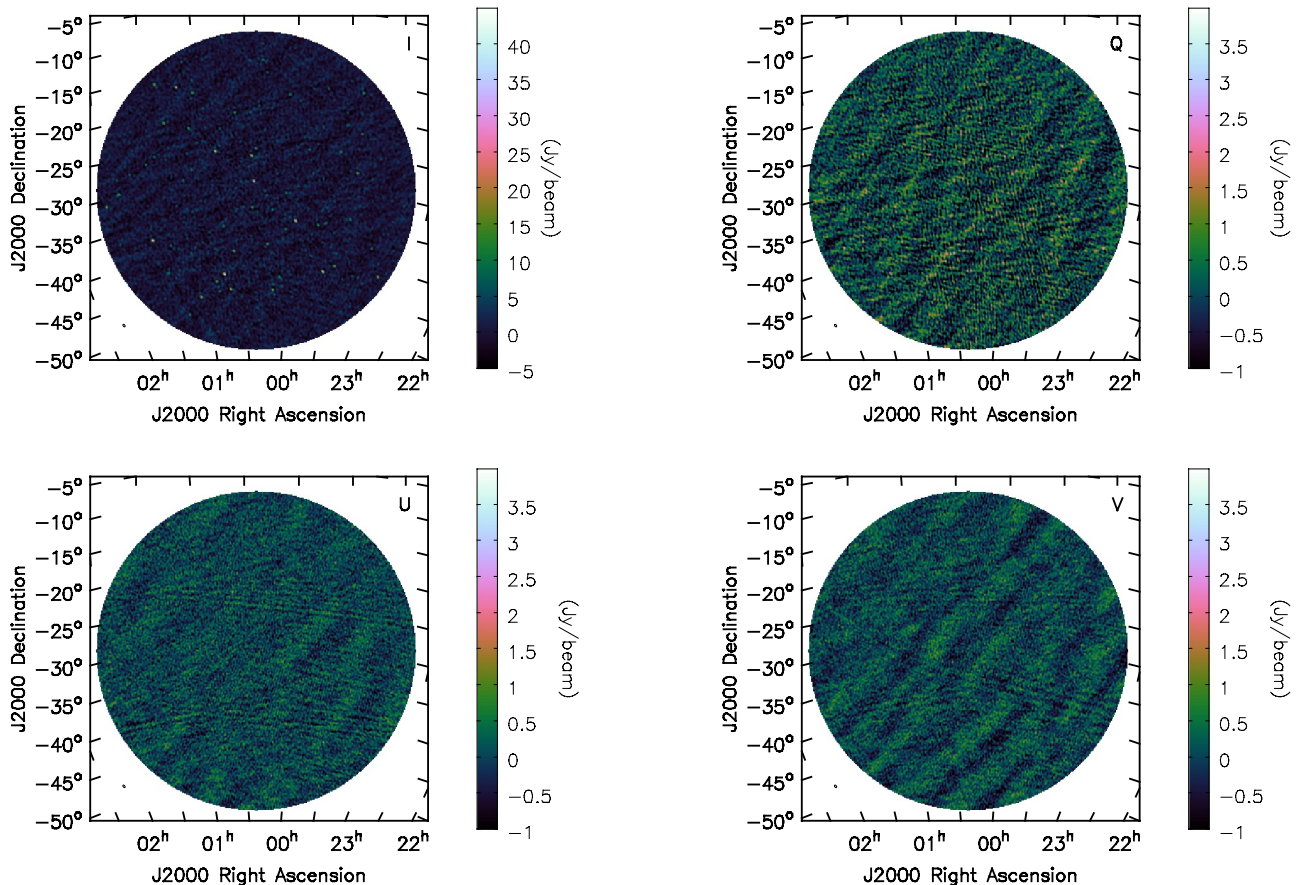


Figure 7.11: Imaging results from a file calibrated with gain values derived from the Pictor A transit, which occurred  $\sim$ 6 hours after these data were acquired. The realistic images suggest that the instrument is stable on such time scales.

### 7.2.3 D-term calibration

Calibration of the off-diagonal terms of the instrumental Jones matrix can be partially calculated using a Stokes I-only sky model. If there were a visible source of known polarization fraction, an absolute phasing could be derived based on its polarization angle. Using the source model described in the section above, we were able to calculate the magnitude of the off-diagonal,  $D$ -terms.

CASA supplies routines for linear-basis feeds that iteratively solve for ‘x’ and ‘y’ gains by, in our case, maximizing pseudo-Stokes I and minimizing pseudo-Stokes Q (if the polarization fraction was known, it would regress on that fraction for pseudo-Stokes Q). The `polcal` routine uses a built-in regressor to find the best fit for the  $D$ -terms, given previous calibrations. That is, one must have supplied an initial gain calibration and a guess of the parallactic angle of the polarized source.

Using `polcal` on the Pictor A field described in the previous section granted  $D$ -term estimates of  $\sim 5\%$ ; comparable to other low-frequency instruments (MWA-32 was found to have  $\sim 2\%$   $D$ -terms [G. Bernardi, private communication]).

Correcting for these granted identical pseudo-Stokes I and Q images and lower-amplitude pseudo-Stokes U and V – as expected for a regime where pseudo-Stokes I leakage dominates over actual polarized power. The improved U and V maps are shown in Figure 7.12.

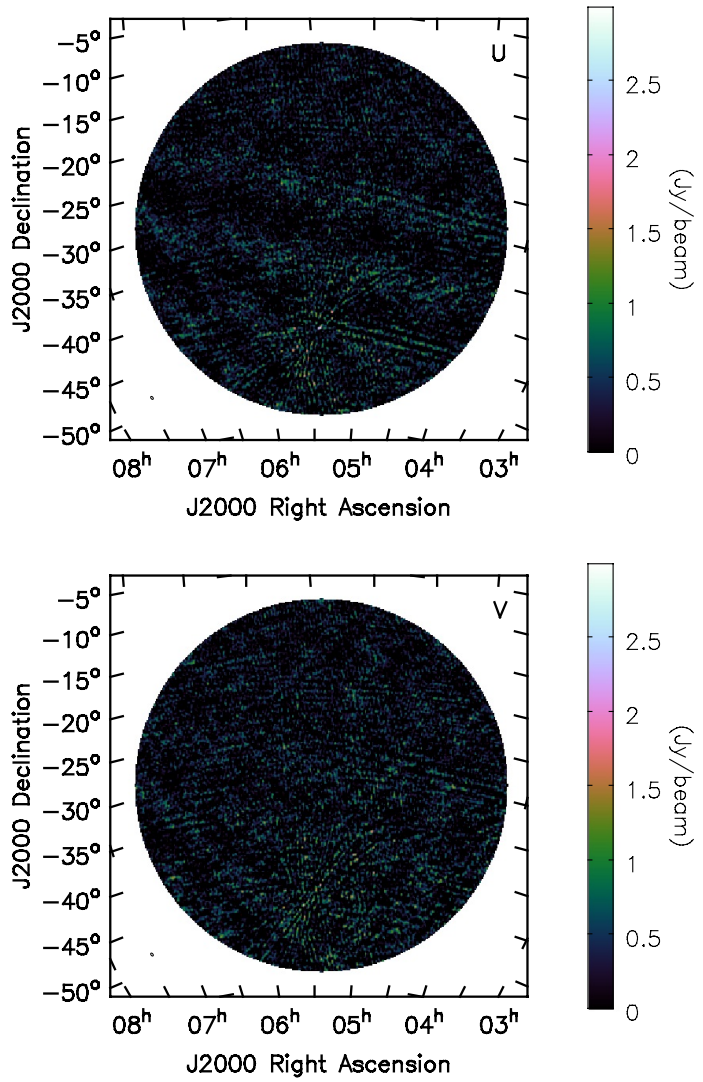


Figure 7.12: The same field as shown in Figure 7.10, but for pseudo Stokes U and V only, with  $D$ -terms partially calibrated. Comparing to Figure 7.10, the amplitude at the position of Pictor A has decreased. Pseudo-Stokes I and Q maps are not shown, since they are qualitatively identical to the images in Figure 7.10 – as expected for a regime in which pseudo-Stokes I leakage dominates over actual polarized power.

# Chapter 8

## The Ionosphere

The ionosphere is a section of Earth’s atmosphere composed of several layers, between 60 and 1000 km in altitude. It overlaps the Troposphere, Stratosphere, Mesosphere, Thermosphere and Exosphere. The ionosphere is an ionized plasma, composed of ions from molecules in the atmospheric layers it overlaps that are ionized by solar radiation. The ionization state of the ionosphere can be quantified by the Total Electron Content (TEC) – an integral of electron count in a given direction – among other metrics.

Spatiotemporal variations of the TEC are tied to solar activity, and therefore largely both diurnal and seasonal. More ionization, and therefore a larger TEC, is to be expected in the day time and closer to the summer solstice. The Solar Cycle also influences TEC, with more sunspots proportional with a higher TEC; at solar maximum, this effect dominates the seasonal variation (Sotomayor-Beltran et al., 2013). Ionospheric variations are typically described as Kolmogorov turbulence (i.e. small scale motions are isotropic in their direction and scale with wavenumber; Zolesi & Cander 2014), however, LOFAR observations report deviations from isotropy in their observations (Intema et al., 2009; Mevius et al., 2016). Regions of the ionosphere that can be assumed to be constant in density and shape at a given time are referred to as “isoplanatic patches”. At 74 MHz, these patches are observed to be  $1^\circ - 2^\circ$  in radius (Cotton & Condon, 2002).

The ionosphere is composed of three main layers: D, E and F, which vary according to

Table 8.1. Ionospheric Layers

Layer	Time	Altitude km	Components	Electron Density $e^- m^{-3}$
D	Day	60–90	$\text{NO}^+$ , $\text{N}_2$ , $\text{Ar}$ , $\text{O}_2^-$	$10^8 - 10^9$
E	Day/Night	90–150	$\text{NO}^+$ , $\text{O}_2^+$ , $\text{O}^+$ , $\text{N}_2^+$	$10^{11}$
$F_1$	Day	140–600	$\text{NO}^+$ , $\text{O}_2^+$ , $\text{O}^+$ , $\text{N}^+$	$10^{11}$
$F_2$	Day/Night	220–800	$\text{O}^+$ , $\text{H}^+$ , $\text{He}^+$	$10^{10} - 10^{13}$

the day-night cycle. These are summarized in Section 8 (which summarizes Chapter 2 of Zolesi & Cander 2014). At night, there are not enough high-energy electrons to penetrate to lower altitudes, causing the D layer to recombine. The E layer increases in altitude at night due to a similar effect. The E and F layers persist at all times, but during daylight the F layer is divided into two sub-layers,  $F_1$  and  $F_2$ .

The diurnal nature of the ionosphere is important to radio propagation. During the day, the D layer reflects radio transmissions much closer to the Earth than during the night, when the E and F layers reflect. This leads to longer-range transmissions being possible after sunset<sup>1</sup>.

The relevance of the ionosphere to this work is its coupling with Earth’s magnetic field. Recall that, as mentioned in previous chapters, a linearly polarized electromagnetic wave, propagating through an ionized plasma which has an incident magnetic field, will experience Faraday Rotation of its original polarization angle  $\chi$ :

$$\chi_{\text{obs}} = \chi + \phi \lambda^2 \quad (8.1)$$

where  $\lambda$  is the wavelength, and

$$\phi(\hat{s}) \approx 0.81 \int_{\text{source}}^{\text{obs}} n_e(\hat{s}) \vec{B}(\hat{s}) \cdot d\vec{s} \quad (8.2)$$

---

<sup>1</sup>This effect was first observed by E. V. Appleton (Appleton, 1946), confirming the ionosphere’s existence, for which he was awarded the 1947 Nobel Prize in Physics.

where the source of the electromagnetic wave is in direction  $\hat{s}$  on the sphere,  $n_e$  is the electron density scalar field and  $\vec{B}$  is the magnetic vector field. The Rotation Measure (RM)  $\phi$  is the integral of the product along the line of sight, and has units of rad m<sup>-2</sup>. Since the ionosphere is capable of imparting an additional RM to polarized radio waves, inducing spectral structure to interferometric visibilities, understanding it is crucial to quantifying the effect of polarization on EoR measurements.

In this chapter, I review historical measurements of the ionospheric TEC and RM distributions in Section 8.1 and modern observations in Section 8.2. In Section 8.3 I present our work on the role of the ionosphere in PAPER and HERA measurements, and software we developed to quantify those effects.

## 8.1 Historical measurements of TEC and RMs

The existence and layered nature of the ionosphere was confirmed between the 1920s and the 1940s. Measurements of the TEC and RM distributions came later, once radio-communications satellites were put in orbit, and are closely tied to the Global Positioning System (GPS) launched in the late 1970s (called the NAVSTAR system). NAVSTAR GPS satellites transmit at two narrow frequency bands, centered about 1.2276 GHz ('L<sub>2</sub>') and 1.57542 GHz ('L<sub>1</sub>'). Encoded in these transmissions are the local clock times per satellite (precisely calibrated with one another and with ground clocks) and their positions. With four satellites in view of a receiver, one is capable of computing their three-dimensional position and their local clock relative deviation from the satellite clock time.

MacDoran & Spitzmesser (1989) showed that one could use a frequency-dependent time delay induced by the ionospheric plasma (Klobuchar, 1983; Brunner & Welsch, 1993):

$$\Delta t_{\text{iono}} = \frac{40.3}{cv^2} \text{TEC} \quad (8.3)$$

to calculate an estimate of the TEC in the direction of a GPS satellite. Their approach

has been continuously refined. Using an estimate of the polarization angle of the emitted L<sub>1,2</sub> transmissions, Titheridge (1972) and Royden et al. (1984) presented measurements of TEC by measuring the Faraday Rotation induced and worked towards an estimate of the TEC based on the RM. Lanyi & Roth (1988) showed that the more accurate method was calculation of the TEC using  $\Delta t_{\text{iono}}$  from Equation 8.3. Mannucci et al. (1998) introduced the Ionosphere Map Exchange Format (IONEX): a method and file format for storing TEC measurements using GPS beacons across the globe, allowing the first global TEC maps to be calculated. IONEX files contain global TEC measurements with a 2 hour cadence and generally 5° by 2.5° resolution in longitude and latitude respectively. They neglect the layered nature the ionosphere, modelling it as a thin sheet. Iijima et al. (1999) provided a server that automatically pushed IONEX files to the World Wide Web as soon as they could be constructed. Komjathy et al. (2005) presented the first measurements with over 1000 GPS stations. Recently, Erdogan et al. (2016) presented a method for time-series forward modelling of the TEC distribution using IONEX files.

Meanwhile, many generations of the International Geomagnetic Reference Field (IGRF Finlay et al., 2010) have continually improved the model of the Earth's magnetic field. This model is composed by spatial interpolation of magnetic field measurements (in up to 13th-order spherical harmonic coefficients) reported by institutions around the world.

Combining these two measurements – IONEX and IGRF data – can provide a map of RM distribution above any given position on Earth to moderate precision (better in the Northern Hemisphere than the Southern one, based on the number of GPS beacons in each). Afraimovich et al. (2008) offered the first such software implementation, with the objective of using it to track Solar Activity<sup>2</sup>. Sotomayor-Beltran et al. (2013) introduced the `ionFR` package, which calculated ionospheric RMs towards a given position on the sky. We generalized their approach for the wide-field measurements in our `radionopy` software package, which we present in Section 8.3.

---

<sup>2</sup>Erickson et al. (2001) were the first to present software capable of calculating ionospheric RMs using the IGRF, but they used local GPS beacons instead of IONEX files

## 8.2 Low frequency observations: discoveries and challenges

Low frequency interferometric observations are effected in two main ways by ionospheric turbulence: scintillation in Stokes I observations, and Faraday Rotation in Stokes Q and U observations.

TEC variations introduce a variable index of refraction across a field of view. Stokes I signal from a point source will scintillate, change position, by an amount (e.g. Thompson et al., 2017):

$$\Delta\theta = -\frac{1}{8\pi^2} \frac{e^2}{\varepsilon_0 m_e} \frac{1}{v^2} \nabla_{\perp}(\text{TEC}) \quad (8.4)$$

at the observed frequency  $v$ , where  $\nabla_{\perp}$  is the transverse gradient in TEC towards the direction of the source. The time, space and frequency dependence of this effect causes difficulty for long integrations, since the scintillation will cause averaging of point sources with empty space, spreading-out their signal over a  $\sim \Delta^2\theta$  area. This can be interpreted as an additional source of noise in a Stokes I map. Vedantham & Koopmans (2015) showed that this scintillation noise can be much larger than image noise for baselines longer than  $\sim 200$  m. Vedantham & Koopmans (2016), extending the previous analysis to the Fourier domain, showed that this noise does not pose large issues to HERA or SKA-Low EoR efforts, since realistic amounts scintillation were not sufficient to wash-out EoR signals on large scales (their dense cores of relatively short baselines also help). However, it could pose large issues for point-source calibration and subtraction methods – as emphasized in a public SKA memo by Cornwell (2016).

Loi et al. (2015) used MWA observation snapshots to map the scintillation as a function of space and time, resulting in the discovery of “tubes” of plasma density waves across the Southern Hemisphere in lines of roughly constant latitude. Comparing the sources in their snapshot images to source positions in the NRAO VLA Sky Survey (NVSS Condon et al., 1998) they were able to calculate displacement vectors, and showed

that they were strongly aligned to Earth’s magnetic field.

The literature surrounding ionospheric Faraday Rotation is less extensive than work focussing on the unpolarized component. Lenc et al. (2016) showed that MWA measurements of diffuse foregrounds could provide a map of ionospheric spatiotemporal variance as their RM changed throughout a series of observations. Lenc et al. (2017) showed that point source power could be seen “twinkling” in and out of polarized intensity maps due to ionospheric activity.

### 8.3 Relevance for PAPER and HERA EoR measurements

Within the PAPER and HERA power spectrum pipelines, many tens to hundreds of days of visibilities are averaged over during binning in LST. The ionosphere-induced spatial and temporal fluctuations in RM could produce sufficient phase scrambling of the celestial Faraday-rotated, polarized signal to suppress a fraction of any polarized signal leaked by some mechanism into Stokes I measurements. The fringe size of the 30 m baselines used in power spectrum analyses is large enough that scintillation effects are negligible.

This effect was first investigated in Moore et al. (2017). Using the `ionFR` package (Sotomayor-Beltran et al., 2013) we calculated the RM distribution at a single zenithal pointing throughout the PAPER-32 observation season. This was a vast simplification given the PAPER primary beam was much larger than a typical isoplanatic patch. Shown in Figure 8.1, there was a large spread of ionospheric RMs for each LST. There was a decrease in the average magnitude of the RM as LST increased. This was expected, given the strong correlation between the day/night cycle and TEC values (e.g. Tariku, 2015), and given that for this observing season, LST=4 hr corresponded to observations taken shortly after sunset, while LST=8 hr was always well into the night.

Treating the single pointing as constant over the sky, we calculated the expected attenuation of polarized signal, leaked into pseudo-Stokes I visibilities, that would be averaged over varying ionospheric conditions during LST binning. These attenuation factors were

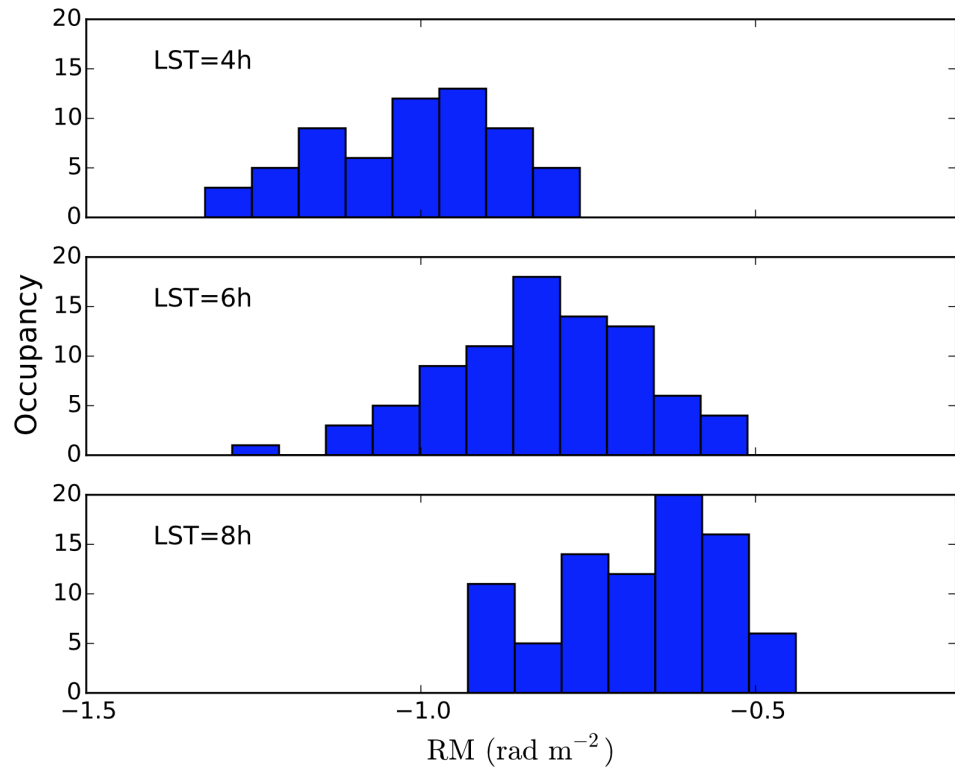


Figure 8.1: Distribution of zenithal ionospheric RMs for 3 LSTs in the PAPER-32 observing season. From top to bottom: a histogram of the zenith ionospheric RMs over the season, for the transit of LSTs 4, 6, and 8 hr. Taken from Moore et al. (2017).

$43 \pm 6\%$  at 165 MHz and  $7 \pm 5\%$  at 126 MHz.

To build on this result, we required more sophisticated simulations of the interaction of the polarized sky with the instrument and whole-sky maps of the ionosphere. To accomplish the latter, we developed the open-source Python package `radionopy`<sup>3</sup>. Like `ionFR`, `radionopy` uses GPS-derived TEC maps from IONEX files and the IGRF to estimate the value of ionospheric RM at a given latitude, longitude and date. Unlike its predecessor, `radionopy` does not necessarily calculate an RM at a given pointing, but instead is capable of calculating the ionospheric RM over a HEALPix grid of the sky (Górski et al., 2005). Such an expression of ionospheric variation is natural to wide-field, drift-scanning EoR arrays, and reflects the format of the IONEX input measurements, which are given in their spherical harmonic decompositions. `radionopy` is vectorized, leading to efficient generation of full-sky ionospheric maps, and object-oriented, allowing for easier collaborative development. Additionally we implemented the interpolation scheme recommended in the IONEX documentation to obtain ‘best-guess’ full-sky maps for arbitrary times between the 2-hour time resolution of IONEX data.

An example output from `radionopy` is shown in Figure 8.2 as a HEALPIX grid of the hemisphere observable from the PAPER site in the Karoo. In Figure 8.3 we show `radionopy` and `ionFR` output for a single pointing towards Cassiopeia A (Cas A; RA= $23^{\text{h}}23^{\text{m}}27.9^{\text{s}}$ , Dec= $+58^{\circ}48'42.4''$ ) from the LOFAR Core site in the Netherlands. The two codes gave qualitative agreement. Slight offsets at the highest RM values that day could be attributed to differences in our interpolation schemes.

Martinot et al. (*in prep.*) investigated the full interaction of the polarized sky with the ionosphere, using realistic polarized sky models and fully-polarized HERA beam models (see Chapter 10 for an example). Their work revealed that the Moore et al. (2017) analysis overestimated the ionospheric attenuation due to their single-pointing and simple beam models. Realistic levels of attenuation for a 100 day HERA integration can be expected to reach a factor of  $\leq 0.1$ . If polarization leakage occurs close to the EoR level, this is

---

<sup>3</sup><https://github.com/UPennEoR/radionopy>

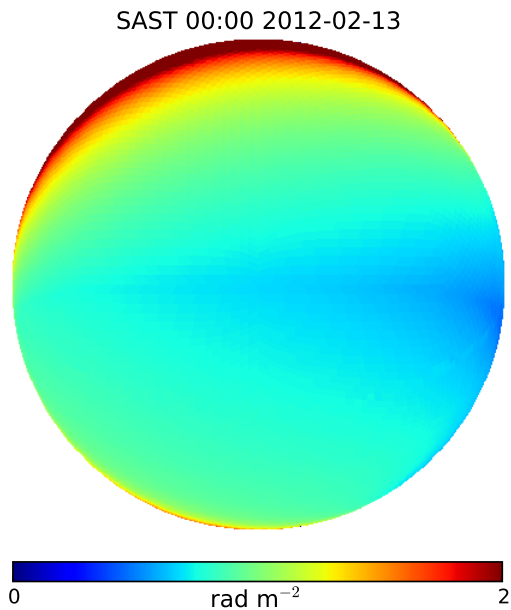


Figure 8.2: An example of widefield ionospheric RMs calculated by radionopy.

sufficient to recover the EoR power spectrum. However, if it is above the EoR level (as expected by Nunhokee et al. 2017), the ionosphere alone will not be sufficient to rule out polarization leakage being detected before the EoR can be recovered.

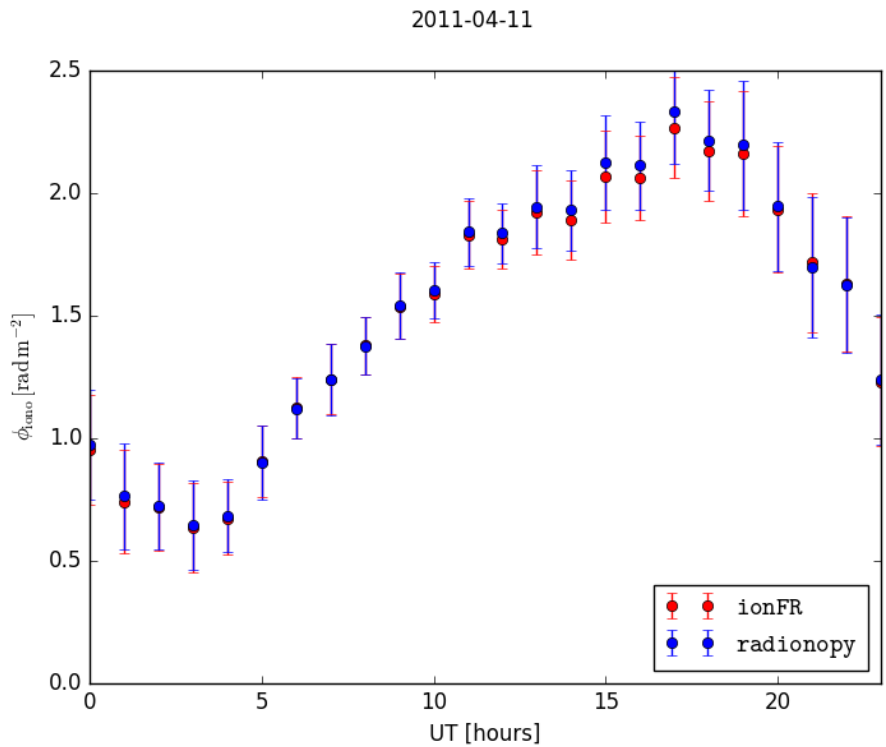


Figure 8.3: The RM of Cas A as viewed from the LOFAR Core site in the Netherlands on April 11th, 2011, according to `ionFR` and `radionropy`. The two codes show quantitative agreement, demonstrating that `radionropy` can be used for single-pointing as well as full-sky RM measurements.

# Chapter 9

## A view of the EoR window from the PAPER-32 imaging array

In this Chapter, we present 2D power spectra created from data taken by the PAPER-32 imaging array in Stokes I, Q, U and V, as reported by Kohn et al. (2016).

The PAPER 32-antenna array relied on its highly redundant configuration in order to take the measurements resulting in the strong upper limits on the 21 cm power spectrum (Parsons et al., 2014; Jacobs et al., 2015; Moore et al., 2017). However, for three nights in 2011 September, the 32 elements were reconfigured into an polarized imaging configuration. Creating power spectra allowed us to observe and diagnose systematic effects in our calibration at high signal-to-noise within the Fourier space most relevant to EoR experiments. We observed well-defined windows in the Stokes visibilities, with Stokes Q, U and V power spectra sharing a similar wedge shape to that seen in Stokes I. With modest polarization calibration, we saw no evidence that polarization calibration errors moved power outside the wedge in any Stokes visibility, to the noise levels attained. Deeper integrations will be required to confirm that this behavior persists to the depth required for EoR detection.

The layout of this Chapter is as follows. In Section 9.1 we provide a brief description of the PAPER array in its imaging configuration, the data from which this paper is based,

and describe its calibration and reduction. We also describe the method used to create 2D power spectra in this section. We analyze the power spectra in Section 9.2, and discuss the implications of our findings and conclude in Section 9.3.

## 9.1 Observations & Reduction

We present measurements taken overnight on 2011 September 14–15 over local sidereal times (LSTs) 0–5 hr.

Antennae were arranged in a pseudo-random scatter within a 300 m-diameter circle, the layout of which is shown in Figure 9.1. This allowed us to obtain resolutions between 15' and 25' across the bandwidth (100–200 MHz nominally, although in reality this extends 110–185 MHz due to band edge effects and VHF TV). Drift-scan visibilities were measured every 10.7 s, and divided into datasets about 10 minutes in length. We express an interferometric visibility  $V_{ij}^{pq}$  between antennae  $i$  (with dipole arm  $p$ , which can be  $x$  (East-West) or  $y$  (North-South) for PAPER dipoles), and  $j$  (with dipole arm  $q$ ), in directional cosines  $l$  and  $m$  for frequency  $\nu$  at time  $t$ , as:

$$V_{ij}^{pq}(\nu, t) = g_i^p g_j^{q*} \exp(-2\pi i \nu \tau_{pq}) \int d\Omega A^{pq}(\Omega, \nu) S(\Omega, \nu) \exp\left(\frac{-i\nu}{c} \vec{b}(t) \cdot \hat{s}(\Omega)\right) \quad (9.1)$$

where the  $g$  terms represent the complex gains for each antenna and dipole arm,  $A^{pq}$  is the polarized beam and  $S$  is the sky. The product  $\vec{b}(t) \cdot \hat{s}(\Omega)$  represents the projection of the baseline between  $i$  and  $j$  with respect to an arbitrary location on the sky. The motivation for including the term for the delay between dipole arms  $p$  and  $q$ ,  $\tau_{pq}$ , is given in Section 9.1.1.3. This delay is clearly zero if  $p = q$ .

Visibilities were obtained from correlating both  $x$  and  $y$  dipoles, forming  $V^{xx}$ ,  $V^{xy}$ ,  $V^{yx}$  and  $V^{yy}$ . Frequencies from 100 to 200 MHz were sampled into 2048 channels. Data were delay-filtered to 203 frequency channels (see the Appendix of Parsons et al., 2014) and Chapter 6. Cross-talk was modelled and removed by subtracting the average power over

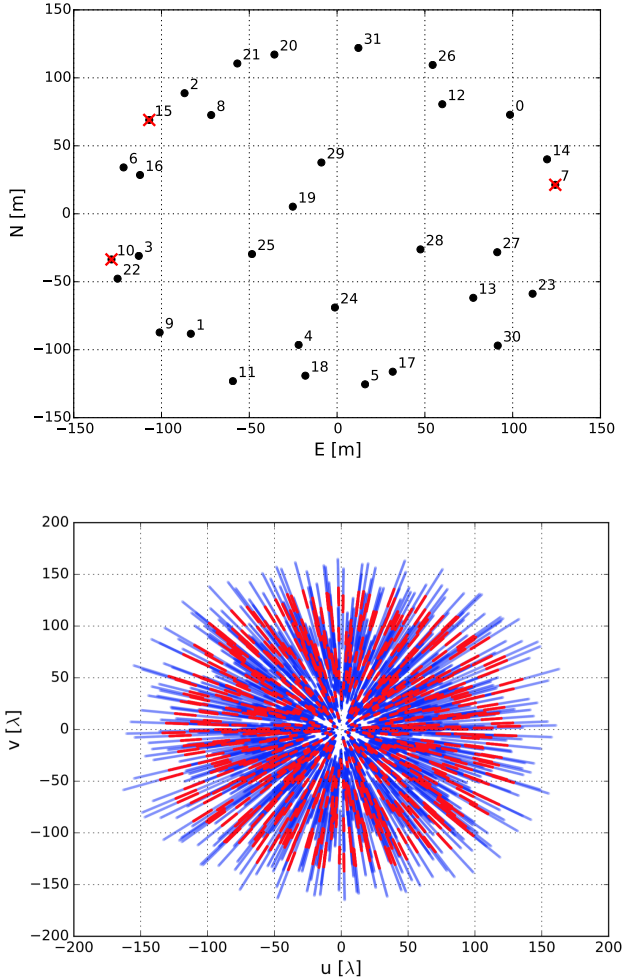


Figure 9.1: The PAPER-32, dual-pol antenna imaging configuration (top). They were arranged in a pseudo-random scatter within in a  $\sim 300$  m diameter circle to maximize instantaneous  $uv$  coverage (bottom).  $uv$  coverage is shown for 100–200 MHz over 203 channels in blue, and 146–166 MHz over 20 channels in red (the latter being the frequencies used in our power spectrum analysis). Malfunctioning antennae identified during calibration are overlaid with red crosses (and are excluded from the  $uv$  coverage map).

the 5 hours of observation, which extended across LST=0h–5h. An initial RFI-flagging removed any outliers more than  $6\sigma$  from a spectrally smooth profile.

### 9.1.1 Calibration

Calibration took place in three stages, detailed below: a first-order delay-space calibration for the initial gains and phases with respect to Pictor A, an absolute calibration using imaging with respect to Pictor A and Fornax A, and a polarimetric correction for the  $\tau_{xy}$  phase term in the  $V^{xy}$  and  $V^{yx}$  visibilities. Traditional polarimetric calibration proceeds by observing a source with a known polarization angle, and solving for up to seven direction-independent terms in the Jones matrix (e.g. Thompson et al., 2017; Hamaker et al., 1996), as well correcting for the effects of the primary beam. Given the dearth of suitable calibrators at our observing frequencies, especially at the relatively low resolution and sensitivity of the array, we proceeded with polarized calibration using different techniques, as described in Section 9.1.1.3 below.

#### 9.1.1.1 Initial calibration

A first-order gain and phase calibration was performed by a similar approach to Jacobs et al. (2013). Each 10 minute drift-scan dataset was phased to the known position of Pictor A using aipy routines.

The gain term in Equation 9.1 was approximated as

$$g_i^p = G_i^p \exp(-2\pi i v \tau_{ip}) \quad (9.2)$$

and the required delay  $\tau_{ip}$  offset of the uncalibrated delay tracks to the real position on the sky solved for to obtain a phase calibration; the absolute flux calibration  $G_i^p$  was found by isolating the tracks of Pictor A in delay space, and applying the required flux scale across the band (for a discussion of delay-space calibration, see Parsons et al., 2012b, and Figure 9.4).

#### 9.1.1.2 Absolute Calibration

Visibilities were converted to CASA Measurement Sets to be further calibrated using a custom pipeline developed around CASA libraries. Snapshot images were generated for

each 10 minute observation by Fourier transforming the visibilities. We used uniform weights and the multi-frequency synthesis algorithm to further improve the *uv* coverage. Dirty images were deconvolved down to a 5 Jy threshold using the Cotton-Schwab algorithm. The sky model generated by the CLEAN components was used to self-calibrate each snapshot over the full bandwidth, using a frequency-independent sky-model and averaging over the 10 minute observation. We corrected for residual cable length errors by computing antenna-based phase solutions for each frequency channel for each snapshot observation. After self-calibration, snapshot visibilities were again Fourier transformed into images and deconvolved down to a 2 Jy threshold to form the final sky models. These final sky models were used to solve for a frequency independent, diagonal, complex Jones matrix (Hamaker et al., 1996; Smirnov, 2011a) for each antenna in order to calibrate gain variations from snapshot to snapshot. We make no attempt to correct sky models for polarized primary beams and, therefore, our gain solutions incorporate both the direction independent and the direction dependent responses of the two gain polarizations. This is a reasonable approximation for the scope of the paper, as, eventually, wide-field polarization corrections cannot be implemented directly in the per-baseline power spectrum estimation (see Section 9.2).

The average correction in magnitude through this second-order calibration was a  $\pm 6\%$  change for *x* gains and  $\pm 7\%$  for *y* gains from those derived in the initial delay-space calibration. If the gain on an antenna deviated by more than 30% from image-to-image during this analysis, it was discarded from future processing stages, since it was likely malfunctioning. This was true for 3 antennae (see the top panel of Figure 9.1).

The final gain amplitude calibration was carried out similarly to Ali et al. (2015). We generated single channel images between 120 and 174 MHz for each snapshot and deconvolved each of them down to 10 Jy. For each snapshot, a source spectrum is derived for Pictor A by fitting a two dimensional Gaussian the source using the PyBDSM<sup>1</sup> source extractor (Mohan & Rafferty, 2015). Spectra were optimally averaged together

---

<sup>1</sup><http://www.lofar.org/wiki/doku.php?id=public:usersoftware:pybdsm>

by weighting them with the primary beam model evaluated in the direction of Pictor A. To fit the absolute calibration, we divided the model spectrum (Jacobs et al., 2013) by the measured one and fit a 6th order polynomial over the 120-174 MHz frequency range. This procedure was repeated using Fornax A with the only difference that a taper was applied to the visibilities (120 m) in order to reduce Fornax A to a point-like source and use the model spectrum from Bernardi et al. (2013). The best fit coefficients for Pictor A and Fornax A were averaged together to obtain the final absolute flux density calibration. Snapshots of fully CASA-calibrated data are shown in Figure 9.2.

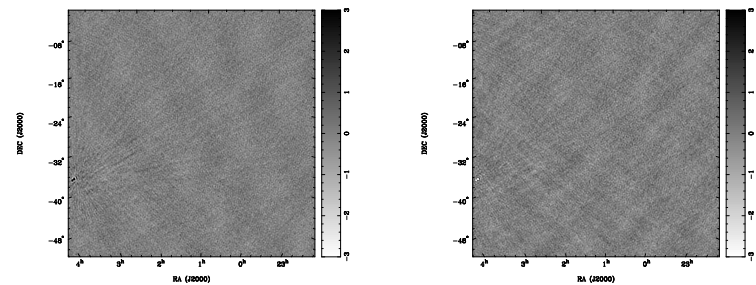
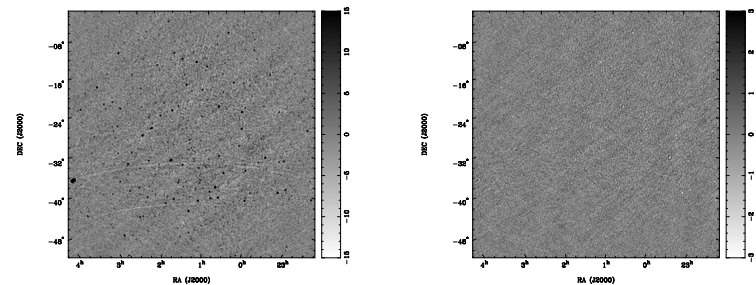
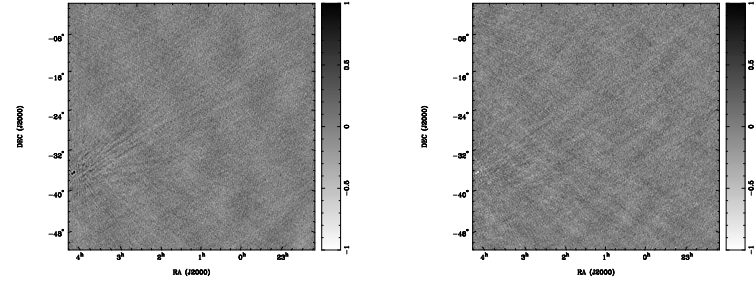
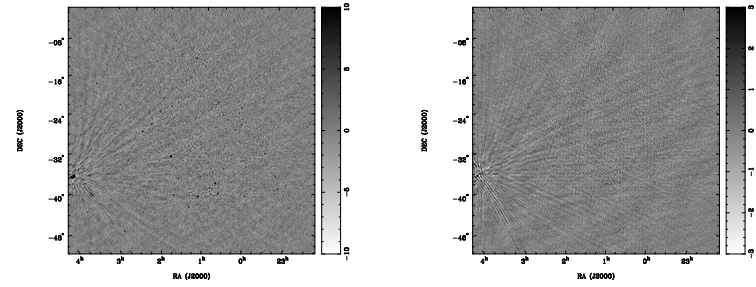


*Figure 9.2: Above:* Example of a Stokes I snapshot image (top left) with corresponding Stokes Q (top right), Stokes U (bottom left) and Stokes V (bottom right) images before absolute calibration. *Below:* The same organization as above, after absolute calibration. No primary beam correction was applied. The Stokes I image was deconvolved down to  $5 \text{ Jy beam}^{-1}$  whereas the other images were not deconvolved. Units are  $\text{Jy beam}^{-1}$ ; note the change in scale between polarizations and calibration stages.

### 9.1.1.3 Polarimetric factors

Standard full polarization calibration involves correcting for leakage of Stokes  $I$  into the  $V_{ij}^{xy}$  and  $V_{ij}^{yx}$  visibilities and leakage of polarized signal into total intensity (the so called Jones  $D$  matrices or  $D$ -terms; e.g. Thompson et al. (2017); Hamaker et al. (1996)), and an unknown phase difference between the  $x$  and  $y$  feeds (e.g. Sault et al., 1996).

We attempt no  $D$  matrix calibration in this paper, as there is not a dominant source to be used for such calibration: the limited sensitivity of our observations does not offer good signal-to-noise ratio on PMN J0351-2744, the only polarized source at low frequencies known so far in our survey area. In addition,  $D$ -term calibration would require determination of the primary beam Mueller matrices beyond our current accuracy. The consequences of this limitation are discussed in the analysis of our power spectra in Section 9.2.

As an intermediate measure compatible with these limitations, we therefore adopted a minimization of the phase difference between the  $V_{ij}^{xy}$  and  $V_{ij}^{yx}$  visibilities, minimizing a sum of squared weighted residuals  $w$ :

$$w(v, t, \tau_{xy}) = \sum_{ij} |V_{ij}^{xy} - V_{ij}^{yx} \exp(-2\pi i v \tau_{xy})|^2 \quad (9.3)$$

to find an estimated value of  $\tau_{xy}$  for the array at each  $(v, t)$  sample. This is equivalent to assuming that the sky is intrinsically not circularly polarized at the frequencies observed by PAPER.

We choose not to correct for ionospheric Faraday rotation in our calibration. Not only is this difficult to do for widefield instruments, but also the ionosphere was relatively stable during the observations, so we expect little incoherent averaging during the power spectrum stage below. We calculated the stability of ionospheric RM ( $\phi_{\text{iono}}$ ) using the IONFR software (Sotomayor-Beltran et al., 2013), which calculates the  $\phi_{\text{iono}}$  for a given longitude, latitude and time by interpolating values of GPS-derived total electron content maps and the International Geomagnetic Reference Field (Finlay et al., 2010). The values

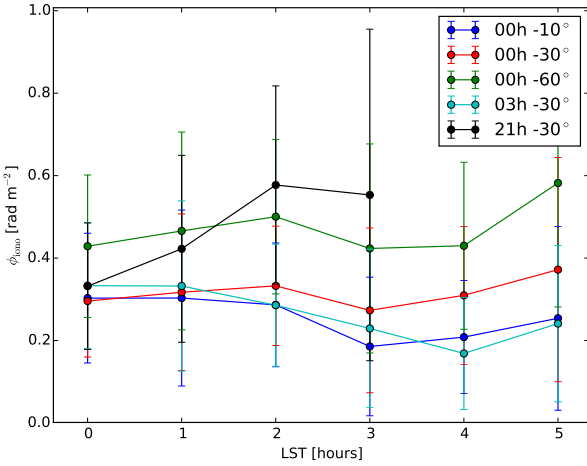


Figure 9.3: The values of ionospheric RM for different lines of sight the range of LSTs in this analysis, as calculated by IONFR (Sotomayor-Beltran et al., 2013). The 21h,0° line of sight goes beneath the horizon after LST=3h, and therefore has fewer data points.

of  $\phi_{iono}$  for different lines of sight are shown in Figure 9.3. Fluctuations of  $\phi_{iono}$  will cause incoherent time-averaging and subsequent loss of polarized signal. Using the formalism of Moore et al. (2017) to calculate the attenuation factor, we found that none of the lines of sight (except for the 21h,0° one which goes beneath the horizon) shown are responsible for attenuating signal by > 20% in power-spectrum space (see Section 9.1.2).

We form linear combinations of the instrument visibilities, the so-called pseudo-Stokes visibilities (see e.g. Moore et al., 2013)  $V^I$ ,  $V^Q$ ,  $V^U$  and  $V^V$  as:

$$\begin{pmatrix} V^I \\ V^Q \\ V^U \\ V^V \end{pmatrix} = \begin{pmatrix} 1 & 0 & 0 & 1 \\ 1 & 0 & 0 & -1 \\ 0 & 1 & 1 & 0 \\ 0 & -i & i & 0 \end{pmatrix} \begin{pmatrix} V^{xx} \\ V^{xy} \\ V^{yx} \\ V^{yy} \end{pmatrix} \quad (9.4)$$

Data that were reduced, calibrated, and formed into Stokes visibilities were separated into delay spectra inside and outside of the horizon for each baseline. We used a 50 ns margin for what was considered ‘inside’ the horizon, in order to confine all supra-horizon emission (e.g. Parsons et al., 2012b; Pober et al., 2013) to the foreground component of

the data. We implemented a one-dimensional CLEAN (Parsons & Backer, 2009; Parsons et al., 2012a) with a Blackman-Harris window to a tolerance of  $10^{-9}$ . RFI is more easily identified in foreground-removed data, so we RFI-flagged again on the background data deviations greater than  $3\sigma$ . We then added the inside- and outside-horizon visibilities back together; RFI flags were preserved in the process.

The effect of our calibration is shown in the delay-transformed visibilities in Figure 9.4. As is apparent in Figure 9.2, after improved calibration there are fewer delay tracks (i.e. sources) in the Stokes Q visibilities, while there is little overall change in Stokes U. The minimization of Stokes V, performed after the imaging calibration stage, moves power from Stokes V into Stokes U, effectively accounting for part of a  $D$ -term correction. But without an accurate  $D$ -term calibrator, Stokes U exhibits additional (and dominant)  $D$ -term leakage from Stokes I, in this case due to Pictor A. Pictor A is the brightest source in Stokes I in our observed field, and thus dominates the visibility shown. There is no reason to suppose that Pictor A is pure Stokes U (compare also Figure 9.2), and thus the bulk of this emission must be leakage.

### 9.1.2 Creating power spectra

Expressing the visibility  $V_{ij}^{pq}(v, t)$  observed at time  $t$  (see Equation 9.1) in terms of the geometrical delay  $\tau_g = \vec{b}(t) \cdot \hat{s}(l, m)/c$  for the baseline  $ij$ , Parsons et al. (2012b) define the delay transform as the Fourier transform of the visibility along the frequency axis:

$$\tilde{V}_{ij}^{pq}(\tau, t) = \int dv V_{ij}^{pq}(v, t) e^{2\pi i v \tau} \quad (9.5)$$

We can represent the power at each frequency and baseline in an array as a power spectrum in terms of their respective Fourier components  $k_{\parallel}$  and  $k_{\perp}$  as:

$$P(k_{\parallel}, k_{\perp}) \approx |\tilde{V}_{ij}^{pq}(\tau, t)|^2 \frac{X^2 Y}{\Omega B} \left( \frac{c^2}{2k_B v^2} \right)^2 \quad (9.6)$$

where  $B$  is the bandwidth,  $\Omega$  is the angular area (i.e. proportional to the beam area), and X and Y are redshift-dependent scalars calculated in Parsons et al. (2012a).

To form  $|\tilde{V}_{ij}^{pq}(\tau, t)|^2$ , consecutive integrations were cross-multiplied, phasing the zenith of latter to the former i.e.:

$$|\tilde{V}_{ij}^{pq}(\tau, t)|^2 \approx |V_{ij}^{pq}(\tau, t) \times V_{ij}^{pq}(\tau, t + \Delta t) e^{i\theta_{ij,\text{zen}}(\Delta t)}|^2 \quad (9.7)$$

where  $\Delta t = 10.7$  seconds and  $\theta_{ij,\text{zen}}(\Delta t)$  is the appropriate zenith rephasing factor. This method should avoid noise-biased power spectra except on very long baselines, which the PAPER configuration does not contain, while sampling essentially identical  $k$ -modes. Note that this is the same method used by Pober et al. (2013) in their investigation of the unpolarized wedge.

## 9.2 Results

Combining visibilities using Equation 9.4, we formed power spectra over frequencies 146–166 MHz according to Equation 9.6 using consecutive integrations for each Stokes visibility over time, and gridded our results into  $k$ -space, averaging in time. The  $k_\perp$ -axis is binned with a resolution of  $4.65 \times 10^{-4} h \text{ Mpc}^{-1}$  to slightly reduce gaps in  $k$ -space due to missing baselines. This gave an average bin occupancy of  $1.7 \pm 0.9$ . The resolution in  $k_\parallel$  ( $5.06 \times 10^{-4} h \text{ Mpc}^{-1}$ ) is set by the 20 MHz bandwidth with 500 kHz resolution that we use in this analysis. Note that the Blackman-Harris window used in the delay-filtering stage after forming Stokes visibilities correlates adjacent frequency bins, and hence  $k_\parallel$  bins. Each  $(k_\perp, k_\parallel)$  bin was normalized by its occupancy.

Two-dimensional power spectra have been proven as powerful tools for large dipole array experiments, not only for assessing cosmology but also in order to constrain instrumental and analytical systematics (e.g. Morales et al., 2012). Polarization axes are a useful addition for such analyses, since we expect Stokes I to be approximately 3 orders of magnitude stronger than the other polarization products at the low radio frequencies and tens-of-arcminute scales native to PAPER observations (e.g. Pen et al., 2009; Moore et al., 2013) and when observing far from the Galactic Plane. This alone allows us to assume that much of the structure in the power spectra with power comparable to Stokes I

is leakage. As we explore below, these leakage terms can come from direction-dependent effects (e.g. wide-field beam leakage; Carozzi & Woan, 2009) or direction independent ones (e.g. Mueller matrix mixing via gain errors and  $D$ -terms; Thompson et al., 2017) and appear with high signal-to-noise in power spectra.

Figure 9.5 shows power spectra in ‘pitchfork’ form (Thyagarajan et al., 2015b,a), with  $k_{\parallel}$  in negative and positive directions (according to the East and West horizons, marked in white (horizon) and orange (horizon+50 ns delay, respectively). Each Stokes parameter pitchfork has its own interesting characteristics, which allow us to analyze different sky and instrument behaviors. The ‘wedges’ described in the literature that define the EoR window are simply the average of negative and positive values of  $k_{\parallel}$ . While we focus on the pitchfork expression of the power spectra in our results, we also show them in wedge form in Figure 9.6<sup>2</sup>.

Simplifying the results of Thyagarajan et al. (2015b,a, see their papers for a full discussion), we expect power from diffuse emission to appear at low values of  $k_{\perp}$  and high values of  $k_{\parallel}$ , while point sources lie at all  $k_{\parallel}$  (all over the sky) but are down-weighted by the primary beam, which is broad, leaving a concentration of the power close to the  $k_{\parallel} = 0$  line.

In Stokes I, we see the strongest power on most baselines arising at values  $k_{\parallel} \approx 0$ . This is expected in a situation of point sources that are relatively bright compared to any diffuse emission. Indeed, at the LSTs we observed at, several unresolved bright point sources transit the field (e.g. Figure 9.2), while the dominant source of diffuse emission at these frequencies, the Galactic plane, was below the horizon. However, we do see strong super-horizon emission at  $0.02 \leq k_{\perp} \leq 0.03$ , biased towards negative  $k_{\parallel}$  values. There is also a decrease in power with increasing  $k_{\perp}$  – both of these effects are consistent with the Thyagarajan et al. (2015a) simulations of faint diffuse structure transiting zenith.

---

<sup>2</sup>Note the difference in the power distribution within the horizon differs from that shown in the Pober et al. (2013)  $V^{yy}$  wedge. That study used the PAPER 64-element, single-polarization imaging array to create power spectra in a ‘loud’ field containing point sources and Galactic signal, causing their wedge to be ‘fuller’ than the ones presented in this study.

The Stokes Q wedge shows a concentration of power close to  $k_{\parallel} \approx 0$ , similar to Stokes I. The inherent low polarization fraction at our frequencies works in our favor in detecting gain errors, since Stokes Q is largely expected to be faint, and thus the gain errors causing leakage from I appear at high signal-to-noise there. Indeed, this power decreases noticeably with more accurate gain amplitude calibration, but bright streaks at specific values of  $k_{\perp}$  remain, suggesting lower-level residual gain calibration errors on select baselines. Another possible source of power in Stokes Q stems from wide-field direction-dependent gain errors causing a non-smooth evolution of the sources on the edges of the beam. However, we would expect this effect to be biased towards horizon values of  $k_{\parallel}$ .

Power appears distributed in ‘pockets’ in the Stokes U power spectrum, not strongly correlated with the distribution of power in I. Stokes I is able to leak into Stokes U via  $D$ -term leakage (Thompson et al., 2017; Geil et al., 2011), which could occur at any post-amplification stage of observations, such as in cables or receivers. These leakages would be direction independent, and therefore uncorrelated in  $k$ -space. Such a mechanism could explain the behavior within Stokes U wedge. Before absolute calibration, similar structure is seen in the Stokes V power spectrum.

At these frequencies, Stokes V is thought to be intrinsically zero, with few exceptions. However, Hamaker et al. (1996) show that antennae rotated with respect to one another can produce erroneous Stokes V power via  $I \rightarrow V$  leakage.<sup>3</sup> This effect may explain some of the small pockets of power that remain in the Stokes V power spectrum after absolute calibration, although such an effect is also consistent with  $D$ -term leakage. The fact that power within the horizon was greater than the noise level may also have been due to  $I \rightarrow V$  leakage through the primary beam.

The relationship between polarizations is highlighted in Figure 9.7. We show a slice of the wedges over  $0.097 < k_{\perp} < 0.098 \text{ } h\text{Mpc}^{-1}$  ( $\sim 175 \text{ m}$ ) for Stokes I, Q, U and V

---

<sup>3</sup>It should be noted that while such an error could plausibly have been made in the antenna placement for this imaging array, it is extremely unlikely that it would be made in the redundant PAPER configuration for EoR seasons. In these cases, the antennae were positioned to sub-cm accuracy.

(right panels) and the average power over these slices as a function of  $k_{\parallel}$  (left panel). The standard deviations for each Stokes parameter are shown as dotted lines. Dashed vertical lines show the horizon at  $k_{\perp}=0.097$  (left) and super-horizon at  $k_{\perp}=0.098$  (right).

A heartening aspect of Figure 9.7, and indeed all of the power spectra in this work, is that the power in Stokes Q, U and V proves to be just as confined within the horizon as Stokes I. Whether the polarized Stokes parameters are due to real polarization or mis-calibration, not enough spectral structure is being introduced to move emission into the EoR window. Outside of the horizon, Stokes I, Q and U are consistent with the noise level expected for this range of  $k$ -modes ( $P_{\text{noise}} \sim 10^9 \text{ mK}^2(h^{-1}\text{Mpc})^3$ ), according to the formalism Parsons et al. (2012a) and assuming a system temperature  $T_{\text{sys}} = 450\text{K}$  (e.g. Moore et al., 2017).

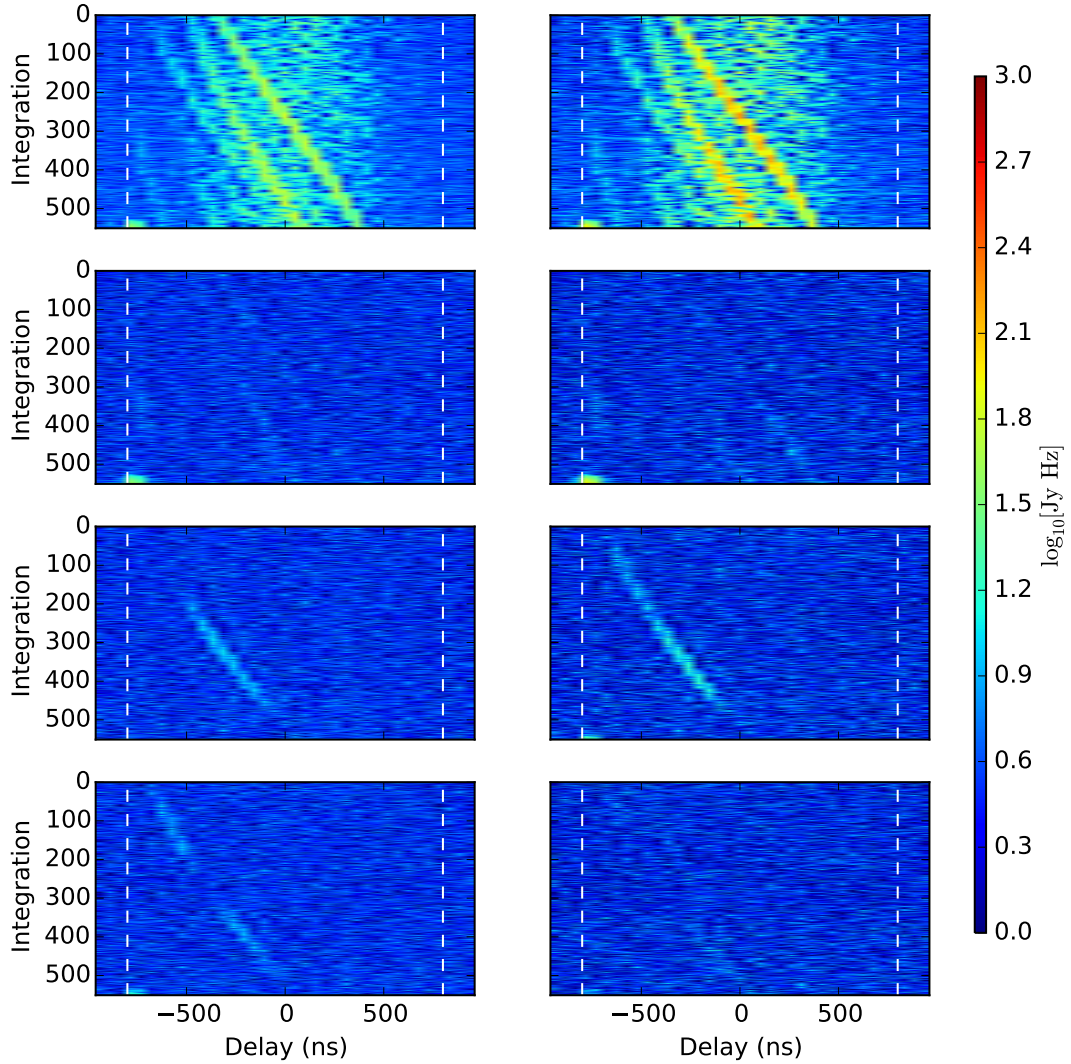


Figure 9.4: The absolute value of delay-transformed visibilities over the bandwidth (146–166 MHz) used to create the power spectra shown in this Chapter. The left and right columns show the visibilities before and after absolute calibration (and for Stokes U and V, the application of the  $\tau_{xy}$  parameter), respectively, for baseline formed by antennae 6 and 14 ( $\sim 250$  m in length, approximately East-West). The flux scale in the left column as been boosted for a more fair comparison to the absolute-calibrated data. From top to bottom, the rows correspond to Stokes I, Q, U and V. The horizon limit is marked by white dashed lines.

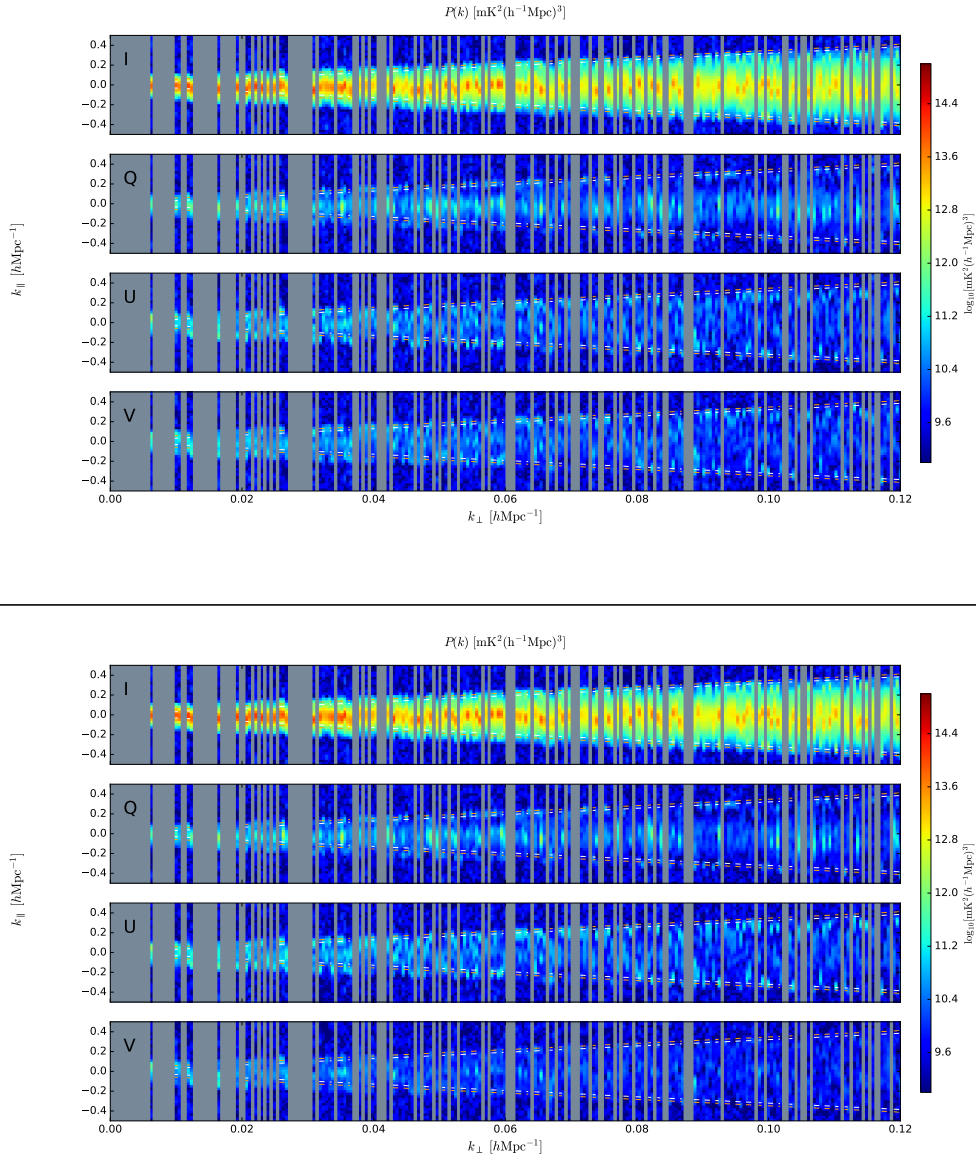


Figure 9.5: *Above:* Log-scaled 2D power spectra formed from (*top to bottom*): I, Q, U and V visibilities after before absolute calibration. Blank regions indicate the incomplete  $uv$  coverage for a given  $k_{\perp}(u)$ . The colorbar spans  $10^9$  to  $10^{15}$   $\text{mK}^2(\text{h}^{-1}\text{Mpc})^3$ . The flux scale has been boosted for a more fair comparison to the absolute-calibrated data. *Below:* The same organization as above, but after absolute calibration.

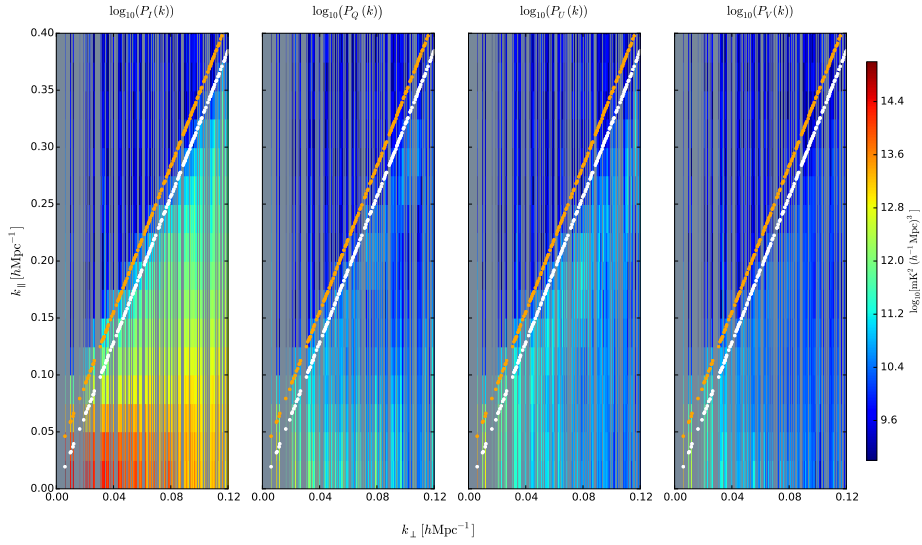


Figure 9.6: Log-scaled 2D power spectra formed from (*left to right*): I, Q, U and V absolute-calibrated visibilities. Blank regions indicate the incomplete *uv* coverage for a given  $k_{\perp}(u)$ . White and orange lines indicate the horizon and horizon plus a 50 ns boundary for super-horizon emission.

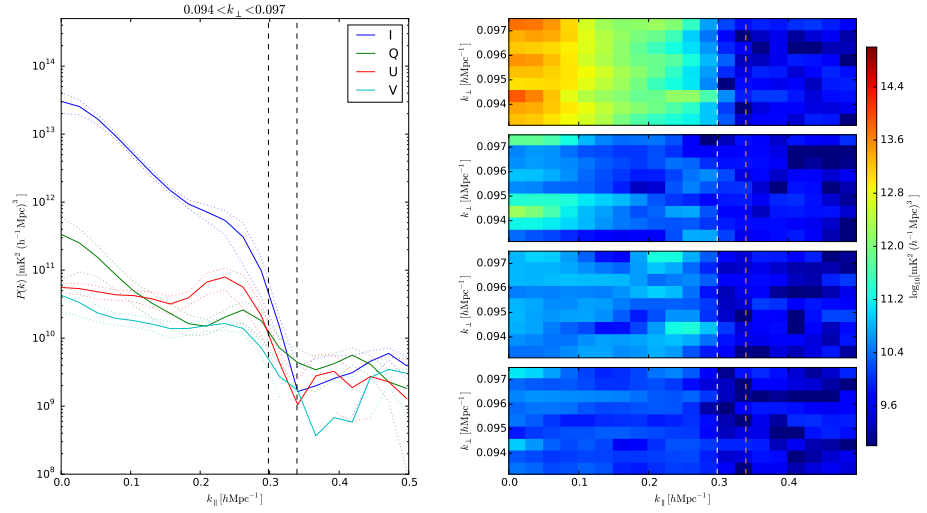


Figure 9.7: *Left:* The average power in  $0.093 < k_{\perp} < 0.098 h\text{Mpc}^{-1}$  as a function of  $k_{\parallel}$  for each polarization. In the horizon–super-horizon range that we see the sharp fall-off in power indicative of the edge of the EoR window. Outside of the wedge, Stokes I, Q and U are at noise level, while Stokes V is below noise level, most likely due to the  $\tau_{xy}$  calibration scheme removing a degree of freedom from this Stokes parameter. *Right:* the region of k-space that was averaged over to create the lines in the left panel. From top to bottom, the panels correspond to Stokes I, Q U and V.

### 9.3 Discussion and Conclusions

We have presented measurements of instrumental polarization leakage in PAPER-32 using 2D power spectra. These have allowed us to quantify some of the possible instrumental effects that could limit a statistical detection of the EoR within the wedge, diagnosed in the Fourier space most relevant EoR statistical detection experiments. To our knowledge, this is the first study of Q, U and V 2D power spectra at these  $k$ -modes. We have shown that power from Stokes Q, U and V is as confined to the wedge as Stokes I. Any calibration errors do not appear to spread power outside the horizon.

In their study of 2D power spectra, Asad et al. (2015) reported evidence of polarized leakage into the EoR window at the sub-percent level, considering a  $4^\circ$  degree field of view. Their study differs from this work not only over the field of view ( $4^\circ$  versus almost whole-sky), but also in the observing mode (tracked versus drift scan) and in the different  $k$ -space probes by LOFAR’s longer baselines. In this work the power spectrum is calculated on a per-baseline basis, whereas their study calculates power spectra for gridded data which are more prone to mode mixing effects (Hazelton et al., 2013).

Our results are expected, in principle, to be more prone to leakage contamination due to the intrinsic extremely wide field of view of the PAPER primary beams, however, we see no evidence of leakage in the EoR window down to our sensitivity limits even without correction for polarized beams that is instead included in Asad et al. (2015). Our analysis indicates therefore that neither intrinsic polarized emission nor the PAPER primary beam are leaking power in the EoR window, although longer integrations are required to demonstrate that this is true down to the sensitivities required for EoR detection.

We showed that systematics can be probed with high signal-to-noise using 2D polarized power spectra, using the inherently low polarization fraction at the frequencies PAPER observes at to our advantage. We found that gain errors on specific baselines were easily probed using Stokes Q power spectra. Gain errors appear as continuous streaks within the horizon at specific values of  $k_\perp$ , allowing us to diagnose the precision of the gain calibration on a per-baseline basis. This is much more difficult to do with

only Stokes I power spectra in a non-redundant array, and can be accomplished quickly without imaging. While the features in the Stokes U power spectra are more difficult to attribute to specific baselines, they appear to be consistent with direction-independent leakage. Stokes V power is slightly higher than noise-level within the horizon, suggesting a small but unaccounted-for leakage term from Stokes I, an effect which was explored Nunhokee et al. (2017) – and found to be consistent with beam-leaked signal from Stokes I.

# **Chapter 10**

## **A view of the EoR window from the HERA-19 commissioning array**

As emphasized in Chapter 9, it is important to constrain intrinsic and leaked polarized signal for any HI EoR experiment. The objective of this Chapter was an exploration of eight nights of data from the Hydrogen Epoch of Reionization Array (HERA) 19-element commissioning array, coupled with simulations of the instrument, in order to forecast how much of a problem polarization would pose for this interferometer. These results we reported by Kohn et al. (2018). This work also represents the first power spectral analysis from HERA. While not in the realm of an EoR-level integration, we were able to offer some initial expectations for this new instrument’s performance in the Fourier domain.

This work is organized as follows: in Section 10.1 we review the theory behind polarization leakage into unpolarized signal and simulate the effect for a model of HERA. In Section 10.2 we describe the HERA data that we used, its calibration and reduction to power spectra. We present our results, and discuss the implications for HERA’s EoR measurements, in Section 10.3, and conclude in Section 10.4. We assume the cosmological parameters reported by Planck Collaboration et al. (2016c) throughout.

## 10.1 Polarization Leakage Simulations

In Chapter 3, we presented direction dependent and independent ways for polarized power to “leak” between visibilities. Direction dependent leakage arises because dipole arm ‘n’ is sensitive to electromagnetic radiation with polarization axis aligned with perpendicular dipole arm ‘e’. Forming pseudo-Stokes visibilities from those in the instrumental basis,

$$\begin{pmatrix} V^I \\ V^Q \\ V^U \\ V^V \end{pmatrix} = \frac{1}{2} \begin{pmatrix} 1 & 0 & 0 & 1 \\ 1 & 0 & 0 & -1 \\ 0 & 1 & 1 & 0 \\ 0 & -i & i & 0 \end{pmatrix} \begin{pmatrix} V^{nn} \\ V^{ne} \\ V^{en} \\ V^{ee} \end{pmatrix}. \quad (10.1)$$

results in each pseudo-Stokes visibility containing a direction-dependent mix of the ‘true’ Stokes parameters on the sky. Using simulations of the HERA feed, faceted parabolic dish and analog signal chain (Fagnoni & de Lera Acedo, 2016), we proceeded to simulate pseudo-Stokes visibilities using the polarized formalism in Chapter 3 (Figure 3.4 shows the direction-dependent leakage matrices used here). We simulated visibilities for the HERA-19 commissioning array, described below, using an *unpolarized* model of the low frequency sky from the Global Sky Model (de Oliveira-Costa et al., 2008; Price, 2016a; Zheng et al., 2017, GSM;) at the appropriate R.A. range to match our observations. Forming power spectra and images from these visibilities allowed for a comparison of our data to a ‘leakage from Stokes I only’ regime. At the low frequencies and large scales probed by HERA, Stokes I is extremely bright compared to the other Stokes parameters (e.g. Chapter 2, Kohn et al. (2016)), so this regime is realistic for the measurements in question.

In Chapter 3, we also presented a formalism for propagating direction-independent calibration errors into polarization leakage. We did not include calibration errors in our simulations, allowing us to build intuition around power spectrum estimates for a “perfectly behaving” instrument.

## 10.2 Observations & Reduction

In this work we used eight nights of observations from the HERA-19 commissioning array. HERA is a low-frequency interferometer composed of 14 m-diameter dishes arranged in a close-packed hexagonal array of 14.7 m spacing. The commissioning array consists of nineteen dishes (see Figure 10.1); HERA is being constructed in staged build-outs, and upon completion will consist of 350 dishes in a fractured hexagon configuration (see Dillon & Parsons, 2016; DeBoer et al., 2017). A feed cage containing two dipole feeds (recycled from the PAPER array, see Parsons et al. 2010), oriented in North-South and East-West directions, is suspended above each dish (Neben et al., 2016; Ewall-Wice et al., 2016a; Thyagarajan et al., 2016).

HERA only observes in drift-scan mode. The observations we used were eight nights, from Julian Date (JD) 2457548 to 2457555; LSTs 10.5 – 23 hr. Drift-scan visibilities were recorded every 10.7 seconds for 1024 evenly-spaced channels across the 100-200 MHz bandwidth. These data were divided into MIRIAD data sets roughly 10 minutes long. A night’s observation lasted 12 hours in total (6pm to 6am South African Standard Time; SAST); of these we used the central 10 hours, to avoid the thermal effects of the Sun.

To identify samples contaminated by radio frequency interference (RFI), a 2D median filter in time and frequency was applied to the visibility data to smooth out high pixel-to-pixel variations, and remove significant outliers that were likely unphysical. The variance of the resulting data was computed, and points with a  $z$ -score greater than 6 (i.e., points where the value is more than  $6\sigma$  away from the mean) were flagged as initial seeds for RFI extraction. A two-dimensional watershed algorithm was applied using these seeds as starting points, enlarging the regions of RFI-contamination to neighboring pixels with  $z$ -scores greater than 2, until all such pixels were flagged. Figure 10.2 shows the fractional RFI flag occupancy per time (displayed in LST) and frequency across the 8 days of observations. The majority of the band is relatively clear of RFI. Some clear features are: the FM radio band (below 110 MHz), ORBCOMM satellite communications (137 MHz), an

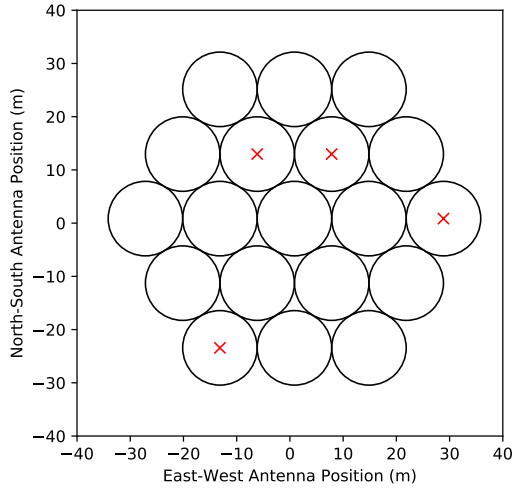


Figure 10.1: The perimeter of each dish in the HERA-19 array. A red “X” marks antennae that were identified during preprocessing and calibration as malfunctioning and were excluded from further analysis.

ISS downlink (150 MHz) and VHF TV channels (above 170 MHz)<sup>1</sup>. The Galaxy, when transiting zenith at  $LST \approx 17.75$  hours, is so bright that it appears to degrade our ability to flag RFI.

### 10.2.1 Calibration

HERA is designed to be calibrated using redundant calibration techniques (Dillon & Parsons, 2016), but for this preliminary view of HERA commissioning data, we used image-based calibration. Future studies with deeper integrations targeting EoR detections will take advantage of redundancy to obtain more precise calibration solutions (DeBoer et al., 2017). We used the CASA (McMullin et al., 2007) package for calibration, taking advantage of its CLEAN, gaincal and bandpass functions.

To enable the use of CASA, we first converted from native MIRIAD to a UVFITS file format which could be ingested by CASA using PYUVDATA (Hazelton et al., 2017). Us-

---

<sup>1</sup>For an extended discussion of RFI as seen by HERA, see the public HERA Memo # 19

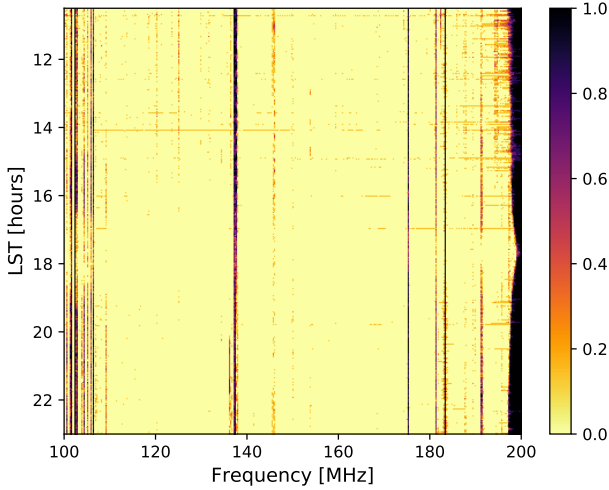


Figure 10.2: Fractional RFI flag occupancy per time and frequency over the eight days of observations.

ing LSTs in which the Galactic center (GC;  $\alpha, \delta = 17h\ 45m\ 40.04s, -29d\ 0m\ 28.12s$ ) was transiting, we built a CLEAN model which modeled the GC as an unpolarized point source of strength 1 Jy and flat spectrum, which could be scaled appropriately later (see Equation 10.2). Clearly, this is an incomplete calibration model. However, as the objective of this work is to explore the response of the instrument in power spectrum space without combining baselines of different lengths, most of the purpose of the calibration is correcting an initial large cable delay per antenna. Treating the GC as unpolarized is adequate for this study. The large optical depth towards the GC (Oppermann et al., 2012) results in large amounts depolarization in the plane of the Galaxy (Wolleben et al., 2006). Moreover, we expected non-negligible amounts of beam depolarization due to the large solid angle of the synthesized beam.

For each night of observations, we used the CASA `gaincal` and `bandpass` functions to obtain frequency-dependent phase and amplitude solutions for each antenna and dipole arm. Four antennae had very deviant solutions, and their inclusion resulted in low-quality images. These were omitted from further analysis (and are marked with red “X”’s in

Figure 10.1). Before calibration, we manually flagged the edges of the band (below 110 MHz and above 190 MHz), where spectral behavior is dominated by the high and low pass filtering in the HERA signal chain (DeBoer et al., 2017).

In Figure 10.3, we show images formed from the simulated pseudo-Stokes visibilities (top panels) and our observations (bottom panels). These are multi-frequency synthesis images, where we used all unflagged frequencies on either side of the band edges; 115 MHz to 188 MHz. We do not specify a beam model during imaging. At HERA’s position ((latitude, longitude) = (-30:43:17.5, 21:25:41.9)) the Galactic Center transits  $2^{\circ}$  from zenith, while the HERA primary beam has a FWHM of  $\sim 5^{\circ}$  at 150 MHz (Neben et al., 2016). For the simulated visibilities, we flagged the same antennae as in the data. As expected for a compact array, the Stokes I images capture only a low-resolution view of the Galactic Center. The simulated and observed visibilities form remarkably similar images in Stokes I, Q and U, but the simulation under-predicts pseudo-Stokes V power. We defer further discussion to Section 10.3.

Example bandpass solutions from JD 2457548 are shown in Figure 10.4. Although some residual RFI remains obvious, the derived bandpasses were smooth. Thus, even though the gains were imprecise, we expected that using them should not add additional spectral structure.

The complex gain solutions were subsequently applied to the MIRIAD files. Figure 10.5 shows the effect of calibration on the visibilities of three nominally redundantly-spaced baselines. Shown in that figure are the phases of three  $V^{mn}$  visibilities from 14.7 m baselines before and after calibration. There were no shared antennae between the visibilities shown. The qualitative agreement is obvious, providing a consistency check on the solutions. We did not attempt to calibrate  $D$ -terms in this work.

We down-selected to two relatively RFI-free 20 MHz sub-bands (Figure 10.2); 115 to 135 MHz and 152 to 172 MHz, henceforth referred to the “low band” and the “high band”. As we discuss in Section 10.2.2, these bands were multiplied by a Blackman-Harris window, centered on their central frequencies, before Fourier transforming in order

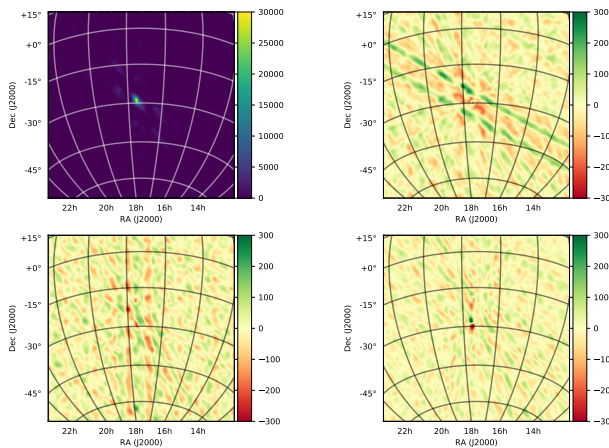
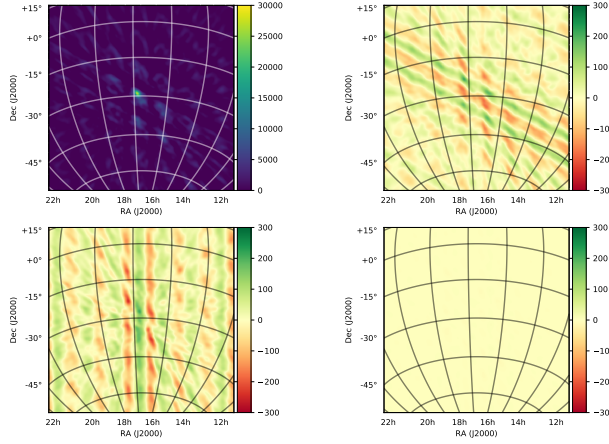


Figure 10.3: *Above:* Multi-frequency synthesis pseudo-Stokes images formed from simulation, where only a Stokes I sky was used; any polarized power is due to direction-dependent polarization leakage (see Section 10.1). *Below:* Multi-frequency synthesis pseudo-Stokes images formed from observed visibilities on JD 2457548. Both sets of panels show the Galactic Center (our calibrator source) close to transit in pseudo-Stokes I, Q, U and V visibilities (*top left, top right, lower left, lower right*). A Briggs-weighting with robustness 0 was used when gridding into the image plane. No deconvolution was performed. The colorbar is in units of Jy/Beam. A separate color scale is used for Stokes I for suitable dynamic range. An R.A., Dec. grid is shown, illustrating the wide-field nature of HERA observations.

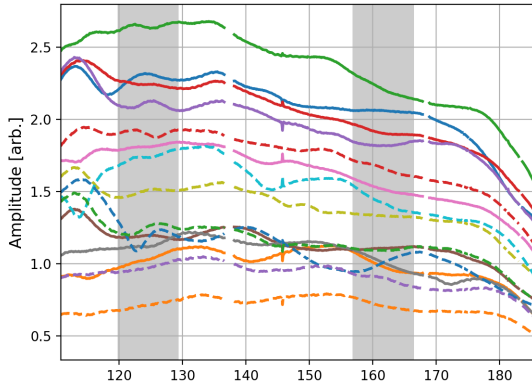


Figure 10.4: Bandpass solutions for the North-South dipole orientation obtained for the functioning antennae in the array on JD 2457548. Differences in line color and style is merely to distinguish different antennae. Shaded regions indicate the effective sub-bands used for power spectrum analysis.

to minimize side-lobes. This windowing lead to an noise-effective bandwidth of 10 MHz, appropriate for EoR analyses since the HI signal is to a reasonable approximation coeval over the corresponding redshift range (Furlanetto et al., 2006).

Pseudo-Stokes visibilities were formed from the instrumental polarizations. These visibilities were then scaled to the appropriate amplitude using a model for the GC spectrum

$$S_{\text{SgrA}^*}(v) \approx 3709 \text{ Jy} \times (v/408 \text{ MHz})^{-0.5} \quad (10.2)$$

drawn from the Global Sky Model (GSM; de Oliveira-Costa et al., 2008; Price, 2016a; Zheng et al., 2017). Note that the GSM is inherently  $\sim 5\%$  uncertain at these frequencies. We note that this scaling is heavily resolution dependent; we are treating the Galactic Center as a point source when it is extended in reality. However, in Section 10.3 we show that we obtain sensible power levels for the foregrounds and noise, lending confidence to our overall scaling.

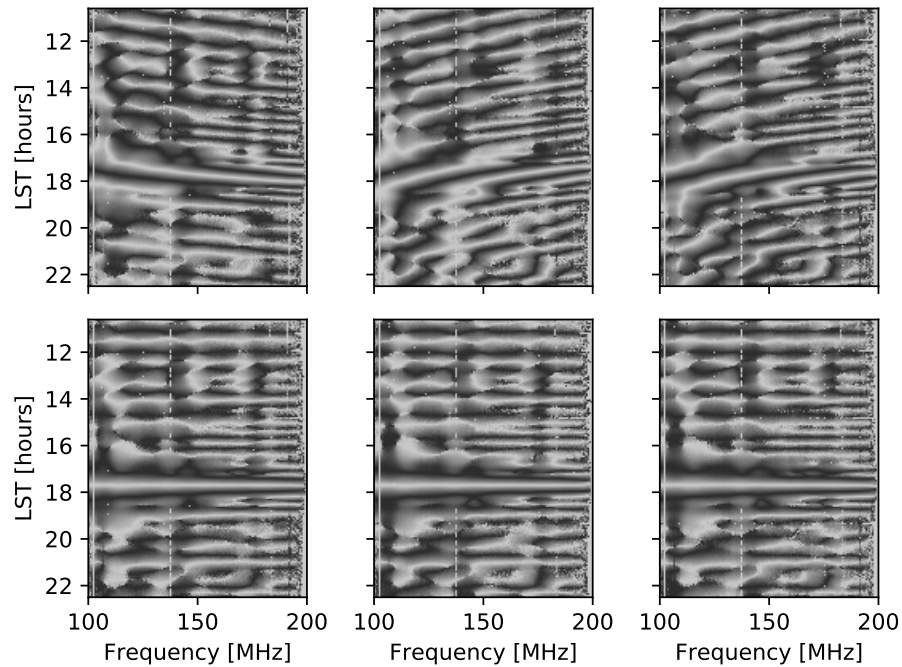


Figure 10.5: The effect of calibration on the phases of visibilities from three redundantly-spaced 14.7 m baselines;  $nn$  polarization. The color scale is cyclic; black is  $\pm\pi/2$  and white is 0 and  $\pm\pi$ . *Above:* before calibration; *below:* after calibration. A simple sky model was sufficient to enforce redundancy for redundant baselines.

### 10.2.2 Forming power spectra

Power spectra were formed according to the method used in Pober et al. (2013) and Kohn et al. (2016), which we briefly review here. All Fourier transforms were windowed using a Blackman-Harris window at the center of the sub-band, which minimized sidelobes. Parsons et al. (2012b) define the *delay transform* as the Fourier transform of a visibility for baseline  $ij$  and pseudo-Stokes parameter  $P$  along the frequency axis

$$\tilde{V}_{ij}^P(\tau, t) = \int dv \tilde{V}_{ij}^P(v, t) e^{2\pi i v \tau}. \quad (10.3)$$

We note that using a Blackman-Harris window will induce a correlation between consecutive  $\tau$  modes. The Fourier transform of the window function in frequency will be sharply peaked in the delay space, and can be ignored to some extent. Hence the self-correlation of  $V_{ij}^P(\tau, t)$  can be used to define the power spectrum, although the small correlation of different  $\tau$  modes could effect the variance of the power spectrum (Parsons et al., 2014).

The power at each delay-mode and baseline can be represented in terms of their respective Fourier components  $k_{\parallel}$  and  $k_{\perp}$  (Parsons et al., 2012b; Thyagarajan et al., 2015a):

$$P(k_{\parallel}, k_{\perp}) \approx |\tilde{V}_{ij}^P(\tau)|^2 \frac{X^2 Y}{\Omega B} \left( \frac{c^2}{2k_B v^2} \right)^2,$$

$$k_{\parallel} = \frac{2\pi v_{21\text{cm}} H(z)}{c(1+z)^2} \tau,$$

$$k_{\perp} = \frac{2\pi}{D(z)\lambda} b$$

for: bandwidth  $B$ , angular area of the beam  $\Omega$ ,  $v_{21\text{cm}} \approx 1420$  MHz, baseline length  $b$ , wavelength of observation  $\lambda$ , Hubble parameter  $H(z)$ , transverse comoving distance  $D(z)$  and redshift-dependent scalars  $X$  and  $Y$  (Parsons et al., 2012a). Note that the angular

area of the beam refers to the diagonal components of the Mueller matrices shown in Figure 3.4. For further discussion of forming polarized power spectra in  $k$ -space, refer to Nunhokee et al. (2017).

To avoid a noise-bias when forming the  $|\tilde{V}_{ij}^P(\tau, t)|^2$  term, we cross-multiplied consecutive integrations, rephasing the zenith angle of the latter to the former:

$$|\tilde{V}_{ij}^P(\tau, t)|^2 \approx |\tilde{V}_{ij}^P(\tau, t) \times \tilde{V}_{ij}^P(\tau, t + \Delta t) e^{i\theta_{ij,\text{zen}}(\Delta t)}| \quad (10.4)$$

where  $\theta_{ij,\text{zen}}(\Delta t)$  was the appropriate phasing for baseline  $ij$  and  $\Delta t = 10.7$  seconds.

Pseudo-stokes power spectra were formed for each pair of integrations, for every baseline. After forming power spectra, baselines of identical lengths were averaged together. Appealing to cosmological isotropy, baselines of the same length but different orientation should be sampling the same cosmological structure. These 2D power spectra were averaged over our 8 days of observations. Note that all averaging was performed after forming power spectra; this incoherent averaging was non-optimal from a signal-to-noise perspective outside the wedge, slightly reducing our sensitivity in the EoR window. However, the intention of this investigation was not a deep integration on noise; we were more interested in the polarized response of the instrument. As such, the power spectra presented in the Section below should be interpreted as approximate.

## 10.3 Results & Discussion

Power spectra are shown for the high and low bands in Figure 10.6 and Figure 10.7, respectively, where white dotted lines mark the boundary of the EoR window on the 2D plots. The same data are presented in middle and lower panels, with the latter overlaid as lines to emphasize common features of the power spectra with respect to baseline length.

Theoretical noise levels for the high and low bands were between  $P_{\text{noise}}(k) \approx 1.7 \times 10^8$  mK $^2$ Mpc $^3$ h $^{-3}$  –  $3.4 \times 10^9$  mK $^2$ Mpc $^3$ h $^{-3}$  in the high band, and  $2.3 \times 10^8$  mK $^2$ Mpc $^3$ h $^{-3}$  –  $6.1 \times 10^9$  mK $^2$ Mpc $^3$ h $^{-3}$  in the low band. These estimates used a temperature model of

the sky

$$T_{\text{sky}} = 180 \text{ K} \left( \frac{\nu}{180 \text{ MHz}} \right)^{-2.55}, \quad (10.5)$$

assumed receiver temperatures of 300 K and 600 K for the high band and low band, respectively (DeBoer et al., 2017, also see the public HERA Memo # 16). They were calculated according to the formalism for noise power spectra in Parsons et al. (2012b), with the inclusion of a baseline-number dependence (to account for different occupancies in each  $k_{\perp}$  bin). The estimates were roughly corroborated by our observations (see Figure 10.8). We observe excess noise on the shortest baselines (also obvious in the lower panels of Figures 10.6 and 10.7).

### 10.3.1 General features of the power spectra

The most striking feature of these power spectra is the degree of foreground isolation achieved in all pseudo-Stokes parameters. In similar studies of 2D polarized power spectra, both PAPER (Kohn et al., 2016) and LOFAR (Asad et al., 2017) measurements found “filled” regions of Fourier space out to the edge of the EoR window (in the delay-spectrum paradigm, this corresponds to the horizon; zenith angle  $\pm 90^\circ$ ), with some supra-horizon leakage (Pober et al., 2013) into the EoR window itself. The power spectra in Figures 10.6 and 10.7 show no such behavior; all foreground emission appears to be contained within a narrow region around  $k_{\parallel} = 0$  h/Mpc. This behavior was predicted for an array of HERA-like dishes by Thyagarajan et al. 2015a (although that study only concentrated on the Stokes I component).

Power at horizon delays, as predicted by Thyagarajan et al. (2015a) and Neben et al. (2016), was not observed. This was likely a resolution effect. To resolve horizon-delay power, one would need to sample many periods of  $\tau_h = b/c$ , where  $b$  is the magnitude of the baseline vector. The maximum length baseline in the HERA-19 array was 58.4 m, corresponding to a  $\sim 5$  MHz period: barely sampled by the 10 MHz windows we use in this study. The lack of horizon power is corroborated by the simulations of the HERA delay

response in Ewall-Wice et al. (2016a) and Thyagarajan et al. (2016), although those studies used a different windowing function for the delay transform. Their simulations also predict a high degree of foreground isolation: the presence of noise in our data of course meant that we do not realize the 11 dex of isolation that can be achieved in simulation, but the  $\sim$ 8 dex we do see, without any foreground subtraction and a simple calibration, speaks to the power of HERA’s future capabilities.

Visible in the observational data, but not in the simulation, is an excess of power at  $k_{\parallel} = 0.04 \text{ h/Mpc}$ , corresponding to a delay of 100 ns, which is independent of baseline length. This suggests that its origins are in the HERA signal chain. There are 15 m coaxial cables at one stage of the signal chain from the HERA dishes to the correlator<sup>2</sup>. In the limit of little delay induced by the cable and our limited delay resolution, a reflection along this stage of the signal chain would produce an alias of the foreground signal at a  $\tau \approx 100 \text{ ns}$  (Beardsley et al., 2016; Ewall-Wice et al., 2016b).

---

<sup>2</sup>This stage of the signal chain is only present in the commissioning array. Future HERA build-outs will transition to a different architecture (DeBoer et al., 2017).

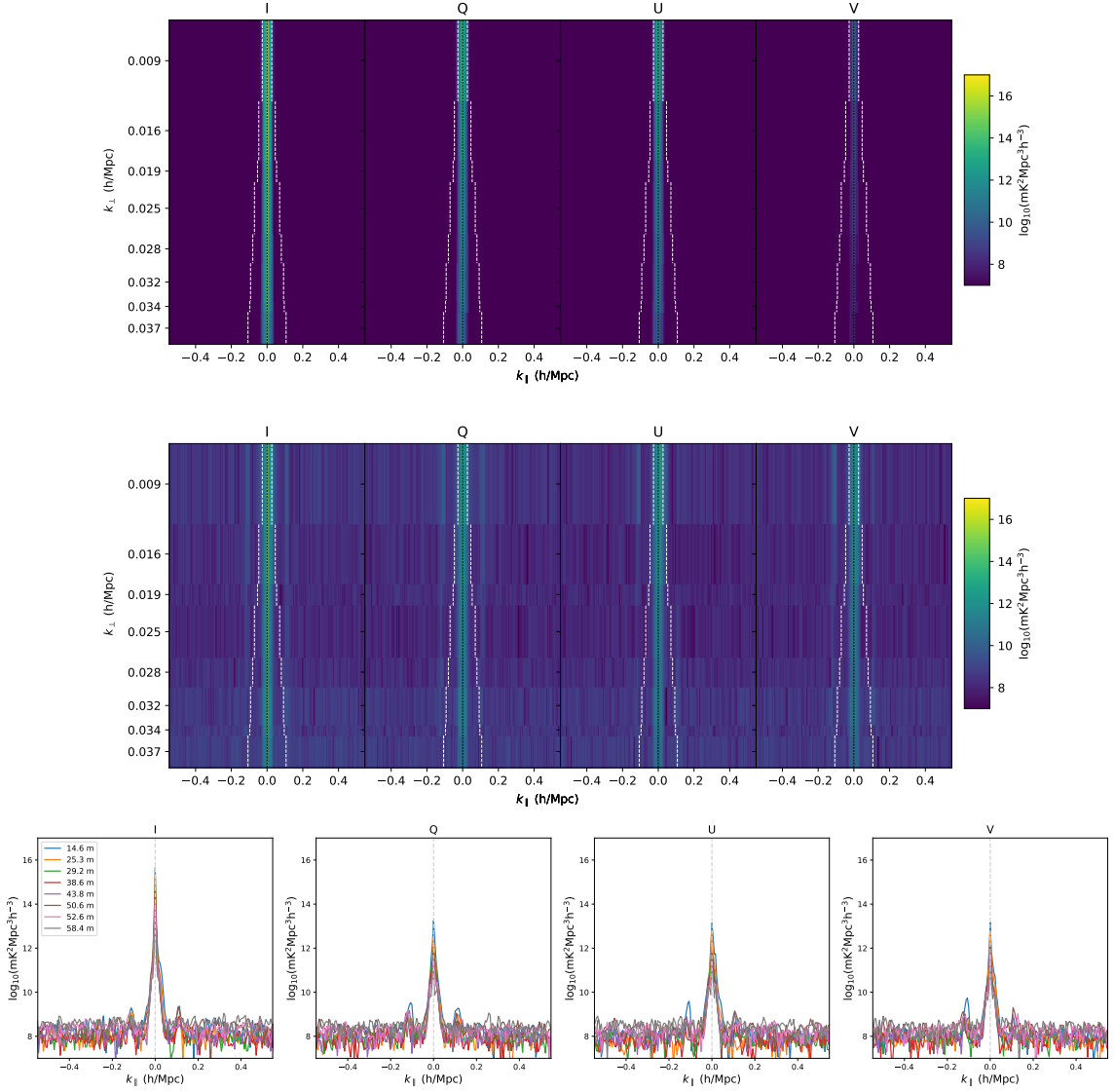


Figure 10.6: Results from the high-band (157–167 MHz). White dotted lines indicate the boundary of the pitchfork and the EoR window. A black dotted line indicates the  $k_{\parallel} = 0$  h/Mpc line. *Top:* Simulated power spectra in Stokes I, Q, U and V, following the formalism in Section 10.1 – no polarized sky model was used, so power in Stokes Q, U and V was only due to direction-dependent leakage from Stokes I. No instrumental noise was included in the simulation. *Middle:* Eight-day average power spectra from data. *Bottom:* The same data as shown in the middle panel, but with each baseline length overlaid on one another to allow shared features to be more easily identified.

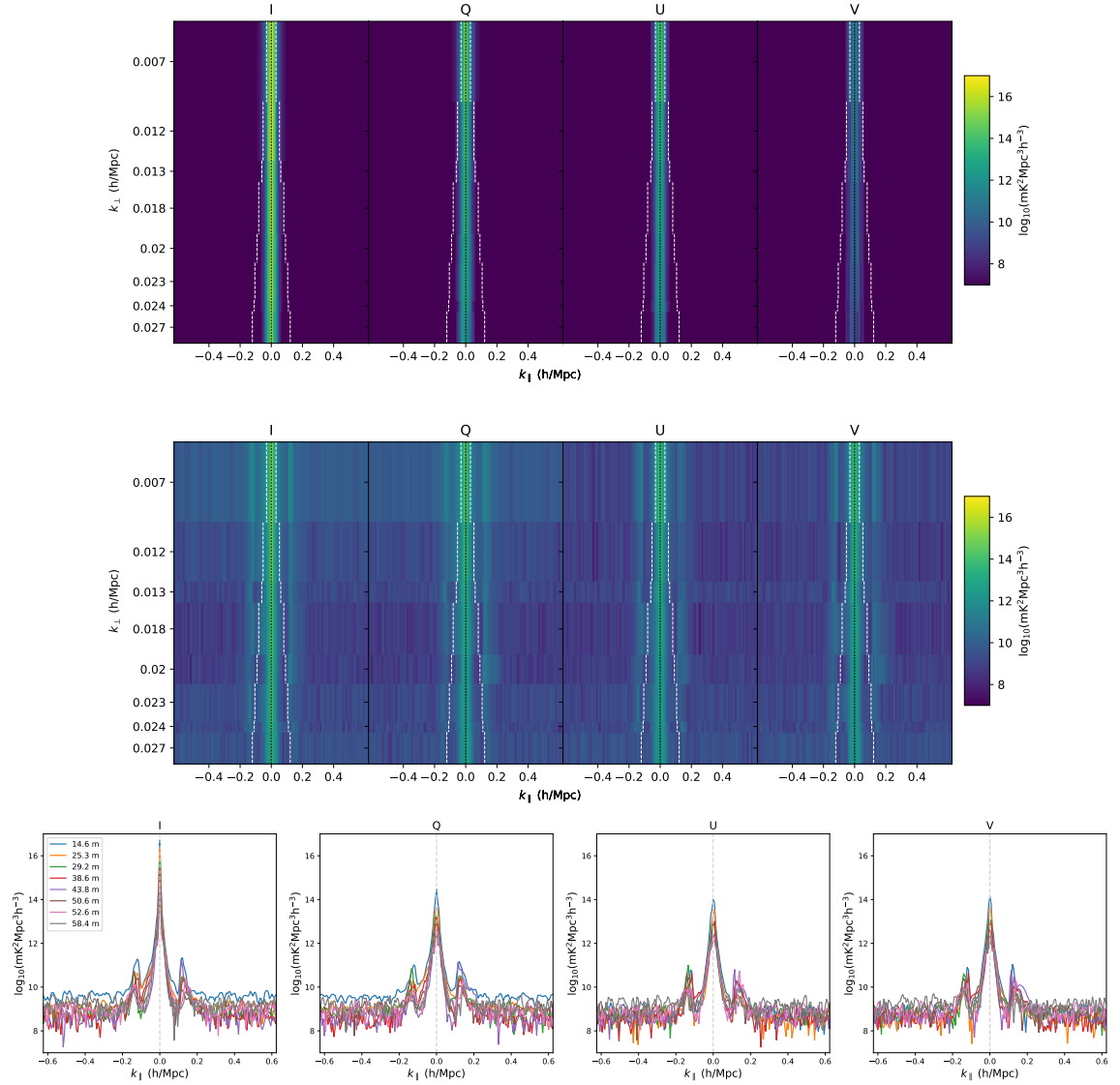


Figure 10.7: Results from the low-band (120–130 MHz), arranged in the same format as Figure 10.6.

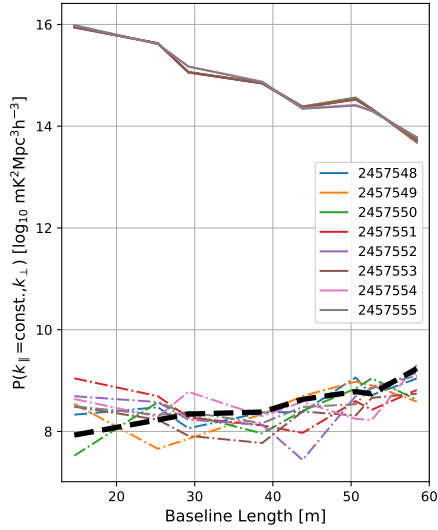


Figure 10.8: High band power as a function of baseline length for the center of the pitch-fork ( $k_{\parallel} = 0$  h/Mpc; solid lines) and in the EoR window ( $k_{\parallel} = 0.2$  h/Mpc; dot-dashed lines) for each JD of observation. The black dashed line represents the approximate noise power assuming a receiver temperature of 300 K. A very similar relationship is shown in the low band, but with a higher noise floor, which is consistent with system temperature as a function of frequency. The noise level climbs with baseline length as the compact nature of the array gives more short baselines to average-over in a given  $(k_{\parallel}, k_{\perp})$  bin than longer ones.

### 10.3.2 Day-to-day variability

The foreground and EoR window power levels appeared to be relatively stable between days, with variation most likely due to the incomplete sky model used for gain calibration. Figure 10.8 shows power as a function of baseline length for  $k_{\parallel} = 0$  h/Mpc (solid lines) and  $k_{\parallel} = 0.2$  h/Mpc (dot-dashed lines). Deviations from the mean at  $k_{\parallel} = 0$  h/Mpc may be a limitation imposed by our simplistic sky model. Since the noise levels in the EoR window region remained noise-like throughout our observations, the uncertainty in the absolute gain scale did not have a large impact on our largely-diagnostic investigation.

### 10.3.3 Polarimetric results

Figures 10.6 and 10.7 qualitatively illustrate that the simulations described in Section 10.1 reproduced the main features of the observed power spectra. The simulations were run only with a Stokes I sky component and no simulated calibration errors, so the only signal in the polarized power spectra was from wide-field beam leakage (Figure 3.4). An example comparison between simulation and observation in the image plane is shown in Figure 10.3.

In Figure 10.9 we show the power levels observed on the shortest baseline (14.7 m) compared to our simulations for each band. The simulations used an unpolarized diffuse sky model (the most recent version of the GSM; Zheng et al., 2017), which should be accurate at the scales probed by a 14.7 m baseline. Inset panels zoom-in on the region around  $k_{\parallel} = 0 \text{ h/Mpc}$ , where most of the foreground power was concentrated. We saw that the simulations reproduced  $\sim 75\%$  of the foreground power observed in pseudo-Stokes I in the high band, and over-predicted foreground power by  $\sim 35\%$  in the low band. This could have been due to unrealistic frequency scaling of the diffuse foregrounds in the GSM.

For pseudo-Stokes Q and U, the simulations accounted for  $\sim 60 - 75\%$  of power seen within the pitchfork region, suggesting that most of the power seen in these power spectra, at least for the shortest baselines, can be mostly attributed to direction-dependent leakage effects. As noted in Section 10.1, residual gain and phase errors are able to leak a fraction of pseudo-Stokes I into Q and U, but some fraction of the observed power ( $\leq 25\%$ ) may have been due to linearly polarized foregrounds. This is corroborated by residual power close to the location of the Galactic Center, and increased power over the sky, in the observed pseudo-Stokes Q and U skies compared to the simulated ones in Figure 10.3. As the Galactic Center is the highest-amplitude source of power, we expect residual gain errors to be most obvious in the same position as it is in the pseudo-Stokes I image. Such an excess is present in the observed pseudo-Stokes Q and U images, but absent in the simulated ones – pointing to direction-independent gain errors being present.

However, the simulated pseudo-Stokes Q and U images contain only direction-dependent leakage from Stokes I. Since they reproduce most of the features seen in the observed data, pseudo-Stokes Q and U are clearly dominated by direction dependent leakage.

Lenc et al. (2016) observed linearly polarized emission from diffuse structure with  $\sim 1.6 - 4.5\%$  fractional polarization at 150 MHz, corresponding to power levels of  $\sim 10^5 \text{ mK}^2 \text{Mpc}^3 \text{h}^{-3}$ . This power level is similar to expected EoR power levels (e.g. Lidz et al., 2007; Moore et al., 2013; Nunhokee et al., 2017); a detection of a power spectrum of polarized galactic synchrotron will require much deeper integrations.

The observed pseudo-Stokes V power spectrum was more poorly modelled by our simulation. In both bands we observed  $\sim 20$  dB more power in pseudo-Stokes V at  $k_{\parallel} = 0 \text{ h/Mpc}$  than predicted by our simulations. The peak power observed in pseudo-Stokes V was roughly 0.1% of the peak power observed in pseudo-Stokes I. Likewise in the sky images shown in Figure 10.3, there is little pseudo-Stokes V power in the simulated images, compared to observation. This suggests that most or all of the power in pseudo-Stokes V is due to direction independent leakage. While the leakage appears localized in Figure 10.3, we see in Figure 10.9 that it is statistically similar to pseudo-Stokes Q and U in power. Since  $D$ -terms cause direction-independent leakage from pseudo-Stokes I to pseudo-Stokes V, the excess power we observed could be interpreted as an approximate  $D$ -term level of  $\sim 1\%$  (Thompson et al., 2017). This is similar to  $D$ -term levels from other low frequency instruments such as MWA-32, which was found to have  $\sim 2\%$   $D$ -terms (G. Bernardi, private communication). The under-prediction of pseudo-Stokes V from the simulation could, of course, also be due to some unmodelled direction-dependent instrumental effect.

To understand which effect, if either, is dominant, a precise  $D$ -term calibration of HERA is required. This effort is underway with data taken with bright polarized point sources in transit, and will be presented in future work. Another potential cause of the discrepancy could have been that our simulations under-predicted Stokes V power, due to lack of accounting for some variety of instrumental circular polarization.

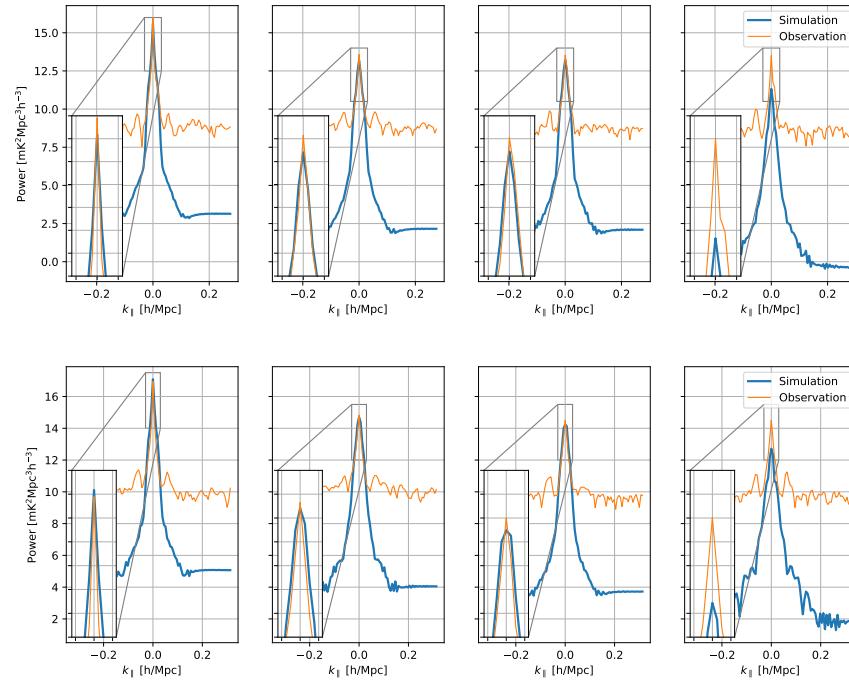


Figure 10.9: Simulated and observed power as a function of  $k_{\parallel}$  for the shortest baseline (14.7 m). *Right to left*: pseudo-Stokes I, Q, U and V; *above*: the high band; *below*: the low band. The simulations were noiseless and used an unpolarized sky model. Inset panels zoom-in on the peak region. They capture the foreground power levels in pseudo-Stokes I, Q and U, suggesting all power in Q and U is due to leakage from Stokes I. The power level in V is highly discrepant, however, suggesting some sort of beam-independent instrumental leakage.

In Section 10.3.1 we noted the presence of excess power at  $k_{\parallel} = \pm 0.04 \text{ h/Mpc}$  ( $\pm 100 \text{ ns}$ ) that was independent of baseline length, suggesting that it was due to a reflection along 15 m cables. Figure 10.9 shows that power at this delay is not consistent between polarizations. Stokes U and V power only exhibited excess signal at -100 ns in the high band, and in the low band, it was only Stokes U that did not exhibit that excess at +100 ns. This may be a clue about the polarization state of cable reflections, perhaps as a function of frequency, but we defer this to future work – noting it as a point of interest here.

## 10.4 Conclusions

In this work we have presented polarized power spectra from the HERA-19 commissioning array. With modest calibration, HERA is able isolate total intensity and polarized foregrounds to within the “pitchfork” region of  $k$ -space, as predicted by Thyagarajan et al. (2015a), lending confidence to its future performance as an instrument capable of both detecting and characterizing the EoR power spectrum. Of course, the array used in this study had just 19 antennae, 15 of which were used for analysis – future build-outs of HERA with up to 350 antennae will require strong quality-assurance efforts.

Simulations of the polarized response of the instrument, mapped into the same Fourier space as the data, suggest that most or all of the polarized power observed in pseudo-Stokes Q and U power spectra is due to direction-dependent beam leakage from pseudo-Stokes I. Residual gain and phase errors could account for the rest of the power, but some fraction of the total ( $\leq 25\%$ ) may be due to linearly polarized foregrounds. Excess power in pseudo-Stokes V may be due to  $D$ -terms at the 1% level, but a full image-based calibration with a polarized point source is required to confirm this. The general accuracy of our simulations suggests current modelling of the complex HERA beam is accurate.

# Chapter 11

## Deep integrations on polarization with PAPER-128

In Chapter 9, I presented polarized power spectra from a short integration – a few hours of one night – over a wide range of  $k_{\perp}$ -modes probed by the PAPER-32 polarized imaging array (Kohn et al., 2016). Chapter 10 presented the first power spectral results from HERA. The HERA-19 commissioning array was small and dense, meaning that only a few  $k_{\perp}$ -modes were accessible. For that study, we averaged over 10 hours per night, for 8 consecutive nights (Kohn et al., 2018). This Chapter presents results from the PAPER-128 array. In this Chapter I present roughly one quarter of the total number of observations recorded by this interferometer (Section 11.1). I show results of a deep integration on a very narrow range of  $k_{\perp}$ -modes (corresponding to  $\sim 30$  m spacings of the redundant grid; Section 11.2) and discuss the implications for deep, fully-polarized integrations with large interferometers (Section 11.3).

### 11.1 Observations & Reduction

PAPER-128 was the largest build-out of the PAPER experiment. As described in Chapter 4, PAPER-128 consisted of 128 antennas, 112 of which were arranged in a redundant

Table 11.1. PAPER-128 Observing Seasons & Epochs

Season	Epoch	Julian Dates	Calendar Dates	Notes
1	1	2456617 - 2456673	Nov 20, 2013 - Jan 15, 2014	1/8 F-Engine failure
	2	2456678 - 2456724	Jan 20, 2014 - Mar 7, 2014	Good
2	1	2456625 - 2456732	Mar 8, 2014 - Mar 7, 2014	Too few data
	2	2456843 - 2456873	Jul 4, 2014 - Aug 3, 2014	Uninteresting LST range
	3	2456881 - 2456928	Aug 11, 2014 - Sep 27, 2014	Many malfunctioning antennas
	4	2456942 - 2457008	Oct 11, 2014 - Dec 11, 2014	Good
	5	2457030 - 2457050	Jan 7, 2015 - Jan 27, 2015	Many malfunctioning antennas

grid. An annotated photograph of the array is shown in Figure 11.1. In this section, I review the PAPER-128 campaign (Section 11.1.1) and the subsequent reduction of roughly one quarter of the total number of observations (Section 11.1.2).

### 11.1.1 Overview of PAPER-128 observations

Observations were recorded for two years, with first light on November 20th 2013 and final readings on January 27th 2015. However, these observations were not always contiguous. Human errors, experimentation and malfunctioning electronics required the correlator and connected electronics to be turned off and restarted, altering the characteristic phasing and gain scale of the array. Each of these restarts constituted the beginning of a new ‘Epoch’ of the array which required different quality assurance steps and initial calibration stages. Table 11.1.1 summarizes the length and nature of these Epochs.

Figure 11.2 illustrates the challenge imposed by the correlator restarts. Epoch changes were characterized by large shifts in the overall phase of visibilities, of course leading to changed magnitudes of the real and imaginary parts of the visibilities recorded. The quality assurance metrics described in Chapter 6 were sensitive to these changes. Of course, absolute calibration – that is phasing to the correct point on the sky and scaling the visibilities from arbitrary to physical flux density units – had to be run separately on

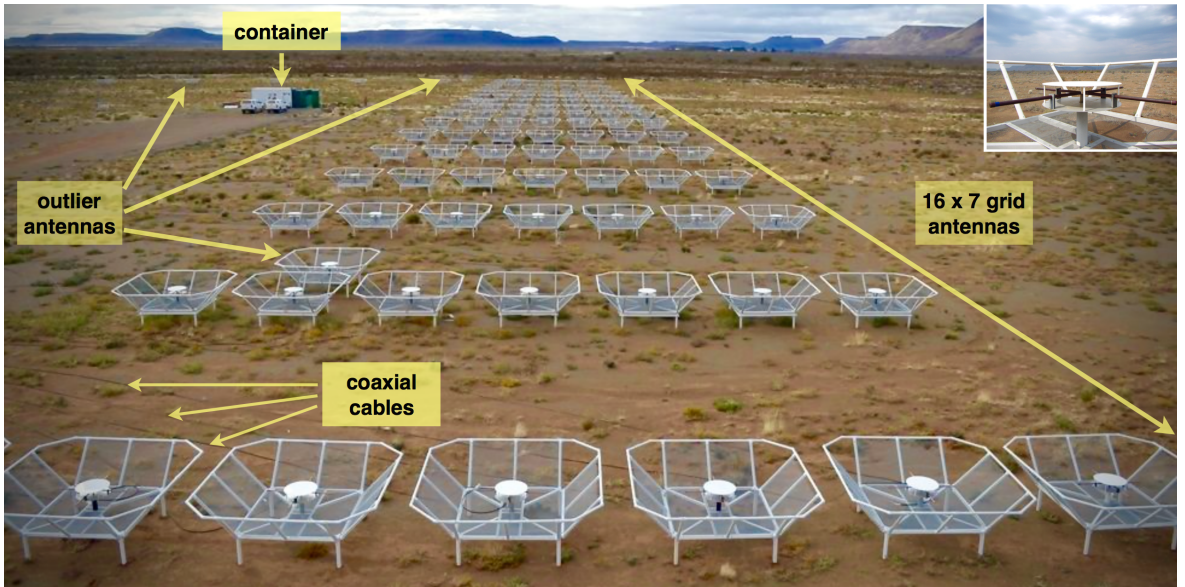


Figure 11.1: An annotated photograph of the PAPER-128 array, looking to the East. Highlighted are the 112 antenna redundant grid, with 15 m East-West spacings between each row; outlier antennas from the main grid used to increase *uv*-coverage; coaxial cables running to the receiverators and correlator (see Chapter 4). An inset panel shows a PAPER sleeved dipole. Photo credit: J. E. Aguirre. Figure credit: C. D. Nunhokee; (Nunhokee, 2018).

individual Epochs.

As shown in Table 11.1.1, Season 2 had a larger number of observed nights than Season 1. However, the analysis of Season 2 was especially challenging due to large numbers of malfunctioning antennas. This may have been due to the antennas ageing past a critical point. Nothing in the array was replaced during build-outs except for the correlator; 32 of the antennas had been out in the desert for 4–5 years (PAPER-32) and another 32 for 3–4 years (PAPER-64). Most of the time, these were the antennas that were identified as malfunctioning.

Season 2 Epoch 4 was relatively well-behaved, and may be analyzed in the future. For this work, we concentrated our analysis on Season 1. Season 1 Epoch 2 was ten days shorter than Season 1 Epoch 1, but Epoch 1 had two major challenges associated with it: a data loss event, and an F-engine failure. Due to human error, Epoch 1 data was deleted and had to be restored and recompressed (see Chapter 6). This was almost entirely successful, at the loss of one week’s worth of observations. The F-engine failure was more critical. We discovered during our analysis that exactly one eighth of the antennas in the array produced noise-like visibilities with the rest of the array, but normal correlations between one another. These antennas had “seceded” from the array. They shared the characteristic of all being attached to the same F-engine (of which there were eight; see Figure 4.2). This suggested that there was a clock-offset on that F-engine, resulting in no correlation between the signal from those antennas and those running through the other in-sync F-engines.

This left Season 1 Epoch 2 as the most well-characterized and well-behaved Epoch of PAPER-128 observations, and we focused on this Epoch alone from now on. Cross-polarization metrics identified seven incorrectly-rotated antennas, which were corrected during initial processing. Eight antennas were identified as malfunctioning by mean visibility amplitude metrics, including one of those that was incorrectly-rotated. The state of the array for Season 1 Epoch 2 is summarized in Figure 11.3.

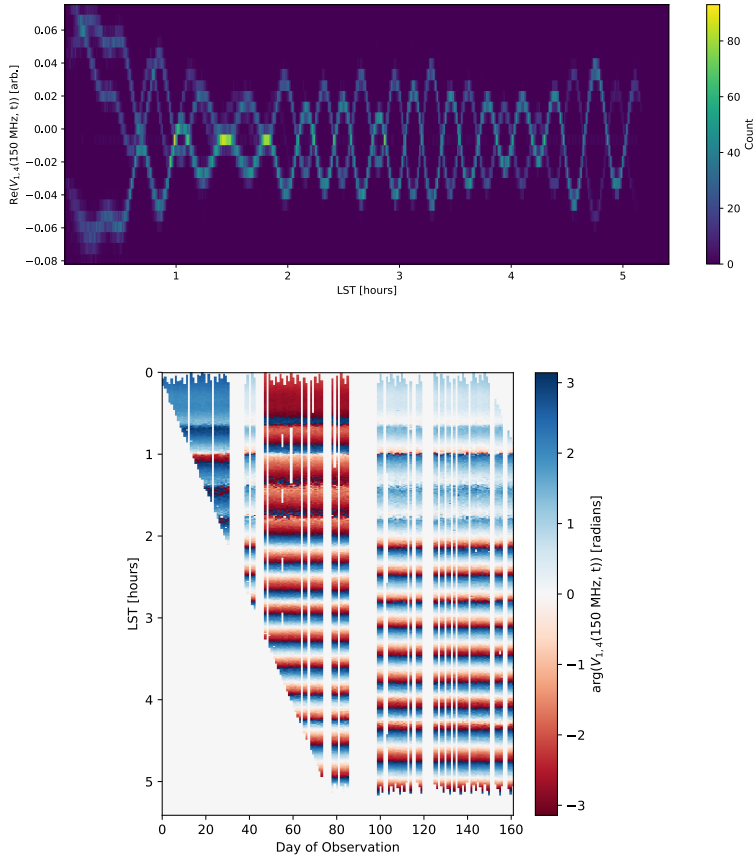


Figure 11.2: The challenge of Epoch changes. Shown are all of the Season 2 time samples of the visibilities recorded by the 30 m baseline between antennas 1 and 4, LSTs 0–5, for only the 150 MHz frequency bin. The above panel shows a histogram of the real part of the visibilities as a function of LST – there is a dramatic change in magnitude with respect to LST. Likewise, the lower panel shows the phase of each visibility sample (color axis) as a function of LST (vertical axis) and day of observation (x axis). There are obvious large shifts in phase, which require separate calibration stages.

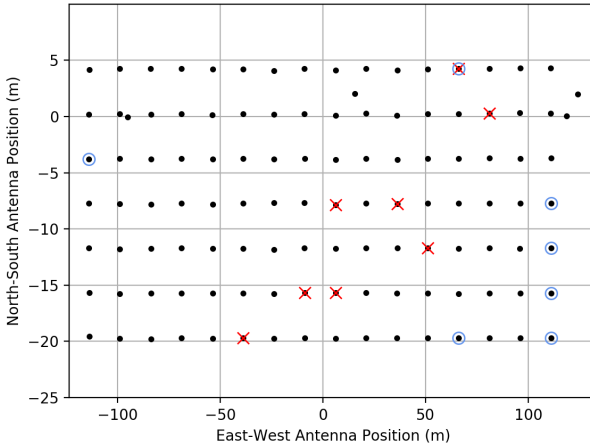


Figure 11.3: Good, bad (red crosses) and rotated (blue circles) antennas in Season 1 Epoch 2, as identified by the cross-polarization and visibility amplitude metrics defined in Chapter 6.

### 11.1.2 Reduction of Season 1 Epoch 2 data

After correcting for cross-polarized and malfunctioning antennas, we were able to begin processing the data using the redundant calibration techniques described in Chapter 7. We used the phase-flattening algorithm described in Section 7.1.2 to solve for phase slopes for each antenna. This was performed for the North-South and East-West feed arms separately using the linear instrumental polarizations ('nn' and 'ee'), as this method is sensitive to signal-to-noise. We performed a single calculation of these overall delays at the start of the Epoch, and applied those to the rest of the days observed. These overall delays are largely due to electrical delays along the cables leading to the receiverators and the correlator, so we did not expect them to vary a by large amount.

#### 11.1.2.1 Redundant calibration

After phase-wraps were flattened, the OMNICAL algorithm could be invoked safely. For this study, we implemented the *4pol+minV* calibration method. For a full exploration of

OMNICALibration methods, see Chapter 7. Briefly, the *4pol+minV* calibration scheme redundantly solves for diagonal gains for the North-South and East-West feed arms at the same time, *and* imposes that the ‘ne’ and ‘en’ visibilities are equal. That is, it produces a redundant calibration which minimizes pseudo-Stokes V. Figures 11.4 and 11.5 show the successful results of the *4pol+minV* OMNICALibration, where visibilities from 30 m East-West baselines showed a high degree of redundancy in all pseudo-Stokes polarizations, and pseudo-Stokes V is almost complete noise-like.

After calibration, we down-selected to only the baselines we sought to analyze for our power spectrum studies. This was partly a utilitarian step: reducing the entire data set would represent a large feat of data processing, since Season 1 Epoch 2 was  $\sim 2.5$  TB in size if all baselines were retained, and several processing stages that would duplicate the data were still required. The baselines kept were the 30 m East-West type and their closest diagonals – that is, 30 m East-West &  $\pm 4$  m North-South baselines (e.g. Parsons et al., 2014).

### 11.1.2.2 Foreground removal

To remove foreground signal from the data, we implemented a variation of the 1D-CLEAN (Parsons & Backer, 2009) used by past PAPER studies (Parsons et al., 2014; Ali et al., 2015; Jacobs et al., 2015; Moore et al., 2017; Kerrigan et al., 2018). Instead of performing an iterative CLEAN we used a linear least-squares approach which we termed linCLEAN.

Using linCLEAN, we endeavoured to model the foreground component of the visibilities using the finite number of Fourier modes that exist within the foreground wedge of the EoR window paradigm. The number of these modes was set by the frequency resolution of the instrument, and the baseline length (see Chapter 5). The Fourier conjugate of the frequency axis, known as the delay axis, is specified through the delay transform of a visibility, which for short baselines may be written as (Parsons et al., 2012a):

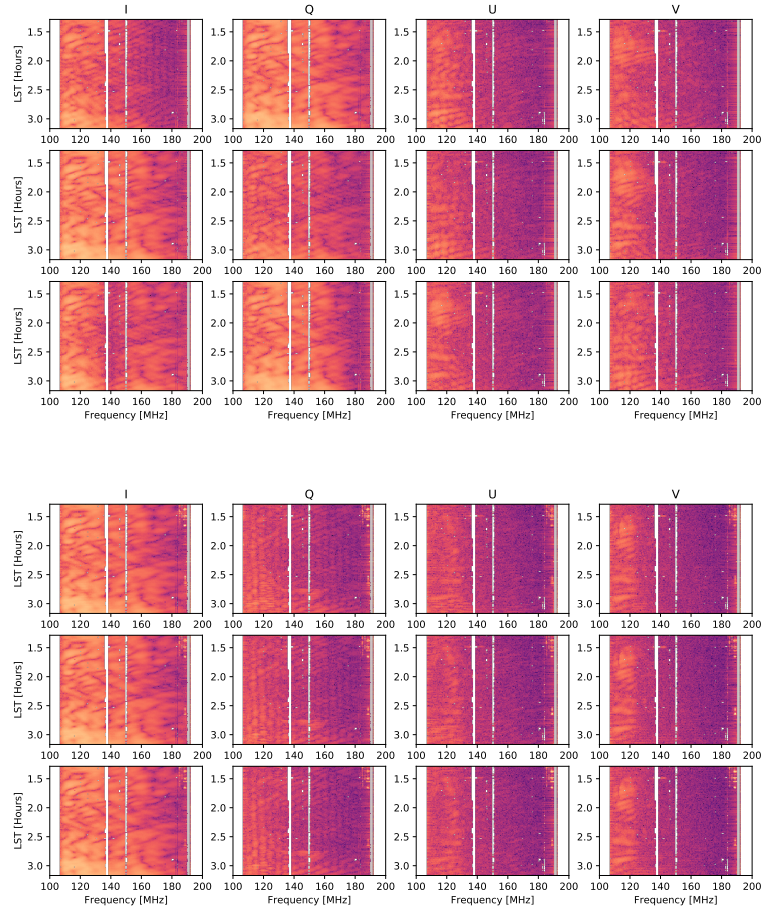


Figure 11.4: Amplitudes of three redundant visibilities before (above) and after (below) OMNICALibration using the *4pol+minV* scheme. All four pseudo-Stokes polarizations attained a high degree of redundancy in magnitude after calibration. The color axis is logarithmic and spans 5 orders of magnitude in arbitrary data units.

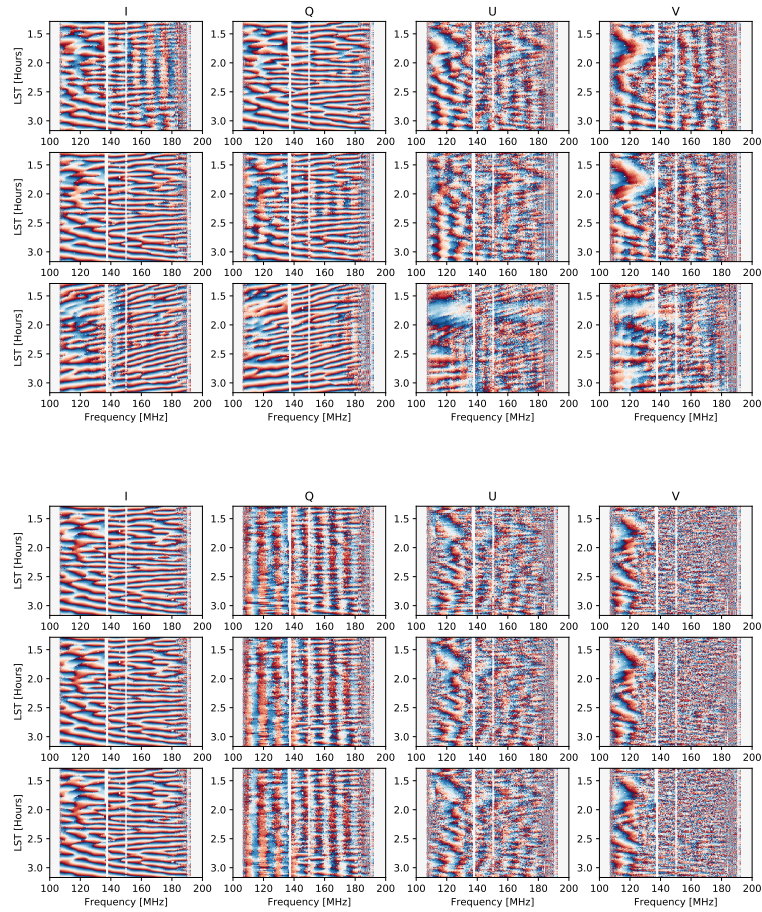


Figure 11.5: The same visibilities as shown in Figure 11.4, but showing their phases instead of their amplitudes. Again, a high degree of redundancy is obtained between baselines for all polarizations. The color axis is linear and spans  $\pi$  (red) to  $-\pi$  (blue) radians.

$$\tilde{V}(\tau) = \int_{v_{\min}}^{v_{\max}} V(v) \exp(2\pi i \tau v) dv \quad (11.1)$$

for visibility  $V(v)$  and delay mode  $\tau$ . Delay modes become estimators for the Fourier-transformed brightness temperature field.

We constructed a visibility  $\vec{m}(v)$  as a model, per time integration, of an individual visibility  $\vec{d}(v)$  (which we represent as a vector along the frequency axis), seeking to minimize the chi-square

$$\chi^2(v) = (\vec{d}(v) - \mathbf{A}(v', \tau)\vec{m}(v))^T \mathbf{W}(v', v) (\vec{d}(v) - \mathbf{A}(v, \tau)\vec{m}(v)). \quad (11.2)$$

In the above equation, the matrix  $\mathbf{A}$  had dimensions “number of frequency channels” by “number of allowed delay modes”. An allowed delay mode  $\tau$  was within the interval  $[0, \frac{|\vec{b}|}{c} + t_{SH}]$ , for baseline vector  $\vec{b}$ , speed of light  $c$  and an allowed “supra-horizon leakage” term  $t_{SH}$  (Pober et al., 2013), which we set to 15ns.

The contents of  $\mathbf{A}$  were the concatenation of matrices  $\mathbf{C}$  and  $\mathbf{S}$ :

$$\mathbf{C}_{ij} = \cos(2\pi v_i \tau_j) \quad (11.3)$$

$$\mathbf{S}_{ij} = \sin(2\pi v_i \tau_j) \quad (11.4)$$

$$(11.5)$$

for frequency channel  $i$  and delay bin  $j$ . The matrix  $\mathbf{W}$  was diagonal, and assigned weighting per frequency channel. With an estimated system temperature one could implement an inverse variance weighting per frequency channel, but we pursued a simpler scheme where the entries were zero for RFI-flagged channels, and unity otherwise.

This system was least-squares solvable for the delay modes, and granted a foreground model

$$\vec{m}(v) = (\mathbf{A}^T \mathbf{W} \mathbf{A})^{-1} \mathbf{A}^T \mathbf{W} \vec{d}(v) \quad (11.6)$$

which could subsequently be subtracted from the  $\vec{d}(v)$ , leaving only the noise-like backgrounds.

We ran linCLEAN on the Epoch of OMNICALibrated data, using the entire unflagged part of the band (for details on flagging of PAPER-128 data, see Chapter 6) to obtain an estimate of  $\mathbf{A}$ . After this, we implemented a round of RFI flagging that clipped any samples that represented  $> 4\sigma$  fluctuations above the average, where averages were performed along the time and frequency axes.

### 11.1.2.3 Binning in LST

We could then average-down on the noise by binning visibilities according to the LST they were observed at. The LST bin size used was 41s long, and we split the Epoch into even and odd days, constructing two separate LST-binned data sets. Cross-multiplying these allowed us to construct an unbiased power spectrum estimate (e.g. Parsons et al., 2014, Cheng et al., *submitted*). Unflagged RFI events would dominate any other signal in a given LST bin. To avoid binning RFI with sky signal, before averaging we computed the median of all observations in a given LST bin and flagged any observations with amplitude  $> 3\sigma$  above the median. This clipping narrowed the distribution of visibilities about the median, altering the thermal noise variance, but leaving the expectation value unchanged, so we expect little loss of signal due to this step.

For this analysis, we created two LST-binned data sets (each split into even and odd days): a set constructed from the foreground subtracted visibilities, and another set with the foregrounds included. We used the latter to calculate an absolute calibration of both data sets.

### 11.1.2.4 Absolute calibration & fringe-rate filtering

We formed images of the Pictor A transit in order to derive an absolute calibration for the ‘n’ and ‘e’ feed arms in the fashion described in Chapter 7. We converted the MIRIAD files of the LST-binned foreground data into CASA (McMullin et al., 2007) Measurement Sets at  $LST \approx 5.3$  hours (the relevant LST for the transit of Pictor A). Our sky model consisted only of Pictor A as a unpolarized point source. Because we had already down-selected to

the power spectrum baselines, Pictor A completely dominated the signal. The images of the four pseudo-Stokes parameters we obtained are shown in Figure 11.6. In that image, pseudo-Stokes I is on a color scale with double the dynamic range of Q, U and V – that is, pseudo-Stokes Q, U and V were almost completely noise-like. In pseudo-Stokes I, Pictor A dominated the field. These images were low quality because only the power spectrum baselines were used to produce the image, leading to large grating lobes and an elongated point-spread function; shown in Figure 11.7.

We used the CASA bandpass routine to derive an overall frequency-dependent scaling that brought the North-South and East-West dipole arms to a physical scale that minimized pseudo-Stokes Q in Pictor A, and converted the data units to a physical level in Janskies. For the Jansky scaling we used the spectrum from Jacobs et al. (2013). CASA provided separate scalings for all antennas used in the analysis. We plot the average scaling for the North-South and East-West dipole arms in Figure 11.8, shading-in the standard deviation between antennas. We implemented aggressive RFI flags, leading to large gaps in the spectrum. The higher frequency portion of the band had a very low variance its bandpass solutions, as expected given that they were OMNICALibrated and that the low band was historically poorly-behaved and characterized (e.g. Chapter 7).

As discussed in Chapter 6, every baseline not only samples characteristic delay modes based on its length, but also characteristic modes in time, per frequency, known as ‘fringe rates’ (if frequency dependence is ignored, they are referred to as “delay rates”; e.g. Parsons & Backer, 2009). For drift-scan telescopes such as PAPER, the sky, beam and fringe terms are locked to one another and can be thought of as an enveloped fringe pattern which varies in time as the Earth rotates. The rate of change of this pattern – the fringe rate – depends only on the baseline length (which gives the fringe width) and the position of the drift-scanning telescope on Earth. By Fourier-transforming along the time axis of recorded visibilities, one can identify a “window” of physical Fourier modes that represent fringe rates reflective of the Earth’s rotation. Such a window is shown for a 30 m single baseline in Figure 11.9, highlighted by red dashed lines. By convolving an

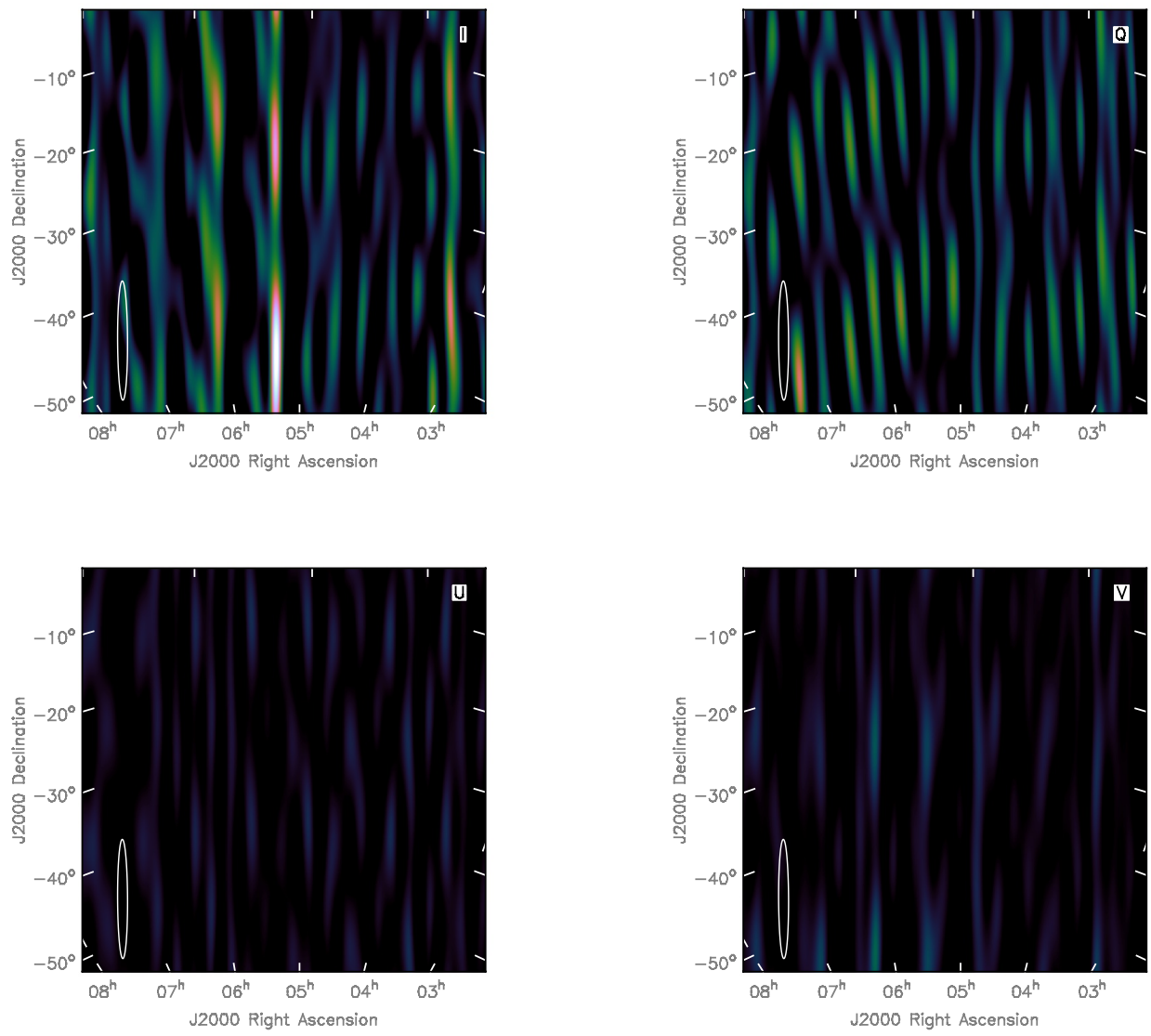


Figure 11.6: Images of Pictor A, used to calibrate the absolute scaling to physical units. These images are multi-frequency syntheses, but we used per-channel information for the final calibration (see Figure 11.8). Pseudo-Stokes I is on a linear scale of twice the dynamic range of pseudo-Stokes Q, U and V. A beam ellipse is shown in the South-West corner of the images. The poor quality of the images is a result of using only the baselines that go into the power spectrum estimates. Pictor A dominates the field in pseudo-Stokes I, and is of the morphology expected given the PSF shown in Figure 11.7.

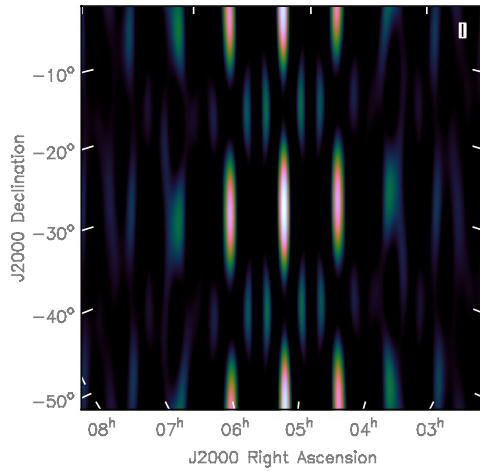


Figure 11.7: The point-spread function of an array consisting only of the  $\sim 30\text{ m}$  power spectrum baselines. The sparseness and asymmetry of the array lead to an elongated PSF with large grating lobes.

appropriate filter, one could extract these physical fringe rates and filter-out noise. This is equivalent to changing the shape of the primary beam of an antenna after observation, and was explored in Parsons et al. (2016), and implemented in Ali et al. (2015). However, because the range of physical fringe rates for a short baseline is narrow, this amounts to correlating a large number of visibility measurements in time, which must be accounted for in signal-to-noise estimates (Ali et al., 2015, Cheng et al., *submitted*).

We implemented such a filter on the LST-binned and absolute-calibrated background data, and proceeded to form power spectra.

### 11.1.3 Forming power spectra

As shown in Figures 11.4 and 11.8, the 150–180 MHz section of the band had lower noise and a more precise calibration. Within this, we down-selected to the 10 MHz-wide 155–165 MHz sub-band to form power spectra. This bandwidth was appropriate for an

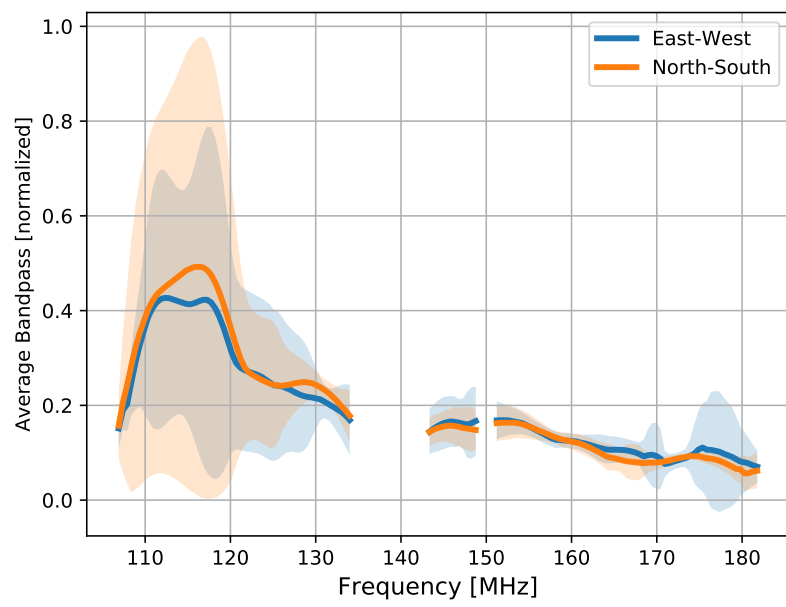


Figure 11.8: The average bandpass scaling used for absolute calibration, with shading indicating the  $1\sigma$  deviation about the average across antennas.

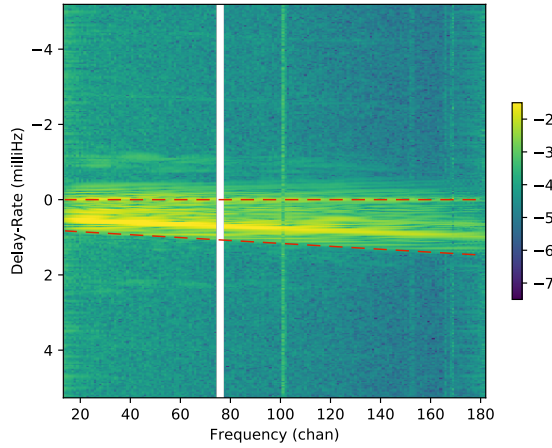


Figure 11.9: Delay-rate vs. frequency for a 30 m baseline in the ‘xx’ (East-East) polarization. The color axis is logarithmic, in arbitrary data units – there is a clear “window” of delay-rate modes of high amplitude, highlighted with red dashed lines. These correspond to physical modes to do with the Earth’s rotation. The rest of the delay-rates are simply noise-modes and can be filtered-out.

EoR analysis, since the HI signal is to a reasonable approximation coeval over the corresponding redshift range (Furlanetto et al., 2006). The central redshift our frequencies corresponded to was  $z = 8.07$  (we assumed the Planck Collaboration et al. (2016c) cosmological parameters throughout this Chapter).

Power spectrum estimators per baseline and time were formed by cross-multiplying delay-transformed visibilities between even and odd days, at identical  $\tau$  modes and LSTs:

$$\hat{P}_{ij}(\tau, t) = \left( \frac{\lambda^2}{2k_B} \right)^2 \frac{X^2 Y}{\Omega_{PP} \Delta v} \left\langle \tilde{V}_{ij}^{*,P,\text{even}}(\tau, t) \tilde{V}_{ij}^{P,\text{odd}}(\tau, t) \right\rangle. \quad (11.7)$$

Above,  $\hat{P}_{ij}(\tau, t)$  is an estimate of the power spectrum for baseline  $ij$ , for delay mode  $\tau$  at LST  $t$ . The  $\lambda^2/2k_B$  term is the conversion from Jansky to Kelvin,  $\Omega_{PP}$  is the solid angle of the squared primary beam,  $\Delta v$  is the 10 MHz bandwidth and  $X^2 Y$  is the conversion from observed volume  $\Omega_{PP} \Delta v$  to cosmological volume in  $h^{-3}\text{Mpc}^3$  (Parsons et al., 2012a).  $\tilde{V}_{ij}^{*,P,\text{even}}$  indicates the delay-transformed visibility for baseline  $ij$ , conjugated, for pseudo-

Stokes polarization  $P$  within the “even days” LST-binned data set.

Delay modes could be converted to  $k_{\parallel}$  line-of-sight modes measured in  $h/\text{Mpc}$  following

$$k_{\parallel} = \frac{2\pi v_{21\text{cm}} H(z)}{c(1+z)^2} \tau, \quad (11.8)$$

where  $v_{21\text{cm}} \approx 1420.1 \text{ MHz}$ , and  $H(z)$  is the Hubble parameter at redshift  $z$ . The angular cosmological distance surveyed was proportional to the magnitude of the baseline length  $b$ , represented in Fourier space by  $k_{\perp}$ :

$$k_{\perp} = \frac{2\pi}{D(z)\lambda} b \quad (11.9)$$

where  $D(z)$  is the transverse comoving distance at redshift  $z$ . For the  $\sim 30 \text{ m}$  baselines used in this study,  $k_{\parallel} \gg k_{\perp}$ .

The spherically-averaged power spectrum estimate  $\hat{P}(k)$  could be formed by averaging over LSTs and redundant baselines, where  $k^2 = k_{\parallel}^2 + k_{\perp}^2$ . These estimates in turn were averaged over the three separation types described in Section 11.1.2.1. Uncertainties were estimated by bootstrapping over groups of redundant baselines and LST samples. Obtaining the correct uncertainties when bootstrapping from the data used to form the estimate is not a trivial process, and we defer the reader to Cheng et al. (*submitted*) for full details of this important step.

Past PAPER power spectrum results have used inverse covariance-weighting and optimal quadratic estimators to improve the accuracy of the final power spectrum estimate (e.g. Parsons et al., 2014, Cheng et al., *submitted*). We do not implement any weighting in our power spectrum estimates. This avoided risk of signal-loss effects, but more generally avoided making any assumptions about the nature of the polarized sky. Down-weighting polarized foregrounds using optimal quadratic estimation is a contemporary analysis challenge that has not yet been implemented on data.

## 11.2 Results

Figure 11.10 shows the spherically-averaged power spectra for pseudo-Stokes I, Q, U and V with 95% confidence intervals. Green curves show analytical thermal noise estimates drawn from a 21CMSENSE model of the array (Pober et al., 2014; Pober, 2016) and given our observing time and bandwidth. The analytical thermal noise estimates used a simplistic model of the polarized beam, leading to different, but valid, noise levels per Stokes parameter. An equivalent series of power spectra based on Gaussian noise of the same variance as our data are shown in Figure 11.11, as a consistency-check on our method.

All of the power spectra in Figure 11.10 showed an excess at low  $k$  values, consistent with spectral structure of the PAPER beam and signal chain leaking power outside of the foreground wedge (Pober et al., 2013; Kerrigan et al., 2018). Excesses at  $k \approx 0.3\text{h/Mpc}$  in these power spectra were also seen in PAPER-32 (Moore et al., 2017) and PAPER-64 (Kolopanis et al., *submitted*), suggesting an artefact from the PAPER signal chain was the cause.

Neglecting these artefacts, pseudo-Stokes I power spectra were broadly consistent with the analytical noise estimate, with a slight bias compared to the pure-noise power spectra of Figure 11.11. This represented an upper limit of  $\Delta_{21\text{cm}}^2(k) \lesssim (140\text{mK})^2$  at  $k = 0.2\text{ h/Mpc}$ , which is competitive with contemporary limits (e.g. Kolopanis et al., *submitted*).

The pseudo-Stokes Q power spectrum was largely inconsistent with noise, with excesses at  $0.15\text{ h/Mpc} \leq k \leq 0.2\text{ h/Mpc}$  and  $0.3\text{ h/Mpc} \leq k \leq 0.35\text{ h/Mpc}$ . For this power to be due to Faraday-rotated emission from the diffuse foregrounds probed by a 30 m baseline would require rotation measures of  $\sim 30\text{ rad m}^{-2}$  and  $\sim 60\text{ rad m}^{-2}$ , respectively (Moore et al., 2013). Such high rotation measures have not been observed on diffuse scales (e.g. Oppermann et al., 2012; Bernardi et al., 2013; Lenc et al., 2016). Neither Asad et al. (2016) nor Lenc et al. (2016) found polarized point sources of such high rotation measure in their surveys of the LOFAR and MWA EoR fields, respectively. Kohn et al. (2016) showed that the PAPER beam was not expected to scatter power to such high  $k_{\parallel}$  values.

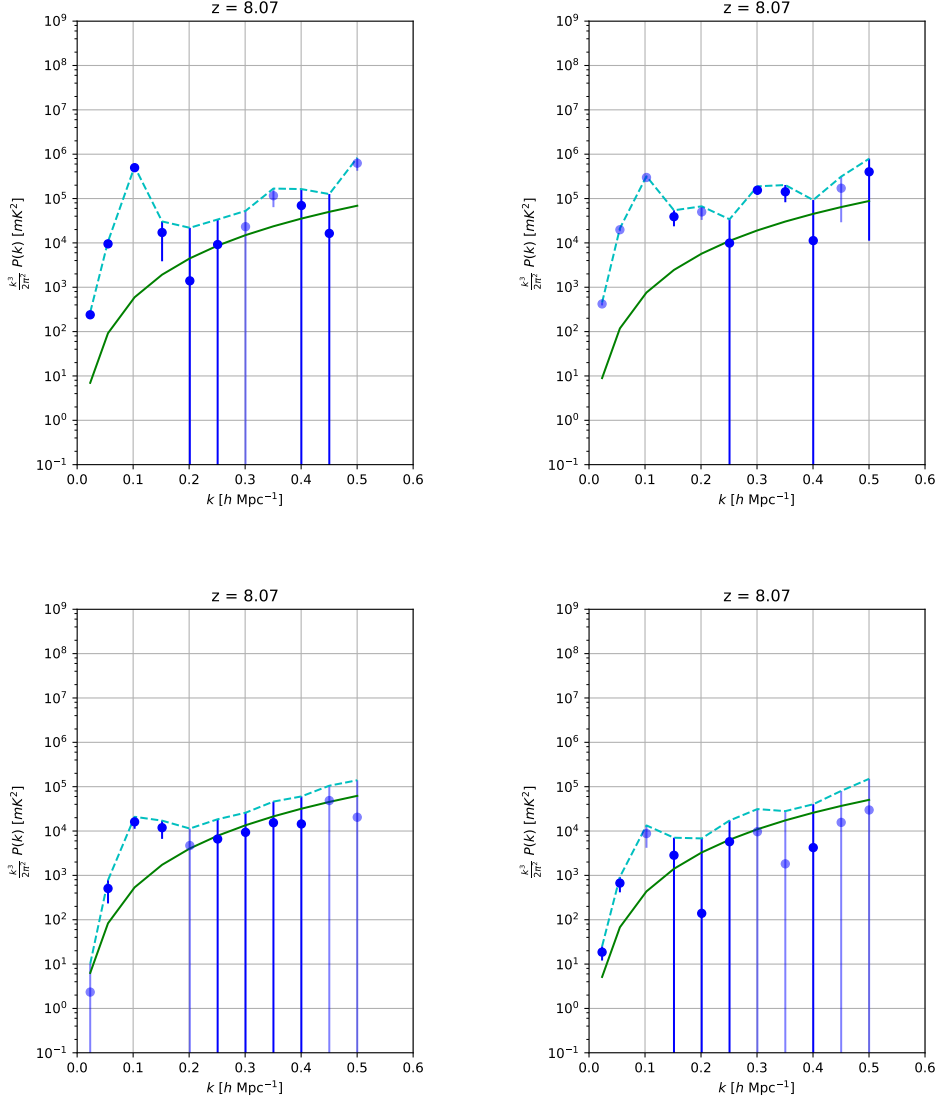


Figure 11.10: Spherically-averaged power spectra in pseudo Stokes I, Q (top left, top right) U and V (bottom left, bottom right). Pale points indicate negative values. Error bars show 95% confidence intervals, and the cyan dashed line indicates the  $1\sigma$  upper-limit given by each power spectrum. The green curve is the analytical thermal noise estimate, drawn from 21CMSENSE.

These factors pointed to the excess of pseudo-Stokes Q power as an indicator of calibration errors and instrument systematics leaking pseudo-Stokes I into Q. The effect is also likely larger than observed in the power spectra, as some attenuation will have occurred during LST binning due to ionospheric effects (Moore et al., 2017, Martinot et al. (*in prep.*)).

Simulations by Nunhokee et al. (2017) showed that Stokes Q and U power may exist at  $\Delta_{Q,U}^2(k) \approx 2 \times 10^4 \text{ mK}^2$  levels as the ensemble average of Faraday-rotated polarized point sources (for a particularly pessimistic sky model). However, it is doubtful that we detected such power, since the pseudo-Stokes U power spectrum is so different from Q.

At  $k > 0.15 \text{ h/Mpc}$ , pseudo-Stokes U and V power spectra showed excellent consistency with noise, both in comparison the analytical noise estimate and the pure-noise power spectra shown in Figure 11.11. This suggests that the excess in pseudo-Stokes Q, if due to calibration errors, was due to the diagonal gains being mis-matched. Uncalibrated off-diagonal gains,  $D$ -terms, leak pseudo-Stokes I into U and V (Thompson et al., 2017). We saw little evidence for such leakage.

Treating power at  $k = 0.2 \text{ h/Mpc}$  as a limit (valid for U and V, but less realistic for Q), our  $1\sigma$  upper limits on polarized power were:  $\Delta_Q^2(k) \lesssim (245 \text{ mK})^2$ ,  $\Delta_U^2(k) \lesssim (100 \text{ mK})^2$  and  $\Delta_V^2(k) \lesssim (83 \text{ mK})^2$ . These are the deepest limits to date on polarized power in the EoR window.

### 11.3 Discussion & Conclusions

This analysis represented the first power spectrum results from PAPER-128. The processing and reduction of the two Season and seven Epochs taught us many lessons about the challenges associated with long integrations of large low-frequency arrays. These lessons were invaluable for the construction and activation of HERA, and the quality assurance techniques developed (see Chapter 6) for such an analysis continue to be essential components of the HERA real-time system (Ali et al., *in prep.*).

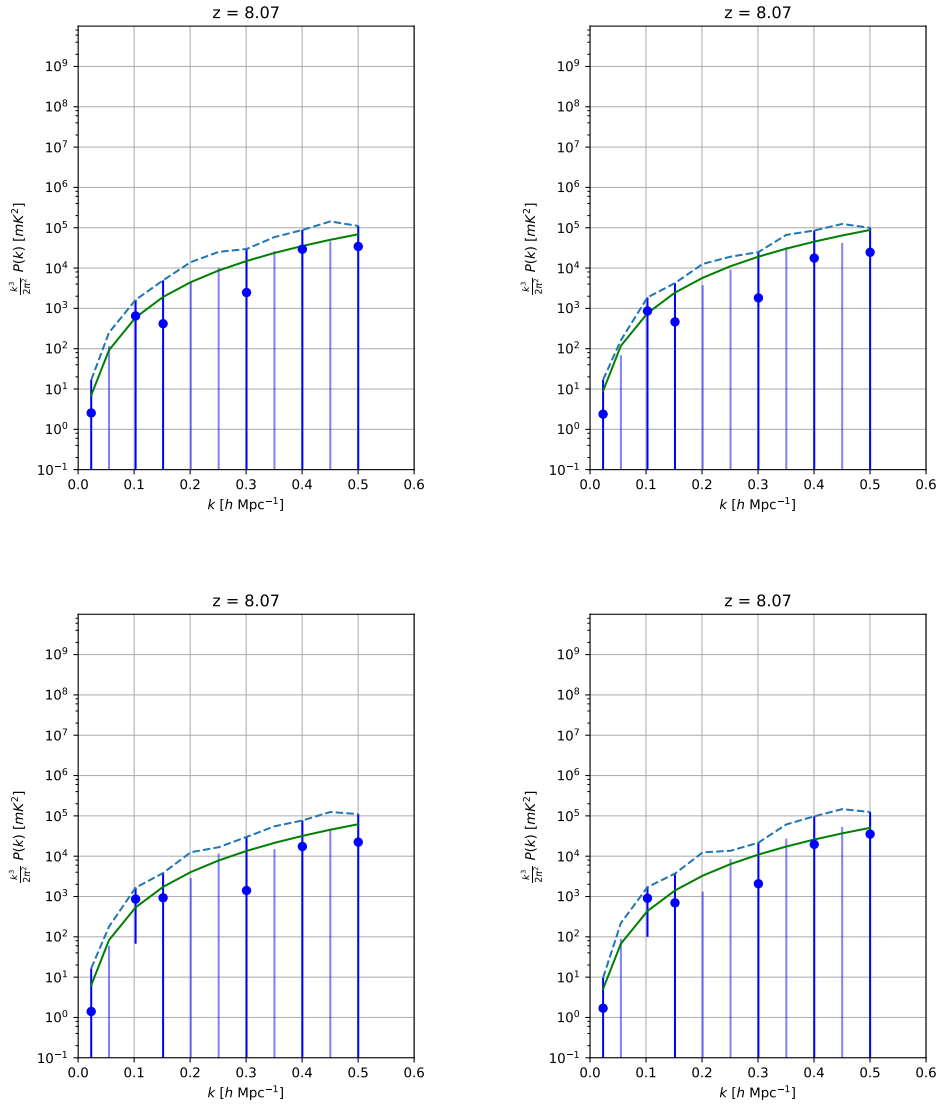


Figure 11.11: Spherically-averaged power spectra of noise based on the variance of the data in our power-spectrum band. Pale points indicate negative values, error bars show 95% confidence intervals, and the dashed line indicates the  $1\sigma$  upper-limit. All power spectrum values are consistent with the analytical noise estimate, showing the accuracy of our methods.

Nunhokee et al. (2017) and Asad et al. (2015) predicted that the power spectrum of diffuse polarized foregrounds should exist outside of the foreground wedge at  $\Delta^2(k) \approx 10^3 \text{ mK}^2$ . This is roughly two orders of magnitude above predicted EoR power (Lidz et al., 2007), and will therefore need to be extremely well characterized, since just 1% of leakage into Stokes I could prevent an EoR detection. This study advanced that effort, setting the most stringent upper limits on pseudo-Stokes Q, U and V power to date. However, any deeper integrations with PAPER-128 may be limited by systematics due to calibration errors.

It is unlikely that the detection of power in much of the pseudo-Stokes Q power spectrum is real. However, this could be tested in the future by collecting a Epoch’s-worth of ionospheric data and calculating the attenuation coefficient for different fractions of the Epoch being LST-binned together. If real pseudo-Stokes Q power is present in the power spectrum, the noise level should decrease with increasing numbers of observations in the LST bin at a rate faster than a coherent average. This variety of “jackknifing on the ionosphere” will be investigated in future work.

In this Part, I have elaborated on the data processing and calibration requirements for wide-field, polarized interferometric measurements. These included compression of the data, flagging or correction of malfunctioning components, and high dynamic-range calibration in Fourier and image space. The objective of all of these steps has, as always, been closing-in on a statistical detection of the EoR. The EoR window is only useful as long as all of the above steps did not introduce spectral structure to the data. As Faraday-rotated polarized foregrounds are one of the few ‘natural’ causes of spectral structure in our measurements. This was the onus for the progressively-deeper (and, in  $k$ -space, narrower) integrations on the EoR window, as presented in the three previous chapters. We have found little evidence for astrophysical emission as a dominant systematic. Instead, it is instrumental polarization, evident in Stokes Q, U and V that is far more troublesome. Leakage from Stokes I into these parameters is theoretically symmetric from those parameters into Stokes I. Close attention to instrumental leakage will be required as HERA provides deeper integrations in the future; characterizing polarization in the Fourier space relevant to an EoR detection is an excellent probe of this effect.

# **Part III**

## **Expanding the potential of EoR**

### **measurements**

There is one glory of the sun, and another glory of the moon, and another  
glory of the stars; for star differs from star in glory.

*1 Corinthians (15:41)*

# Chapter 12

## Interferometric sensitivity to the global signal

As described in Chapter 1, the EoR global signal contains key information about the thermal history of the IGM as a function of redshift, across  $80 < z < 6$  at the least. Observational efforts to detect the global signal typically consist of a single element (or duplicates of a single element for systematic cross-checks), while interferometric measurements concentrate on the anisotropic signal.

Traditionally, an interferometer is not regarded as sensitive to the average signal on the sky. Indeed, in the limit of a flat, infinite sky, the sky-averaged visibility of any pair of baselines is identically zero. This is because the average signal is equivalent to the  $(u, v) = (0, 0)$  spatial Fourier mode, which for interferometers with narrow fields-of-view is inaccessible as the two antennae would need to be co-incident. However, when the flat-sky approximation is no longer valid, a monopole moment may be detectable in principle. Presley et al. (2015) argued that the curved nature of the sky implies the integrated response of an interferometer to a constant signal is not zero. Experimentally, these types of results are quite exciting, because the full power of cross-correlation – negation of correlated noise and increased sampling of Fourier modes – can be brought to bear on the problem of very bright foregrounds. As a result, it may be possible to detect

the 21 cm global signal without the necessity of performing extensive self-calibration of an individual antenna response.

However, Venumadhav et al. (2016) presented a general argument that an interferometer is not sensitive to the global signal, except by means of instrument imperfections. They argued that sensitivity to a global signal only enters an interferometric measurement by way of: (1) direct cross-talk between two antennas, (2) cross-talk between two antennas by way of a mutual coupling with a third antenna, or (3) a mutual coherent noise source between two antennas. The authors claimed that upon performing a cross-correlation operation on the received voltage measurements, any correlations disappear. They also claimed that interferometers are incapable of understanding these noise properties.

In this Chapter, we present a formalism that shows that interferometers may be sensitive to the global signal. Our analysis is complimentary to the one presented by Presley et al. (2015), but approaches the problem from a more spherical basis. We also present measurements that are suggestive, but not conclusive, of measurements of the global signal of Galactic foregrounds with the PAPER interferometer. We assume the Condon-Shortley phase convention throughout (Condon & Shortley, 1951).

## 12.1 Mathematical Formalism

We wish to answer the question of whether an interferometer can measure the spherical harmonic monopole, that is, the specific mode  $\ell = m = 0$ . The main characteristic of this mode is constant power, coming from all angles  $\Omega$  on the sky. We assume, however, that this emission from any particular pointing  $\hat{s}$  is *incoherent* with that from any other direction, but that the average emission in any direction is the same.

In other words, we assume that the emitters in the far field of the instrument are uncorrelated, and thus the monopole moment of the radiation satisfies

$$\frac{1}{Z_0} \left\langle \vec{E}(\hat{r}) \vec{E}(\hat{r}') \right\rangle = P(v) \delta(\hat{r} - \hat{r}'). \quad (12.1)$$

The power received is independent of direction, but the fields in any two directions are

uncorrelated.

To gain insight into how an interferometer responds to an isotropic sky signal, we will begin with the classical interferometric visibility equation. We note that there are several assumptions that enter to the visibility equation, though these are typically well-justified in the applications of interest. In particular, we assume that:

1. The emission is in the far field of the pair of antennas.
2. The emission is incoherent.
3. The antennas do not affect one another's radiation patterns.
4. The antennas or their structures do not scatter the incident radiation.
5. The antennas are perfectly terminated and do not reflect incident radiation.
6. There is no loss in the antennas elements except for at the detector.

In general, all of these assumptions except for (1) and (2) are violated for real experiments. As noted in Venumadhav et al. (2016), an important consideration for an interferometer's sensitivity to the monopole is the sensitivity along the line of sight connecting the two antennas. Thus, the extent to which assumptions (3–5) hold will affect the extent to which an interferometer is theoretically sensitive to the sky monopole.

### 12.1.1 Spherical Harmonic Transform of the Visibility Equation

We can rewrite the visibility observed by baseline  $\vec{b}$  (with horizon-delay of  $\tau_h = b/c$ ) by expanding the fringe term using spherical harmonics and spherical Bessel functions:

$$\exp(-2\pi i v \tau_h \hat{b} \cdot \hat{s}) = 2\pi \sum_{\ell,m} (-i)^\ell j_\ell(2\pi \tau_h v) Y_\ell^m(\hat{b}) Y_\ell^{m*}(\hat{s}), \quad (12.2)$$

and expanding the chromatic beam ( $A(\hat{s}, v)$ ) and sky terms ( $S(\hat{s}, v)$ ) in terms of spherical harmonics:

$$A(\hat{s}, v) = \sum_{\ell,m} a_{\ell,m}(v) Y_\ell^m(\hat{s}), \quad (12.3)$$

$$S(\hat{s}, v) = \sum_{\ell, m} s_{\ell, m}(v) Y_{\ell}^m(\hat{s}). \quad (12.4)$$

Finally, we can write Equation 12.2 consistently with the above two terms:

$$\exp(-2\pi i v \tau_h \hat{b} \cdot \hat{s}) = \sum_{\ell, m} f_{\ell, m}(\hat{b}, v) Y_{\ell}^{m*}(\hat{s}), \quad (12.5)$$

where we have defined a ‘fringe harmonic’ term:

$$f_{\ell, m}(\hat{b}, v) \equiv 2\pi \sum_{\ell, m} (-i)^{\ell} j_{\ell}(2\pi \tau_h v) Y_{\ell}^m(\hat{b}). \quad (12.6)$$

Combining all of the above allows us to formulate the classical visibility equation as a sum of spherical harmonic terms, which we will denote using separate indices:

$$V(v) = \sum_{\substack{\ell_1, m_1 \\ \ell_2, m_2 \\ \ell_3, m_3}} a_{\ell_1, m_1}(v) s_{\ell_2, m_2}(v) f_{\ell_3, m_3}(\hat{b}, v) \times \int Y_{\ell_1}^{m_1}(\hat{s}) Y_{\ell_2}^{m_2}(\hat{s}) Y_{\ell_3}^{m_3*}(\hat{s}) d\Omega. \quad (12.7)$$

The integral over  $\Omega$  can be expressed in terms of Wigner-3j symbols (Wigner, 1951):

$$\begin{aligned} \int Y_{\ell_1}^{m_1}(\hat{s}) Y_{\ell_2}^{m_2}(\hat{s}) Y_{\ell_3}^{m_3*}(\hat{s}) d\hat{s} = \\ \sqrt{\frac{(2\ell_1+1)(2\ell_2+1)(2\ell_3+1)}{4\pi}} \\ \times \begin{pmatrix} \ell_1 & \ell_2 & \ell_3 \\ 0 & 0 & 0 \end{pmatrix} \begin{pmatrix} \ell_1 & \ell_2 & \ell_3 \\ m_1 & m_2 & -m_3 \end{pmatrix} \end{aligned} \quad (12.8)$$

### 12.1.2 Coupling to the Sky Monopole

Thus far, we have made no assumptions about the form of the terms in the visibility equation. The sky monopole is defined in our notation as  $\ell_2 = m_2 = 0$ . For these modes, the Wigner-3j symbols can undergo two odd permutations of the columns:

$$\begin{pmatrix} \ell_1 & 0 & \ell_3 \\ 0 & 0 & 0 \end{pmatrix} \begin{pmatrix} \ell_1 & 0 & \ell_3 \\ m_1 & 0 & -m_3 \end{pmatrix} = \begin{pmatrix} \ell_1 & \ell_3 & 0 \\ 0 & 0 & 0 \end{pmatrix} \begin{pmatrix} \ell_1 & \ell_3 & 0 \\ m_1 & -m_3 & 0 \end{pmatrix} \quad (12.9)$$

which will have the resultant selection rules:

$$|\ell_1 - \ell_3| \leq 0 \leq \ell_1 + \ell_3; m_1 - m_3 = 0. \quad (12.10)$$

These constraints require that  $\ell_1 = \ell_3 \equiv \ell$  and  $m_1 = m_3 \equiv m$ , resulting in the factor

$$\begin{pmatrix} \ell & \ell & 0 \\ 0 & 0 & 0 \end{pmatrix} \begin{pmatrix} \ell & \ell & 0 \\ m & -m & 0 \end{pmatrix} = \frac{(-1)^m}{2\ell+1}. \quad (12.11)$$

We can define a component of the visibility containing the sky monopole  $s_{00}$  as

$$V_0(v) = \frac{s_{00}(v)}{\sqrt{4\pi}} \sum_{\ell,m} (-1)^m a_{\ell,m}(v) f_{\ell,m}(\hat{b}, v) = s_{00}(v) \Xi(\hat{b}, v) \quad (12.12)$$

where  $\Xi(\hat{b}, v)$  is a transfer function containing the response of the beam and fringe terms to the monopole. If  $\Xi(\hat{b}, v)$  is non-zero, the interferometer is capable of measuring the global signal.

## 12.2 Analytic and Numeric Calculations

The expression for  $\Xi(\hat{b}, v)$  shows that the sensitivity to the monopole is closely connected to the baseline length and spherical harmonic coefficients of the beam. One can expand a given model beam and baseline to an arbitrary  $\ell, m$ . The spherical Bessel function falls exponentially with  $\ell$ , so the sum should converge.

### 12.2.1 Toy Model

To build intuition, we implement a simple toy model for  $V_0(v)$ . We assume a global sky model of  $s_{00}(v) = S_0 v^{-\alpha}$  (which is roughly consistent with current global low-frequency measurements Mozdzen et al. 2017), and a beam model such that  $a_{00}(v) = A_0 v^{-\beta}$ . We only endeavour to calculate the  $(\ell, m) = (0, 0)$  component; the first term of the sum. Figure 12.1 shows  $\Xi(\hat{b}, v)$  for  $\alpha = 1.5$ ,  $\beta = 1$ .

As we will find below, using the delay transform (Parsons et al., 2012a) is an extremely useful method for understanding whether or not fringing, multipolar terms are present in the data. For this toy model, the delay transform  $\tilde{V}_{00}(\tau)$  can be expressed analytically:

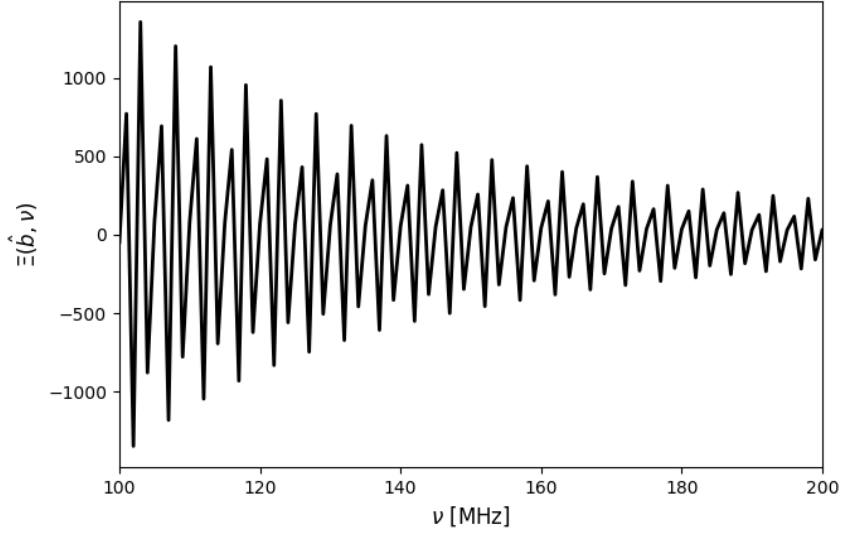


Figure 12.1: The transfer function for a simple beam and sky model, both as power laws in harmonic space, and only using the  $(\ell, m) = (0, 0)$  mode, for a 30 m East-West baseline.

$$\begin{aligned} \tilde{V}_{00}(\tau) = & i^{1+3(\alpha+\beta)} \frac{s_0 a_0 (2\pi)^{\alpha+\beta}}{4\pi\tau_h} \\ & \times \left[ (\tau - \tau_h)^{\alpha+\beta} \Gamma_{+--} - (\tau - \tau_h)^{\alpha+\beta} \Gamma_{-+-} \right. \\ & \quad \left. - (\tau + \tau_h)^{\alpha+\beta} \Gamma_{++-} + (\tau + \tau_h)^{\alpha+\beta} \Gamma_{-++} \right], \end{aligned} \quad (12.13)$$

where the functions  $\Gamma_{\pm\pm\pm}$  are defined as

$$\Gamma_{\pm\pm\pm} \equiv \Gamma(-\alpha - \beta, \pm i\pi(B \pm 2v_0)(\tau \pm \tau_h)), \quad (12.14)$$

and  $\Gamma(s, z)$  is the upper incomplete Gamma function.

In Figure 12.2, we show the delay transform for  $\alpha = 1.5$  and  $\beta = 0$  (i.e. no frequency evolution) and  $\beta = 1$  for a 30 m baseline. Clear in both Equation 12.13 and Figure 12.2 is the selection of the horizon delay (100 ns) as the location of monopole signal in delay space. The interpretation of this effect is that while the monopole, by definition, emits across the sky, an interferometer is maximally sensitive to it at the horizon. This is the

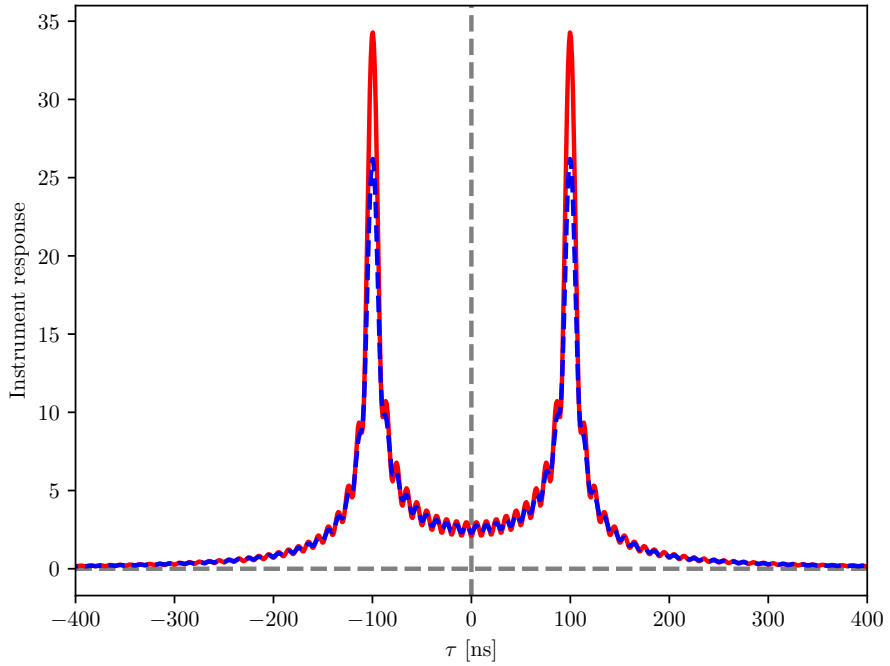


Figure 12.2: The delay transform of the interferometer response to the monopole moment of the global signal, including only the zeroth-order response of the instrument. The functional form of this result is given by Equation 12.13. The plot uses a value of  $\alpha = 1.5$  for the power law index of the monopole moment, and  $\beta = 0$  (solid red curve) and  $\beta = 1$  (dashed blue curve) as the power law index for the instrument response. The light-crossing time separation between the antennas  $\tau_h$  was chosen to be 100 ns, which sets the location of the peaks in the delay spectrum. The y-axis has arbitrary units.

location where the baseline vector is coincident with the  $\hat{s}$  term integrated-over in the visibility equation. Venumadhav et al. (2016) showed the same effect (see their Section 5), but not in the delay formalism. The oscillations were due to the toy model being undersampled in frequency – this level of accuracy was acceptable for these relatively qualitative results.

The prefactor of Equation 12.13 also indicates that the power in delay space will decrease with baselines of increasing length. This is illustrated in Figure 12.3, which shows  $\tilde{V}_{00}(\tau)$  for three baselines of increasing length. The largest response for each of

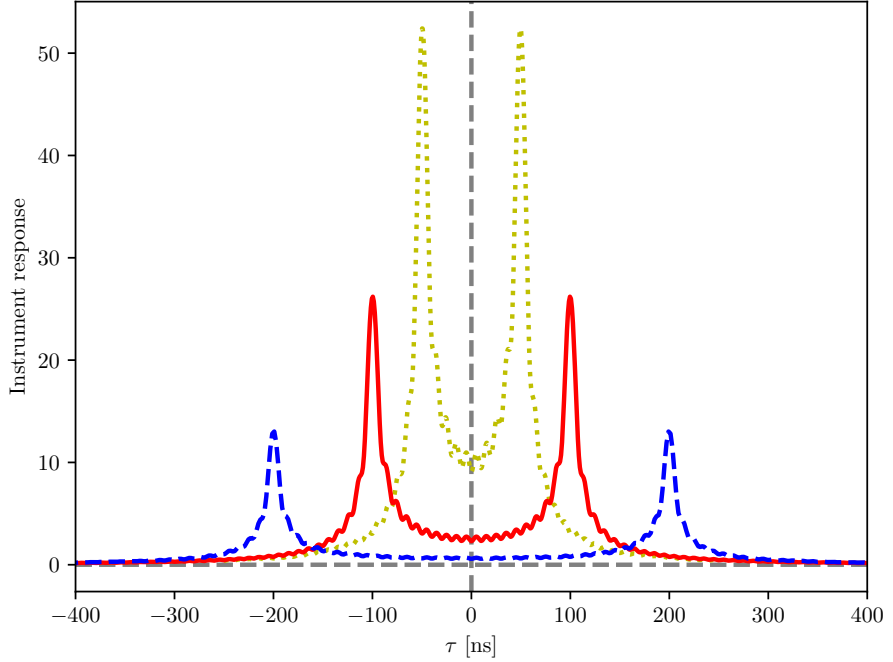


Figure 12.3: The delay transform for different values of  $\tau_h$  for a fixed value of  $\beta = 1$ . The values of  $\tau_h$  are  $\tau_h = 50$  ns (dotted yellow line),  $\tau_h = 100$  ns (solid red line), and  $\tau_h = 200$  ns (dashed blue line). Note that in all cases, the largest response occurs when  $\tau \approx \tau_h$ . Further, note that the amplitude of the response is inversely proportional to the value of  $\tau_h$ : smaller values of  $\tau_h$  result in a larger response.

the lengths occurs at the value of  $\tau \approx \tau_h$ , and the amplitude decreases accordingly. Note that the strength and location in delay space are exactly in line with the simulations of (Thyagarajan et al., 2015a, see their Figure 2), although the main purpose of their study was simulating the power spectrum response of different interferometers. This relationship was also predicted by Venumadhav et al. (2016).

### 12.2.2 Instrument Simulation

Using the Jones formalism developed in Chapter 3 (also see Chapter 10) and a complex-voltage model of the PAPER dipole beam (Parsons et al., 2010; Pober et al., 2012), we

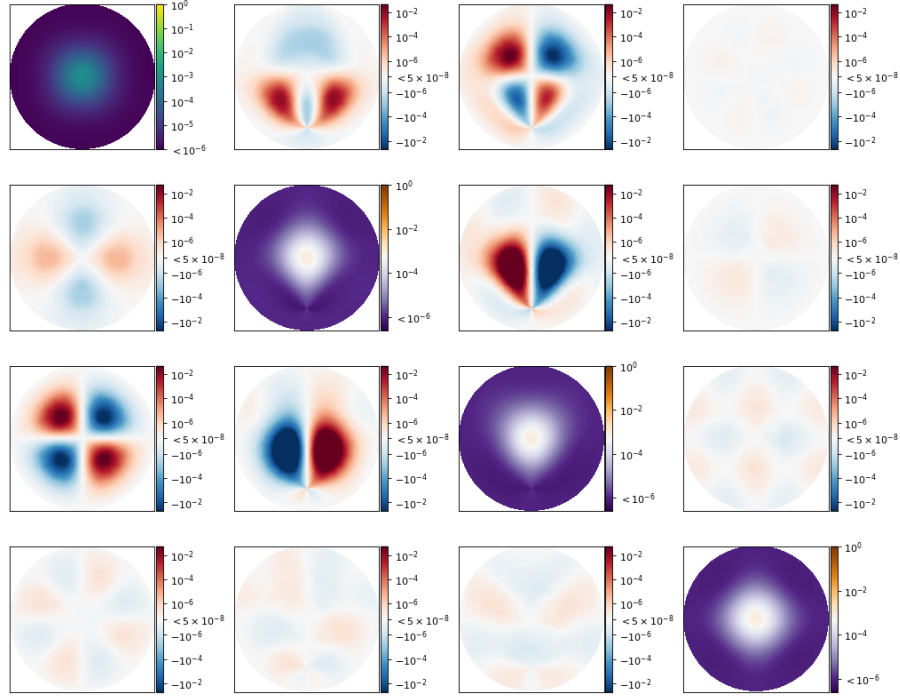


Figure 12.4: The direction-dependent Jones matrix for a model PAPER beam at 150 MHz. For a review of Jones and Mueller matrices, see Chapter 3. Note the separate color maps for  $I \rightarrow I$ , the other diagonal terms, and the off-diagonal ones, which we use for dynamic range changes in order capture sufficient detail.

were able to simulate  $\Xi(\hat{b}, v)$ . The beam was calculated using an electromagnetic simulation (in the HFSS software package) of plane waves incident upon the dipole and ground-screen. Figure 12.4 shows the direction-dependent Mueller matrix for the PAPER beam at 150 MHz. Note the separate color maps for  $I \rightarrow I$ , the other diagonal terms, and the off-diagonal ones, which we use for dynamic range changes in order capture sufficient detail. The dipole beam, as expected, extends across the sky.

Figure 12.5 shows the value of  $\Xi(\hat{b}, v)$  as a function of frequency computed from the beam models from Figure 12.4, for East-West ('ee') and North-South ('nn') instrumental linear polarizations. The non-zero nature of the curves represent that the global signal is, in principle, measurable from interferometric visibilities. However, as shown in Equation 12.12, in order to measure the global signal  $s_{00}(v)$ ,  $\Xi(\hat{b}, v)$  must be fit-out from

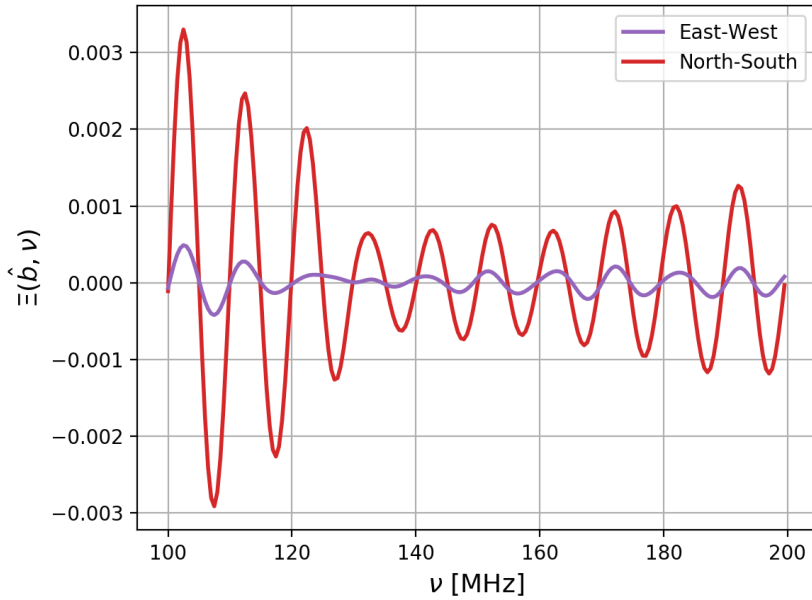


Figure 12.5: The global signal transfer function as a function of frequency for PAPER. It's non-zero nature indicates that the global signal is in principle measurable by an interferometer.

the visibility  $V_0(\nu)$  (the fact that the visibility shown in Equation 12.12 contains only the monopole sky will be discussed below).

### 12.2.3 Attenuating other harmonics

Of course, the visibility  $V_0(\nu) = s_{00}(\nu)\Xi(\hat{b}, \nu)$  contains only the monopole signal of the sky to begin with. The visibility equation is linear, so the total visibility observed can be represented as  $V(\nu) = V_0(\nu) + V_{>0}(\nu)$ . There are several ways one could separate  $V_{>0}(\nu)$  from the total visibility, but for drift-scanning telescopes with long observing seasons, the simplest solution is just to average visibilities over time.

The expression in Equation 12.7 does not take time into account – it is the instantaneous visibility. For a drift-scanning interferometer, time dependence is only introduced by the rotation of the Earth. In the formalism above, this can be introduced by multiplica-

tion of a factor  $\exp(-im_2\omega_{\oplus}t)$ , where  $m_2$  is an index of the spherical harmonic modes of the sky and  $\omega_{\oplus}$  is the rate of the Earth's rotation. The symmetry of  $m$ -modes with respect to  $\ell$  cause an sum over these terms to select the  $m_2 = 0$  mode. In the resultant expression:

$$\langle V(\mathbf{v}, t) \rangle_t = \sum_{\substack{\ell_1, m_1 \\ \ell_2 \\ \ell_3, m_3}} a_{\ell_1, m_1}(\mathbf{v}) s_{\ell_2, 0}(\mathbf{v}) f_{\ell_3, m_3}(\hat{\mathbf{b}}, \mathbf{v}) \times \sqrt{\frac{(2\ell_1 + 1)(2\ell_2 + 1)(2\ell_3 + 1)}{4\pi}} \times \begin{pmatrix} \ell_1 & \ell_2 & \ell_3 \\ 0 & 0 & 0 \end{pmatrix} \begin{pmatrix} \ell_1 & \ell_2 & \ell_3 \\ m_1 & 0 & -m_3 \end{pmatrix}, \quad (12.15)$$

the second Wigner-3j symbol obeys the selection rule that  $m_1 = m_3$ . This leaves all sky  $m$ -modes attenuated, save for the zero mode, but higher multipole  $\ell$  modes survive. These are ‘stripes’ of constant declination along the sky. How to account for contamination from these higher  $\ell$  modes is not a solved problem.

## 12.3 Time-averages from PAPER

The Season 1 Epoch 2 observations of PAPER-128 were defined and described in Chapter 11. In Chapters 4, 6 and 11 we elaborated upon the instrumental design, quality assurance metrics and compression implemented on the data. Season 1 Epoch 2 consists of  $\sim 45$  nights of well-characterized observations. In this Chapter, we used Season 1 Epoch 2 PAPER-128 data that was quality assured, and calibrated using the OMNICAL (Zheng et al., 2014) *4pol+minV* calibration scheme (see Chapter 7).

We then extracted only the 30 m East-West baselines, in the instrumental ‘nn’ polarization, for analysis. Unlike in Chapter 11, we did not implement a foreground avoidance scheme. The data were gridded and binned according to their LST of observation, and absolute-calibrated according to the flux density and position of Pictor A at transit (Jacobs et al., 2013, the same calibration shown in Chapter 11).

To isolate the global ( $m = 0$ ) component of the signal, which does not ‘fringe’ on the sky as observed by the interferometer, we averaged all LSTs into a single frequency spec-

trum. The real part of the averaged spectrum is shown in the upper panel of Figure 12.6, with the simulated PAPER transfer function (Figure 12.5) over-plotted for reference. The delay transforms of the two spectra are shown in the lower panel of the Figure.

There were some enticing qualitative agreements. Clearly, the phases of the oscillations between simulation and data were very similar to one another; noticeable in the upper panel and very clear in the lower one. The power within the foreground wedge region (e.g. Chapter 5) was at the level of noise in the EoR window, indicating that foregrounds were attenuated at the appropriate delays, save, of course, the horizon delays.

As predicted by the toy model in Section 12.2.1, the only unattenuated foreground signal appeared at the horizon delays of the 30 m East-West baselines used in this analysis. As noted above, the observed and simulated delays aligned almost perfectly in delay space. This indicated that the dipole beam, as expected, was accurately described by a small number of spherical harmonic modes. The width of the peaks is determined by the width of the beam in delay space: that the simulated and observed widths matched relatively closely was indicative of an accurate polarized beam model.

The imperfect alignment of the oscillatory spectra may have been due to some frequency-dependent phase slope, possibly from an imperfect projection of redundant calibration degeneracies (e.g. Dillon et al., 2017, Chapter 7). A more likely source of the misalignment was imperfect modelling of the beam. Higher  $\ell$  values introduce additional spherical Bessel functions, each with their own phase that will superimpose for the final value of  $\Xi(\hat{b}, v)$ . Higher  $\ell$ -mode contamination may also be the source of the asymmetry of the observed delay peaks. Presley et al. (2015) provided an optimal quadratic estimator formalism to address this problem, which may be a promising route to pursue in future investigations.

The amplitude of the observed spectrum in frequency space increased towards higher frequencies, the opposite direction as predicted by the simulations and as expected for a signal tied to low-frequency synchrotron radiation (Mozdzen et al., 2017). The cause of

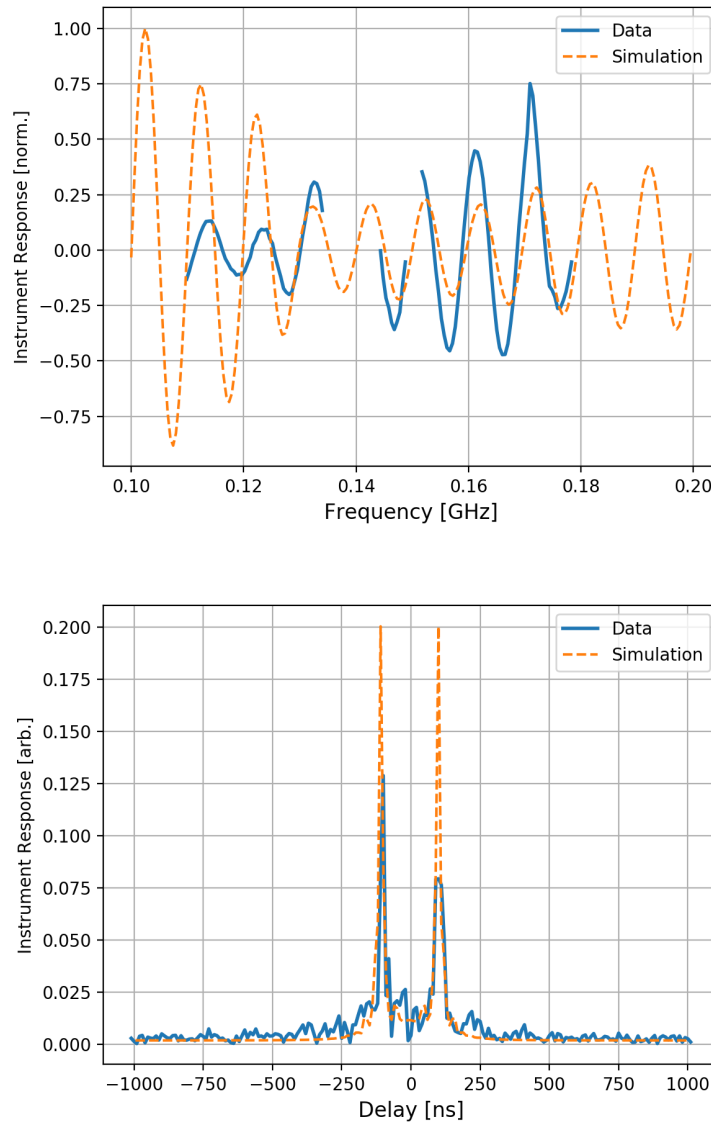


Figure 12.6: Comparison of time-averaged, LST-binned PAPER-128 visibilities to the simulated transfer function in the ‘nn’ polarization. Upper and lower panels show the spectra in frequency and delay space. See the text for discussion.

this effect was unclear, but may be due to imperfect wide-band bandpass calibration<sup>1</sup>.

## 12.4 Discussion

This analysis was an exploratory one, driven by investigations in to time-averages from PAPER-64 data as reported in the public HERA memo #6. In that memo I investigated the impact of calibration errors and antenna cross-talk on time-averaged visibilities, showing that D-term leakage (e.g. Chapter 7) could introduce low levels of spectral structure into the time-average, broadening the ‘wings’ of horizon-power in delay space. Understanding the cause and shape of this delay space power is essential for obtaining EoR power spectra at  $k$ -values close to the foreground wedge.

The above analyses have shown that the PAPER beam and sky signal are quite accurately described by a low number of spherical harmonic modes. In our toy model we obtained delay-space signatures similar to those observed in data using only the  $(\ell, m)=(0,0)$  mode of the beam and sky, which had a relatively simple analytical form. The selection rules in our formalism do allow an arbitrary number of even  $\ell$  modes to contribute to  $\Xi(\hat{b}, v)$ , and developing a better understanding of those contributions may lead to a resolution to some of the problems described in the previous Section. Furthermore, a more advanced understanding of the effect of mis-calibration on the data that exceeds the conjectures above may resolve the offset between data and simulation. There may also be redundant calibration schemes that could provide an estimate of  $\Xi(\hat{b}, v)$  directly from the observed data.

HERA (DeBoer et al., 2017) will represent the most powerful low-frequency interferometer of its kind, with far more redundant baselines to average-over and experiment with in its search for the EoR power spectrum. However, it may not be the best instrument for a search for the global signal. Its faceted dish structure leads to smaller beams, which

---

<sup>1</sup>Note that such imperfections were unlikely to affect the power spectra reported in Chapter 11, as these used only a narrow range of frequencies.

in turn leads to a large number of spherical harmonic modes required for its description. This complicates an accurate simulation of  $\Xi(\hat{b}, v)$  and hence the extraction of the global signal from observations. Interferometers specifically designed to target the global signal and adhere to prescriptions set by Venumadhav et al. (2016) may be more fruitful efforts.

We have shown that the global signal is, in theory, detectable by an interferometer. Our exploration with PAPER-128 data yielded imperfect but promising results. We detected a time-constant signal that is characterized by the length of the baseline used for the measurement; it was not simply electrical crosstalk. However, that signal may contain more than the  $(\ell, m) = (0, 0)$  mode of the sky, as we have not removed higher  $\ell$  modes. That said, we appear to be quite close to a characterization of monopole power, following a relatively simple scheme. Much more work is required before a definitive claim of a detection, but in the meantime, our present observations remain exciting.

## Note: interpretation in light of Venumadhav et al. (2016)

The paper by Venumadhav et al. 2016 conceptualizes a single interferometer receiving element as a lossless electromagnetic junction, and as such obeys conservation of energy on a microscopic level. As a consequence, the entire array can be treated as being unitary, with input and output corresponding to the sky, readout channels, and dissipative elements. By invoking unitarity, the authors of Venumadhav et al. 2016 show that a general interferometer is only sensitive to the monopole moment either through cross-talk between elements, or through coupling of distinct elements to a common dissipative noise source. Explicitly, Equation 21 of Venumadhav et al. 2016 can be written as:

$$\frac{1}{k_B} \frac{\partial}{\partial \bar{T}_s} \langle \psi_{c_i}^* \psi_{c_j} \rangle = - \sum_k U(c_i; c_k)^* U(c_j; c_k) - \sum_{d_k} \frac{1}{k_B} \frac{\partial}{\partial T_{d_k}} \langle \psi_{c_i}^* \psi_{c_j} \rangle, \quad (12.16)$$

where  $\bar{T}_s$  is the monopole moment (position-independent portion) of the sky signal,  $\psi_i$  is the amplitude of the electromagnetic vector potential  $\vec{A}$  for a given frequency and polarization in a particular readout channel  $i$ ,  $U(c_i; c_j)$  is the cross-talk between readout channels

$i$  and  $j$ ,  $d_k$  is the set of dissipative elements of the interferometer,  $T_{d_k}$  is the effective noise temperature of dissipative element  $d_k$ , and  $k_B$  is Boltzmann's constant. Accordingly, one consequence of Venumadhav et al. 2016 is that a “perfect” interferometer (one with no cross-talk or losses) is insensitive to the monopole moment. Mathematically, the no cross-talk condition equates to the elements  $U(c_i; c_j) = 0$  for all  $i \neq j$ , and the lossless condition means that  $U(c_i; d_k) = 0$  for all readout channels  $i$  and dissipate elements  $k$ .

In the main body of this Chapter, we showed that when directly computing the integral of the interferometer equation, there is indeed sensitivity to the global signal if the individual elements have certain properties (see Section 12.1 for these requirements listed explicitly). In the language of Venumadhav et al. 2016, we have assumed that there is indeed cross-talk between individual receiving elements. Specifically, since most of the sensitivity to the sky monopole comes from the baseline connecting two antennas, both antennas must be sensitive to signal along the line-of-sight to the horizon. Because the antenna closer to the horizon is not electromagnetically transparent to the incoming radiation – indeed, there would be no detection of the signal if it were – it must necessarily re-broadcast the incoming radiation. This radiation is then detected by the antenna farther from the horizon, which leads to over-the-air cross-talk between the two antennas. Thus, in the language of Venumadhav et al. 2016, the matrix element  $U(c_i; c_j)$  is non-zero for this pair of antennas  $i$  and  $j$ , and as such there is sensitivity to the global signal. If we assume the interferometer is lossless (but *not* that there is no cross-talk), then the sensitivity to the global signal can be expressed as:

$$\frac{1}{k_B} \frac{\partial}{\partial T_s} \langle \psi_{c_i}^* \psi_{c_j} \rangle = - \sum_k U(c_i; c_k)^* U(c_j; c_k). \quad (12.17)$$

We note that in Venumadhav et al. 2016, for the lossless case, the unitarity constraint of the system can be expressed as:

$$\sum_{\alpha, a} U(c_i; \alpha, \hat{n}_a)^* U(c_j; \alpha, \hat{n}_a) + \sum_k U(c_i; c_k)^* U(c_j; c_k) = 0, \quad (12.18)$$

where  $U(c_i; \beta, \hat{n}_b)$  is the amount of signal captured in readout channel  $c_i$  of polarization  $\beta$  and pixel  $\hat{n}_b$  of the sky (once it has been discretized, see Appendix A of Venumadhav

et al. 2016). This also assumes the readout channels are distinct, *i.e.*,  $i \neq j$ . This relation can be substituted into Equation 12.17, which leads to:

$$\frac{1}{k_B} \frac{\partial}{\partial \bar{T}_s} \langle \psi_{c_i}^* \psi_{c_j} \rangle = \sum_{\alpha, a} U(c_i; \alpha, \hat{n}_a)^* U(c_j; \alpha, \hat{n}_a). \quad (12.19)$$

Further, in the limit of a lossless interferometer, the formalism of Venumadhav et al. 2016 leads to the traditional interferometer equation. Specifically, for two antennas  $c_1$  and  $c_2$  at a frequency  $\nu_m$ , the interferometer equation can be expressed as:

$$\sum_{\alpha, a} U(\nu_m, c_1; \alpha, \hat{n}_a)^* U(\nu_m, c_2; \alpha, \hat{n}_a) k_B T_s(\hat{n}_a) = \int d\hat{n} A(\nu_m, \hat{n}) \frac{\nu_m^2}{c^2} k_B T_s(\hat{n}_a) e^{2\pi i \nu_m (\vec{r}_2 - \vec{r}_1) \cdot \hat{n}_a}, \quad (12.20)$$

which is simply the visibility equation, where the sky signal has been converted to a brightness temperature.

# Chapter 13

## Higher-order correlation functions between kSZ and 21cm observations

In Chapter 1, it was discussed that there are many probes of the EoR beyond HI. Secondary anisotropies of the CMB can be used as probes of reionization, mainly due to the fact that reionization represents a large source of free electrons, which CMB photons can scatter off of. The pattern of scattering – the secondary anisotropies – is sensitive to the topology of the HI field. This Chapter focuses on a particular mechanism for producing secondary anisotropies; the kinetic Sunyaev-Zel'dovich effect (kSZ). We present novel mathematical theories for understanding the correlation between future CMB and EoR measurements, taking instrumental noise and the EoR window into account in a way not presently explored in the literature. In Section 13.1 we make clear the link between the EoR and the kSZ effect. In Sections 13.2 and 13.3, we present semi-analytic theory and results from simulation for the  $\text{kSZ}^2$ -21cm bispectrum and the  $\text{kSZ}^2$ -21cm<sup>2</sup> trispectrum, respectively. We derive noise estimates in Section 13.4, and provide a brief discussion in Section 13.5.

## 13.1 The kSZ-21cm connection

The kSZ probes the cosmic momentum field; photons are Doppler-boosted off of clouds of electrons around ionizing sources. The 21 cm signal, of course, probes where those ionizing sources *are not*, so we should expect the kSZ and 21 cm signal to be anti-correlated.

The anisotropies induced on the CMB by the kSZ are given by (Equation 1.3):

$$\frac{\delta T_{\text{kSZ}}}{T_{\text{CMB}}}(\hat{s}) = \frac{\sigma_T}{c} \int_0^{z_{\text{recomb}}} \frac{ds}{dz} dz n_e(z) e^{-\tau(z)} \hat{s} \cdot \vec{q}(\vec{x}), \quad (13.1)$$

where  $\sigma_T$  is the Thomson Cross Section,  $n_e(z)$  is the average number density of electrons at redshift  $z$ ,  $\tau(z)$  is the optical depth to redshift  $z$ , and  $ds/dz$  is the cosmological line element to redshift  $z$  along direction  $\hat{s}$ . The momentum field  $q$  can be expressed as:

$$\vec{q}(\hat{s}) = (1 + \delta_x(\vec{x}))(1 + \delta_b(\vec{x})) \vec{v}(\vec{x}) \cdot \hat{s}, \quad (13.2)$$

where  $1 + \delta_x(\vec{x}) = x_i(\vec{x}) / \langle x_i(\vec{x}) \rangle$  for ionization fraction  $x_i(\vec{x})$ ,  $1 + \delta_b(\vec{x}) = \rho_b(\vec{x}) / \langle \rho_b(\vec{x}) \rangle$ ,  $\vec{v}(\vec{x})$  is the free electron bulk flow, and  $\langle \dots \rangle$  indicates an average over position  $\vec{x}$ . The kSZ is sourced by momentum of ionized gas, but we only detect the component of that momentum over a given line-of-sight  $\hat{n}$ , of which only the integrated, transverse component of the wavevector  $\vec{k}$  will survive. This representation allows us to approximate  $\delta T_{\text{kSZ}}$  as

$$\delta T_{\text{kSZ}} \propto \vec{q} \cdot \hat{n}(\vec{k}) = \vec{v}(\vec{x}) [1 + \delta_x(\vec{x}) + \delta_\rho(\vec{x})] \cdot \hat{n}(\vec{k}) \quad (13.3)$$

$$= \int \frac{d^3 k'}{(2\pi)^3} \vec{v}(\vec{k}') \hat{k}' \cdot \hat{n} [\delta_x(\vec{k} - \vec{k}') + \delta_\rho(\vec{k} - \vec{k}')]. \quad (13.4)$$

where in the first equality we expanded the mass component of the momentum term to first order, and in the second described the problem in  $k$ -space. The constant of proportionality can be expressed as a window function, described below in Equation 13.11.

Likewise, the 21 cm brightness temperature as a function of position can be expressed as (see Chapter 1):

$$\delta_{21\text{cm}}(\vec{x}) \approx T_0^{21\text{cm}} \langle x_{\text{HI}} \rangle [1 + \delta_{x_{\text{HI}}}(\vec{x})] [1 + \delta_\rho(\vec{x})] \quad (13.5)$$

To compare with the kSZ, it will be useful to speak in terms of the ionization overdensity field rather than neutral overdensity  $\delta_{x_{\text{HI}}}(\vec{x})$ . This just brings out a prefactor,

$$\delta_{x_{\text{HI}}}(\vec{x}) = \frac{-\langle x_i \rangle}{1 - \langle x_i \rangle} \delta_x(\vec{x}). \quad (13.6)$$

So our representation of the 21 cm temperature contrast becomes

$$\delta_{21\text{cm}}(\vec{x}) = T_0^{21\text{cm}}(1 - \langle x_i \rangle) \left[ 1 - \frac{\langle x_i \rangle}{1 - \langle x_i \rangle} \delta_x(\vec{x}) + \delta_\rho(\vec{x}) - \frac{\langle x_i \rangle}{1 - \langle x_i \rangle} \delta_x(\vec{x}) \delta_\rho(\vec{x}) \right] \quad (13.7)$$

While the 21 cm field is positive-definite, the kSZ anisotropies are not. Cosmic bulk flows could be oriented towards or away from the observer. This motivated moving beyond the power spectrum (the Fourier analog of the two-point function) in the investigation of the kSZ-21 cm connection, since

$$\langle \delta_{21\text{cm}}(\vec{x}) \delta_{\text{kSZ}}(\vec{x}) \rangle \approx 0. \quad (13.8)$$

We required at least the square of the kSZ field – and hence a higher-order correlation function. In the following sections, we form higher-order correlation functions represented as bispectra (the Fourier analog of the three-point function) and trispectra (the Fourier analog of the four-point function). .

To simplify the mathematical derivations, we made a few simplifying assumptions: (i) at high redshifts, peculiar velocities along the line-of-sight were small compared to the Hubble Flow, (ii) X-ray heating effects close to the start of reionization pushed the spin temperature of HI  $T_S \gg T_{\text{CMB}}$  (e.g. Meiksin et al., 2017), and (iii) the velocity field was coherent on large scales (e.g. Smith & Ferraro, 2016).

### 13.1.1 Simulations

We simulated the redshift evolution of the 21 cm brightness temperature field and the integrated kSZ using a similar approach to La Plante et al. (2014); using semi-analytic models of reionization coupled with an N-body simulation. Initial conditions for the N-body simulation – with  $512^3$  resolution elements in a 500 comoving Mpc/h box – were

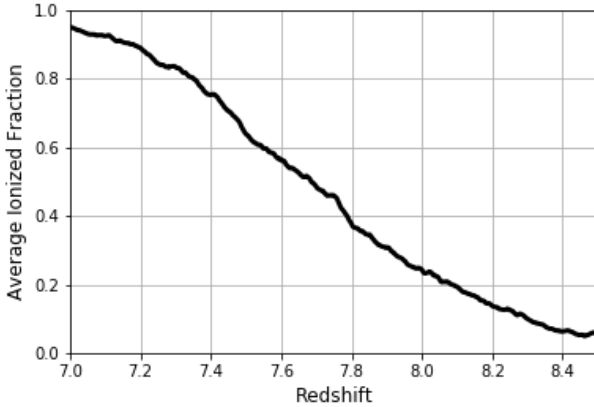


Figure 13.1: The average ionized fraction as a function of redshift in our cosmological simulation.

set by a matter power spectrum as predicted by CAMB (Lewis et al., 2000a) at redshift  $z = 150$  assuming the WMAP cosmology (Hinshaw et al., 2013).

The N-body simulation gave a realization of the density field at the midpoint of reionization (around  $z \sim 8$ , see Figure 13.1). Using this and the  $k$ -space semi-analytic bias model of reionization from Battaglia et al. (2013), we were able to ‘paint-on’ the 21 cm brightness temperature to each point of the volume (La Plante et al., 2014). For each point in the volume we also saved velocity and electron density. To obtain the kSZ, we built a light-cone projection of the box. For each point in the volume, we traced rays through the box at lines of constant angle (*not* constant comoving distance) and computed the contribution to the kSZ from that sight line. These calculations resulted in a 3D 21 cm field cube of fixed comoving size, and a 2D kSZ field map of fixed angular size. In Figure 13.1 we show the global ionization history of the cube. Figure 13.2 shows an example slice of the 21 cm brightness temperature cube at redshift and the resultant kSZ map.

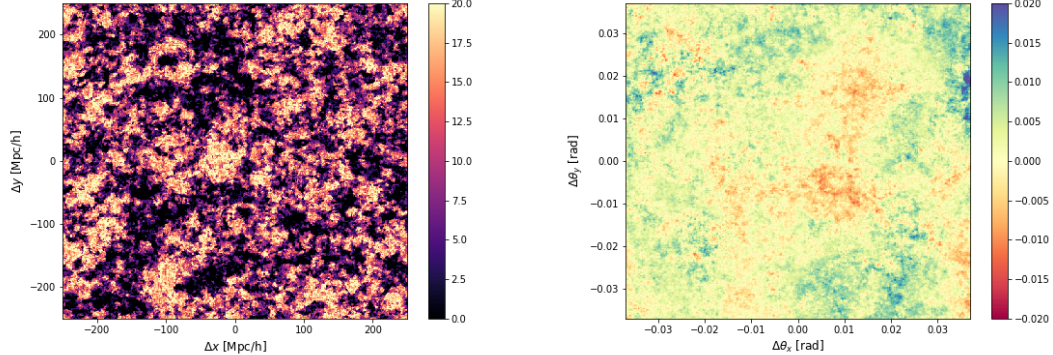


Figure 13.2: An example 21 cm brightness temperature field at redshift  $z \sim 7.8$  (left) and integrated kSZ map (right) from our cosmological simulation. Both have color bars in units of mK. Note the lack of obvious correlation or anti-correlation.

## 13.2 kSZ<sup>2</sup>-21cm squeezed-triangle bispectra

In this section we present an estimate for bispectra formed from future HERA 21 cm intensity maps (large scales;  $\ell < 300$ ) and Stage 3 or 4 CMB maps (smaller scales;  $\ell > 3000$ ). These disparate scales stretch the three-point correlation function into a ‘squeezed triangle’ in Fourier space.

### 13.2.1 Semi-analytic approximation

Consider the bispectrum of two Fourier transformed kSZ maps and one Fourier transformed 21 cm map under the Limber approximation (i.e. the assumption that line-of-sight modes are negligible for projected fields such as the kSZ, allowing us to describe them using only transverse modes):

$$\begin{aligned} \langle T_{\text{kSZ}}(\ell_1)T_{\text{kSZ}}(\ell_2)T_{\text{21cm}}(\ell_3) \rangle &= (2\pi)^2 \delta_D(\ell_1 + \ell_2 + \ell_3) \times \int \frac{d\chi}{\chi^4} W_{\text{21cm}}(\chi) W_{\text{kSZ}}^2(\chi) \\ &\quad \times B_{\text{21cm,kSZ,kSZ}}(\ell_1/\chi, \ell_2/\chi, \ell_3/\chi; \chi) \end{aligned} \quad (13.9)$$

where the window functions are based on global quantities associated with the maps:

$$W_{\text{21cm}}(\chi) = \frac{d}{d\chi} (T_{\text{21cm}}(z)) \quad (13.10)$$

where  $d\chi$  is the comoving distance probed by the 21 cm map, given by the observing bandwidth, and

$$W_{\text{KSZ}}(\chi) = T_{\text{CMB}} \frac{\sigma_T n_e(z)}{c} \frac{\langle x_i \rangle e^{-\langle \tau(z) \rangle}}{1+z} \quad (13.11)$$

where redshift  $z$  corresponds to a given comoving distance  $\chi$ , as determined by the central redshift of the 21 cm cube,  $n_e(z)$  is the average number density of electrons at that redshift,  $\langle x_i \rangle$  is the average ionization fraction at that redshift,  $\sigma_T$  is the Thomson cross section and  $\tau(z)$  is the optical depth to redshift  $z$ .  $T_{\text{CMB}} = 2.725 \pm 0.002$  K (Mather et al., 1999; Fixsen et al., 2004).

Now we consider the Limber approximation of a related quantity: the 21 cm field correlated with the square of the line-of-sight-projected momentum field:

$$\begin{aligned} \left\langle \vec{q} \cdot \hat{n}(\vec{k}_1) \vec{q} \cdot \hat{n}(\vec{k}_2) T_{21\text{cm}}(\vec{k}_3) \right\rangle &= \int \int \frac{d^3 k' d^3 k''}{(2\pi)^6} (\hat{k}' \cdot \hat{n})(\hat{k}'' \cdot \hat{n}) \times \\ &\left\langle \vec{v}(\vec{k}') \vec{v}(\vec{k}'') \left[ \delta_x(\vec{k}_1 - \vec{k}') + \delta_\rho(\vec{k}_1 - \vec{k}') \right] \left[ \delta_x(\vec{k}_2 - \vec{k}'') + \delta_\rho(\vec{k}_2 - \vec{k}'') \right] T_{21\text{cm}}(\vec{k}_3) \right\rangle \end{aligned} \quad (13.12)$$

where we shifted our concentration from  $\ell$  space to  $\vec{k}$ -space, which was more convenient to work in for the derivations below. One of our assumptions in Section 13.1 was that the velocity was coherent on large scales, and therefore should not correlate with  $\delta_x$  or  $\delta_\rho$ . This allows us to expand the [...] terms in Equation 13.12 in their own spatial averages, and take the product of velocities into its own spatial average:

$$\left\langle \vec{v}(\vec{k}') \vec{v}(\vec{k}'') \right\rangle = (2\pi)^3 \delta_D(\vec{k}' + \vec{k}'') P_{vv}(\vec{k}') \quad (13.13)$$

where the  $\delta_D(\vec{k}' + \vec{k}'')$  in the above relation allowed us to integrate-out our  $k''$  dependence. Referring to terms of the form  $\langle \delta_i(\vec{k}_1 - \vec{k}') \delta_j(\vec{k}_2 - \vec{k}'') \delta_{21\text{cm}} \rangle$  as  $B_{i,j,21\text{cm}}$ , we could express the overall correlator  $\left\langle \vec{q} \cdot \hat{n}(\vec{k}_1) \vec{q} \cdot \hat{n}(\vec{k}_2) T_{21\text{cm}}(\vec{k}_3) \right\rangle$  in terms of “component bispectra”:

$$\begin{aligned} \left\langle \vec{q} \cdot \hat{n}(\vec{k}_1) \vec{q} \cdot \hat{n}(\vec{k}_2) T_{21\text{cm}}(\vec{k}_3) \right\rangle &= (2\pi)^3 \delta_D(\vec{k}_1 + \vec{k}_2 + \vec{k}_3) \times \\ &\int \frac{d^3 k'}{(2\pi)^3} (\hat{k}' \cdot \hat{n})^2 P_{vv}(k') [B_{x,x,21\text{cm}} + B_{x,\rho,21\text{cm}} + B_{\rho,x,21\text{cm}} + B_{\rho,\rho,21\text{cm}}]. \end{aligned} \quad (13.14)$$

In the squeezed-triangle limit, where  $k_3 \ll k_1, k_2$ , this reduced to:

$$\begin{aligned} \left\langle \vec{q} \cdot \hat{n}(\vec{k}_1) \vec{q} \cdot \hat{n}(\vec{k}_2) T_{21\text{cm}}(\vec{k}_3) \right\rangle &= (2\pi)^3 \delta_D(\vec{k}_1 + \vec{k}_2 + \vec{k}_3) \times \\ &\frac{v_{\text{rms}}^2}{3} [B_{x,x,21\text{cm}} + B_{x,\rho,21\text{cm}} + B_{\rho,x,21\text{cm}} + B_{\rho,\rho,21\text{cm}}] \end{aligned} \quad (13.15)$$

Of course,  $\delta_{21\text{cm}}$  also contains information about  $\delta_x$  and  $\delta_\rho$ . Using Equation 13.7, we expanded each component bispectrum as functions of  $\delta_x$ ,  $\delta_\rho$  and  $\delta_x \delta_\rho$ :

$$\begin{aligned} B_{x,x,21\text{cm}} &\propto B_{x,x,x} + B_{x,x,\rho} + B_{x,x,x\rho} \\ B_{x,\rho,21\text{cm}} &\propto B_{x,\rho,x} + B_{x,\rho,\rho} + B_{x,\rho,x\rho} \\ B_{\rho,x,21\text{cm}} &\propto B_{\rho,x,x} + B_{\rho,x,\rho} + B_{\rho,x,x\rho} \\ B_{\rho,\rho,21\text{cm}} &\propto B_{\rho,\rho,x} + B_{\rho,\rho,\rho} + B_{\rho,\rho,x\rho} \end{aligned} \quad (13.16)$$

where the third index corresponds to large scales, and the first and second indices are probing the same small scale. To gain intuition for what to expect from simulations, we could make some approximations that allow us to reduce each subcomponent bispectrum into power spectra, which are inexpensively estimated from simulations.

### 13.2.1.1 $B_{x,x,21\text{cm}}$

Using Equations 13.7 and 13.9, we can write:

$$\begin{aligned} \langle \delta_x(\vec{k}_1) \delta_x(\vec{k}_2) \delta_{21\text{cm}}(\vec{k}_3) \rangle &= \langle T_0(1 - \langle x_i \rangle) \times \\ &\left[ -\frac{\langle x_i \rangle}{1 - \langle x_i \rangle} \delta_x(\vec{k}_1) \delta_x(\vec{k}_2) \delta_x(\vec{k}_3) + \delta_x(\vec{k}_1) \delta_x(\vec{k}_2) \delta_\rho(\vec{k}_3) - \frac{\langle x_i \rangle}{1 - \langle x_i \rangle} \delta_x(\vec{k}_1) \delta_x(\vec{k}_2) \int \frac{d^3 k'}{(2\pi)^3} \delta_x(\vec{k}_3 - \vec{k}') \delta_\rho(\vec{k}') \right] \\ &\times \delta_D(\vec{k}_1 + \vec{k}_2 + \vec{k}_3) \rangle. \end{aligned} \quad (13.17)$$

Taking the averages inside the square brackets reduces all the terms to the to component bispectra written in Equation 13.16. The first and second terms are simpler to understand, whereas the third term contains a convolution left-over from Fourier transforming  $\delta_x(\vec{x})\delta_\rho(\vec{x})$  from Equation 13.7:

$$B_{x,x,21\text{cm}} = \left( -T_0 \langle x_i \rangle B_{x,x,x} + T_0 (1 - \langle x_i \rangle) B_{x,x,\rho} - T_0 \langle x_i \rangle \int \frac{d^3 k'}{(2\pi)^3} \langle \delta_x(\vec{k}_1) \delta_x(\vec{k}_2) \delta_x(\vec{k}_3 - \vec{k}') \delta_\rho(\vec{k}') \rangle \right) \times \delta_D(\vec{k}_1 + \vec{k}_2 + \vec{k}_3) \quad (13.18)$$

$$B_{x,x,x}$$

Consider the bispectrum  $\langle \delta_x(\vec{k}_1) \delta_x(\vec{k}_2) \delta_x(\vec{k}_3) \rangle$ . In the squeezed triangle limit of  $k_3 \ll k_1, k_2$ , we concentrated on the correlator

$$\langle \langle \delta_x(\vec{k}_1) \delta_x(\vec{k}_2) | \delta_x(\vec{k}_3) \rangle \delta_x(\vec{k}_3) \rangle \quad (13.19)$$

This could be interpreted as: what is the correlation between expectation value of  $\delta_x(\vec{k}_1) \delta_x(\vec{k}_2)$  given that  $\delta_x(\vec{k}_3)$  has some value, with the ionization overdensity field  $\delta_x(\vec{k}_1)$ ? If  $\delta_x(\vec{k}_3)$  is sufficiently small, the expectation value may be expanded as a Taylor Series:

$$\langle \delta_x(\vec{k}_1) \delta_x(\vec{k}_2) | \delta_x(\vec{k}_3) \rangle = \langle \delta_x(\vec{k}_1) \delta_x(\vec{k}_2) \rangle + \delta_x(\vec{k}_3) \frac{d \langle \delta_x(\vec{k}_1) \delta_x(\vec{k}_2) | \delta_x(\vec{k}_3) \rangle}{d \delta_x(\vec{k}_3)}|_{\delta_x(\vec{k}_3)=0} + \dots \quad (13.20)$$

We could evaluate the derivative by assuming that the small-scale power  $P_{\delta_x, \delta_x}(\vec{k}_1) = \langle \delta_x(\vec{k}_1) \delta_x(\vec{k}_2) \rangle$  in a large-scale ionized region is *identical* to a typical region some time later when  $\langle x_i \rangle$  has increased. This allows us to express the subcomponent bispectrum as

$$B_{x,x,x} \approx P_{\delta_x, \delta_x}(\vec{k}_3) \frac{\partial P_{\delta_x, \delta_x}(\vec{k}_2)}{\partial \delta_x}|_{x_i=\langle x_i \rangle} \quad (13.21)$$

Using the definition of  $\delta_x = (x_i - \langle x_i \rangle) / \langle x_i \rangle$ , we can rewrite the derivative with respect

to  $\langle x_i \rangle$  and use the chain rule

$$B_{x,x,x} = P_{\delta_x, \delta_x}(\vec{k}_1) P_{\delta_x, \delta_x}(\vec{k}_3) \langle x_i \rangle \frac{d \ln(P_{\delta_x, \delta_x}(\vec{k}_1))}{d \langle x_i \rangle} \quad (13.22)$$

$$B_{x,x,\rho}$$

This subcomponent could be neglected for our estimate, since large-scale  $\delta_\rho$  should be negligible.

$$B_{x,x,x\rho}$$

The third term of  $B_{x,x,21\text{cm}}$  takes the unflattering form of

$$-T_0 \langle x_i \rangle \int \frac{d^3 k'}{(2\pi)^3} \langle \delta_x(\vec{k}_1) \delta_x(\vec{k}_2) \delta_x(\vec{k}_3 - \vec{k}') \delta_\rho(\vec{k}') \rangle. \quad (13.23)$$

Making the assumption that all our fields are Gaussian<sup>1</sup>, we could expand the four-point function as three products of two-point functions. Evaluating them one-at-a-time:

$$\int \frac{d^3 k'}{(2\pi)^3} \langle \delta_x(\vec{k}_1) \delta_x(\vec{k}_2) \rangle \langle \delta_x(\vec{k}_3 - \vec{k}') \delta_\rho(\vec{k}') \rangle \quad (13.24)$$

This vanishes, since the integration of the second term picks-out the  $\vec{k}_3 = \vec{k}'$  mode. Under the squeezed triangle approximation we can send  $k_3 \rightarrow 0$ , and  $\delta_\rho(k' = 0) = 0$ .

$$\int \frac{d^3 k'}{(2\pi)^3} \langle \delta_x(\vec{k}_1) \delta_x(\vec{k}_3 - \vec{k}') \rangle \langle \delta_x(\vec{k}_2) \delta_\rho(\vec{k}') \rangle \approx P_{\delta_x, \delta_x}(\vec{k}_1) P_{\delta_x, \delta_\rho}(\vec{k}_2) \quad (13.25)$$

The integration of the first term selects the  $\vec{k}_1 + \vec{k}_3 = \vec{k}'$  mode. Under the squeezed triangle approximation,  $\vec{k}_1 \approx \vec{k}'$ .

The third integral was just a permutation of the second, above. This meant that we can write the third subcomponent bispectrum as

---

<sup>1</sup>This is a highly-idealistic assumption, but allows the mathematics to be tangible. For a fast estimator this is acceptable, but it should not be interpreted as extremely physically motivated.

$$-T_0 \langle x_i \rangle \left( P_{\delta_x, \delta_x}(\vec{k}_1) P_{\delta_x, \delta_\rho}(\vec{k}_2) + P_{\delta_x, \delta_\rho}(\vec{k}_1) P_{\delta_x, \delta_x}(\vec{k}_2) \right) \quad (13.26)$$

and the component bispectrum from this subsection can be expressed as

$$\begin{aligned} B_{x,x,21\text{cm}} \approx & -T_0 \langle x_i \rangle P_{\delta_x, \delta_x}(\vec{k}_1) \times \\ & \left( P_{\delta_x, \delta_x}(\vec{k}_3) \langle x_i \rangle \frac{d \ln(P_{\delta_x, \delta_x}(\vec{k}_1))}{d \langle x_i \rangle} + P_{\delta_x, \delta_\rho}(\vec{k}_2) + \frac{P_{\delta_x, \delta_\rho}(\vec{k}_1) P_{\delta_x, \delta_x}(\vec{k}_2)}{P_{\delta_x, \delta_x}(\vec{k}_1)} \right) \\ & \times \delta_D(\vec{k}_1 + \vec{k}_2 + \vec{k}_3) \end{aligned} \quad (13.27)$$

### 13.2.1.2 $B_{x,\rho,21\text{cm}}$ and $B_{x,\rho,21\text{cm}}$

In the squeezed triangle limit, these two component bispectra are identical. Their joint contribution can be expressed as:

$$\begin{aligned} 2\langle \delta_x(\vec{k}_1) \delta_x(\vec{k}_2) \delta_{21\text{cm}} \rangle = & 2T_0(1 - \langle x_i \rangle) \\ & \left\langle -\frac{\langle x_i \rangle}{1 - \langle x_i \rangle} \delta_x(\vec{k}_1) \delta_\rho(\vec{k}_2) \delta_x(\vec{k}_3) + \delta_x(\vec{k}_1) \delta_\rho(\vec{k}_2) \delta_\rho(\vec{k}_3) \right. \\ & \left. - \frac{\langle x_i \rangle}{1 - \langle x_i \rangle} \delta_x(\vec{k}_1) \delta_\rho(\vec{k}_2) \int \frac{d^3 k'}{(2\pi)^3} \delta_x(\vec{k}_3 - \vec{k}') \delta_\rho(\vec{k}') \right\rangle \end{aligned} \quad (13.28)$$

$B_{x,\rho,x}$

We could follow a similar line of reasoning as in Section 13.2.1.1 by assuming that the small-scale  $\delta_x \delta_\rho$  cross-power in an ionized region is the same as a typical region some time later when  $\langle x_i \rangle$  has increased. This allowed us to express:

$$B_{x,\rho,x} \approx P_{\delta_x, \delta_\rho}(\vec{k}_1) P_{\delta_x, \delta_x}(\vec{k}_3) \langle x_i \rangle \frac{d \ln(P_{\delta_x, \delta_\rho}(\vec{k}_1))}{d \langle x_i \rangle} \quad (13.29)$$

$B_{x,\rho,\rho}$

This subcomponent could be neglected for our estimate, since large-scale  $\delta_\rho$  should be negligible.

$$B_{x,\rho,x\rho}$$

Following the same reasoning as in Section 13.2.1.1, we arrived at the expression

$$\delta_x(\vec{k}_1)\delta_\rho(\vec{k}_2) \int \frac{d\mathbf{k}'}{(2\pi)^3} \delta_x(\vec{k}_3 - \vec{k}')\delta_\rho(\vec{k}') \approx P_{\delta_x,\delta_x}(\vec{k}_1)P_{\delta_\rho,\delta_\rho}(\vec{k}_2) + P_{\delta_x,\delta_\rho}(\vec{k}_1)P_{\delta_x,\delta_\rho}(\vec{k}_2) \quad (13.30)$$

so the component bispectrum from this subsection can be expressed as

$$\begin{aligned} -2T_0 \langle x_i \rangle & \left( P_{\delta_x,\delta_\rho}(\vec{k}_1)P_{\delta_x,\delta_x}(\vec{k}_3) \langle x_i \rangle \frac{d \ln(P_{\delta_x,\delta_\rho}(\vec{k}_1))}{d \langle x_i \rangle} + P_{\delta_x,\delta_x}(\vec{k}_1)P_{\delta_\rho,\delta_\rho}(\vec{k}_2) + P_{\delta_x,\delta_\rho}(\vec{k}_1)P_{\delta_x,\delta_\rho}(\vec{k}_2) \right) \\ & \times \delta_D(\vec{k}_1 + \vec{k}_2 + \vec{k}_3) \end{aligned} \quad (13.31)$$

### 13.2.1.3 $B_{\rho,\rho,21\text{cm}}$

This component bispectrum was much simpler to calculate, as we expected the overdensity power to be subdominant to the ionization field.

$$B_{\rho,\rho,x}$$

Following results from Section 13.2.1.1, this should be negligible so long as  $P_{\delta_\rho,\delta_\rho}(\vec{k}_1) < P_{\delta_x,\delta_x}(\vec{k}_1)$ , as expected.

$$B_{\rho,\rho,\rho}$$

This subcomponent could be neglected for our estimate, since large-scale  $\delta_\rho$  should be negligible.

$$B_{\rho,\rho,x\rho}$$

As in Sections 13.2.1.1 and 13.2.1.2, we could take advantage of the convolution term in the Fourier transform to obtain

$$\delta_x(\vec{k}_1)\delta_\rho(\vec{k}_2)\int\frac{d\vec{k}'}{(2\pi)^3}\delta_x(\vec{k}_3-\vec{k}')\delta_\rho(\vec{k}')\approx P_{\delta_\rho,\delta_x}(\vec{k}_1)P_{\delta_\rho,\delta_\rho}(\vec{k}_2)+P_{\delta_\rho,\delta_\rho}(\vec{k}_1)P_{\delta_\rho,\delta_x}(\vec{k}_2) \quad (13.32)$$

So the overall component bispectrum is the above, multiplied by a factor of  $-T_0 \langle x_i \rangle$ .

#### 13.2.1.4 Full estimator

Under the above assumptions, and simplifying with the squeezed triangle  $P_{f,f}(\vec{k}_1) \approx P_{f,f}(\vec{k}_2)$  for  $f = [x, \rho]$ , we obtained our estimate for the bispectrum:

$$B_{\text{KSZ,KSZ,21cm}}(\vec{k}_1, \vec{k}_2, \vec{k}_3) \approx -2T_0 \langle x_i \rangle \times \\ \left[ P_{\delta_x, \delta_x}(\vec{k}_1) \left( P_{\delta_x, \delta_x}(\vec{k}_3) \frac{\langle x_i \rangle}{2} \frac{d \ln(P_{\delta_x, \delta_x}(\vec{k}_1))}{d \langle x_i \rangle} + P_{\delta_x, \delta_\rho}(\vec{k}_1) + P_{\delta_\rho, \delta_\rho}(\vec{k}_1) \right) \right. \\ \left. + P_{\delta_x, \delta_\rho}(\vec{k}_1) \left( P_{\delta_x, \delta_x}(\vec{k}_3) \langle x_i \rangle \frac{d \ln(P_{\delta_x, \delta_\rho}(\vec{k}_1))}{d \langle x_i \rangle} + P_{\delta_x, \delta_\rho}(\vec{k}_1) + P_{\delta_\rho, \delta_\rho}(\vec{k}_1) \right) \right] \\ \times \delta_D(\vec{k}_1 + \vec{k}_2 + \vec{k}_3). \quad (13.33)$$

Equation 13.33 shows our estimator consists of several small-scale power spectral components ‘riding’ a large-scale ionization fluctuation. In the expected situation that power spectra consisting of density fluctuation components are subdominant to ionization fluctuations, we may expect a maximum or minimum at the mid-point of reionization, where the gradient of ionization power with respect average ionization is at an extreme.

#### 13.2.2 Counting triangles

The signal-to-noise of the bispectrum scales with  $\sqrt{N_{\text{Tri}}}$ , where  $N_{\text{Tri}}$  is the number of triangles (also see Section 13.4). A closed triangle in  $\ell$ -space can be represented by a two-dimensional Dirac delta-distribution  $\delta_D^{(2)}(\vec{\ell}_1 + \vec{\ell}_2 + \vec{\ell}_3)$ . A count of the different orientations of such a triangle was formulated by Joachimi et al. (2009) as:

$$\int_0^{2\pi} d\phi_{\ell 1} \int_0^{2\pi} d\phi_{\ell 2} \int_0^{2\pi} d\phi_{\ell 3} \delta_D^{(2)}(\vec{\ell}_1 + \vec{\ell}_2 + \vec{\ell}_3) \quad (13.34)$$

Which can be represented as an exponential:

$$\begin{aligned} & \int_0^{2\pi} d\phi_{\ell 1} \int_0^{2\pi} d\phi_{\ell 2} \int_0^{2\pi} d\phi_{\ell 3} \int_0^{\infty} \frac{d^2\theta}{(2\pi)^2} \exp\left(i(\vec{\ell}_1 + \vec{\ell}_2 + \vec{\ell}_3) \cdot \vec{\theta}\right) \\ &= (2\pi)^2 \int_0^{\infty} d\theta \theta J_0(\ell_1 \theta) J_0(\ell_2 \theta) J_0(\ell_3 \theta) \end{aligned} \quad (13.35)$$

Where they used the definition  $J_0(x) = \int_0^{2\pi} d\phi e^{ix \cos \phi} / 2\pi$ . Gradshteyn & Ryzhik (2000) give the analytic solution for the final integral for closed-triangle configurations for triple products of any order of Bessel Function. For zeroth-order Bessel Functions, their solution reduces to the reciprocal of the area of the triangle:

$$(2\pi)^2 \int_0^{\infty} d\theta \theta J_0(\ell_1 \theta) J_0(\ell_2 \theta) J_0(\ell_3 \theta) = \left( \frac{1}{4} \sqrt{2\ell_1^2 \ell_2^2 + 2\ell_1^2 \ell_3^2 + 2\ell_2^2 \ell_3^2 - \ell_1^4 - \ell_2^4 - \ell_3^4} \right)^{-1} \quad (13.36)$$

In reality, measurements of any bispectrum or power spectrum will be binned in  $\ell$ , with central values and widths of  $\bar{\ell}$  and  $\Delta\ell$  respectively. The number of triangles in a kSZ<sup>2</sup>-21cm bispectrum bin will be given by:

$$N_{\text{Tri}} \approx 2\pi \Omega_S^2 \bar{\ell}_1 \bar{\ell}_2 \bar{\ell}_3 \Delta\ell_1 \Delta\ell_2 \Delta\ell_3 \int_0^{\infty} d\theta \theta J_0(\bar{\ell}_1 \theta) J_0(\bar{\ell}_2 \theta) J_0(\bar{\ell}_3 \theta) \quad (13.37)$$

For the limits on  $\ell_{1,2,3}$  mentioned at the beginning of Section 13.2 concerning near-future CMB experiments and HERA's most-numerous short baselines, Equation 13.37 gives  $N_{\text{Tri}} \sim 10^9$ , for a sky fraction of 0.03, surveyed by the HERA drift-scanned stripe.

### 13.2.3 Results

The  $P_{\delta_p, \delta_p}(k)$ ,  $P_{\delta_x, \delta_x}(k)$  and  $P_{\delta_x, \delta_p}(k)$  power spectra relevant to the estimator are shown (from top to bottom) in Figure 13.3 . The line colors, as labelled, correspond to different redshift slices from the simulation cube. As expected, the density power spectrum slowly

increased in amplitude with decreasing redshift, as structure grew hierarchically. The ionization power spectrum was highest at the midpoint of reionization, when there was maximal contrast in the brightness temperature field. This latter trend dominated their cross-power spectrum.

Coupled with relevant derivatives with respect to ionization fraction, and averages with respect to redshift, we could use the power spectra above to calculate the estimator in Equation 13.33 as a function of redshift – shown in Figure 13.4. As expected, the magnitude of the estimated bispectrum is at an extreme close to the center of reionization. Also as expected, it is negative, showing that the 21 cm and kSZ power are anti-correlated. It also appears to be quite noisy, with the large dip at  $z \sim 7.3$  lacking a clear explanation.

Of course, we were also able to calculate the bispectrum directly from the simulated 21 cm and kSZ fields, restricting ourselves to relevant  $\ell$  modes for HERA baselines and CMB experiments. However, we found that the box was too small to sample an appropriate number of large-scale modes, such that there were too few triangles in the box to converge on a given magnitude. In Figure 13.5, we show bispectrum power binned as a function of angle between the  $\vec{k}$  vector for the 21 cm field and one of the  $\vec{k}$  vectors from the kSZ map (a dimension which our semianalytic estimator does not probe, as it uses power spectra and assumes the ultimate squeezed triangle limit of  $\theta = 0$ ) from  $z = 7.3, 7.8$  and  $8.3$ . Error bars indicate the standard deviation of values in that  $\theta$  bin. The values, while larger than the expected experimental noise by a factor of at least 10 (see Section 13.4), are consistent with numerical noise, oscillating about zero with high variance. This is true for all redshifts probed, likely due to too few large-scale modes existing in the relatively small simulation box used.

Figure 13.5 highlights one of the limitations of using the bispectrum as a statistic to probe reionization. It is difficult to obtain sufficient numbers of triangles in a simulation cube to converge on a bispectrum value. While it was possible to calculate the bispectrum for a single redshift on a  $512^3$  resolution element box in minutes, running the same calculation on a  $2048^3$  element box would take roughly six hours. This means that characteri-

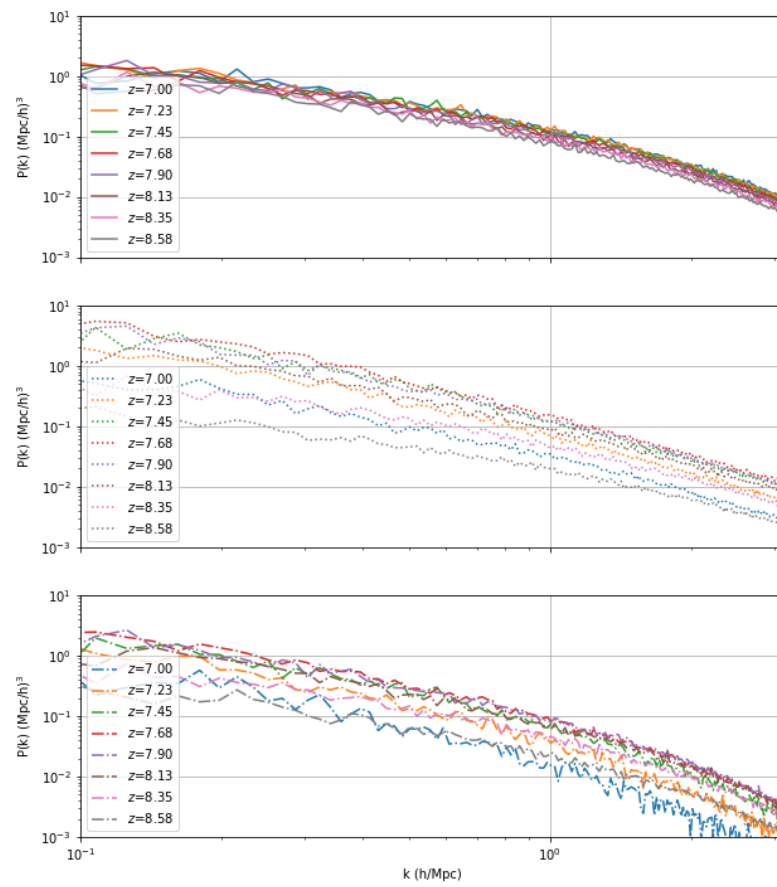


Figure 13.3: The (top to bottom)  $P_{\delta\rho,\delta\rho}(k)$ ,  $P_{\delta_x,\delta_x}(k)$  and  $P_{\delta_x,\delta\rho}(k)$  power spectra relevant to our semianalytic estimate of the bispectrum.

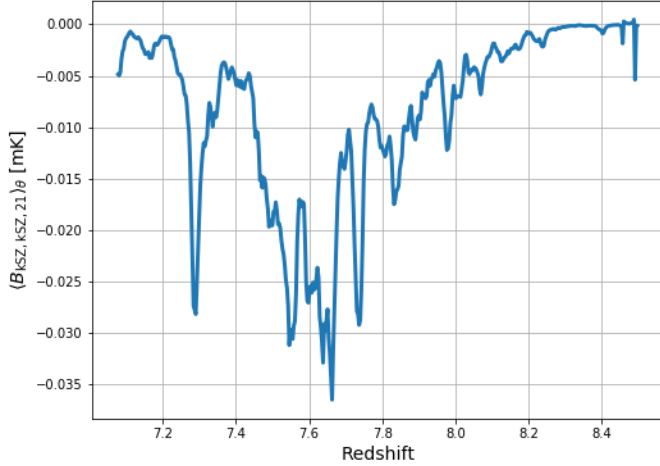


Figure 13.4: The semianalytic expression of the bispectrum, calculated as a function of redshift from our simulation.

zation of the bispectrum – understanding its sensitivity to astrophysical and cosmological parameters – is difficult to obtain, as this would require large numbers of simulations with varied parameters, large enough to produce higher signal-to-noise bispectra than we are capable of in this work. Sefusatti et al. (2016) and Watkinson et al. (2017) have suggested FFT-based estimators to overcome the poor scaling associated with bispectrum calculations; pursuing these methods in future investigations may prove worthwhile.

Possibly the largest limitation of the bispectrum is one that has been brushed under the carpet in most of the discussion above. The kSZ only exists in the  $k_{\parallel} = 0$  plane, since by its integral definition it has not line-of-sight component. Because two kSZ terms are required, this forces any closed triangle (enforced by the Dirac delta functions throughout Section 13.2.1) to exist only at  $k_{\parallel} = 0$  values: the 21 cm component is trapped within the center of the wedge! One could argue that the foreground contamination problem is not strictly the same for the bispectrum as it is for the 21 cm power spectrum, as the ‘true’ foreground for the bispectrum is the correlation of the CMB with low-frequency Galactic synchrotron, which is low (e.g. Ichiki, 2014). However, while the effective  $T_{\text{sys}}^2$

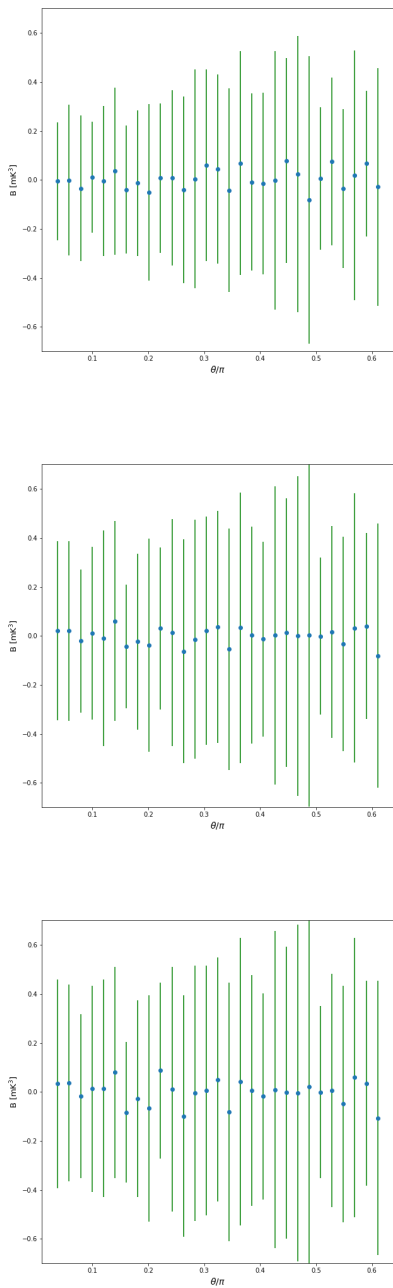


Figure 13.5: Bispectrum values, binned as a function of angle between the 21 cm and CMB  $\vec{k}$  vectors, measured directly from the simulation at  $z = 7.3, 7.8$  and  $8.3$  from top to bottom. The values are consistent with zero, most likely due to too few large-scale modes present in the cube.

in Equation 13.49 is close to receiver noise outside of the wedge, at  $k_{\parallel} = 0$  its value becomes very large, as it is dominated by  $T_{\text{sky}}$ .

To be non-zero outside of the wedge, two 21 cm fields are required in the correlation function. This moved us to a minimum of a four point function, which we explored using trispectra, below.

### 13.3 kSZ<sup>2</sup>-21cm<sup>2</sup> squeezed-rectangle trispectra

As noted above, to correlate with a kSZ map, we have to square the it to force it to be positive-definite. If we use a single 21 cm map to correlate with two kSZ maps (i.e. a bispectrum), we must satisfy a Dirac delta function of the form  $\delta_D(\vec{k}_1 + \vec{k}_2 + \vec{k}_3)$ . Since the kSZ is a projected quantity, it contains no line-of-sight modes, so two of the k vectors have no line-of-sight component; the third k vector must also have no line-of-sight component. That means that the 21 cm contribution is stuck in the center of the wedge.

The trispectrum of these fields, with two 21 cm maps and two kSZ maps, does not share this problem. Its Dirac delta function has two  $k$  vectors associated with the 21 cm field, and these can cancel each other to satisfy a closed-quadrilateral condition. We limit ourselves to discussion of the squeezed trispectrum, where the k modes of the 21cm field are much larger than the k modes of the kSZ field. This is a realistic regime for the combination of HERA with Stage 3 or 4 CMB experiments. The geometry of these statistics are shown in Figure 13.6.

#### 13.3.1 Mathematical formulation

The trispectrum can be written as follows (note that in terms such as  $\vec{k}_{\perp}^2$ , the 2 is a label and not an exponent; we will define terms below):

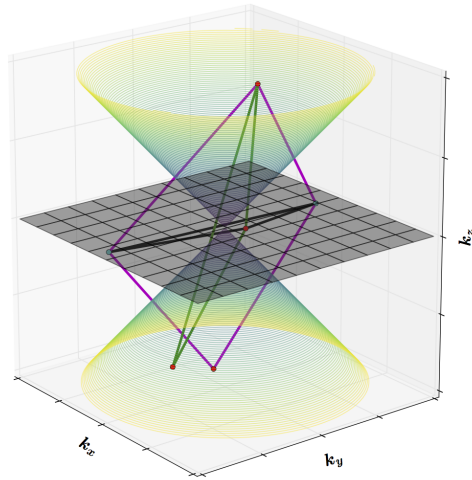


Figure 13.6: The geometry of the correlation statistics considered in this Chapter. The conical shape indicates the boundaries of the wedge in  $k_x, k_y, k_z$  space (i.e. not cylindrically averaged into  $k_\perp, k_\parallel$ ), where being ‘within’ the wedge is being outside of the boundaries. Closed triangles of the 21 cm-kSZ<sup>2</sup> bispectrum are represented by the black lines – because of the projected nature of the kSZ, they must exist within the wedge. 21 cm<sup>3</sup> bispectra, the green lines, could potentially recover 21 cm statistics from within the wedge. 21 cm<sup>2</sup>-kSZ<sup>2</sup> trispectra, the magenta lines, allow us to correlate the 21 cm signal and the kSZ without the limitations of working within foreground-contaminated regions.

$$\begin{aligned}
\mathcal{T}(\delta_{21\text{cm}}^{2D}, \delta_{21\text{cm}}^{2D}, \delta_{\text{kSZ}}, \delta_{\text{kSZ}}; z) &= \langle \delta_{21\text{cm}}^{2D}(\vec{k}_\perp^1) \delta_{21\text{cm}}^{2D}(\vec{k}_\perp^2) \delta_{\text{kSZ}}(\vec{k}_\perp^3) \delta_{\text{kSZ}}(\vec{k}_\perp^4) \rangle \\
&= \int \frac{dk_\parallel^1}{2\pi} \frac{dk_\parallel^2}{2\pi} \frac{dk_\parallel^3}{2\pi} \frac{dk_\parallel^4}{2\pi} W_{21\text{cm}}(k_\parallel^1) W_{21\text{cm}}(k_\parallel^2) W_{\text{kSZ}}(k_\parallel^3) W_{\text{kSZ}}(k_\parallel^4) \\
&\quad \times \langle \delta_{21\text{cm}}^{3D}(k_\parallel^1, \vec{k}_\perp^1) \delta_{21\text{cm}}^{3D}(k_\parallel^2, \vec{k}_\perp^2) \delta_{\text{kSZ}}(k_\parallel^3, \vec{k}_\perp^3) \delta_{\text{kSZ}}(k_\parallel^4, \vec{k}_\perp^4) \rangle \\
&\quad \times \delta_D(\vec{k}^1 + \vec{k}^2 + \vec{k}^3 + \vec{k}^4)
\end{aligned} \tag{13.38}$$

The window functions above represent the key motivation for calculating the trispectrum.

$$W_{21\text{cm}}(k_\parallel) = \begin{cases} 1 & k_{\parallel,\min} \leq k_\parallel \leq k_{\parallel,\max} \\ 0 & \text{otherwise} \end{cases}, \tag{13.39}$$

where  $k_{\parallel,\min}$  is set by the interferometer baseline  $\vec{b}$  and is the boundary of the wedge, and  $k_{\parallel,\max}$  could take a range of values, the smallest of which proportional to the Fourier conjugate of a single frequency channel-width. This window function filters-out the wedge.  $W_{\text{kSZ}}$  is given by Equation 13.11. We represent the wedge-filtered 21 cm field as

$$\delta_{21\text{cm}}^{2D}(\vec{k}_\perp) = \int \frac{dk_\parallel}{2\pi} W_{21\text{cm}}(k_\parallel) \delta_{21\text{cm}}^{3D}(k_\parallel, \vec{k}_\perp). \tag{13.40}$$

Equation 13.38 could be simplified. The Dirac delta functions may be factored into line-of-sight and transverse components,

$$\delta_D(\vec{k}^1 + \vec{k}^2 + \vec{k}^3 + \vec{k}^4) = \delta_D(k_\parallel^1 + k_\parallel^2 + k_\parallel^3 + k_\parallel^4) \delta_D(\vec{k}_\perp^1 + \vec{k}_\perp^2 + \vec{k}_\perp^3 + \vec{k}_\perp^4). \tag{13.41}$$

In the squeezed limit,  $k_\parallel^3, k_\parallel^4 \ll k_\parallel^1, k_\parallel^2$ . This allowed us to use the Limber approximation for the kSZ window function, as written in Equation 13.11.

We may also approximate the central  $k$  mode picked-out by the 21 cm window function in Equation 13.39 as a single  $k_{\parallel,\alpha}$ . We write  $\delta_{21\text{cm}}^{3D}(k_\parallel^\alpha, \vec{k}_\perp) = \delta_{21\text{cm},\alpha}^{2D}(\vec{k}_\perp)$ .

Together these simplifications allowed three of the four integrations to be performed:

$$\begin{aligned}
\mathcal{T}(\delta_{21\text{cm}}^{2D}, \delta_{21\text{cm}}^{2D}, \delta_{\text{kSZ}}, \delta_{\text{kSZ}}; z) &= \langle \delta_{21\text{cm},\alpha}^{2D}(\vec{k}_\perp^1) \delta_{21\text{cm},\alpha}^{2D}(\vec{k}_\perp^2) \delta_{\text{kSZ}}(\vec{k}_\perp^3) \delta_{\text{kSZ}}(\vec{k}_\perp^4) \rangle \\
&\quad \times \delta_D(\vec{k}_\perp^1 + \vec{k}_\perp^2 + \vec{k}_\perp^3 + \vec{k}_\perp^4) |W_{\text{kSZ}}(z)|^2 \int \frac{dk_\parallel^1}{2\pi} |W_{21\text{cm},\alpha}(k_\parallel^1)|^2
\end{aligned} \tag{13.42}$$

### 13.3.2 Effects of filtering

It is valuable to note that filtering the 21 cm and kSZ maps has a dire effect on how simple it is to interpret these objects in image space. As an illustration, in Figure 13.7 we show a representative slice of our 21 cm brightness temperature cube before and after wedge filtering, and the kSZ map before and after low- and high-pass filtering. The effect on the kSZ is relatively easy to understand – most of the large diffuse features ( $\ell < 3000$ ) are eliminated by the high-pass cutoff, while the low-pass is not as stringent ( $\ell > 13000$ ), leaving only small-scale modes within the image. However, removing the wedge does not constitute a simple high or low-pass filter. Instead, power is shifted around in image-space. This effect lead to Beardsley et al. (2015) showing that a given cell in a wedge-filtered image can only be used to obtain a model-dependent estimate of the ionization fraction.

We can also see strange effects of wedge filtering more qualitatively by forming 1D power spectra of the  $21\text{ cm}^2$  brightness temperature before and after the cube has been filtered. This is shown for several different redshifts in Figure 13.8. As expected, removing modes from inside the wedge results in a decrease in power. However, the hierarchy of power as a function of redshift also changes after the filter. This lacks an easy explanation.

### 13.3.3 $\text{kSZ}^2\text{-21cm}^2$ cross-power spectrum

While bispectra are computationally costly to calculate, trispectra are even more so. However, unlike the bispectrum, the trispectrum lacks an easy-to-understand semianalytic estimator. When we applied the same tactics as used in Section 13.2.1, all terms vanished except for the ‘connected’ Gaussian term, that we would need to subtract from our final trispectrum estimate in the end, anyway:

$$\Delta\mathcal{T} \approx P_{21\text{cm}}(\vec{k}_\perp^1)P_{\text{kSZ}}(\vec{k}_\perp^3) \times |W_{\text{kSZ}}(z)|^2. \quad (13.43)$$

However, the form of Equation 13.42 suggests that one term in the overall trispectrum that may be an interesting and efficient quantity to calculate is the cross-power spectrum

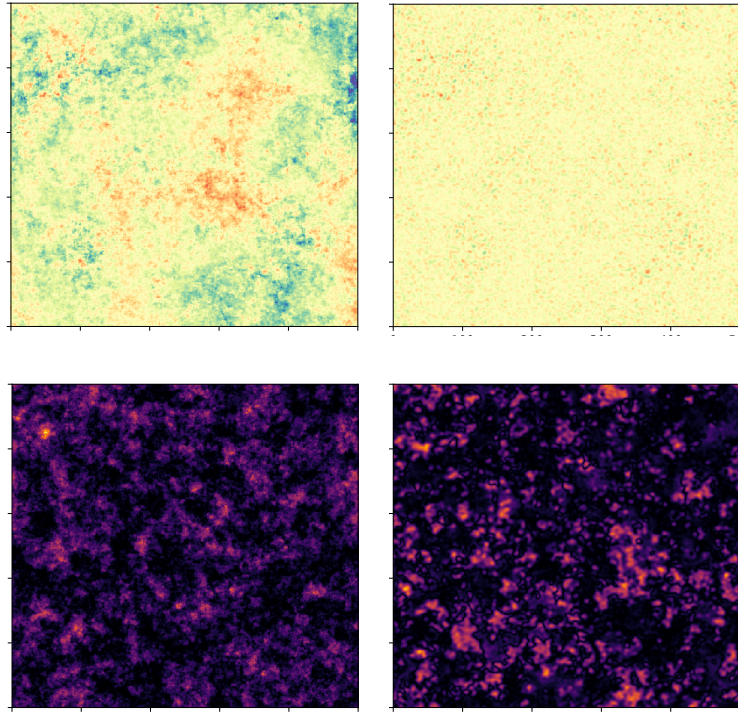


Figure 13.7: The effect of filtering kSZ and 21cm maps to avoid foreground contamination. Top panels are the kSZ map from our simulation, before (left) and after (right) high and low pass filtering. After filtering, only small-scale modes survive. The bottom panels show a slice of the 21 cm brightness temperature cube before (left) and after (right) wedge-filtering. Power is entirely scrambled, and small-scale details are removed. The colorbars are matched for pre- and post- filtered maps.

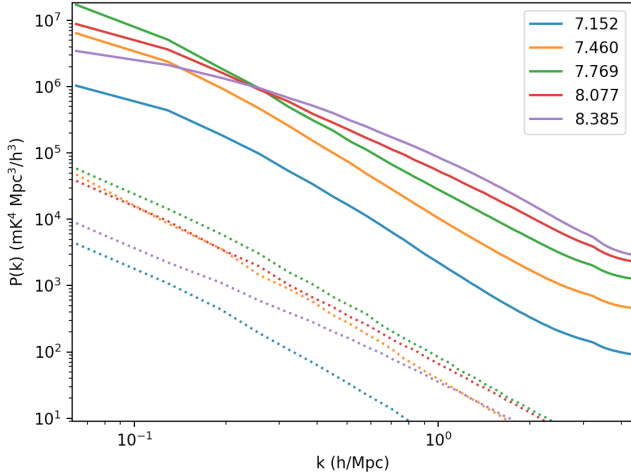


Figure 13.8: 21 cm power spectra before (solid) and after (dotted) filtering the wedge for several redshifts. Not only does filtering the wedge decrease power, it also changes the hierarchy of power between power spectra, with respect to redshift.

between the squared 21 cm and squared kSZ fields. Each would have to be filtered before squaring, in order to not convolve foreground-contaminated modes with otherwise clean ones. This cross-power spectrum is defined as

$$P_X(k) = \langle \delta_{21\text{cm}}^{2D*}(k_1) \delta_{21\text{cm}}^{2D}(k_1) \delta_{\text{kSZ}}^*(k_3) \delta_{\text{kSZ}}(k_3) \rangle \quad (13.44)$$

for large-scale modes  $k_1$  and small-scale modes  $k_3$ . This was an inexpensive way to probe the correlation of the squared fields, without calculating the full trispectrum. This quantity is shown in Figure 13.9, as a function of redshift of the 21 cm contribution. Colors indicate redshift, while the solid lines are for unfiltered fields (in which the 21 cm field is averaged without a window function to form  $\delta_{21\text{cm}}^{2D}$ ) and dotted lines indicate data after filtering. The statistic is noisy, but is significantly above theoretical noise levels (passing Gaussian noise fields through the same calculation resulted in a flat power spectrum; see Section 13.4). Power decreases with redshift, suggesting some dependence on the ionized fraction. Like the  $21\text{ cm}^2$  power spectra shown in Figure 13.8, filtering the wedge changes this trend. The correlation was strongest on large scales before and after filtering, which also suggests that the 21 cm field dominates the correlation.

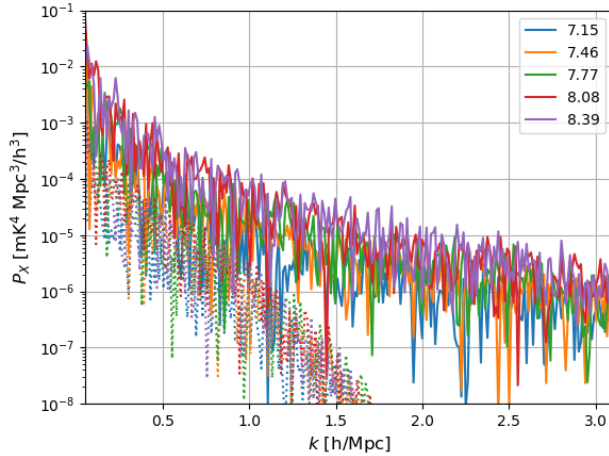


Figure 13.9: The cross-power spectrum of the squared 21 cm and kSZ fields, as a function of redshift of the 21 cm contribution.

## 13.4 Foregrounds and Noise

As discussed throughout this work, the major foreground EoR experiments face is bright Galactic and extragalactic synchrotron. We ignore polarization contamination for this Chapter. In Section 13.2, we showed that the bispectrum, while theoretically and computationally tangible, is extremely sub-optimal in the context of 21 cm observations, forcing the power measured to be sourced from within the wedge. The study of the trispectrum, presented in Section 13.3, was motivated by this limitation and overcomes it in a rather elegant fashion.

The dominant foregrounds for the kSZ are the other anisotropies present in the CMB. The primary anisotropies are extremely powerful at multipoles  $\ell \lesssim 2500$ , with additional contributions from the thermal Sunyaev-Zeldovich effect (e.g. George et al., 2015). On small scales,  $\ell > 6000$ , the far-infrared background (FIB) is the primary contaminant. Its contribution, which is essentially a shot-noise term, could be reasonably-well subtracted out to  $\ell \sim 13000$  for near-future CMB surveys (known as ‘Stage 3 and 4’ in the cosmology community; Abazajian et al. 2016).

The signal-to-noise of a single bispectrum triangle  $(\ell_1, \ell_2, \ell_3)$  is given by:

$$\left(\frac{S}{N}\right)^2 = \frac{B(\ell_1, \ell_2, \ell_3)}{C_{\text{CMB}}^N(\ell_1)C_{\text{CMB}}^N(\ell_2)C_{21\text{cm}}^N(\ell_3)}, \quad (13.45)$$

and for a single trispectrum quadrilateral  $(\ell_1, \ell_2, \ell_3, \ell_4)$ :

$$\left(\frac{S}{N}\right)^2 = \frac{\mathcal{T}(\ell_1, \ell_2, \ell_3, \ell_4)}{C_{\text{CMB}}^N(\ell_1)C_{\text{CMB}}^N(\ell_2)C_{21\text{cm}}^N(\ell_3)C_{21\text{cm}}^N(\ell_4)} \quad (13.46)$$

for CMB and 21 cm noise-power spectra  $C_{\text{CMB}}^N(\ell)$  and  $C_{21\text{cm}}^N(\ell)$ , respectively.

For the CMB, as noted above, measurements at appropriate  $\ell$  values will leave the FIB as the dominant noise source. The minimum value of this term was reported by George et al. (2015) as

$$\hat{D}_{\ell=3501-3900} = \left\langle \frac{\ell(\ell+1)}{2\pi} C_\ell \right\rangle_{\ell=3501-3900} = 30.8 \pm 1.2 \mu\text{K}^2. \quad (13.47)$$

Massively-redundant interferometers typically make for poor imaging instruments, since they probe a relatively small number of  $uv$  modes (e.g. Chapter 3). One of HERA's innovations is that, once fully constructed, it will be both highly redundant and a relatively high-fidelity imager. This is due to its raw number of baselines, but also because it will be split in to three dense sections with a cloud of outriggers, each positioned on a redundant sub-grid. This allows HERA to gain the long baselines required for point-source imaging and a more fully-populated  $uv$ -plane, while maintaining redundant calibratability (Dillon & Parsons, 2016; DeBoer et al., 2017).

As such, the expression for  $C_\ell^N$  spherically-averaged power spectrum for noise on multipole  $\ell$ , observed by redundant baselines and binned in LST, has not yet been formulated in the literature. We calculate it here, starting from Equation 57 of Zaldarriaga et al. (2004), assuming it holds for a single baseline:

$$C_{\ell, \text{single}}^N = \frac{T_{\text{sys}}^2}{\Delta v t_v d^2 u} = 4\pi^2 \frac{T_{\text{sys}}^2}{\Delta v t_v d^2 \ell} \quad (13.48)$$

where  $T_{\text{sys}}$  is the system temperature,  $\Delta v$  is the bandwidth integrated over time  $t_v$ , for baseline probing a spread of values  $du$  over  $\Delta v$ . We assumed that each baseline could be

added coherently for an amount of time each day (e.g. the length of time a given source takes to transit the main lobe of the beam)  $t_c$ , observed  $N_{\text{obs}}$  times over an observing season. For the term  $d^2\ell \equiv (\Delta\ell)^2$ , we note that for HERA, the effective  $\ell$  range most-probed has  $\Delta\ell \approx 20$  (given by the redundant 14.6 m baselines for a wavelength 2 m).

For an estimate of the noise levels achieved by an entire array over an observing season, we used the fact that the noise for a single baseline should average down linearly in time over the coherence time scale, i.e.  $t_v = N_{\text{obs}}t_c$ . The noise should be reduced linearly by the total number of baselines  $N_{\text{bl}}$  and the square-root of the incoherently-averaged time samples,  $N_i = t_i/t_c$ , for the length of time for incoherent time averages  $t_i$ . This leads to the expression

$$C_{\ell,\text{total}}^N = 4\pi^2 \frac{T_{\text{sys}}^2}{\Delta v(\Delta\ell)^2 t_c N_{\text{obs}} N_{\text{bl}} \sqrt{N_i}}. \quad (13.49)$$

Assuming a  $T_{\text{sys}}=400$  K. For HERA, the coherent integration time is  $t_c \approx 15$  minutes, with  $N_{\text{obs}} \approx 100$  over a season. For delay-spectrum measurements, the typical parameters used are  $\Delta v=8$  MHz and  $t_i=8$  hours (Ali et al., 2015). As noted above, the most numerous HERA baselines have  $\Delta\ell \approx 20$ , and there are roughly 4200 of them in the final HERA core. Together, these grant a noise level of  $C_{\ell,\text{total}}^N \approx 1\mu\text{K}^2$ .

Using the Equations from Zaldarriaga et al. (2004) directly without explicit modification for redundancy (the redundancy instead arising implicitly from considerations of the aperture of the array), one arrives at a similar figure of  $C_{\ell,\text{total}}^N \approx 7\mu\text{K}^2$ .

These noise calculations grant estimated noise levels of  $31 - 82\mu\text{K}^3$  for the bispectrum, and  $31 - 217\mu\text{K}^4$  for the trispectrum.

## 13.5 Discussion

Higher-order correlation functions are complicated statistical objects. While they are expensive to compute and prove difficult to initially interpret, they can provide elegant methods for obtaining greater confidence of the data in their correlations.

While forming kSZ<sup>2</sup>-21 cm bispectra forces the calculation to occur within the wedge, source-subtraction on long baselines could lower the noise sufficiently for a low signal-to-noise detection of some bispectrum triangles. This would provide confidence to both the 21 cm and CMB experiments that their detections of the respective fields were truly detections.

The trispectrum, while less theoretically tangible, provides elegant window functions that allow both 21 cm and CMB experiments to avoid their respective foreground contaminants in Fourier space. We have provided an initial look at an estimate of this signal. Much more thought must be put into the calculation of the trispectrum for it to be computationally feasible for large-box simulations that sample the low  $k$  values HERA will probe.

The delay spectrum is an elegant method to avoid foreground contamination. However, a large fraction of the overall information about the EoR is contained at low  $k_{\parallel}$  modes (e.g. Jensen et al., 2016). Being able to extract even some component of that information from within the wedge would prove extremely powerful. One tool that might be used for such a task is a three point correlation function in Fourier space – with two points outside of the wedge, and one within it (see Figure 13.6). Choosing appropriate ( $k_{\perp}, k_{\parallel}$ ) coordinates could potentially decorrelate the foregrounds to allow such a measurement.

# Chapter 14

## Deep Learning for 21cm Observations

Modern cosmological theory is capable of predicting the statistical features of many aspects of the observable Universe, using either theoretical calculations (e.g. Bond et al., 1991; Sheth & Tormen, 1999) or sophisticated numerical simulations (e.g. Lewis et al., 2000b; Vogelsberger et al., 2014). These theories may be tested by making observations of various large-scale fields, in surveys spanning large cosmological volumes in space and time. The ultimate goal of measurements is extract from the data some parameters which are believed to describe the underlying processes, and to relate these parameters to a theoretical understanding of the physics at work. In some cases – most conspicuously the primordial CMB – the statistics of the fields are Gaussian, and are completely described by the two-point correlation function, or its Fourier conjugate, the power spectrum (e.g. Liddle & Lyth, 2000, for a review).

A field described only by Gaussian statistics practically does not exist in cosmology beyond the CMB. For nearly every other scenario involving the non-linear interactions of gravity, radiation, and fluid mechanics, the resultant fields are non-Gaussian. Within the non-Gaussianity of these fields is encoded additional valuable information about the astrophysical processes at work, and can also serve as a cross-validation of two-point statistics of the same field (Alvarez, 2016; Majumdar et al., 2017). The specific details of the non-Gaussianity are not usually straightforwardly obtained from the theory, and thus

devising appropriate higher-order statistics to efficiently probe the non-Gaussian information is in general a difficult problem.

By analyzing a field using power spectra, one explicitly neglects all non-Gaussian information. In Chapter 13, we presented higher-order correlation functions that are sensitive to non-Gaussian information in Fourier space. In the case of 21 cm emission, working in Fourier space provides a natural and relatively simple way to avoid foreground contamination. Another solution could be to search for non-Gaussian information in image space, assuming some future development that could overcome the foreground challenge (e.g. Shaw et al., 2014, 2015; Zhu et al., 2016; Patil et al., 2017), or that we may operate on wedge-filtered image fields in a physically meaningful way (Beardsley et al., 2015). Staying in image space allows us to retain the non-Gaussian information in our data.

## 14.1 Neural Networks

A potential solution for parameter extraction is available due to advances in computation, allowing us to generate large numbers of numerical simulations which are realizations that capture the relevant physics of an astrophysical process (e.g. Mesinger et al., 2011), and the development of deep learning algorithms which can be “trained” to recognize patterns in data (e.g. Hinton & Salakhutdinov, 2006; Hinton et al., 2012).

Convolutional Neural Networks (CNNs; e.g. LeCun et al., 1995) have proven exceptionally useful for extracting non-Gaussian information from images in order to classify or extract information from their contents to a very high accuracy (e.g. Krizhevsky et al., 2012). There are many, many explanations of the inner calculus of neural networks, and the intention of this chapter is not a comprehensive review of that field. For the purposes of this chapter, a few concepts must be mentioned:

- Convolutional Neural Networks are systems of 1, 2 or 3-dimensional matrices that are used as convolutional kernels on an input image. An image is propagated forward through the network via consecutive convolutions by these kernels. Each

kernel entry (i.e. pixel) is known as a ‘weight’  $w$ .

- The desired output of a ‘training set’, for example, the contents of an image, is given as a vector which the total of all the convolutions must reproduce.
- Inevitably, if the convolutional kernels are initially randomly generated, the output vector will not contain the desired quantities. A ‘cost function’ is a metric that specifies how ‘wrong’ an output is. This could be the mean squared error, for example.
- Neural networks ‘learn’ through a process called ‘backpropagation’. Based on the cost function, a chain rule can be applied backwards along the network for each input, updating the values of the weights by some fraction of the user-specified ‘learning rate’ (Rumelhart et al., 1986).
- Associated with each weight is an ‘activation function’,  $a(x)$ . The value of  $a(w * x)$  (the output of the activation function given the convolved input) is actually what is handed to the next convolutional kernel along the network. Activation functions can be non-linear, allowing neural networks to learn complex decision boundaries.
- In order to down-sample the data to a more manageable size, ‘pooling layers’ are often implemented. These extract a moving statistic such as the moving average or maximum in a given region of the image.
- CNNs often end with a ‘fully connected’ or ‘dense’ layer. These are multi-layer perceptrons (e.g. Rosenblatt, 1961) that propagate the value  $s$  of  $a(wx)$  – that is, no convolution is applied, and each layer is 1-dimensional.
- After training on some subset of the total data (which may be done several times over), a neural network can be ‘tested’ by forward-propagating new images, not used in training, and not backpropagating. Testing can also be implemented after some subsample of the training data has been propagated – i.e., as the network is in the middle of training – often called ‘validation’.

With this primer in mind, we will present two uses of CNNs for understanding simulated realizations of reionization: classifying the main causes (galaxies or active galactic nuclei) of reionization (Hassan et al., 2018), and regressing upon a physical parameter of interest.

## 14.2 Classifying reionization models

The 21 cm power spectrum is a powerful tool for quantifying the relative clustering of large and small scaled ionized regions (Hassan et al., 2017). However, the topology of the regions themselves can provide information on the dominant mechanism of their formation. We considered two scenarios: one in which only galaxies, and the other in which only active galactic nuclei (AGN), provided ionizing photons.

We used SIMFAST21 (Santos et al., 2010; Hassan et al., 2017) to generate a dark matter density field, evolve it into the non-linear regime using the Zel'dovich approximation. Dark matter halos were generated using the excursion set formalism (Bond et al., 1991). Either galaxies or AGN were placed in halos, with populations following the parametrization of Hassan et al. (2016). Ionized regions are “painted on top of” the dark matter halos according to parametrizations from high-resolution radiative transfer simulations and large-volume hydrodynamic simulations (see Hassan et al. (2016); Hassan et al. (2018)). An example of a galaxy-dominated and AGN-dominated reionization field is shown in Figure 14.1. For this study, we focused on the field at redshift  $z = 8$ . Galaxies produce more, small, ionized regions, whereas AGN produce larger more spherical ones. This is due to the strong clustering AGN and their harder X-ray spectrum.

We used Tensorflow (Abadi et al., 2016) to build a classifying CNN with 2 layers of 2-dimensional convolutional kernels interleaved with two maximum-pooling layers, a single dense layer, and an output layer. The convolutional and dense layers used the ReLU activation function, which is defined as

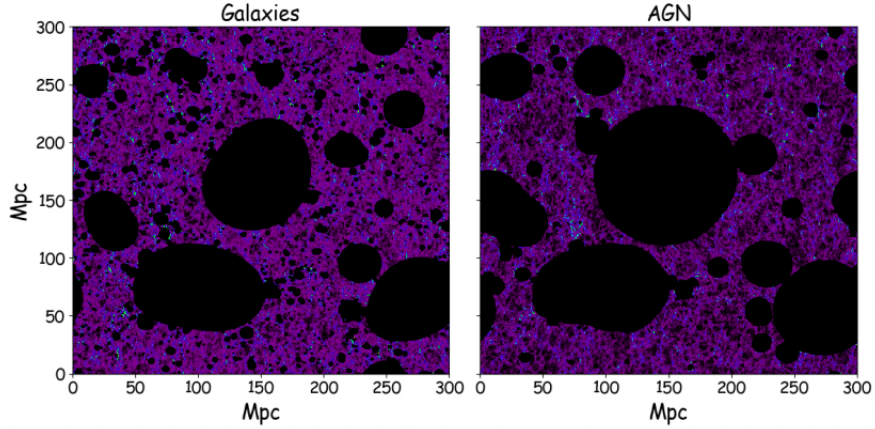


Figure 14.1: 21 cm brightness temperature fields (in arbitrary units) for Galaxy-Only (left) and AGN-only (right) models. Figure from Hassan et al. (2018).

$$\text{ReLU}(x) = \begin{cases} 0 & x < 0 \\ x & x > 0 \end{cases} \quad (14.1)$$

The network is shown in Figure 14.2. To train it, we used  $\sim 1000$  images of  $z = 8$  realizations. Each image was a  $140 \times 140$  greyscale image of 21 cm brightness temperature, with a simulation box size of 75 Mpc. Each image came from a separate simulation, which varied the photon escape fraction, X-ray spectrum of the ionizing sources and the ionizing efficiency of those sources. The testing set was  $\sim 100$  additional images. To prevent over-fitting, only a random set of 75% of neurons were used during each forward propagation (a method known as ‘dropout’). The logistic cross-entropy function was used as the cost function.

Using the 21CMSENSE package (Pober et al., 2014), we could simulate the expected thermal noise of a foreground-decontaminated image cube for LOFAR, HERA-331 and SKA-Low (see Chapter 4). Adding this noise to each image allowed us to make predictions of the accuracy of such a tool for predicting ionization models for actual data.

The results of training and validation are shown in Figure 14.3. During training, the HERA and SKA fields quickly become  $> 99\%$  accurately classified. Systematic gaps

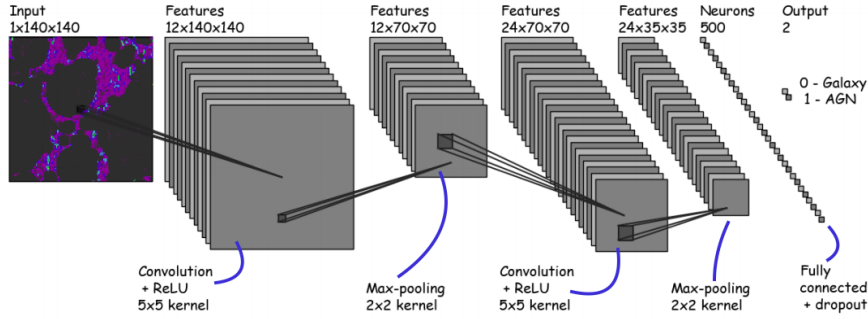


Figure 14.2: The classification CNN used in this study. Figure taken from Hassan et al. (2018).

between training and validation data for HERA suggests that an additional linear bias parameter may be useful for future networks. While the LOFAR classification eventually reaches high accuracy during training, validation shows that the network is strongly overfitting in this case – suggesting that LOFAR will not be able to produce data in which the galaxy and AGN contributions to reionization. This result is substantiated by power spectrum studies by Hassan et al. (2017).

We can inspect the effect that kernels of a given layer have on an input image to gain some interpretation of what the network regards as ‘important’ for the classification. An example of such an inspection is shown in Figure 14.4, which shows a single (galaxy-dominated) training image propagated through the trained kernels of the first convolutional layer. Some form of edge detection emphasizing the small, high-temperature regions of the map has been learned by the kernels. A comprehensive understanding of the relationship between the physical processes and the kernels required to identify them will be the subject of future work.

### 14.3 Regressing upon reionization parameters

Cosmological studies often want to go beyond binary classifications, instead seeking to understand the value of some collection of variables that describe physical processes in

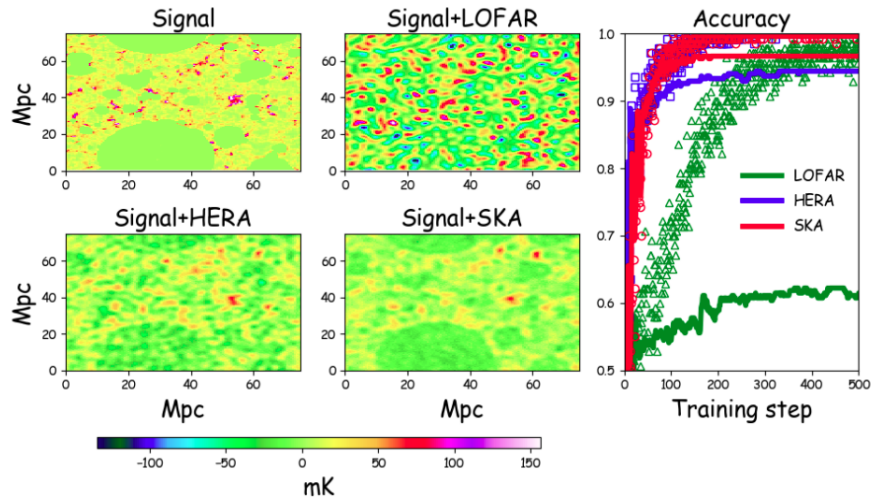


Figure 14.3: Training data and results of the classifier. On the left, an example 21 cm brightness temperature field from the training set, with different thermal noise instances according to instrument designs. On the right, the accuracy of training (open symbols) and testing (solid lines) for the three different instruments considered. Figure taken from Hassan et al. (2018).

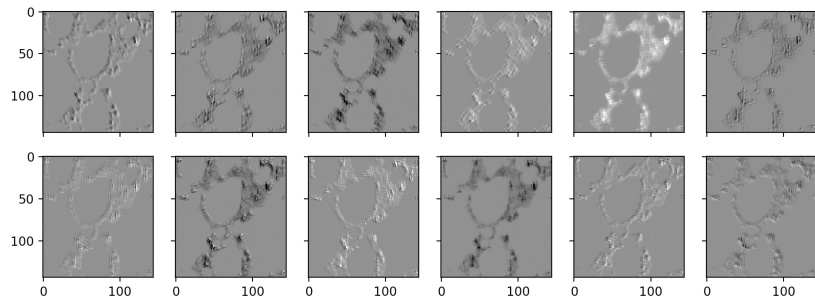


Figure 14.4: An input image propagated through the trained kernels of the first layer of the classifier. In this case, the color scale is arbitrary – contrasts within an image are more important. The axes are labelled by pixel index. Small, high-temperature regions are frequently emphasized.

the Universe. The 21CMFAST (Mesinger et al., 2011) and 21CMMC (Greig & Mesinger, 2015) software packages, widely used for realizations of the 21 cm brightness temperature field, parametrize reionization according to a few variables: the mean free path of ionizing photons ( $R_{\text{mfp}}$ ) the minimum virial temperature of star-forming haloes ( $T_{\text{vir}}$ ) and the ionizing efficiency of high-redshift galaxies ( $\zeta$ ).

We investigated the effectiveness of using CNNs to regress upon  $\zeta$ , holding all other parameters constant.  $\zeta$  is defined as:

$$\zeta = \frac{f_{\text{esc}} f_* N_\gamma}{1 + n_{\text{rec}}}, \quad (14.2)$$

where  $f_{\text{esc}}$  is the fraction of ionizing photons that escape into the IGM,  $f_*$  is the fraction of galactic gas in stars,  $N_\gamma$  is the number if ionizing photons produced per baryon in stars, and  $n_{\text{rec}}$  is the expected number of recombinations per hydrogen atom. The theoretical values of  $f_{\text{esc}}$  and  $f_*$  are highly uncertain at high redshifts (e.g. Paardekooper et al., 2015; Meiksin et al., 2017). For the Population II stars at the redshift range of the EoR,  $N_\gamma \approx 4000$  (Barkana & Loeb, 2005). During the EoR, it is expected that  $n_{\text{rec}} \sim 1$  (e.g. McQuinn et al., 2011; Sobacchi & Mesinger, 2014). In 21CMFAST,  $\zeta$  is typically varied between 5 and 100, corresponding to  $f_{\text{esc}}$  values between 5% and 100%.

The  $\zeta$  is an attractive parameter for an initial analysis, as it has a large effect on the topology of the temperature field and a relatively intuitive interpretation. We generated 2000 21 cm brightness temperature fields with values of  $\zeta$  between 10 and 50, all at redshift  $z = 10$ , in a 150 Mpc box with 200 pixels on a side. Figure 14.5 shows two of these fields on the same mK color scale – one with  $\zeta = 30$ , the other with  $\zeta = 50$ . The effect of increased efficiency is extreme.

We built a CNN using keras (Chollet et al., 2015) to learn to regress on the value of  $\zeta$  for a training set of 1400 images (70% of the data). We used 3 convolutional layers interleaved with 3 average pooling layers and two dense layers with 10% dropout. Every kernel and dense-layer weight had an additive linear bias term which could also be learned by the network. We used ReLU activation functions throughout, and a mean squared error

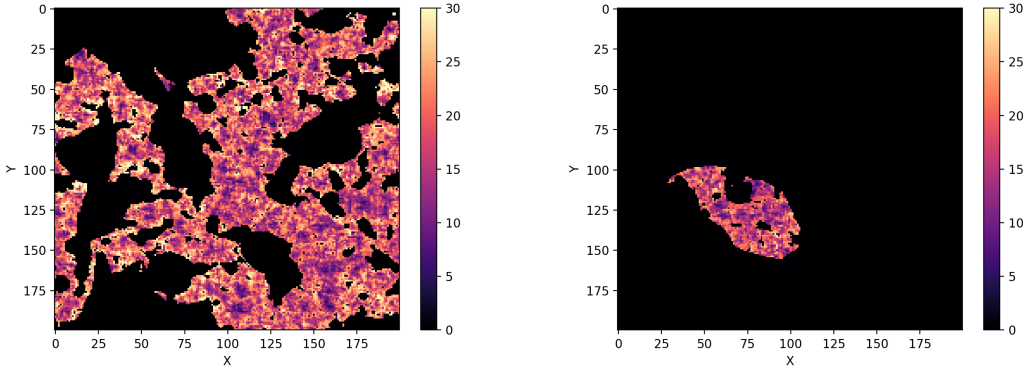


Figure 14.5: The effect of changing  $\zeta$  on the 21 cm brightness temperature field. The left panel shows a realization of reionization at  $z = 10$  with  $\zeta = 30$ . On the right, with all other parameters fixed and at the same redshift, is a realization with  $\zeta = 50$ . In the latter, almost the entire region has been reionized. The color scale is in mK.

cost function. A diagram of the CNN is shown in Figure 14.6.

The results of training are shown in Figure 14.7. For each step of training, we computed the cost function and the coefficient of determination ( $R^2$ ), which measured what fraction of the variance of the overall distribution of  $\zeta$  values the model, represented by forward propagation through the CNN, is capturing (e.g. Glantz & Slinker, 1990). The CNN quickly learns to regress to a mean squared error of  $\sim 5$ , which explains  $\sim 80\%$  of the variance of the  $\zeta$  distribution. Note that the number of steps is far fewer than the number of images in the training set. This is because, for computational efficiency, we only implemented backpropagation after a batch of training images had propagated forward through the network (this is known as ‘batch learning’). Batches were chosen randomly from the training set.

Figure 14.8 shows the predicted and true values of  $\zeta$  from the test set. The CNN was able to predict values to an accuracy suggested by the training results shown in Figure 14.7, but with a systematic bias towards lower  $\zeta$ . Agreement is better at the lowest values of  $\zeta$ . This is most likely due to the fact that the ReLU function is only extracting positive-valued information. In higher  $\zeta$  regimes, as shown in Figure 14.5,

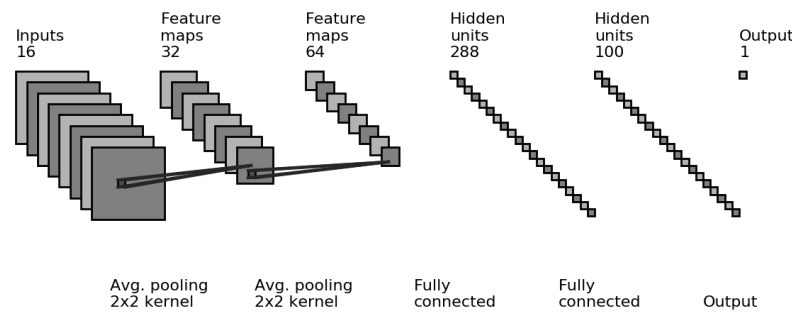


Figure 14.6: The CNN used for regression.

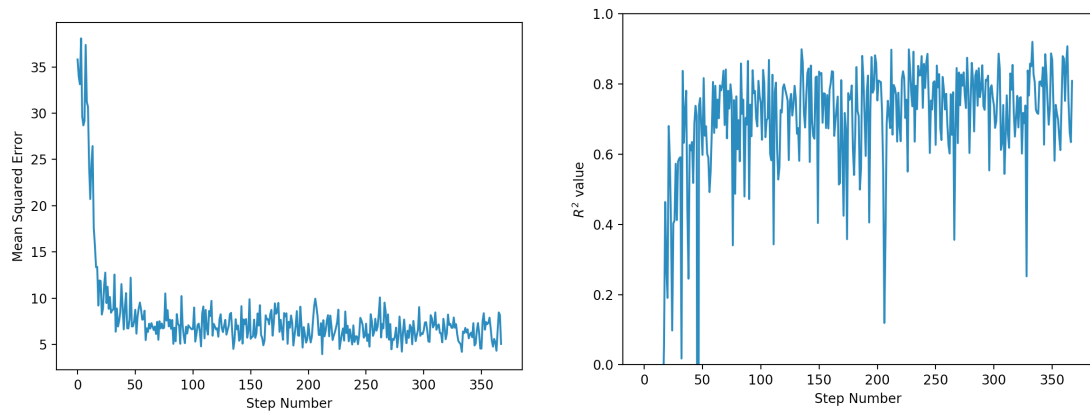


Figure 14.7: The results of training the CNN regressor. The left panel shows the value of the cost function at each step of training, which quickly reduces to a value of  $\sim 5$ . At each training step we also calculate the  $R^2$  value. Its value suggests that the CNN is capturing about 80% of the variance of the  $\zeta$  distribution.

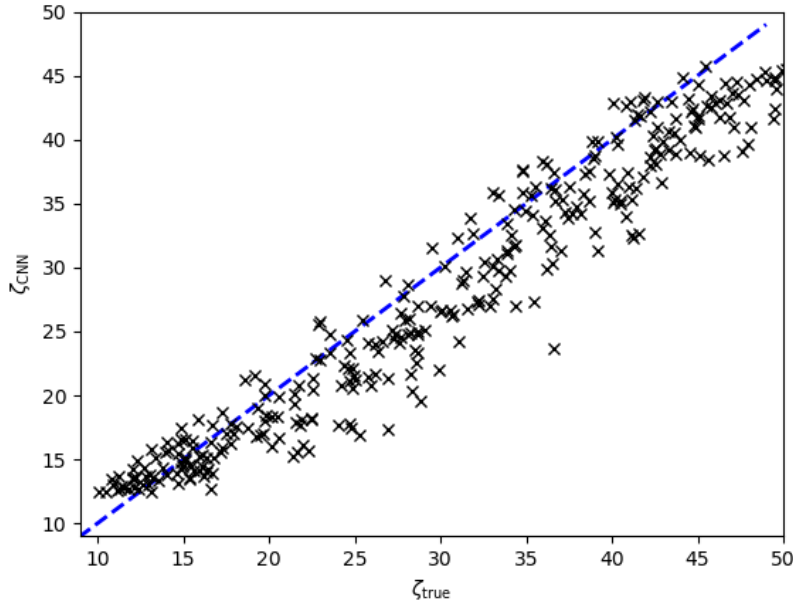


Figure 14.8: True vs. predicted values of  $\zeta$  from the test set. A 1:1 line is overplotted in blue.

reionization occurs very quickly, leaving much of the map reionized and blank – as far as the CNN can tell, featureless – so the examples it is able to learn had a lower-valued  $\zeta$  than they should. Moving to a ‘Leaky ReLU’ activation function in future attempts could help to rectify this issue.

## 14.4 Future directions

We have presented some basic test that showed that deep learning techniques may be worth developing to analyze 21 cm measurements. There are a host of directions to pursue in the future, as the field of deep learning is ripe for exploration. An immediate step to take is the development of a formalism for analyzing the trained convolutional kernels. These may contain useful data about what features in a 21 cm map are the most important for extracting physical parameters.

By moving to 3-dimensional cosmological maps and kernels, rather than reducing the information to a power spectrum, CNNs should be sensitive to the particular kinds of non-Gaussianity present in the data, without a priori knowledge. The result should be both more precise parameter estimates, due to extracting more information than the traditional methods. We hope to pursue the extraction of the bispectrum of the 21 cm field, or some proxy for it, in future work. Related to Chapter 13, one could also build a correlational neural network (Chandar et al., 2015) capable of calculating the optimal combination of two fields (for example, the HI and dark matter density fields, or the HI and kSZ fields) to extract the maximum amount of information (Feng et al., 2004). This may be the most useful avenue to pursue, to build the best tools for combining future survey data. However, it may be difficult to form a training set for such a network.

Finally, Chapter 6 presented large amounts of work building metrics to understand how to assure the quality of visibility data. The result of that work could be configured into a very large training set of ‘how and where interferometric visibilities can be corrupted’. The major challenge of using visibility data is their complex nature. Backpropagation of complex-valued input is a contemporary challenge (Guberman, 2016; Popa, 2017; Zhang et al., 2017) that is not fully-supported by any mainstream deep learning software packages. However, the volume of data generated by an interferometer such as HERA and the automatic flagging algorithms we have created could prove to be a powerful combination for future deep learning studies.

# Chapter 15

## Conclusions

A detection of the EoR would change the landscape of observational cosmology. Direct observation of the large scale structure of HI as it evolves through time would profoundly impact the understanding of the birth of the first galaxies and black holes, their influence on the IGM, and the cosmological density field. In combination with other probes of the early universe, EoR measurements will provide a complete picture of reionization and break measurement degeneracies in fundamental cosmological parameters. It's awesome, and it's worth the effort.

At the time of writing, the observational cosmology community is at the stage of setting limits on the power spectrum of the EoR. The primary challenges of astrophysical foregrounds and chromatic, noisy instruments force long integrations with high dynamic range calibration and innovative digital signal processing techniques. The spectral smoothness of synchrotron radiation – the dominant emission mechanism for low-frequency sources – compared to the spectrally structured emission from the 21 cm brightness contrast gives us our most powerful tool. We are able to isolate foreground power into a wedge-shaped region of Fourier space, while the 21 cm radiation scatters in to the EoR window during the Fourier transform. In order to keep the foregrounds isolated, the instrument, signal path, calibration and reduction stages must all maintain spectral smoothness. One astrophysical effect that violates this paradigm is Faraday-rotated po-

larized synchrotron, which can be both bright and spectrally structured.

The risk of contamination of the Stokes I EoR window from Faraday-rotated Stokes Q and U foregrounds motivated my study of polarization in Fourier space. Mapping polarized interferometric measurements into the mathematical space relevant to EoR measurements has proven to be rich in its information content, providing useful measurements of the polarized sky and the instrument itself. I have presented both the widest uniform sampling of polarized power in Fourier space, from the PAPER-32 imaging array, and the deepest integration on polarized power to date, using the PAPER-128 redundant grid. These measurements, and an intermediate-depth integration on polarized power with the HERA commissioning array, are all consistent with current models and observations of the diffuse low frequency sky.

As with the search for the EoR itself, observation of polarized power in Fourier space is currently in the business of limit-setting. The predicted weakness of polarized power at the low  $k_{\perp}$ , high  $k_{\parallel}$  Fourier modes is useful in the sense that contamination levels are inherently low, but makes characterization of polarized power difficult. A definitive measurement of the polarized fraction at the relevant  $k$  modes for an EoR detection is a crucial, but elusive measurement.

Throughout this work I have developed an intuition surrounding polarized leakage through direction-dependent and independent Jones matrices. I created a new redundant calibration scheme to account for the diagonal terms of the direction-independent Jones matrix in a polarization-conscious way, which gives very good agreement with instrumental simulations. Imaging-based calibration schemes were shown to correct the off-diagonal terms. HERA, capable of redundant and imaging calibration, will be able to capitalize on both of these schemes. With many more degrees of freedom, the direction-dependent Jones matrix is more difficult to manipulate and correct for. By simulating pseudo-Stokes HERA visibilities using a model Mueller matrix, we were able to verify the accuracy of our beam models, replicating most of the observations in image and Fourier space. A relatively simple next step would be to produce simulations for each

Mueller leakage term and subtract it from the total pseudo-Stokes visibility, in order to recover the diagonal parameters. This could provide a relatively cheap route to images of Stokes Q, U and V, ‘cleaned’ of Stokes I leakage.

For very precise measurements of the polarized sky, the effects of the ionosphere must be taken in to account. Most HERA observations will take place during solar minimum. As such, ionospheric depolarization will be very small. However, for longer-term projects such as SKA-Low, we have developed software packages and mathematical tools for understanding the impact of ionospheric fluctuations on polarized power. To verify our models, jackknives of polarized measurements taken during solar maximum, such as PAPER-64 or 128, could be used and checked for depolarization.

All of our current work suggests that HERA, once fully constructed, is on-track for a statistical detection of the EoR. The latter part of this work has given some suggestions on where we might go from there. Using PAPER-128 measurements, we were able to qualitatively reproduce a global signature in delay-space. While this looks promising, to adhere fully to the theory surrounding interferometric measurements of a monopole signal, it really requires a dedicated experiment, as well as further theoretical work to account for contamination from  $\ell > 0$  modes.

I have developed an exciting new formalism to perform cross-correlations between 21 cm power and other cosmological probes in Fourier space. Using higher-order correlation functions allows for recovery of non-Gaussian signals as well as avoidance of the foreground wedge. While we have concentrated on the kSZ in this work as the most near-term correlation available given the overlapping schedules of HERA and Stage 3 CMB experiments, similar relationships could be derived for ultra-deep pencil-beam integrations from JWST and ALMA, or for future intensity mapping surveys of CO and CI.

The machine learning and deep learning communities are currently undergoing radical and rapid innovations. These techniques have huge potential applications for the ‘big data’ inherent to interferometry. Clustering of quality-assurance metrics and automatic,

trained detection of RFI and other instrument systematics would be incredibly useful. These tools are currently under construction at UPenn and elsewhere. In this work we have shown the potential for recovery of cosmological information from futuristic EoR measurements.

Through hard-core theoretical work, unconventional instrument design and characterization, observational expertise, and a lot of international cooperation, the cosmology community is closer than ever to a detection of HI at cosmological distances. I am optimistic and excited to find out what the future holds.

# **Appendices**

# Appendix A

## Software

Software engineering and maintenance of existing codebases has been, generally speaking, historically undervalued and unappreciated by the astronomy community (Muna et al., 2016). In this Appendix I would like to provide a brief description of the major software packages used in this work – without which, the work would not exist.

### A.1 Astronomical Interferometry in Python (aipy)

The aipy software package (Parsons, 2016) was developed by a team based largely at the University of California, Berkeley and led by Aaron Parsons. Developed under NSF funding for the PAPER experiment, it provides a Python API to interact with interferometric visibilities stored in the MIRIAD file format (Sault et al., 2011). It is able to efficiently query large MIRIAD files due the APIs closeness to the underlying C code. It also contains calibration, deconvolution, imaging and phasing code in Python, and interfaces with HEALPix (see Section A.5, below) as well as other astronomical Python packages.

aipy is maintained by the HERA software team, and can be found at: <https://github.com/HERA-Team/aipy>.

## A.2 Astronomy in Python (astropy)

astropy is an open-source and community-developed core Python package for Astronomy, containing a host of extremely useful utility functions and objects (Astropy Collaboration et al., 2013).

## A.3 Common Astronomy Software Applications (CASA)

CASA is under active development, with the primary goal of supporting the data post-processing needs of the next generation of radio telescopes. It is developed by an international consortium of scientists based at the National Radio Astronomical Observatory (NRAO), the European Southern Observatory (ESO), the National Astronomical Observatory of Japan (NAOJ), the CSIRO Australia Telescope National Facility (CSIRO/ATNF), and the Netherlands Institute for Radio Astronomy (ASTRON), under the guidance of NRAO (McMullin et al., 2007).

## A.4 Deep Learning packages

Experimentation with deep learning analyses of 21 cm simulated observations took place in Keras (Chollet et al., 2015), PyTorch (Paszke et al., 2017) and Tensorflow (Abadi et al., 2016).

## A.5 Hierarchical Equal Area isoLatitude Pixelization of the sphere (HEALPix)

The HEALPix software, and its Python wrapper healpy, provide a pixelization which subdivides a spherical surface into pixels which each cover the same surface area as every other pixel. Pixel centers occur on a discrete number of rings of constant latitude. This

scheme makes natively spherical measurements, such as angular power spectra and wide-field images, simple and efficient to interact with (Górski et al., 2005).

## A.6 pyuvdata

pyuvdata provides a Python interface to interferometric data. It can read and write MIRIAD and UVFITS file formats, as well as read CASA measurement sets and FHD (Sullivan et al., 2012b) visibility save files (Hazelton et al., 2017).

pyuvdata is maintained by the HERA software team, and can be found at: <https://github.com/HERA-Team/pyuvdata>.

## A.7 The Scientific Python Ecosystem (scipy)

Many of the above tools require at least one of the many packages under the `scipy` ecosystem. It is truly foundational to almost any scientific analysis that takes place in Python (Jones et al., 2001).

# Bibliography

Abadi, M. et al. 2016, ArXiv e-prints

Abazajian, K. N. et al. 2016, ArXiv e-prints

Afraimovich, E. L., Astafyeva, E. I., Oinats, A. V., Yasukevich, Y. V., & Zhivetiev, I. V. 2008, *Annales Geophysicae*, 26, 335

Ali, Z. S. et al. 2015, ArXiv e-prints

Alvarez, M. A. 2016, *ApJ*, 824, 118

Appleton, E. V. 1946, *Nature*, 157, 691

Asad, K. M. B., Koopmans, L. V. E., Jelić, V., de Bruyn, A. G., Pandey, V. N., & Gehlot, B. K. 2017, ArXiv e-prints

Asad, K. M. B. et al. 2016, *MNRAS*, 462, 4482

—. 2015, *MNRAS*, 451, 3709

Astropy Collaboration et al. 2013, *A&A*, 558, A33

Asvarov, A. I. 2014, *A&A*, 561, A70

Babich, D. & Loeb, A. 2005, *ApJ*, 635, 1

Backer, D. C. et al. 2010, HERA - Hydrogen Epoch of Reionization Arrays, Submitted for consideration by the Astro2010 Decadal Survey Program Panel

- Badman, S. V., Branduardi-Raymont, G., Galand, M., Hess, S. L., Krupp, N., Lamy, L., Melin, H., & Tao, C. 2015, Space Science Reviews, 187, 99
- Barkana, R. 2018, Nature, 555, 71
- Barkana, R. & Loeb, A. 2005, The Astrophysical Journal, 626, 1
- Barnett, R., Warren, S. J., Becker, G. D., Mortlock, D. J., Hewett, P. C., McMahon, R. G., Simpson, C., & Venemans, B. P. 2017, A&A, 601, A16
- Barry, N., Hazelton, B., Sullivan, I., Morales, M. F., & Pober, J. C. 2016, MNRAS, 461, 3135
- Battaglia, N., Trac, H., Cen, R., & Loeb, A. 2013, ApJ, 776, 81
- Beardsley, A. P. et al. 2016, ApJ, 833, 102
- Beardsley, A. P., Morales, M. F., Lidz, A., Malloy, M., & Sutter, P. M. 2015, ApJ, 800, 128
- Beck, R. 2003, ArXiv Astrophysics e-prints
- Becker, R. H. et al. 2001, AJ, 122, 2850
- Bernardi, G. et al. 2009, A&A, 500, 965
- . 2010, A&A, 522, A67
- . 2013, ApJ, 771, 105
- Bond, J. R., Cole, S., Efstathiou, G., & Kaiser, N. 1991, ApJ, 379, 440
- Bouwens, R. J. et al. 2015, ApJ, 803, 34
- . 2016, ApJ, 830, 67
- Bowman, J. D. et al. 2013, PASA, 30, e031

- Bowman, J. D. & Rogers, A. E. E. 2010, *Nature*, 468, 796
- Bowman, J. D., Rogers, A. E. E., Monsalve, R. A., Mozdzen, T. J., & Mahesh, N. 2018, *Nature*, 555, 67
- Brentjens, M. A. & de Bruyn, A. G. 2005, *A&A*, 441, 1217
- Brunner, F. K. & Welsch, W. M. 1993, *GPS World*, 4, 42
- Carilli, C. L. & Rawlings, S. 2004, *NewAR*, 48, 979
- Carozzi, T. D. & Woan, G. 2009, *MNRAS*, 395, 1558
- Chandar, S., Khapra, M. M., Larochelle, H., & Ravindran, B. 2015, ArXiv e-prints
- Chollet, F. et al. 2015, Keras, <https://github.com/fchollet/keras>
- Civil Aviation Authority. 2016, <http://wwwcaa.co.za/>, website
- Cohen, M. H. 1958, *Proceedings of the IRE*, 46, 172
- Condon, E. U. & Shortley, G. H. 1951, *The theory of atomic spectra* (Cambridge University Press)
- Condon, J. J., Cotton, W. D., Greisen, E. W., Yin, Q. F., Perley, R. A., Taylor, G. B., & Broderick, J. J. 1998, *AJ*, 115, 1693
- Cooray, A., Bock, J. J., Keatin, B., Lange, A. E., & Matsumoto, T. 2004, *ApJ*, 606, 611
- Cornwell, T. 2016
- Cornwell, T. J. 1983, *A&A*, 121, 281
- Cotton, W. & Condon, J. 2002, in *Proceedings of the URSI General Assembly*
- Datta, A., Bowman, J. D., & Carilli, C. L. 2010, *ApJ*, 724, 526

- de Oliveira-Costa, A., Tegmark, M., Gaensler, B. M., Jonas, J., Landecker, T. L., & Reich, P. 2008, MNRAS, 388, 247
- DeBoer, D. R. et al. 2017, PASP, 129, 045001
- Dewdney, P. E., Hall, P. J., Schilizzi, R. T., & Lazio, T. J. L. 2009, Proceedings of the IEEE, 97, 1482
- Di Matteo, T., Perna, R., Abel, T., & Rees, M. J. 2002, ApJ, 564, 576
- Dillon, J. S. et al. 2017, ArXiv e-prints
- . 2014, Phys. Rev. D, 89, 023002
- . 2015, Phys. Rev. D, 91, 123011
- Dillon, J. S. & Parsons, A. R. 2016, ApJ, 826, 181
- Erdogan, E. et al. 2016, in EGU General Assembly Conference Abstracts, Vol. 18, EGU General Assembly Conference Abstracts, 12685
- Erickson, W. C., Perley, R. A., Flatters, C., & Kassim, N. E. 2001, A&A, 366, 1071
- Ewall-Wice, A. et al. 2016a, ApJ, 831, 196
- Ewall-Wice, A., Chang, T.-C., Lazio, J., Dore, O., Seiffert, M., & Monsalve, R. A. 2018, ArXiv e-prints
- Ewall-Wice, A. et al. 2016b, MNRAS, 460, 4320
- Fagnoni, N. & de Lera Acedo, E. 2016, ArXiv e-prints
- Fan, X., Carilli, C. L., & Keating, B. 2006a, ARA&A, 44, 415
- Fan, X. et al. 2006b, AJ, 132, 117
- Farnes, J. S., Gaensler, B. M., & Carretti, E. 2014, ApJS, 212, 15

- Feng, D.-Z., Zhang, X.-D., & Bao, Z. 2004, IEEE Transactions on Neural Networks, 15, 1541
- Field, G. B. 1956, ApJ, 124, 555
- . 1959, ApJ, 129, 536
- Finlay, C. C. et al. 2010, Geophysical Journal International, 183, 1216
- Fixsen, D. J., Kogut, A., Levin, S., Limon, M., Lubin, P., Mirel, P., Seiffert, M., & Wollack, E. 2004, ApJ, 612, 86
- Fomalont, E. B., Ebneter, K. A., van Breugel, W. J. M., & Ekers, R. D. 1989, ApJL, 346, L17
- Furlanetto, S. R., Oh, S. P., & Briggs, F. H. 2006, Physics Review, 433, 181
- Gardner, J. P. et al. 2009, in Astrophysics in the Next Decade (Springer), 1–29
- Geil, P. M., Gaensler, B. M., & Wyithe, J. S. B. 2011, MNRAS, 418, 516
- George, E. M. et al. 2015, ApJ, 799, 177
- Glantz, S. A. & Slinker, B. K. 1990, Primer of applied regression and analysis of variance  
No. Sirsi) i9780070234079
- Gong, Y., Cooray, A., Silva, M., Santos, M. G., Bock, J., Bradford, C. M., & Zemcov, M. 2012, ApJ, 745, 49
- Górski, K. M., Hivon, E., Banday, A. J., Wandelt, B. D., Hansen, F. K., Reinecke, M., & Bartelmann, M. 2005, ApJ, 622, 759
- Gradshteyn, I. S. & Ryzhik, I. 2000, Table of integrals, series, and products. Translated from the Russian. Translation edited and with a preface by Alan Jeffrey and Daniel Zwillinger

- Greig, B. & Mesinger, A. 2015, MNRAS, 449, 4246
- . 2017, MNRAS, 465, 4838
- Guberman, N. 2016, ArXiv e-prints
- Gunn, J. E. & Peterson, B. A. 1965, ApJ, 142, 1633
- Hamaker, J. P. & Bregman, J. D. 1996, A&AS, 117, 161
- Hamaker, J. P., Bregman, J. D., & Sault, R. J. 1996, A&AS, 117, 137
- Hand, N. et al. 2012, Physical Review Letters, 109, 041101
- Hassan, S., Davé, R., Finlator, K., & Santos, M. G. 2016, Monthly Notices of the Royal Astronomical Society, 457, 1550
- Hassan, S., Davé, R., Finlator, K., & Santos, M. G. 2017, MNRAS, 468, 122
- Hassan, S., Davé, R., Mitra, S., Finlator, K., Ciardi, B., & Santos, M. G. 2017, Monthly Notices of the Royal Astronomical Society, 473, 227
- Hassan, S., Liu, A., Kohn, S., Aguirre, J. E., La Plante, P., & Lidz, A. 2018
- Haverkorn, M. 2015, in Astrophysics and Space Science Library, Vol. 407, Magnetic Fields in Diffuse Media, ed. A. Lazarian, E. M. de Gouveia Dal Pino, & C. Melioli, 483
- Hazelton, B., Beardsley, A., Pober, J., Jacobs, D., Ali, Z., & Lanman, A. 2017, HERA-Team/pyuvdata: Version 1.1
- Hazelton, B. J., Morales, M. F., & Sullivan, I. S. 2013, ApJ, 770, 156
- Hinshaw, G. et al. 2013, ApJS, 208, 19
- Hinton, G. E. & Salakhutdinov, R. R. 2006, Science, 313, 504

- Hinton, G. E., Srivastava, N., Krizhevsky, A., Sutskever, I., & Salakhutdinov, R. R. 2012,  
ArXiv e-prints
- Högbom, J. A. 1974, A&AS, 15, 417
- Huffenberger, K. M. et al. 2015, ApJ, 806, 112
- Hunacek, J. et al. 2016, in Proc. SPIE, Vol. 9914, Millimeter, Submillimeter, and Far-Infrared Detectors and Instrumentation for Astronomy VIII, 99140L
- Hurley-Walker, N. et al. 2017, MNRAS, 464, 1146
- Ichiki, K. 2014, Progress of Theoretical and Experimental Physics, 2014, 06B109
- Iglewicz, B. & Hoaglin, D. 2010, Engineering Statistical Handbook, 1
- Iijima, B. et al. 1999, Journal of Atmospheric and Solar-Terrestrial Physics, 61, 1205
- Intema, H., Van der Tol, S., Cotton, W., Cohen, A., Van Bemmel, I., & Röttgering, H. 2009, Astronomy & Astrophysics, 501, 1185
- Jacobs, D. C. 2011, PhD thesis, University of Pennsylvania
- Jacobs, D. C. et al. 2011, ApJ, 734, L34
- . 2016, ApJ, 825, 114
- . 2013, ApJ, 776, 108
- . 2015, ApJ, 801, 51
- Jelić, V. et al. 2014, A&A, 568, A101
- . 2015, A&A, 583, A137
- Jelić, V., Zaroubi, S., Labropoulos, P., Bernardi, G., de Bruyn, A. G., & Koopmans, L. V. E. 2010, MNRAS, 409, 1647

- Jensen, H., Majumdar, S., Mellema, G., Lidz, A., Iliev, I. T., & Dixon, K. L. 2016,  
MNRAS, 456, 66
- Joachimi, B., Shi, X., & Schneider, P. 2009, A&A, 508, 1193
- Jones, E., Oliphant, T., Peterson, P., et al. 2001, SciPy: Open source scientific tools for  
Python
- Jones, R. C. 1941, Journal of the Optical Society of America (1917-1983), 31, 488
- Kern, N. S., Liu, A., Parsons, A. R., Mesinger, A., & Greig, B. 2017, ApJ, 848, 23
- Kerrigan, J. et al. 2018, ArXiv e-prints
- Klobuchar, J. A. 1983, Ionospheric Effects on Earth-Space Propagation
- Kogut, A. et al. 2003, ApJS, 148, 161
- Kohn, S. et al. 2018, ArXiv e-prints
- Kohn, S. A. et al. 2016, ApJ, 823, 88
- Komatsu, E. et al. 2009, The Astrophysical Journal Supplement Series, 180, 330
- Komjathy, A., Sparks, L., Wilson, B. D., & Mannucci, A. J. 2005, Radio Science, 40
- Krizhevsky, A., Sutskever, I., & Hinton, G. E. 2012, in Advances in neural information  
processing systems, 1097–1105
- La Plante, P., Battaglia, N., Natarajan, A., Peterson, J. B., Trac, H., Cen, R., & Loeb, A.  
2014, ApJ, 789, 31
- Lanyi, G. E. & Roth, T. 1988, Radio Science, 23, 483
- LeCun, Y., Bengio, Y., et al. 1995, The Handbook of Brain Theory and Neural Networks,  
3361, 1995

- Lenc, E. et al. 2017, PA&A, 34, e040
- . 2016, ApJ, 830, 38
- Lewis, A., Challinor, A., & Lasenby, A. 2000a, ApJ, 538, 473
- . 2000b, ApJ, 538, 473
- Liddle, A. R. & Lyth, D. H. 2000, Cosmological inflation and large-scale structure (Cambridge University Press)
- Lidz, A., Furlanetto, S. R., Oh, S. P., Aguirre, J., Chang, T.-C., Doré, O., & Pritchard, J. R. 2011, ApJ, 741, 70
- Lidz, A., Zahn, O., McQuinn, M., Zaldarriaga, M., Dutta, S., & Hernquist, L. 2007, ApJ, 659, 865
- Liu, A. & Parsons, A. R. 2016, Monthly Notices of the Royal Astronomical Society, 457, 1864
- Liu, A., Parsons, A. R., & Trott, C. M. 2014a, Phys. Rev. D, 90, 023018
- . 2014b, Phys. Rev. D, 90, 023019
- Liu, A., Pritchard, J. R., Allison, R., Parsons, A. R., Seljak, U., & Sherwin, B. D. 2016, Phys. Rev. D, 93, 043013
- Liu, A., Tegmark, M., Morrison, S., Lutomirski, A., & Zaldarriaga, M. 2010, MNRAS, 408, 1029
- Loi, S. T. et al. 2015, Geophys. Res. Lett., 42, 3707
- López-Caniego, M., Massardi, M., González-Nuevo, J., Lanz, L., Herranz, D., De Zotti, G., Sanz, J. L., & Argüeso, F. 2009, ApJ, 705, 868
- Ludwig, A. C. 1973, IEEE Transactions on Antennas and Propagation, 21, 116

- MacDoran, P. & Spitzmesser, D. 1989, Method and apparatus for deriving pseudo range from earth-orbiting satellites, uS Patent 4,797,677
- Macquart, J.-P. & Fender, R. P. 2004 (Springer Science & Business Media)
- Madau, P., Meiksin, A., & Rees, M. J. 1997, ApJ, 475, 429
- Majumdar, S., Pritchard, J. R., Mondal, R., Watkinson, C. A., Bharadwaj, S., & Mellemma, G. 2017, ArXiv e-prints
- Mannucci, A., Wilson, B., Yuan, D., Ho, C., Lindqwister, U., & Runge, T. 1998, Radio science, 33, 565
- Manti, S., Gallerani, S., Ferrara, A., Greig, B., & Feruglio, C. 2017, MNRAS, 466, 1160
- Mather, J. C., Fixsen, D. J., Shafer, R. A., Mosier, C., & Wilkinson, D. T. 1999, ApJ, 512, 511
- McKinley, B. et al. 2015, MNRAS, 446, 3478
- McMullin, J. P., Waters, B., Schiebel, D., Young, W., & Golap, K. 2007, in Astronomical Data Analysis Software and Systems XVI, ed. R. A. Shaw, F. Hill, & D. J. Bell, 376, ASP, San Francisco, CA, 127
- McQuinn, M., Lidz, A., Zahn, O., Dutta, S., Hernquist, L., & Zaldarriaga, M. 2007, MNRAS, 377, 1043
- McQuinn, M., Oh, S. P., & Faucher-Giguère, C.-A. 2011, ApJ, 743, 82
- Meiksin, A., Khochfar, S., Paardekooper, J.-P., Dalla Vecchia, C., & Kohn, S. 2017, MNRAS, 471, 3632
- Mesinger, A., Furlanetto, S., & Cen, R. 2011, MNRAS, 411, 955
- Mevius, M. et al. 2016, Radio Science, 51, 927

- Mirocha, J., Skory, S., Burns, J. O., & Wise, J. H. 2012, ApJ, 756, 94
- Mohan, N. & Rafferty, D. 2015, PyBDSM: Python Blob Detection and Source Measurement, Astrophysics Source Code Library, record 1502.007
- Moore, D. F. 2014, PhD thesis, University of Pennsylvania
- Moore, D. F. et al. 2017, ApJ, 836, 154
- Moore, D. F., Aguirre, J. E., Parsons, A. R., Jacobs, D. C., & Pober, J. C. 2013, ApJ, 769, 154
- Morales, M. F., Hazelton, B., Sullivan, I., & Beardsley, A. 2012, ApJ, 752, 137
- Mozdzen, T. J., Bowman, J. D., Monsalve, R. A., & Rogers, A. E. E. 2017, MNRAS, 464, 4995
- Mueller, H. 1948, The foundation of optics, Vol. 38, 661
- Muna, D. et al. 2016, ArXiv e-prints
- Neben, A. R. et al. 2016, ApJ, 826, 199
- Nhan, B. D., Bradley, R. F., & Burns, J. O. 2016, ArXiv e-prints
- NRC, N. R. C. 2010, New Worlds, New Horizons in Astronomy and Astrophysics (Washington, DC: The National Academies Press)
- Nunhokee, C. D. 2018, PhD thesis, Rhodes University
- Nunhokee, C. D. et al. 2017, ApJ, 848, 47
- Offringa, A. R., van de Gronde, J. J., & Roerdink, J. B. T. M. 2012, A&A, 539, A95
- Oh, S. P. & Mack, K. J. 2003, MNRAS, 346, 871
- Oppermann, N. et al. 2012, A& A, 542, A93

- Paardekooper, J.-P., Khochfar, S., & Dalla Vecchia, C. 2015, MNRAS, 451, 2544
- Paciga, G. et al. 2013, MNRAS, 433, 639
- Parashare, C. R. & Bradley, R. F. 2006, 120-205 MHz Receiver for PAPER: Precision Array to Probe the Epoch of Reionization, Dynamic Spectroscopy Laboratory Report Series 4, NRAO NTC-DSL Laboratory Report
- Parsons, A. 2016, AIPY: Astronomical Interferometry in PYthon, Astrophysics Source Code Library
- Parsons, A. et al. 2008, PASA, 120, 1207
- Parsons, A., Pober, J., McQuinn, M., Jacobs, D., & Aguirre, J. 2012a, ApJ, 753, 81
- Parsons, A. R. & Backer, D. C. 2009, AJ, 138, 219
- Parsons, A. R. et al. 2010, AJ, 139, 1468
- . 2014, ApJ, 788, 106
- Parsons, A. R., Liu, A., Ali, Z. S., & Cheng, C. 2016, ApJ, 820, 51
- Parsons, A. R., Pober, J. C., Aguirre, J. E., Carilli, C. L., Jacobs, D. C., & Moore, D. F. 2012b, ApJ, 756, 165
- Paszke, A. et al. 2017
- Patil, A. H. et al. 2017, ApJ, 838, 65
- Pen, U.-L., Chang, T.-C., Hirata, C. M., Peterson, J. B., Roy, J., Gupta, Y., Odegova, J., & Sigurdson, K. 2009, MNRAS, 399, 181
- Pentericci, L. et al. 2016, ApJ, 829, L11
- Perley, R. A., Roser, H.-J., & Meisenheimer, K. 1997, A& A, 328, 12

- Planck Collaboration et al. 2016a, A&A, 594, A1
- . 2016b, A&A, 596, A108
- . 2016c, A&A, 594, A13
- Pober, J. 2015, Updated 21cm Experiment Sensitivities, Tech. Rep. 4, Brown University
- . 2016, 21cmSense: Calculating the sensitivity of 21cm experiments to the EoR power spectrum, Astrophysics Source Code Library
- Pober, J. C. et al. 2015, ApJ, 809, 62
- . 2014, ApJ, 782, 66
- . 2013, ApJL, 768, L36
- . 2012, AJ, 143, 53
- Popa, C.-A. 2017, in Neural Networks (IJCNN), 2017 International Joint Conference on, IEEE, 816–822
- Presley, M. E., Liu, A., & Parsons, A. R. 2015, ApJ, 809, 18
- Press, W. H. & Schechter, P. 1974, ApJ, 187, 425
- Price, D. C. 2016a, PyGSM: Python interface to the Global Sky Model, Astrophysics Source Code Library
- . 2016b, ArXiv e-prints
- Pritchard, J. R. & Loeb, A. 2010, PRD, 82, 023006
- Ricotti, M. 2016, MNRAS, 462, 601
- Righi, M., Hernández-Monteagudo, C., & Sunyaev, R. A. 2008, A&A, 489, 489
- Robertson, B. E. & Ellis, R. S. 2012, ApJ, 744, 95

Robertson, B. E., Ellis, R. S., Furlanetto, S. R., & Dunlop, J. S. 2015, ApJ, 802, L19

Robertson, B. E. et al. 2013, ApJ, 768, 71

Rogers, A. E. E. & Bowman, J. D. 2008, AJ, 136, 641

Rosenblatt, F. 1961, Principles of neurodynamics. perceptrons and the theory of brain mechanisms, Tech. rep., Cornell Aeronautical Lab Inc., Buffalo NY

Royden, H., Miller, R., & Buennagel, L. 1984, Radio science, 19, 798

Rumelhart, D. E., Hinton, G. E., & Williams, R. J. 1986, nature, 323, 533

Rybicki, G. B. & Lightman, A. P. 1979, Radiative processes in astrophysics

Salvaterra, R., Ferrara, A., & Dayal, P. 2011, MNRAS, 414, 847

Santos, M. G., Cooray, A., & Knox, L. 2005, ApJ, 625, 575

Santos, M. G., Ferramacho, L., Silva, M. B., Amblard, A., & Cooray, A. 2010, MNRAS, 406, 2421

Sathyaranayana Rao, M., Subrahmanyam, R., Udaya Shankar, N., & Chluba, J. 2017, ApJ, 840, 33

Sault, R. J., Hamaker, J. P., & Bregman, J. D. 1996, A&AS, 117, 149

Sault, R. J., Teuben, P., & Wright, M. C. H. 2011, MIRIAD: Multi-channel Image Reconstruction, Image Analysis, and Display, Astrophysics Source Code Library

Schilizzi, R. et al. 2007, SKA Memorandum, 100

Sefusatti, E., Crocce, M., Scoccimarro, R., & Couchman, H. M. P. 2016, MNRAS, 460, 3624

Shaw, J. R., Sigurdson, K., Pen, U.-L., Stebbins, A., & Sitwell, M. 2014, ApJ, 781, 57

- Shaw, J. R., Sigurdson, K., Sitwell, M., Stebbins, A., & Pen, U.-L. 2015, Phys. Rev. D, 91, 083514
- Shaw, L. D., Nagai, D., Bhattacharya, S., & Lau, E. T. 2010, ApJ, 725, 1452
- Sheth, R. K. & Tormen, G. 1999, MNRAS, 308, 119
- Silk, J. 1968, ApJ, 151, 459
- Silva, M. B., Santos, M. G., Gong, Y., Cooray, A., & Bock, J. 2013, ApJ, 763, 132
- SKA Panel. 2012, Expert Panel on Radio Quiet Zone and RFI Regulation Report, Tech. rep., Square Kilometer Array, [https://www.skatelescope.org/wp-content/uploads/2012/06/79\\_Report\\_of\\_The\\_Expert\\_Panel\\_on\\_Radio\\_Quiet\\_Zone\\_and\\_RFI\\_Regulation.pdf](https://www.skatelescope.org/wp-content/uploads/2012/06/79_Report_of_The_Expert_Panel_on_Radio_Quiet_Zone_and_RFI_Regulation.pdf)
- Smirnov, O. M. 2011a, A&A, 527, A106
- . 2011b, A&A, 527, A107
- . 2011c, A&A, 527, A108
- . 2011d, A&A, 531, A159
- Smith, K. M. & Ferraro, S. 2016, ArXiv e-prints
- Sobacchi, E. & Mesinger, A. 2014, Monthly Notices of the Royal Astronomical Society, 440, 1662
- Sobral, D., Matthee, J., Darvish, B., Schaerer, D., Mobasher, B., Röttgering, H. J. A., Santos, S., & Hemmati, S. 2015, ApJ, 808, 139
- Sokolowski, M. et al. 2017, PASA, 34, e062
- Sotomayor-Beltran, C. et al. 2013, A&A, 552, A58

- South African Civil Aviation Authority. 2008, Flight calibration dates of VOR's in the Republic of South Africa, Tech. Rep. 25.6, Aeronautical Information Circular, <http://209.203.9.244/resource%20center/AIC'S/25.6.pdf>
- Spergel, D. N. et al. 2003, ApJS, 148, 175
- Spreeuw, H., Scheers, B., & Wijers, R. A. M. J. 2010, A&A, 509, A99
- Staatskoerant. 2008, South African Table of Frequency Allocations, Tech. Rep. 31264, ICASA, [http://thornton.co.za/resources/31264\\_890\\_complete-1.pdf](http://thornton.co.za/resources/31264_890_complete-1.pdf)
- Stefan, I. I. et al. 2013, MNRAS, 432, 1285
- Sullivan, I. S. et al. 2012a, ApJ, 759, 17
- . 2012b, ApJ, 759, 17
- Sunyaev, R. A. & Zeldovich, Y. B. 1970, Astrophysics and Space Science, 7, 3
- Tariku, Y. A. 2015, Earth, Planets, and Space, 67, 35
- Thompson, A. R., Moran, J. M., & Swenson, Jr., G. W. 2017, Interferometry and Synthesis in Radio Astronomy, 3rd Edition
- Thomson, R. C., Crane, P., & Mackay, C. D. 1995, ApJL, 446, L93
- Thyagarajan, N. et al. 2015a, ApJ, 804, 14
- . 2015b, ApJ, 807, L28
- Thyagarajan, N., Parsons, A. R., DeBoer, D. R., Bowman, J. D., Ewall-Wice, A. M., Neben, A. R., & Patra, N. 2016, ApJ, 825, 9
- Tingay, S. J. et al. 2013, PASA, 30, 7
- Titheridge, J. E. 1972, P& SS, 20, 353

- Trott, C. M. et al. 2016, ApJ, 818, 139
- Trott, C. M., Wayth, R. B., & Tingay, S. J. 2012, ApJ, 757, 101
- Van Eck, C. L. et al. 2018, ArXiv e-prints
- van Haarlem, M. P. et al. 2013, A&A, 556, A2
- van Straten, W., Manchester, R. N., Johnston, S., & Reynolds, J. E. 2010, PASA, 27, 104
- Vedantham, H., Udaya Shankar, N., & Subrahmanyan, R. 2012, ApJ, 745, 176
- Vedantham, H. K. & Koopmans, L. V. E. 2015, MNRAS, 453, 925
- . 2016, MNRAS, 458, 3099
- Venumadhav, T., Chang, T.-C., Doré, O., & Hirata, C. M. 2016, ApJ, 826, 116
- Vogelsberger, M. et al. 2014, MNRAS, 444, 1518
- Voytek, T. C., Natarajan, A., Jáuregui García, J. M., Peterson, J. B., & López-Cruz, O. 2014, ApJ, 782, L9
- Wang, F. Y. & Dai, Z. G. 2009, MNRAS, 400, L10
- Wang, F. Y., Dai, Z. G., & Liang, E. W. 2015, New Astronomy Reviews, 67, 1
- Wang, X., Tegmark, M., Santos, M. G., & Knox, L. 2006, ApJ, 650, 529
- Watkinson, C. A., Majumdar, S., Pritchard, J. R., & Mondal, R. 2017, MNRAS, 472, 2436
- Wayth, R. B. et al. 2015, PASA, 32, e025
- Wieringa, M. H. 1992, Experimental Astronomy, 2, 203
- Wigner, E. P. 1951in , Cambridge University Press, 790–798

- Wolleben, M., Landecker, T. L., Reich, W., & Wielebinski, R. 2006, A& A, 448, 411
- World Aero Data. 2016, <http://worldaerodata.com/>, website
- Wouthuysen, S. A. 1952, AJ, 57, 31
- Yatawatta, S. et al. 2013, A&A, 550, A136
- Zackrisson, E., Rydberg, C.-E., Schaefer, D., Östlin, G., & Tuli, M. 2011, The Astrophysical Journal, 740, 13
- Zahn, O. et al. 2012, ApJ, 756, 65
- Zaldarriaga, M. 1997, Phys. Rev. D, 55, 1822
- Zaldarriaga, M., Furlanetto, S. R., & Hernquist, L. 2004, ApJ, 608, 622
- Zarka, P. & Kurth, W. 2005, Space science reviews, 116, 371
- Zeldovich, Y. B. & Sunyaev, R. A. 1969, Astrophysics and Space Science, 4, 301
- Zhang, Z., Wang, H., Xu, F., & Jin, Y.-Q. 2017, IEEE Transactions on Geoscience and Remote Sensing, 55, 7177
- Zheng, H. et al. 2014, MNRAS, 445, 1084
- Zheng, H. et al. 2017, MNRAS, 464, 3486
- Zhu, H.-M., Pen, U.-L., Yu, Y., Er, X., & Chen, X. 2016, Physical Review D, 93, 103504
- Zolesi, B. & Cander, L. R. 2014, Ionospheric prediction and forecasting (Springer)